Multi-source domain adaptation on imbalanced data: application to the improvement of chairlifts safety

Kevin Bascol





École Doctorale ED488 Sciences, Ingénierie, Santé

Multi-source domain adaptation on imbalanced data: application to the improvement of chairlifts safety

---

Adaptation de domaine multisource sur données déséquilibrées : application à l'amélioration de la sécurité des télésièges

Thèse préparée par **Kevin Bascol**
au sein de l'**Université Jean Monnet de Saint-Étienne**
pour obtenir le grade de :

Docteur de l'Université de Lyon
Spécialité : **Informatique**

Univ Lyon, UJM-Saint-Etienne, CNRS, Institut d'Optique Graduate School,
Laboratoire Hubert Curien UMR 5516, F-42023, Saint-Etienne, France.

Bluecime, 38330, Montbonnot Saint-Martin, France.

Thèse soutenue publiquement le **16 Décembre 2019** devant le jury composé de :

Diane Larlus	Researcher, NAVER LABS	Examinatrice
Patrick Pérez	Scientific Director, HDR, Valeo.ai	Rapporteur
Laure Tougne	Professeure, Université Lumière Lyon 2	Examinatrice
Christian Wolf	Maître de Conférences, HDR, INSA de Lyon	Rapporteur
Florent Dutrech	Ingénieur R&D, Bluecime	Membre invité
Rémi Emonet	Maître de Conférences, Université de Saint-Étienne	Co-encadrant
Élisa Fromont	Professeure, Université de Rennes I	Directrice

Contents

Introduction

Each winter, millions of people across the world go skiing, snowboarding, or sledding in ski resorts. In summer also, the resorts may be open, for hiking or cycling. Regardless of the season, chairlifts are widely spread means of transportation across a resort. In the peak season, a chairlift can transport thousands of people a day. Keeping all the passengers safe is a great concern for the resorts managers.

In France, a study analyzed the 108 *severe* accidents which happened on chairlifts between 2006 and 2014[1]. The results of the study showed that 70% of the accidents happened either at boarding or while disembarking the chairlifts vehicles. Moreover, they showed that 90% of the accidents were caused by the behavior of the passengers. Ensuring that the passengers are correctly seated in the vehicle and that they have properly closed the restraining bar may allow the resorts to avoid numerous accidents.

In 2015, Bluecime was created to design a surveillance system to detect risky situations at the boarding station of a chairlift. The proposed system is called "Système Intelligent de Vision Artificielle par Ordinateur" (SIVAO) (Fig.1), and is composed of a camera, a computer, an alarm, and since winter 2018 a warning panel. If a risky situation is detected, the alarm is triggered to warn the chairlift operator, and the panel is lit to enjoin the passengers to close the restraining bar. For privacy reasons, we do not give the chairlifts true names, we only associate each of them to a letter (so, from "Chair. A" to "Chair. U").

(a) SIVAO camera

(b) Screenshot from Chair. D

Figure 1 – Bluecime's "Système Intelligent de Vision Artificielle par Ordinateur" (SIVAO)

For each chairlift, a "detection pyramid" is configured (blue area on Fig.1b), marking the

[1] http://www.domaines-skiables.fr/fr/smedia/filer_private/41/b9/41b95513-e9d4-4159-a261-5925e6d9f030/magazine-39.pdf#page=28

zone where the chairlift vehicle is tracked. We call the *back* of the pyramid the entry point of the vehicle in the detection zone. We call the *front* of the pyramid, the exit point of the vehicle from the detection zone, thus, the point where the decision to trigger or not the alarm, is made. At each frame inside the detection pyramid, different detections, using non learning-based image processing techniques, are performed:

- Presence of passengers
- Restraining bar in *up* position (totally opened)
- Restraining bar in *down* position (totally closed)

At the last frame of the detection pyramid, according to the detections made during the tracking of the vehicle, the system must assess the danger of a situation. For instance, if no passenger is detected or if passengers are detected and the restraining bar is detected in *down* position, then the situation is safe (the alarm should not be triggered). However, if passengers are detected and the restraining bar is detected in *up* position (or neither *up* nor *down*), the situation is risky (the alarm should be triggered).

Each year, more chairlifts are equipped with SIVAO, allowing Bluecime to obtain more and more data. Meanwhile, the SIVAO processes evolve to improve the detections and facilitate the system configuration. Moreover, some research projects are currently underway to extend the range of the detections. For instance, the system may localize, evaluate the height, and count the number of passengers on a vehicle: this would allow Bluecime to give the resort an insight into the presence and the distribution of passengers on the chairlift. It could also warn the chairlift operator if a child is alone on a vehicle.

Even after a series of improvements of the configuration process, setting up a system is still time-consuming for Bluecime engineers. Moreover, during the skiing season, some new conditions can appear. For instance, the position of the sun slightly changes from a month to another, so that different shadows can appear on the video, which may force Bluecime to manually reconfigure the system. Using machine learning techniques in this situation, would allow Bluecime to automatically configure the system. In addition, the performance of the machine learning techniques relies on a good generalization of the learned models. This makes the models more robust to shift in the input image distributions, such as new shadows, as mentioned previously.

Since 2012, deep learning models have shown remarkable results, especially in image processing, and have thus drawn more and more the attention of the industry. In this context, Bluecime considers using deep learning techniques to tackle their detection problems. Moreover, the SIVAO product includes a computer which could provide the computational power required by deep learning techniques.

This CIFRE PhD thesis is carried out in collaboration with Bluecime and the Hubert Curien laboratory. The objectives are to propose machine learning (particularly deep learning) techniques to improve the performances of SIVAO and, more generally, improve the Bluecime processes.

In this context, different contributions have been made during this thesis:

An experimental setting We propose a complete experimental set up to evaluate the possible machine learning use cases for Bluecime. This was described in *Improving Chairlift Security with Deep Learning* published at IDA 2017 (Bascol et al., 2017).

A baseline architecture We propose a deep learning architecture as a baseline to solve the risk assessment problem of Bluecime. The architecture uses different state-of-the-art techniques: an object classification architecture (here: ResNet), a domain adaptation component, and several (some proposed as contributions) data augmentation and learning tricks. These contributions were partially presented in *Improving Chairlift Security with Deep Learning* at IDA 2017 (Bascol et al., 2017).

Two F-measure optimization techniques The F-measure is a well known performance measure which provides a trade-off between the Recall and the Precision of a given classifier. As such, it is well suited when one is particularly interested in the performance of the classifier on a given class: the minority (here the risky) one. So, we propose two cost-sensitive methods to better optimize our model performance in terms of F-measure. They consist in weighting each error made during training depending on the corresponding example label. First, we propose a method suited for the usual iterative training of a neural network. At each iteration, the training is oriented by the gain of F-measure we could have obtained at the previous iteration without making a mistake on the considered example. The second method is an iterative method based on a theoretical bound over the training F-measure. The classes weights depend on a parameter t. With a classifier trained according to a given t, the bound indicates the F-measure values unreachable for any other classifier trained with the surrounding t values. We propose an exploration algorithm which iteratively removes the unreachable F-measure values, allowing to test a small set of t values. This second method was presented in *From Cost-Sensitive Classification to Tight F-measure Bounds* at AISTATS 2019 (Bascol et al., 2019b).

A training set selection technique The data annotation and system configuration phases are time consuming but necessary to obtain satisfactory results for both Bluecime and their clients. In that context, we propose to train a model specialized for each newly installed chairlift. However, using images from chairlifts too different from the new one may harm the performance: this phenomenon is called *negative transfer*. To tackle this problem, we propose to build the training sets so that they are composed of only the visually nearest already labeled chairlifts. This approach is presented in *Improving Domain Adaptation By Source Selection* at ICIP 2019 (Bascol et al., 2019a).

A study of multi-source domain adaptation with varying imbalance ratio We show that applying domain adaptation in the multi-source setting may in fact harm the performance of a classifier solely trained on the source data. We show that we can link this phenomenon to the varying imbalance ratio between the sources and the target sets. Considering this observation, we propose two ways of improving our approach in the

multi-source setting. First, using pseudo-labels acquired from a model learned without the target domain. The second method is to change our selected domain adaptation technique for one that considers the class distribution during the domain adaptation.

Outline

Chapter 1 This first chapter is dedicated to presenting some background on machine learning in the context of our chairlift safety problem. We first define the two machine learning paradigms we encounter in this thesis. After, we explore some machine learning algorithms, focusing on deep learning algorithms and architectures. Then, we present the domain adaptation problem, and show different domain adaptation techniques used with general machine learning models but particularly with deep learning models. Finally, we present the challenge of learning with imbalanced datasets, and techniques to optimize the F-measure.

Chapter 2 In the first part of this second chapter, we present the datasets used during this thesis. We present our benchmark datasets, then we present in details, the Bluecime dataset. In the second part, we present our experimental settings and the different performance measures we use.

Chapter 3 We propose in this third chapter two contributions. First a baseline approach based on deep learning and domain adaptation. We show that this approach presents a great potential, even in our most challenging setting. We then present our second contribution, which is a new data augmentation technique. This technique is based on the occlusion of regions of interest in the images, allowing to train a more robust model.

Chapter 4 This fourth chapter presents our contributions to F-measure optimization. We first present our F-measure gain oriented training method. We show that this method based on cost-sensitive learning allows us to choose the trade-off between Precision and Recall. We then present another algorithm to optimize the F-measure. This algorithm is based on a theoretical bound over the F-measure depending on a weight applied to each class.

Chapter 5 We conclude this thesis with a chapter questioning the usual domain adaptation results. We first propose a method to improve multi-source domain adaptation by selecting the relevant sources for a given target domain. This method aims at reducing the effect of *negative transfer*. This phenomenon impairs the performance of domain adaptation methods when using source domains too different from the target one. We then discuss domain adaptation results when adapting from multiple source domains with varying imbalance ratio. We show that in the varying imbalance ratio scenario, using domain adaptation can be harmfull for the performance. We also propose methods to address this problem.

Chapter 1

Background on machine learning (for the chairlift safety problem)

In this chapter, we present different aspects of machine learning in the context of the chairlifts safety problem, and provide insight of the literature available on each aspect. First we introduce generalities on machine learning, and present some machine learning algorithms, mostly in deep learning, that we will apply during this thesis. We, then, introduce domain adaptation and different methods, putting again the emphasis on deep learning based approaches. Finally, we present the challenges of learning a model with imbalanced data, and some methods to optimize the right performance measure in this context.

1.1 Machine learning settings

The purpose of machine learning is to learn (or train) a *model* from some given data in order to take decisions (for example predictions) on new unseen data. For instance, a model, called "classifier" in this case, could be learned to predict if a bank transaction is a fraud (or not) from different features of the data such as the amount associated with the transaction or the time it was emitted. To learn such a model, different algorithms exist. The choice of the algorithm depends on the type of data (e.g. images, sounds, ...), the task (e.g. detect the objects in images, predict the next note in a music track, ...). But, first of all, this choice depends on the data availability. In this thesis, we will consider two machine learning paradigms (see Bishop (2006) for more details about machine learning):

Unsupervised learning This setting implies that no label is available, only unlabeled examples. This could be the most natural setting to tackle Bluecime's anomaly detection problem, since it allows detecting risky situations unavailable in the data. For instance, no example of a passenger falling off the vehicle is available, moreover, it is so rare that it will probably be never available. In Bascol et al. (2016), we presented an antoencoder-based method to find recurrent patterns (motifs) in time series in an unsupervised fashion. To use this method on Bluecime's problem, we could transform the videos into

temporal documents, our method's required input (for example with optical flows), and learn the patterns characterizing a normal behavior. After training the autoencoder, an example with an anomaly is expected to be badly reconstructed by the autoencoder, so we could use the reconstruction error to detect anomalies (high reconstruction errors). You can find more information on this method in appendix A. However, Bluecime provides labeled data (see below) covering the most common situations, thus, we choose not to use this method.

Supervised learning This setting implies that we have access to a sufficiently large amount of labeled examples. This setting yields the best performance among the two considered paradigms, because it is the one with the largest information on the task. Considering that Bluecime already labeled a fair number of images (into three defined classes: *Empty*, *Safe*, and *Unsafe*), we will focus on this setting in the following.

In both paradigms, we learn from training data and test the performances of our model on different testing examples. We test the *generalization* of our model which means that we test how well the model generalizes the knowledge learned from the training examples to apply it on the other examples from the same data distribution. When training, the model risks to become too specialized to the training set, and so cannot generalize to new examples. This phenomenon is called "overfitting".

1.2 Algorithms

In this section, we present the machine learning methods and algorithms used during this thesis with a strong focus on methods based on deep learning.

1.2.1 Deep learning

Deep learning is nowadays almost a synonym for learning with deep (more than 2 layers) neural networks. We first give some generalities on neural networks, then we focus on a few architectures which yield good performances in image processing. We refer the user to Goodfellow et al. (2016) for more details.

1.2.1.1 Neural Networks (NN)

Multi-layer perceptron Rosenblatt (1958) presented an algorithm to learn a linear classifier, named "perceptron" (Fig. 1.1a), used to solve binary classification tasks. We define the dataset $\boldsymbol{X} \in \mathbb{R}^{N \times M}$ of N examples represented by M features and the corresponding set of labels $\boldsymbol{Y} \in \{0,1\}^N$. We note the ith example $\boldsymbol{X}^i = (x_1^i, x_2^i, \ldots, x_M^i)$ and its associated label y^i. The perceptron computes a weighted sum of an example by some learned parameters $\boldsymbol{W} = (w_1, w_2, \ldots, w_M)$, plus a bias term b. The results are given to a threshold function f such that:

$$f(\mathbf{X}^i, \mathbf{W}, b) = \begin{cases} 1 & \text{if } (\mathbf{W} \cdot \mathbf{X}^i + b) > 0 \\ 0 & \text{otherwise} \end{cases}$$

The resulting linear classifier is defined by the hyperplane $\widehat{y} = \boldsymbol{W} \cdot \boldsymbol{X}^i + b$. The weights of the perceptron are iteratively learned, during each learning iteration a training example is given to the perceptron. Then, the weights are updated following the rule: $\boldsymbol{W}(t) = \boldsymbol{W}(t-1) - \nu(y^i - \widehat{y}^i)\boldsymbol{x}^i$, where ν is the learning rate, and $\widehat{y}^i$ is the prediction for the example i. A loop over all the training set is called an "epoch". The algorithm loops until reaching a given number of epochs, or until the classification error of an epoch is below a given threshold.

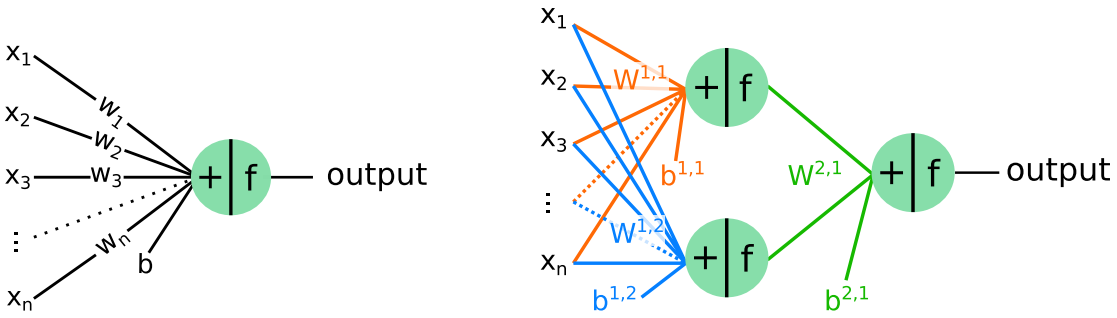

(a) A perceptron.

(b) A multi-layer perceptron with two hidden layers.

Figure 1.1

Learning with a single perceptron is limited to linearly separable problems. However, to tackle more complex problems, a solution is to stack perceptrons in layers, as shown in Figure 1.1b.

A multi-layer perceptron is composed of three subparts: an input layer, multiple hidden layers, and an output layer. In stacked perceptrons, the weight update is done by a different algorithm than simple perceptron, called the *backpropagation* algorithm. This algorithm uses stochastic gradient decent (SGD) over a loss function according to the weights. Each weight is updated according to the partial derivative of the error generated by an example. The error may be computed with different "loss functions" (e.g the hinge loss, or the log loss).

To compute the gradient, we need to replace the non differentiable threshold function used in the original perceptron by another activation function. We give in Figure 1.2 examples of commonly used functions. In the following we use the rectified linear unit (ReLU).

Extending multi-layer perceptrons to multi-class problems, where $\boldsymbol{y} \notin \{0,1\}^N$, is straightforward as it only requires to have a neuron for each class in the output layer. In this setting, we represent the labels as one hot vectors:

$$\boldsymbol{Y} = (\boldsymbol{y}^1, \boldsymbol{y}^2, \ldots, \boldsymbol{y}^n) \text{ with } \boldsymbol{y}^k \in \left\{ \boldsymbol{y} \in \{0,1\}^C \mid \sum_{j=1}^{C} y_j = 1 \right\} \forall k \in [1, N]$$

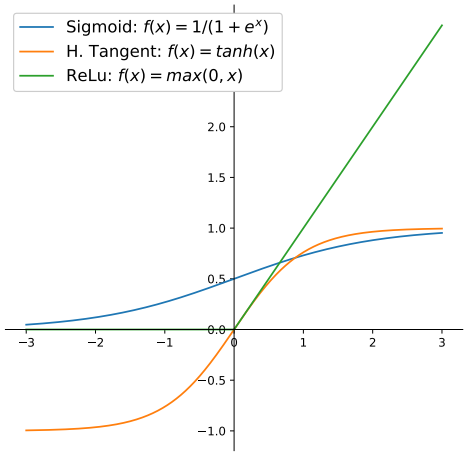

Figure 1.2 – Behavior of different activation functions.

The threshold functions of the output neurons are replaced by the softmax function:

$$S(\widehat{\boldsymbol{Y}}^i) = \left(\frac{e^{\widehat{y}_k^i}}{\sum_{j=1}^{C} e^{\widehat{y}_j^i}} \;\middle|\; k \in (1, 2, \ldots, C) \right)$$

with C the number of classes, i the index of the considered examples. The softmax function transforms the output vector into a "probability vector", giving the probability that the input belongs to each class. In this setting, the hinge loss is formulated:

$$\mathcal{L}_{Hinge}(\hat{\boldsymbol{y}}^i, t) = \frac{1}{C} \sum_{j=1; j \neq t}^{C} \max(0, \mu + \widehat{y}_j^i - \widehat{y}_t^i)$$

With i the index of the considered example, t the index of its true class, and μ a hyperparameter (the *margin*). The log loss is formulated:

$$\mathcal{L}_{Log}(\hat{\boldsymbol{y}}^i, t) = -\log(\widehat{\boldsymbol{y}}_t^i)$$

The multi-layer perceptron is the simplest neural network architecture. At each layer, each neuron is connected to all the outputs of the previous layer (or all the input for the first layer), this type of neural network is called "fully-connected feedforward network".

In practice, minibatch gradient descent (MGD) algorithms are preferred over SGD for the backpropagation algorithm. Instead of updating the weights according to each training example, in MGD, the weight update is computed over a small set of training examples (named minibatch). Thus, the training is more robust to outlier examples with MGD than with SGD algorithms.

Convolutional Neural Networks (CNN) In the context of image or text analysis, fully-connected networks present two major weaknesses that are "solved" by another type of architecture called "convolutional neural networks" (CNN).

Our images are of dimensions $224 \times 224 \times 3$ (see *pre-training* in "training tricks" section) meaning that with only one neuron we would have 150 528 parameters to learn. So, the complexity of the model would dramatically increase with the size of the network.

With structured inputs as images or text, the spatial aspect is crucial. The order of the sentences, and the order of the words within them, play an important role in the semantic of a text. In an image, the position of the objects gives clues to understand the whole image (a person on a chairlift vehicle should be all right, contrary to a person under...). In fully-connected networks, because the whole input is connected to each neuron, considering all the possible combinations of sentences or objects would require a high number of neurons. Moreover, most of the connections would be useless making the network highly inefficient.

To tackle such problems, the use of convolution has been decisive. In the following paragraphs we will explain the convolution operator applied to images but note that convolution can be applied to any signal (e.g. electrocardiogram, or videos from security camera). An image convolution can be seen as a sliding window going through all pixels of the original image. The result of the convolution is another image (called *feature map*) containing the weighted sum of the sliding window values with the values of each position in the image (see Fig. 1.3a). Convolutions have been widely used in image processing techniques to extract features from images. For instance, on Figure 1.3b, we show the effect of a convolution with a Sobel filter which extracts information on edges in an image.

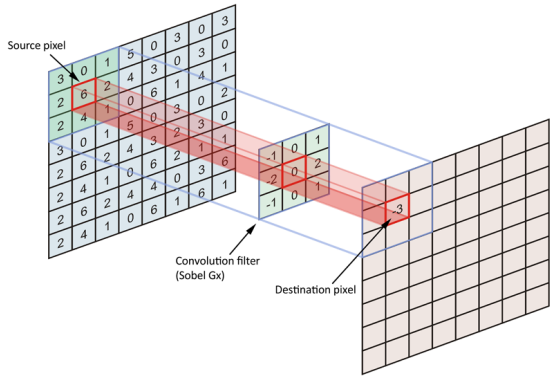

(a) Computation of a convolution with Sobel Gx filter[1]

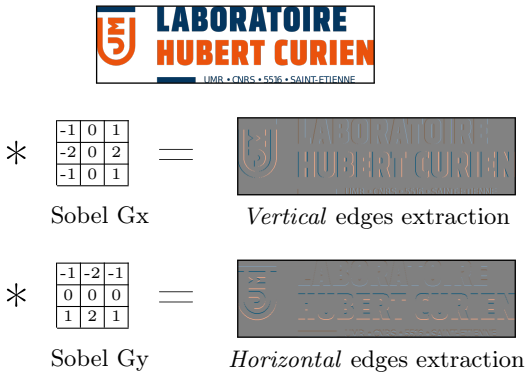

(b) Result of convolution by Sobel filters.

Figure 1.3 – Examples of 2D convolutions.

In deep learning, convolutions are implemented in convolutional layers, where the values of the filters are the learned weights. This implies that the filters are not designed by human but learned so that they can extract the best features for a given task.

Moreover, in a convolutional layer, we use 3D convolution filters, so that the filters span over the spatial dimension but also over the channel one. Thus, the number of parameters to learn depends on the number of filters, the number of input channels, and the spatial size

[1] Schema from https://github.com/OKStateACM/AI_Workshop/wiki/Computer-Vision-with-Convolution-Networks

of the filters. Since their spatial size is, most of the time, smaller than the input one (from 3×3 to 9×9 pixels), replacing a fully-connected layer by a convolutional one dramatically decreases the number of parameters, and so, the complexity of the learned model.

To tackle classification problems, the first layers in the architecture correspond to a convolutional neural network (CNN), i.e. stacked convolutional layers. This CNN is called the *feature extractor*, whose purpose is to learn a representation smaller but more powerful than the input, to facilitate the classification task. From the extracted features, one or more fully connected layers are added to get the classification output.

In convolutional networks, the field of view of an output pixel is its corresponding resolution on the input image as shown on Figure 1.4. The more we stack convolutional layers, the larger the receptive field of the output pixels. This means that the farther the layers are from the input, the larger and more complex the objects detected by the filters are. In Zeiler and Fergus (2014), the authors propose to visualize the input features detected by filters from different layers in a CNN. They showed that in the first layers the neurons are activated by simple features such as edges or texture. In deeper layers, however, the neurons are activated by higher level features as faces or pieces of text.

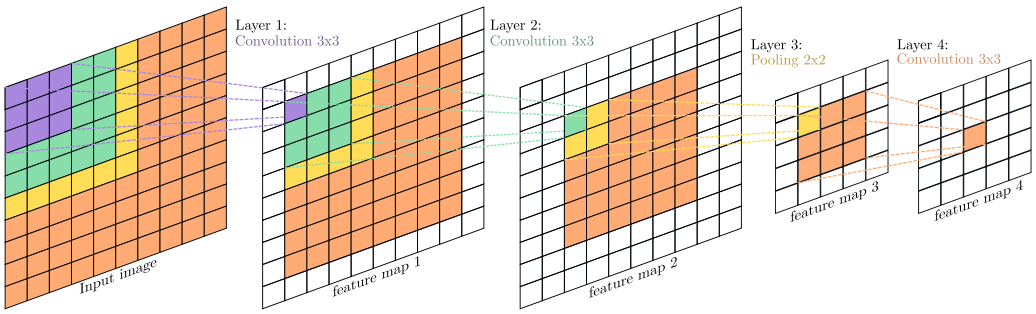

Figure 1.4 – Receptive fields across convolutionnal and pooling+subsampling layers.

The purpose of the feature extractor is to obtain features of interest, a small but powerful representation of the input. The spatial dimensions of the feature maps is progressively reduced as we go deeper in the layers. As you can see on Figure 1.4, after the downsampling layer (layer 3), the receptive field increased more than when stacking convolutions, and thus allowed finding higher level features with fewer parameters. A downsampling layer can be a convolutional layer or a pooling layer, associated with *subsampling*. Subsampling corresponds to using a sliding window step greater than one pixel. Note that all the input pixels are still considered if the sliding window size is greater than its step. Pooling operators are non-parametrized 2D convolutional filters (thus applied channel-wise), using them allows reducing, even more, the number of parameters in the model. Different pooling operators exist: one of the most used is the "max pooling" operator, where only the maximum value is kept at each position of the sliding window.

Autoencoders (AE) An autoencoder (e.g. Bengio et al. (2007)) is a specific neural network which purpose is to reconstruct its input. As shown on Figure 1.5, an autoencoder is composed

of a first neural network, the *encoder*. This network's purpose is to find a new representation of the AE inputs, called the *latent* representation. Then, from this representation, a second neural network, the *decoder*, aims at reconstructing the inputs of the AE. To train an AE, no labels are needed, the loss function used is a reconstruction error measuring how well the input is reconstructed by the model. For instance, we can use the Mean Squared Error (MSE):

$$\mathcal{L}_{MSE}(\mathbf{X}, \widehat{\mathbf{X}}) = \frac{1}{B} \sum_{i=1}^{B} \sum_{j=1}^{M} \left(\boldsymbol{x}_j^i - \widehat{\boldsymbol{x}}_j^i \right)^2$$

With $\boldsymbol{X} \in \mathcal{R}^{B \times M}$ a minibatch of B examples represented by M features, we note the ith example $\boldsymbol{X}^i = (\boldsymbol{x}_1^i, \boldsymbol{x}_2^i, ..., \boldsymbol{x}_M^i)$.

An autoencoder is an unsupervised way to extract powerful representations, but also to reconstruct the inputs. This last property is used, for instance, in the denoising autoencoders (Vincent et al., 2008) which provide a uncorrupted version of their inputs.

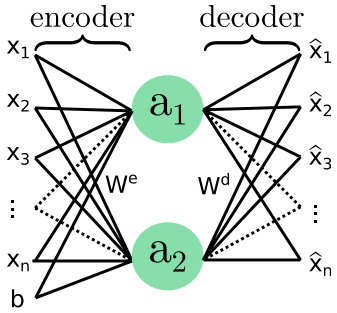

Figure 1.5 – An autoencoder with a latent space of size 2.

1.2.1.2 Particular Architectures

Deep learning techniques have become tremendously popular since 2012, when a deep architecture, called AlexNet, proposed by Krizhevsky et al. (2012) was able to win the ImageNet Large Scale Visual Recognition Challenge (ILSVRC) with an outstanding improvement of the classification results over the existing systems: the error rate was 15% compared to 25% for the next ranked team. Since then, countless different deep learning architectures have shown excellent performance in many domains such as computer vision, natural language processing or speech recognition (Goodfellow et al., 2016).

The amount of labeled data available, the systematic use of convolutions, the better optimization techniques and the advances in manufacturing graphical processing units (GPU) have contributed to this success. However, **deep** networks were supposed to suffer from (at least) three curses:

1. The deeper the network, the more difficult it is to update the weights of the first layers (the ones closer to the input): deep networks are subject to *vanishing* and *exploding gradient* that leads to convergence problems;

2. The bigger the network, the more weights need to be learned. In statistical machine learning, it is well-known that more complex models require more training examples to avoid overfitting phenomena and guarantee relatively good test accuracy;
3. Neural network training aims at minimizing a loss which is a measure of the difference between the computed output of the network and the target. The computed outputs depend on (i) the inputs, (ii) all the weights of the network and (iii) the non-linear activation functions that are applied at each layer of the network. The function to minimize is thus high-dimensional and non-convex. As the minimization process is usually achieved using stochastic gradient descent and back-propagation, it can easily get trapped in local optimum.

Simonyan and Zisserman (2014) created VGGNet 16 and VGGNet 19 composed of respectively 13 and 16 convolutional layers followed by 3 fully-connected layers. As for the previously mentioned AlexNet, the spatial dimensions were reduced with max-pooling layers, the inputs of the convolutions being typically padded so as to keep the same spatial size as before pooling. However, each time the spatial dimensions were divided by two (because of the pooling operator), the number of filters in the next layers was doubled to compensate for the information loss (thus doubling the number of channels in the output). With this method, Simonyan et al. managed to obtain an error rate of 7% at ILSVRC 2014.

Following these results, several other techniques have been designed to train deeper networks:

Residual Networks (ResNet) He et al. (2016) introduced the concept of *residual mapping* which allowed them to create a network with 18 to 152 convolutional layers called a Residual Network (ResNet). Their architecture is divided into blocks composed of 2 or 3 convolutional layers (depending on the total depth of the network). At the end of a block, its input is added to the output of the last layers of the block. This sum of an identity mapping with a "residual mapping" has proven effective to overcome the vanishing gradient phenomenon during the back-propagation phase and allows training very deep networks. Using residual blocks, the network is learned faster and with better performance. At ILSVRC 2015, ResNet 152 showed the best performance with less than 4% of error rate. They also used other tricks such as *batch normalization* (Ioffe and Szegedy, 2015) on the first (or first two) layer(s) of each residual block (the training tricks that are useful in our context are presented in section 1.2.1.3). We use this architecture as the backbone for our solution for the Bluecime's problem, and thus, will be presented in more details in Section 3.1.1.

Inception Networks In Szegedy et al. (2017), the authors propose inception-v4, the fourth version of inception networks, first presented as "GoogLeNet" in Szegedy et al. (2015). This architecture is composed of different *inception modules* shown in Figure 1.6. These modules are composed of several convolution layers in parallel with different filter sizes. Having different size of filter at the same level in the network allows to extract a large variety of features and provides a powerful representation of the inputs.

(a) Inception-v4 backbone.

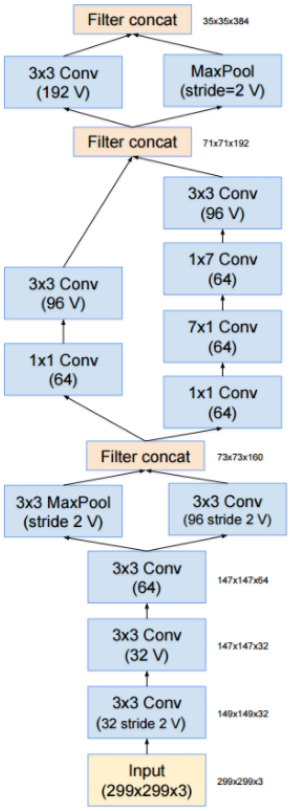

(b) Stem.

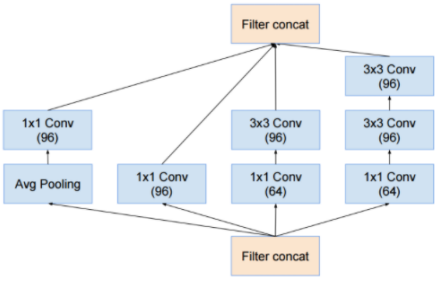

(c) Inception-A.

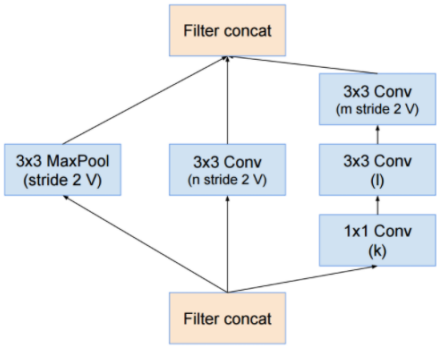

(d) Reduction-A.

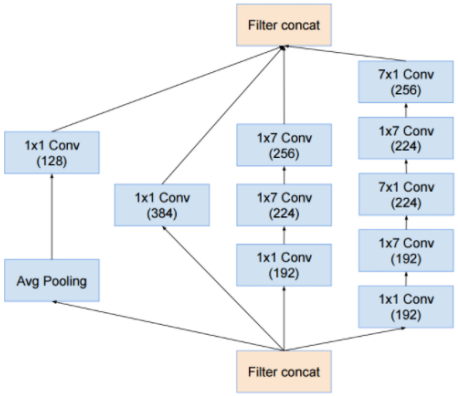

(e) Inception-B.

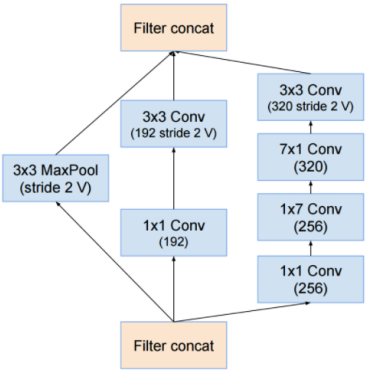

(f) Reduction-B.

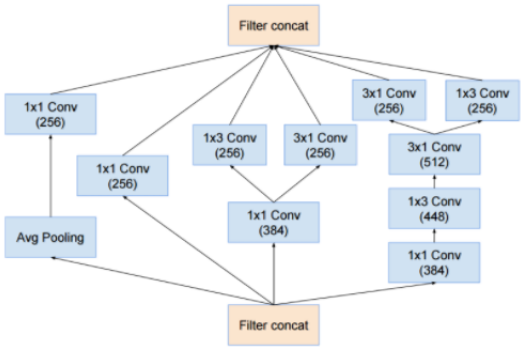

(g) Inception-C.

Figure 1.6 – Inception-v4.

MobileNet In Howard et al. (2017), the authors propose an architecture called *MobileNet* (later improved in Sandler et al. (2018)). This architecture is designed to give good performance in real time. To achieve this, the authors propose to replace the classical convolutional layers by 2 layers: a *depth-wise* convolution layer and a *point-wise* convolution layer.

We show on Figure 1.7 a comparison between the filters of a classical convolution layer (1.7a) and the filters of the proposed depth-wise layers (1.7b and 1.7c). In classical convolution, the filters extract features across all the inputs channel simultaneously. However, in the depth-wise convolution layer, each filter extract features in a different input channel. Then, the point-wise layer use 1×1 filters to linearly combine the extracted features over the channel dimension. Using these layers greatly reduce the number of operation required to compute a convolution, thus increases the speed of the model.

In the second version proposed in Sandler et al. (2018), the authors propose to add identity connections, as in ResNet, to improve MobileNet performance.

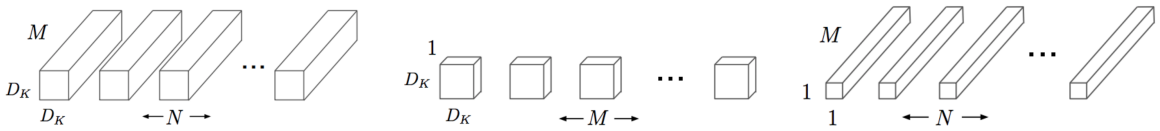

(a) Classical convolution filters. (b) Depth-wise convolution filters. (c) Point-wise convolution filters.

Figure 1.7 – Depth-wise convolutions from MobileNets. Where D_K is the filters size, M is the number of channels in the input, and N the number of channels in the output.

1.2.1.3 Training tricks

Pre-training In Chatfield et al. (2014), it was shown that image classification tasks could all benefit from a pre-training step on a large dataset such as ImageNet (Deng et al., 2009). The ImageNet dataset contains images grouped in 1000 different classes. The output of a network trained on ImageNet thus consists in a 1000-D vector. To use such a network on a new task (with much fewer and different target classes), the idea is to "cut" the last layers (the fully-connected ones) of the pre-trained network. Only the convolutional part is kept and its output is considered as a generic image descriptor. A new network can be built from this pre-trained generic feature extractor by training new additional fully-connected layers. The whole network can then be further *fine-tuned*, i.e., trained end-to-end on the new problem of interest. This procedure is part of the *inductive transfer learning* methods.

Data augmentation *Data augmentation* regroups all the techniques allowing to virtually create new examples by applying random transformations on the existing images, in order to "augment" a dataset with scarce data and to enforce the invariance of the trained model with respect to theses transformations. In the following, we give a non-exhaustive list of techniques often used in image contexts:

- Cropping images (translation variations).

- Zooming in images (scale variations).
- Flipping vertically or horizontally.
- Rotating images.
- Adding Gaussian noise to the pixels.

Successful data augmentation happens when the created images "stay" in the original dataset distribution. For instance, with the Bluecime dataset, applying vertical flip to the images should be ineffective since the vehicles never appear upside down in real cases (the chairlifts are close in case of strong wind). However, adding horizontal flipping may be useful as we still have coherent images.

Batch normalization *Batch normalization*, presented in Ioffe and Szegedy (2015) is a simple yet very effective idea which consists in normalizing the activation outputs $\boldsymbol{Z}$ of each layer of the network according to the current input batch:

$$\boldsymbol{Z}' = \frac{\boldsymbol{Z} - \boldsymbol{\mu}}{\sqrt{\boldsymbol{\sigma}^2 + \epsilon}}$$

with $\boldsymbol{Z} \in \mathbb{R}^{D \times K}$. In convolutional layers, $D = B \times W \times H$, with B the minibatch size and $W \times H$ the spatial dimensions, K is the number of channels. In fully-connected layers, $D = B$, the minibatch size, K is the number of features. μ is the mean of each activation: $\boldsymbol{\mu} = \frac{1}{D} \sum_{\boldsymbol{z} \in \boldsymbol{Z}} \boldsymbol{z}$, and $\boldsymbol{\sigma}^2$ is the vector of per-dimension variances such that: $\sigma_j^2 = \frac{1}{D} \sum_{\boldsymbol{z} \in \boldsymbol{Z}} (z_j - \mu_j)^2$ (thus, both $\boldsymbol{\mu}$ and $\boldsymbol{\sigma}^2$ are vectors of size K). The resulting normalized activations are then scaled and shifted with two learned parameters γ and β (both are vectors of size K):

$$\boldsymbol{Z}'' = \boldsymbol{\gamma} \boldsymbol{Z}' + \boldsymbol{\beta}$$

During the inference (testing) phase, $\boldsymbol{\mu}$ and $\boldsymbol{\sigma}^2$ are fixed with constant values that have been estimated over all the training set. In practice, we use moving mean and variance updated during each training iteration.

The main benefit of batch normalization is to reduce the internal covariate shift. This phenomenon corresponds to the amplification of small changes in the input distribution after each layer, and so creates high perturbations in the inputs of the deepest layers.

Dropout Based on the observation that, to reduce the overfitting and improve the performance of a neural network approach, we can combine a set of models, Srivastava et al. (2014) propose a regularization named *dropout*. At each iteration, in given layers, a random set of neurons is discarded, by setting their activation to zero (Fig. 1.8). So, during each training iteration only a reduced set of neurons are trained, which can be considered as a sub-network. However, during inference, all the neurons are used. This implies that, during the testing phase, the network corresponds to a combination of the trained sub-networks. Thus reducing the overfitting of our model. In Fourure et al. (2017), the authors propose to use dropout to

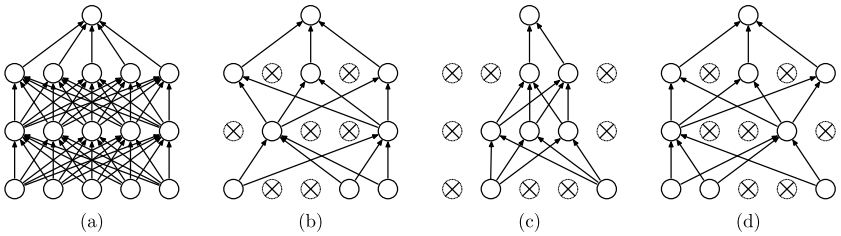

Figure 1.8 – Dropout. (a) A classical neural network. (b-d) A neural network with dropout at 3 different iterations. (image from Srivastava et al. (2014))

discard entire layers, they call their method *total dropout*. The authors use a neural network with a grid pattern (called *GridNet*) to tackle semantic segmentation (classification of each pixel in an image). In that context, total dropout allows them to address the vanishing gradient phenomenon reducing the training speed of the layers constituting the longest paths in the grid.

Ghiasi et al. (2018) observes that dropout is less effective on convolutional layers than on fully-connected layers. The authors therefore propose to extends dropout with *block dropout*. The authors hypothesize that the spatial aspect of the input impairs the dropout effectiveness. Indeed, with dropout the activation are randomly discarded so that we only loose sparse portions of the input image. Thus, with dropout, the sub-networks would learn from nearly the same input. In block dropout, the dropped activations are contiguous. This way, complete features may be discarded during the training enforcing the sub-networks to rely on diverse features. Thus, it improves the robustness of the final model.

Similarly to Ghiasi et al. (2018), DeVries and Taylor (2017) propose to randomly discard blocks during the training, however, only on the input. When an image is loaded, they randomly choose a square area to be masked. The authors also present their method as a data augmentation technique. Indeed, this method reduces the overfitting by augmenting the dataset and improves the robustness of the network against occlusions in the inputs. At the same time as DeVries and Taylor (2017), Zhong et al. (2017) propose a very similar method discarding blocks of pixel in the input image. The main difference between these two papers resides in the size of the blocks: DeVries and Taylor (2017) use fixed size blocks, whereas Zhong et al. (2017) use randomly sized blocks. In Zhong et al. (2017), the authors also try different colors to replace the image pixels, however, using random values seems to be the best choice.

1.2.2 Other machine learning techniques

In this section, we present the other machine learning algorithms we used during this thesis: *logistic regression* (LR) and linear *support vector machine* (SVM). Both are linear classifiers, we thus keep the notation from the perceptron section. Given a dataset $\boldsymbol{X} \in \mathcal{R}^{N \times M}$ of N examples represented by M features and the corresponding set of labels $\boldsymbol{Y} \in \{-1, 1\}^N$ (note the difference with perceptron where $\boldsymbol{Y} \in \{0, 1\}^N$), we note the ith example $\boldsymbol{X}^i =$

$(x_1^i, x_2^i, ..., x_M^i)$ and its associated label y^i. The final classifier is defined by the hyperplane $\widehat{y} = \boldsymbol{W} \cdot \boldsymbol{X}^i + b$.

Several formulations exist (Bishop, 2006), we present here the formulation with L2 regularization, and the primal formulation of the soft-margin SVM with the (binary) hinge loss:

Logistic regression:

$$\min_{\boldsymbol{W},b} \frac{1}{2} \parallel \boldsymbol{W} \parallel_2^2 + C \sum_{i=1}^{N} \log(e^{-y^i(\boldsymbol{W} \cdot \boldsymbol{X}^i + b)} + 1)$$

Support vector machine:

$$\min_{\boldsymbol{W},b} \frac{1}{2} \parallel \boldsymbol{W} \parallel_2^2 + C \sum_{i=1}^{N} \max(0, 1 - y^i(\boldsymbol{W} \cdot \boldsymbol{X}^i + b))$$

In both problems, the first term is the L2 regularization, used to penalize the classifier complexity. The second term penalizes the errors made on the training data, in LR this term is the *logistic loss*, in SVM it corresponds to the *hinge loss*. With the *logistic loss*, LR uses the probability of the examples to be well classified, whereas, SVM uses the distances between the hyperplane and the examples nearest to it (the *hinge loss* is zero if the considered example is well classified and far from the hyperplane $y^i(\boldsymbol{W} \cdot \boldsymbol{X}^i + b) > 1$). C is a hyperparameter controlling the importance of the errors. If C has a high value, the classifier will do few errors on the training set. It could, however, overfit the training set and thus give poor performance on the test set.

1.3 Domain adaptation

In this section, we first present generalities about domain adaptation. Then, we introduce some methods using optimal transport. Finally, we present and put the emphasis on techniques to tackle domain adaptation problems with deep learning.

1.3.1 Introduction

As we stated in Section 1.1, in machine learning, the data and the corresponding labels are crucial to obtain the best models. In some cases, we may not have access to labels, but have access to a labeled dataset different but related to ours. So, we would like to learn a model on the second dataset usable on our task. For instance, in Bluecime's application, we will consider each chairlift as a particular data distribution, called a *domain*. For a new installation we will learn with images from different chairlifts, but with related features. Domain adaptation (Ben-David et al., 2010) consists in learning, from one or more (labeled) *source* domain, a model that will be used on a different (but related and often unlabeled) *target* domain. Many real world tasks require the use of domain adaptation simply because of a lack of (target) labeled data or because of some shift between the source and the target data distribution that prevents from successfully using the learned model on the target data.

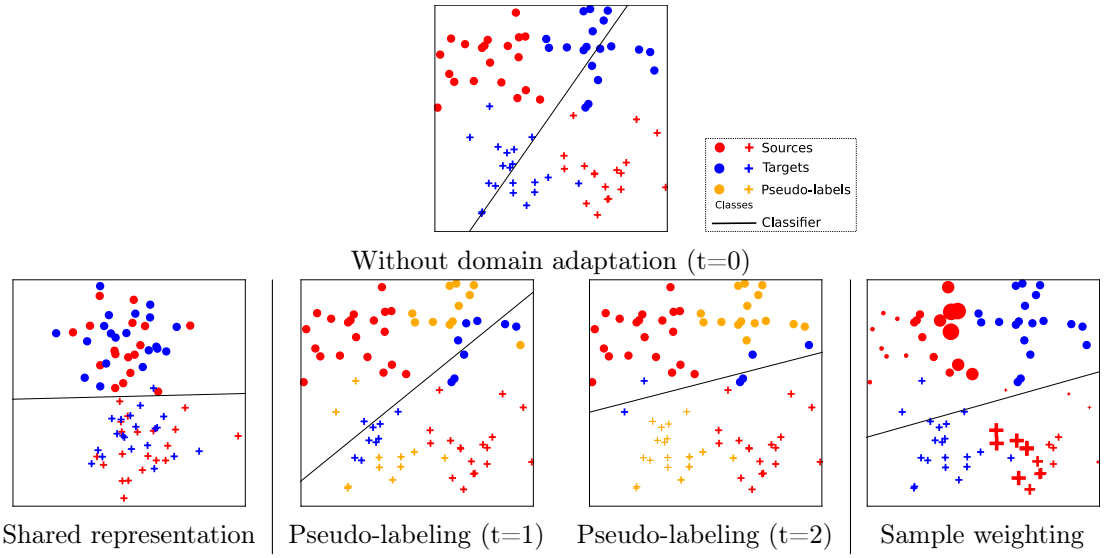

Figure 1.9 – Domain adaptation paradigms.

If one or more source domains are too different from the target one, the domain adaptation procedure can be unsuccessful. We call this phenomenon *negative transfer*. In Rosenstein et al. (2005), the authors have empirically identified positive and negative transfer situations.

Current domain adaptation algorithms rely on three methods:

1. finding of a shared representation between the source and the target domains;
2. reducing the covariate shift by weighting the source instances, particularly in multi-source domain adaptation;
3. using a source classifiers to obtain target pseudo-labels allowing to train a classifier on target samples;

In the following sections we will give more details about each method and the corresponding literature. Then, we will focus on deep learning approaches. On Figure 1.9, we illustrate the three methods on a 2D binary classification toy example. The top figure shows a classifier trained only with the source examples (red points), showing poor performance on the target set (blue points). On the second line, the leftmost image shows the effect of finding a shared representation between the source and the target sets. The two figures in the center, illustrate pseudo-labeling. At t=1, we added to the training set the farthest examples from the decision boundary of the t=0 classifier. Meaning that we used the surest predictions as labels (which are then called "pseudo-labels") to train a better classifier on the target domain. Again, we can create pseudo-labels (orange points) and train a new classifier (t=2). We can continue to learn new classifiers until a given convergence criterion (e.g. no creation of new pseudo-labels). On the rightmost figure, we show a classifier trained on a weighted version of the source set: as an example, we put more weights on examples close to the target examples.

Shared representation

Some approaches aim at finding a shared representation between the source and the target domains so that a classifier learned from this representation may show good performance both on the source domains and the target domain.

For instance, in Blitzer et al. (2006), the authors propose the "Structural Correspondence Learning" (SCL), which aims at finding *pivot features* which correspond to domain-independent features allowing training classifiers efficiently for both the source and the target domains.

Sample weighting

Other methods select the most relevant source examples to learn a good classifier for the target. In multi-source domain adaptation we can use the same weight for all the examples of a source. The weights may be applied during the training of the target classifier so that the most relevant examples have more impact than the irrelevant ones. In multi-source techniques, the weights may also be used to do a weighted vote of classifiers trained on the different sources.

In Chattopadhyay et al. (2012) the authors present two algorithms for domain adaptation. In "CP-MDA" (Conditional Probability based Multi-source Domain Adaptation), a target classifier is trained on a small set of target labels. They add a regularization term for the domain adaptation, stating that the predictions on the target set should match the predictions from a weighted vote between the sources classifiers. The weights are computed according to the homogeneity of their predictions over the target domain (close examples should have the same label).

The second algorithm, "2SW-MDA" (Two Stage Weighting framework for Multi-source Domain Adaptation) is a two steps domain adaptation algorithm. The first step is to learn sources classifiers with weights on the examples minimizing the Maximum Mean Discrepancy (MMD) between them and the target examples. The second step corresponds to getting the best source classifier on the target domain. The method thus optimizes the loss on a small labeled target set and on the source sets according to the MMD weights and on the homogeneity of their predictions like in CP-MDA.

In Duan et al. (2012), a target classifier is trained with pseudo-labels from source classifiers. They also add a regularization such that the outputs from the target classifier are close to the ones from relevant source classifiers. Unlike Chattopadhyay et al. (2012), the source classifiers are considered either relevant or not (with a constraint such that there is at least one relevant source).

Ge et al. (2014) propose an approach similar to CP-MDA (Chattopadhyay et al. (2012)), the main difference residing in the homogeneity criteria. The authors propose to find clusters on the target domains and consider the homogeneity of the predictions over each cluster individually. Then, the relevance of a source domain depends on the corresponding classifier's prediction on the examples of each cluster.

Target pseudo-labels

Learning a classifier in a supervised manner should yield the best performance on a given domain, however it needs a sufficient amount of labeled examples which we may not have. The idea here is to iteratively create labels for the target examples: at each iteration a source classifier is trained, the most reliable predictions on the targets examples are used as labels so that we can add those examples to the training set of the next iteration. For instance, in Bhatt et al. (2016), the authors mix the three methods to optimize the adaptation. They first select K source domains thanks to a similarity function based on the $\mathcal{H}$-divergence (Ben-David et al. (2010)) and a complementarity measure based on pivot features (Blitzer et al. (2006)). Then they find a shared representation between the K sources and the target with SCL. Finally, they iteratively train a target classifier corresponding to a weighted vote of classifiers trained on each source domain and a classifier trained on target pseudo-labels. The voting weights are adjusted in function of the sureness of the predictions of each classifier.

1.3.2 Domain adaptation using optimal transport

In this section, we first introduce the optimal transport paradigm. Then, we present different domain adaptation methods which use optimal transport.

1.3.2.1 Optimal transport

The optimal transport problem aims at finding the transport plan for transforming a data distribution into another one with the smallest transport cost (Villani, 2008). This plan, represented as a matrix, is called the "optimal transport plan". The transport cost is defined as a sum of the (probability) mass to move multiplied by the corresponding displacement price (which can be obtained using, for instance, the euclidean distance). The optimal transport plan $\gamma^\star$ is obtained by solving the optimal transport problem:

$$\gamma^\star = \underset{\gamma \in \Pi(\hat{\boldsymbol{\mu}}_S, \hat{\boldsymbol{\mu}}_T)}{\arg\min} \langle \boldsymbol{\gamma}, \boldsymbol{C} \rangle_F$$

$$\Pi(\hat{\boldsymbol{\mu}}_S, \hat{\boldsymbol{\mu}}_T) = \left\{ \gamma \in \mathbb{R}_+^{|\boldsymbol{X}_S| \times |\boldsymbol{X}_T|} \mid \gamma \mathbf{1} = \hat{\boldsymbol{\mu}}_S, \gamma^T \mathbf{1} = \hat{\boldsymbol{\mu}}_T \right\}$$

Where $\boldsymbol{C}$ is a distance matrix between all pairs of elements of the two domains, and $\langle ., . \rangle_F$ is the Frobenius dot product between 2 matrices. $\Pi(\hat{\mu}_S, \hat{\mu}_T)$ is the constraint set which ensures that the transport plan $\boldsymbol{\gamma}$ does not create or remove some mass (by ensuring that the marginal distributions $\hat{\mu}_S$ and $\hat{\mu}_T$ are preserved). We provide, in Figure 1.10, an example of a solved optimal transport problem.

In the next sections, we present domain adaptation methods using the optimal transport plan to find a common feature space between the target and source domains. Later in this thesis, we also use the *Wasserstein distance* which corresponds to the transportation cost of the optimal transport between two domains.

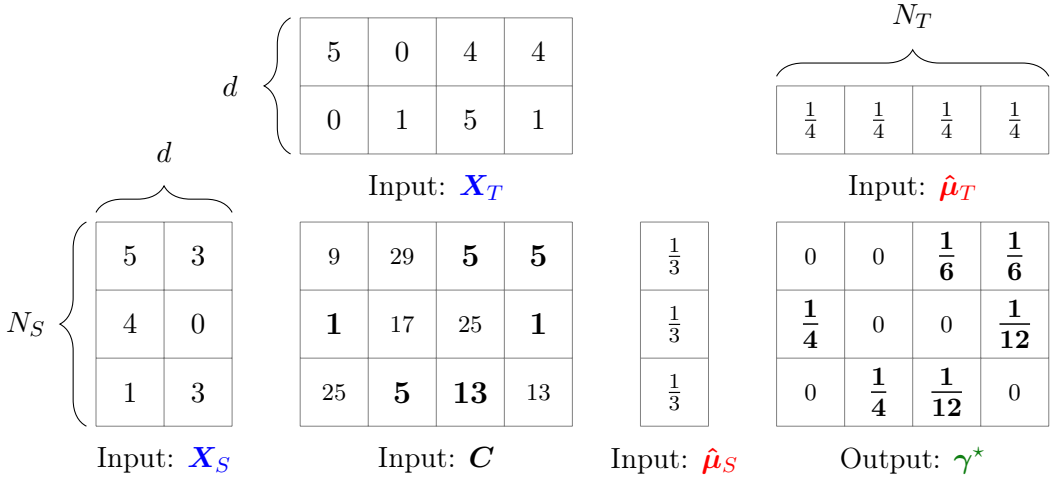

Figure 1.10 – Example of optimal transport result. $\boldsymbol{X}_S$ and $\boldsymbol{X}_T$ are respectively the source and the target sets ($\boldsymbol{X}_S \in \mathbb{R}^{N_S \times d}$, $\boldsymbol{X}_T \in \mathbb{R}^{N_T \times d}$), $\hat{\boldsymbol{\mu}}_S$ and $\hat{\boldsymbol{\mu}}_T$ are their corresponding marginal distributions. $\boldsymbol{C}$ is the cost matrix computed, here, using the squared Euclidean distance. $\gamma^\star$ is the optimal transport plan. (Figure from the presentation of Gautheron et al. (2018)).

1.3.2.2 Domain adaptation methods

In Courty et al. (2014), the authors propose to regularize the optimal transport problem with a term promoting the mass transport from sources of only one class to each target example. So, the transport obtained is coherent with the labels provided by the source set. Their optimal transport is formulated:

$$\gamma^\star = \underset{\gamma \in \Pi(\hat{\mu}_j, \hat{\mu}_i)}{\arg\min} \langle \gamma, \boldsymbol{C} \rangle_F - \frac{1}{\lambda}\Omega_e(\gamma) + \eta\Omega_c(\gamma)$$

where $\Omega_e(\gamma) = -\sum_{i,j} \gamma_{i,j} \log(\gamma_{i,j})$ is the entropy of gamma (the transport plan). This regularization is introduced in Cuturi (2013), and reduces the sparsity of gamma inducing more coupling between the source and target distributions. Adding this term allows to use the Sinkhorn-Knopp algorithm (Knight, 2008) to solve the optimal transport problem efficiently. $\Omega_c(\gamma) = \sum_j \sum_c \|\gamma_{\mathbf{I}_c,j}\|_q^p$, with $\mathbf{I}_c$ the indexes of the source examples of class c, so that, $\gamma_{\mathbf{I_c},\mathbf{j}}$ is a vector containing the transport coefficients between the source examples of class c and the target example j. This term is the regularization introduced by the authors to ensure that the mass transported to a given target example comes from sources with the same class. In practice the authors propose to use $p = \frac{1}{2}$ and $q = 1$, mostly due to optimization issues. With the resulting optimal transport plan, the source set is transported to the target set according to: $\hat{\mathbf{X}}_S = diag((\gamma^\star \mathbf{1}_{N_T})^{-1})\gamma^\star \mathbf{X}_T$ (note that $\hat{\mathbf{X}}_S = N_S \gamma^\star \mathbf{X}_T$ if $\hat{\mu}_S$ is uniform). The transported set is then used to train a classifier, which should thus present good performance on the target set.

In Courty et al. (2016), the authors complete the work published in Courty et al. (2014). They propose another regularization called "Laplacian regularization", which ensure that sim-

ilar examples are still similar after transport. Ω_c is then formulated:

$$\Omega_c(\gamma) = \frac{1}{{N_S}^2} \sum_{i,j} \mathbf{S}^S_{i,j} \|\hat{\mathbf{x}}^S_i - \hat{\mathbf{x}}^S_j\|_2^2$$

Where $\mathbf{S}^S$ is a matrix containing the similarity values between the source examples. To keep the label information after the transport, the authors propose to use $\mathbf{S}^s_{i,j} = 0$ if the examples i and j have a different class. They propose also to consider the similarity between the target examples if available, such that:

$$\Omega_c(\gamma) = \frac{(1-\alpha)}{{N_S}^2} \sum_{i,j} \mathbf{S}^S_{i,j} \|\hat{\mathbf{x}}^S_i - \hat{\mathbf{x}}^S_j\|_2^2 + \frac{\alpha}{{N_T}^2} \sum_{i,j} \mathbf{S}^T_{i,j} \|\hat{\mathbf{x}}^T_i - \hat{\mathbf{x}}^T_j\|_2^2$$

with α a hyperparameter controlling the trade-off between the two terms.
Note that in the target case, $\mathbf{S}^T$ cannot be constrained to 0 according to the classes. To optimize their problem, they propose to use the generalized conditional gradient algorithm (Bredies et al., 2009). They also propose to use $p = 1$ and $q = 2$ in the Courty et al. (2014) formulation. Their experiments show that the formulation in Courty et al. (2014) gives better results than the Laplacian one. Moreover, tuning the p and q values gives better the performance than the one used in the original paper.

Courty et al. (2017) propose another method called joint distribution optimal transport (JDOT). This method aims at finding the optimal transport plan and training the classifier in the same time, the authors suggests that this method allows to consider both the data distribution shift between source and target and the class distribution shift. The JDOT problem is formulated as:

$$\min_{\gamma \in \Pi(\hat{\mu}_T, \hat{\mu}_S), f \in \mathcal{H}} \sum_{i,j} \gamma_{i,j} \left[\alpha d(\mathbf{x}^S_i, \mathbf{x}^T_j) + \mathcal{L}(y^S_i, f(\mathbf{x}^T_j)) \right] + \lambda \Omega(f)$$

where $\mathcal{L}$ is any loss function continuous and differentiable, d is a metric (the authors propose to use the squared Euclidean distance), and Ω is a regularization over the classifier parameters.

The optimization of the JDOT problem is conducted by alternatively considering f and γ fixed: with f fixed the problem is a classical optimal transport problem with each element of the cost matrix defined such that: $\mathbf{C}_{i,j} = \alpha d(\mathbf{x}^S_i, \mathbf{x}^T_j) + \mathcal{L}(y^S_i, f(\mathbf{x}^T_j))$. With γ fixed, we obtain another optimization problem: $\min_{f \in \mathcal{H}} \sum_{i,j} \gamma_{i,j} \mathcal{L}(y^S_i, f(\mathbf{x}^T_j)) + \lambda \Omega(f)$.

In Redko et al. (2018), the author propose the joint class proportion and optimal transport method (JCPOT), a multi-source domain adaptation method. This approach allows to find a transportation plan compensating the shift between the sources and the target class distributions. With the resulting transport plan, the authors propose two methods to classify the target examples. Based on the regularized optimal transport presented in Cuturi (2013), the authors propose an optimal transport solved by a Bregman projection problem (Benamou et al., 2015) formulated as:

$$\gamma^\star = \underset{\gamma \in \Pi(\mu_1, \mu_2)}{\arg\min} \; KL(\gamma | \zeta)$$

with $\zeta = \exp(-\frac{\mathbf{C}}{\epsilon})$, and $\mathbf{C}$ the optimal transport problem cost matrix. KL is the Kullback-Liebler divergence. If μ_2 is undefined, $\gamma^\star$ can be formulated only depending on μ_1:

$$\gamma^\star = diag(\frac{\mu_1}{\zeta 1})\zeta, \tag{1.1}$$

We note K the number of available sources. The empirical data distribution of the k^{th} source $\hat{\mu}_S^k$ can be estimated with: $\hat{\mu}_S^k = (\mathbf{m}^k)^T \delta_{\mathbf{X}^k}$ where $\mathbf{m}^k = (m_1^k, m_2^k, \dots, m_{n^k}^k)$ is a vector containing the probability mass of each example in the source k, and $\delta_{\mathbf{X}^k}$ is a vector of Dirac measures located at each example of the source k. We note $\mathbf{h}^k = (h_1^k, h_2^k, \dots, h_L^k)$ the class probability vector with L the number of classes, and $h_l^k = \sum_{i=1}^{n^k} \delta(y_i^k = l) m_i^k$. Let $\mathbf{U}^k \in \mathbb{R}^{L \times n^k}$ and $\mathbf{V}^k \in \mathbb{R}^{n^k \times L}$ be two linear operators such that:

$$U_{l,i}^k = \begin{cases} 1 & \text{if } y_i^k = l \\ 0 & \text{otherwise} \end{cases}$$

$$V_{i,l}^k = \begin{cases} \frac{1}{|\{y_j^k = l \ \mid \ \forall j \in \{1,2,\dots,n^k\}\}|} & \text{if } y_i^k = l \\ 0 & \text{otherwise} \end{cases}$$

These two operators allow retrieving $\mathbf{m}^k$ from $\mathbf{h}^k$ and vice versa, such that: $\mathbf{h}^k = \mathbf{U}^k \mathbf{m}^k$, and $\mathbf{m}^k = \mathbf{V}^k \mathbf{h}^k$.

The estimation of the class distribution of the target set is done with a constrained Wasserstein barycenter problem (Benamou et al., 2015):

$$\underset{\mathbf{h} \in \Delta_L}{\arg\min} \sum_{k=1}^{K} \lambda^k W_{\epsilon, \mathbf{C}^k}\left((\mathbf{V}^k \mathbf{h})^T \delta_{\mathbf{X}^k}, \hat{\mu}_T\right)$$

where λ^k is a weight representing the k^{th} source relevance ($\sum_{k=1}^{K} \lambda^k = 1$), and $W_{\epsilon, \mathbf{C}^k}$ is the regularized Wasserstein distance:

$$W_{\epsilon, \mathbf{C}^k}(\hat{\mu}_S^k, \hat{\mu}_T) = \min_{\gamma^k \in \Pi(\hat{\mu}_S^k, \hat{\mu}_T)} KL(\gamma^k | \zeta^k)$$

For each source k we then have two constraints: ${\gamma^k}^T \mathbf{1}_n = \mathbf{1}_n / n$ (considering $\hat{\mu}_T$ uniform), and $\mathbf{U}^k \gamma^k \mathbf{1}_n = \mathbf{h}$. The first constraint can be solved for each source independently with the solution of the Bregman projection defined in equation 1.1. The second constraint must be solved simultaneously on the K sources, to do so the authors propose a Bergman projection problem:

$$\mathbf{h}^\star = \underset{\mathbf{h} \in \Delta_L, \Gamma}{\arg\min} \sum_{k=1}^{K} \lambda^k KL(\gamma^k | \zeta^k)$$

$$\text{s.t. } \forall k \ \mathbf{U}^k \gamma^k \mathbf{1}_n = \mathbf{h}$$

with $\mathbf{\Gamma} = (\gamma^1, \gamma^2, ..., \gamma^K)$.

This problem admits the solution:

$$\gamma^k = \text{diag}\big(\tfrac{\mathbf{V}^k\mathbf{h}}{\zeta^k\mathbf{1}_n}\big)\zeta^k$$
$$\forall k$$
$$\mathbf{h} = \prod_{k=1}^{K}\big(\mathbf{U}^k(\zeta^k\mathbf{1}_n)\big)^{\lambda^k}$$

Finally, to classify the target examples from the optimal transport plan, the authors compare two methods. First, they use the method presented in Courty et al. (2014), where they transport the source examples on the target distribution and learn a classifier on the transported set. Then, they propose another method, which consists in estimating the label of each target example by measuring the proportion of transported mass coming from each class. The experiments conducted by the authors show that their approach gives better results than different other approaches, including Courty et al. (2014). They also show that their label propagation method gives better results than Courty et al. (2014) method for a given optimal plan.

In this thesis, we are mainly interested in deep learning, thus, we now focus on deep learning-based domain adaptation techniques.

1.3.3 Domain adaptation in deep learning

In this section, we present different techniques to tackle domain adaptation problems with deep learning.

1.3.3.1 Shared representation

When using deep learning, the most common domain adaptation algorithmic setting is to construct a common representation space for the two domains while keeping good performance on the source labeling task. This can be achieved through the use of adversarial techniques where feature representations from samples in different domains are encouraged to be indistinguishable as in Ganin et al. (2016) and Tzeng et al. (2017).

Domain adversarial neural networks (DANN) Ganin et al. (2016) propose to train two networks that share the same first (convolutional) layers called the *feature extractor* (as shown in Figure 1.11). The first network is dedicated to the classification task on one particular domain. The second network aims at predicting the domain of an input example from the output of the feature extractor. We call this classifier a *domain discriminator*. Note that to train the discriminator, the examples of the target domain do not need to be labeled (and are not in the work of Ganin et al. (2016)). The only information needed to train the second network is whether an example belongs to the source or to the target domain. The two networks are trained in an adversarial way according to the shared layers (using a mechanism called gradient reversal on the second network optimization). As a consequence, the shared features of the networks are discriminative for the classification task as well as

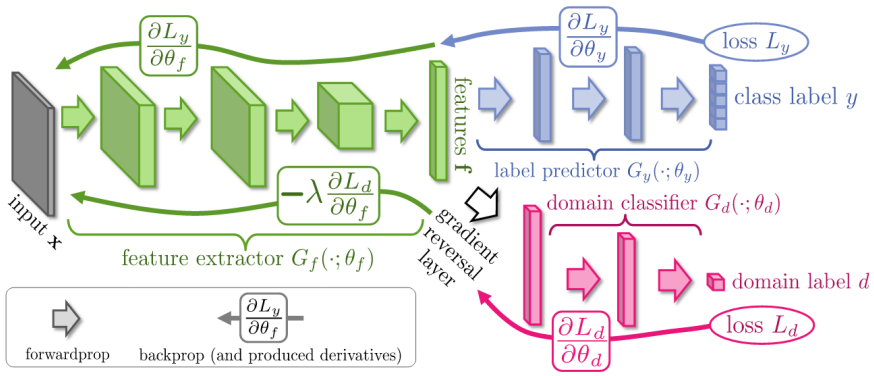

Figure 1.11 – The DANN approach (figure from Ganin et al. (2016)).

domain invariant. We note $\mathcal{L}_c$, and $\mathcal{L}_d$ the losses respectively on the classifier, and the discriminator. The loss on the feature extractor then is:

$$\mathcal{L}_e(h, d, \boldsymbol{X}) = \mathcal{L}_c(h, \boldsymbol{X}) - \lambda \mathcal{L}_d(d, \boldsymbol{X})$$

with h the classifier, $\boldsymbol{d}$ the domain discriminator, and $\boldsymbol{X}$ a minibatch. λ is the gradient reversal parameter increasing during the iteration i of the training procedure according to:

$$\lambda(i) = \frac{2}{1 + e^{-\gamma(i/I)}} - 1$$

with γ a hyperparameter (fixed to 10 in the authors' experiments), i the current iteration, and I the number of iterations. During the first iterations, $\lambda \approx 0$, so, the discriminator can be trained without adversary features. Then λ increases so that the features progressively become domain independent. In that way, the discriminator outputs are accurate during the adaptation of the features, thus, the feature extractor is correctly adversarially trained.

In Cao et al. (2018), the authors tackle "partial transfer", considering that the target task is a sub-task of the source task (target labels being unavailable). To do that, they extend the work of Ganin et al. (2016) and propose *Selective Adversarial Networks* (SAN). Instead of a unique domain discriminator, they propose to learn class-wise discriminators. To select the right discriminator during training, without target labels, they use the classifier output: in each domain discriminator loss, the target examples are weighted according to their classification probability vector. Thus, this method should improve the domain adaption over the target predicted classes.

Correlation alignment for deep learning (Deep CORAL) Correlation alignment (CORAL), presented in Sun et al. (2016), is a domain adaptation method aiming at matching the source distribution $\mathcal{D}_S$ on the target one $\mathcal{D}_T$. To do so, the authors propose to align the covariance of the two distributions. The transformed source distribution $\widehat{\mathcal{D}}_S$ is computed by:

$$\widehat{\mathcal{D}}_S = (\mathcal{D}_S \times \boldsymbol{C}_S^{-\frac{1}{2}}) \times \boldsymbol{C}_T^{\frac{1}{2}}$$

where $\boldsymbol{C}_S$ (resp. $\boldsymbol{C}_T$) is the covariance matrix of $\mathcal{D}_S$ (resp. $\mathcal{D}_T$).

In Sun and Saenko (2016), the authors propose to extend CORAL to deep learning techniques by training neural networks with two losses: the classification loss and the CORAL loss. The classification loss is used to train the model to tackle the task. The CORAL loss encourages the feature extractor to be independent of the domains. It is formulated as:

$$\mathcal{L}_{CORAL} = \frac{1}{4d^2} \parallel \boldsymbol{C}_S - \boldsymbol{C}_T \parallel_F^2$$

where $\parallel . \parallel_F$ is the Frobenius norm. As in Ganin et al. (2016), during the training phase, only the source examples are used to compute the classification loss and both source and target sets are used in the CORAL loss.

Adaptive batch normalization (AdaBN) AdaBN, presented in Li et al. (2016), is a simple, yet effective, method to do domain adaptation with batch normalization (see Section 1.2.1.3). At training time, the batch normalization is conducted classically by normalizing activations by mean and variance estimated over the minibatch. However, at test time, the mean and variance parameters are estimated over *all* the target set. By doing so, source and target distribution are standardized to a similar one. Thus, this method aims at reducing the effect of domain shift.

Automatic domain alignment layers (AutoDIAL) In Cariucci et al. (2017), the authors also propose to extend batch normalization to do domain adaptation. They use batch normalization layers to align the source and target feature distributions at different levels of a neural network (they call these layers "DA-layers"). During training, both source and target examples are given to the network, each distribution having its own loss. The source examples being labeled, a classical log loss is used. However, the target examples being unlabeled, the authors use the entropy of the predictions as a loss. In the DA-layers, the sources and target examples normalization is computed separately according to:

$$\boldsymbol{z}'_S = \frac{\boldsymbol{z}_S - \boldsymbol{\mu}_{ST,\alpha}}{\sqrt{\boldsymbol{\sigma}^2_{ST,\alpha} + \epsilon}}; \; \boldsymbol{z}'_T = \frac{\boldsymbol{z}_T - \boldsymbol{\mu}_{TS,\alpha}}{\sqrt{\boldsymbol{\sigma}^2_{TS,\alpha} + \epsilon}}$$

with $\boldsymbol{z}_S$ ($\boldsymbol{z}_T$) the input of the DA-layer from source (resp. target) examples, and $\boldsymbol{z}'_S$ ($\boldsymbol{z}'_T$) the corresponding outputs. $\boldsymbol{\mu}$ and $\boldsymbol{\sigma}^2$ are respectively the mean and the variance, both are estimated over a minibatch. Such that, $\boldsymbol{\mu}_{ST,\alpha}$ and $\boldsymbol{\sigma}^2_{ST,\alpha}$ are computed in $\boldsymbol{z}_{ST,\alpha} = \alpha \boldsymbol{z}_S + (1-\alpha)\boldsymbol{z}_T$, and $\boldsymbol{\mu}_{TS,\alpha}$ and $\boldsymbol{\sigma}^2_{TS,\alpha}$ in $\boldsymbol{z}_{TS,\alpha} = \alpha \boldsymbol{z}_T + (1-\alpha)\boldsymbol{z}_S$. The α is a learned parameter, clipped so that $\alpha \in [0.5, 1]$: if $\alpha = 1$ we have an independent alignment of the two domains, whereas, if $\alpha = 0.5$ we have a coupled normalization.

Adversarial discriminative domain adaptation (ADDA) ADDA, presented in Tzeng et al. (2017), is another adversarial technique designed to get a shared representation between the target and the source domains. This approach is divided into two steps. First, a neural network is trained on the source domain. Then, a discriminator is trained so that it has to distinguish between features extracted from source and target examples. The source features

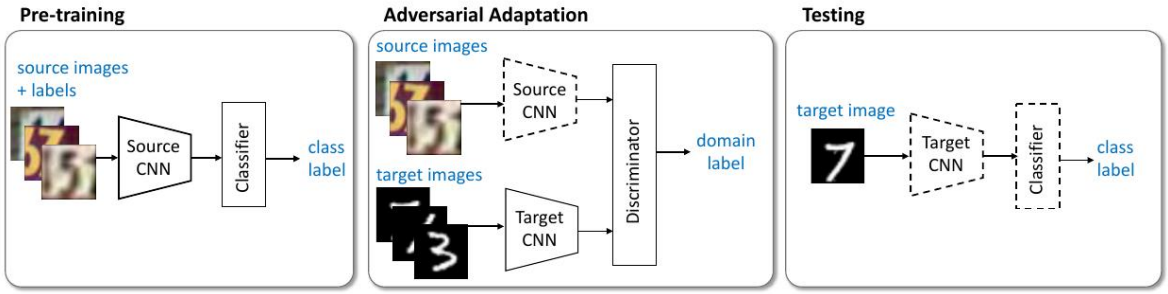

Figure 1.12 – ADDA training and testing steps (figure from Tzeng et al. (2017)).

come from the feature extractor part of the source classifier with its weights *fixed*. The target features come from a feature extractor pre-trained with the weights from the source one, *fine-tuned* in an adversarial fashion with the discriminator. With the discriminator trained to distinguish between source and target features, and the target features trained to fool the discriminator, the resulting target features extractor should produce source-like features from the target images. Thus, the loss used to train the target feature extractor slightly changes from the one used in DANN method:

$$\mathcal{L}_e(h, d, \boldsymbol{X}) = \mathcal{L}_c(h, \boldsymbol{X}) + \mathcal{L}_d(1 - d, \boldsymbol{X})$$

The final target classifier is composed of the target feature extractor and the classification part of the source classifier, as it should be effective on source-like features. This process is graphically shown on Figure 1.12.

Decision-boundary iterative refinement training (DIRT-T) In Shu et al. (2018), the authors first propose the virtual adversarial domain adaptation (VADA) model. VADA is based on the Ganin et al. (2016) method, extended so that the cluster assumption holds on both source and target training sets. The cluster assumption states that all the data point from a given distribution with a given class must belong to the same cluster. Here, the authors use a loss to minimize the entropy of the classifier on the target domain:

$$\mathcal{L}_{Ent}(h, \boldsymbol{X}_T) = -\frac{1}{B_T} \sum_{\boldsymbol{x}_T \in \boldsymbol{X}_T} \boldsymbol{h}(\boldsymbol{x}_T) \cdot \log(\boldsymbol{h}(\boldsymbol{x}_T))$$

with $\boldsymbol{X}_T = (x_T^1, x_T^2, ..., x_T^{B_T})$ the subset of a minibatch containing B_T target examples, h the classifier, and $\boldsymbol{h}(\boldsymbol{x}_T)$ the prediction vector for example $\boldsymbol{x}_T$. This loss encourages the classifier to be confident in its predictions, thus encourages the classifier's decision boundary to be far away from the target examples. This implies that the decision boundary should not cross any cluster of target example, so, according to the cluster assumption, this loss enforces the classifier to discriminate well the target classes. However, the learned classifier must be locally-Lipschitz to use this approximation (Grandvalet and Bengio, 2005). To respect this constraint, the authors propose to add another loss based on the Kullback-Liebler divergence

(noted D_{KL}):

$$\mathcal{L}_{KL}(h, \boldsymbol{X}) = \frac{1}{B} \sum_{\boldsymbol{x} \in \boldsymbol{X}} \max_{||\boldsymbol{r}|| < \epsilon} D_{KL}(\boldsymbol{h}(x) || \boldsymbol{h}(x + r))$$

where $\boldsymbol{X} = (\boldsymbol{x}^1, \boldsymbol{x}^2, ..., \boldsymbol{x}^B)$ is a minibatch containing B examples from both source and target domains, and r represents the adversarial perturbation (Miyato et al., 2018).

The authors present also a second algorithm named *decision-boundary iterative refinement training* (DIRT-T). They use VADA as a pre-training step, then iteratively fine-tune the model with target pseudo-labels. They use both $\mathcal{L}_{Ent}$, and $\mathcal{L}_{KL}$ (using only the target examples). They also use a regularization term corresponding to the Kullback-Liebler divergence between the model at the current iteration and the model at the previous iteration:

$$\mathcal{R}_{KL}(h_{t-1}, h_t, \boldsymbol{X}) = \frac{1}{B} \sum_{\boldsymbol{x} \in \boldsymbol{X}} D_{KL}(\boldsymbol{h_{t-1}}(x) || \boldsymbol{h_t}(x))$$

This term ensures that each iteration has a small impact on the prediction. So that, the final model fits the target pseudo-labels without "loosing" the VADA pre-training on the source domain.

Wasserstein distance guided representation learning (WDGRL) Shen et al. (2018) propose another adversarial method to tackle domain adaptation, named WDGRL. In their approach, the discriminator is replaced by a *domain critic*. This critic estimates a function $f_w : \mathcal{R}^K \to \mathcal{R}$ which takes as input the K outputs from the feature extractor such that:

$$W(\mathbb{P}_{x_S}, \mathbb{P}_{x_T}) = \sup_{||f_w|| \leq 1} \mathbb{E}_{\mathbb{P}_{x_S}}[f_w(f_g(x))] - \mathbb{E}_{\mathbb{P}_{x_T}}[f_w(f_g(x))]$$

with f_g the feature extractor, $W(\mathbb{P}_{x_S}, \mathbb{P}_{x_T})$ the Wasserstein distance between the source and the target distributions. To train this domain critic, the authors propose to maximize a loss approximating W:

$$\mathcal{L}_{wd}(\boldsymbol{X}_S, \boldsymbol{X}_T) = \frac{1}{B_S} \sum_{\boldsymbol{x}_S \in \boldsymbol{X}_S} f_w\big(f_g(\boldsymbol{x}_S)\big) + \frac{1}{B_T} \sum_{\boldsymbol{x}_T \in \boldsymbol{X}_T} f_w\big(f_g(\boldsymbol{x}_T)\big)$$

with $\boldsymbol{X}_S = \{\boldsymbol{x}_S^1, \boldsymbol{x}_S^2, ..., \boldsymbol{x}_S^{B_S}\}$ and $\boldsymbol{X}_T = \{\boldsymbol{x}_T^1, \boldsymbol{x}_T^2, ..., \boldsymbol{x}_T^{B_T}\}$ the subsets of a minibatch respectively containing B_S source examples and B_T target examples.

This approach holds if f_w is 1-Lipschitz. To ensure it, the authors use a loss function on the gradient applied to f_w:

$$\mathcal{L}_{grad}(\hat{g}) = \big(||\nabla_{\hat{g}} f_w(\hat{g})||_2 - 1\big)^2$$

where $\hat{g}$ contains the features corresponding to the source and target examples, but also to features interpolated between each source and target features. The final loss on the domain critic is expressed as: $\mathcal{L}_w = \mathcal{L}_{grad} - \mathcal{L}_{wd}$. The Wasserstein distance loss is maximized and the gradient loss is minimized. The loss on the classifier is a classical classification loss noted $\mathcal{L}_c$. The feature extractor loss is: $\mathcal{L}_g = \mathcal{L}_c + \lambda \mathcal{L}_{wd}$, so that, both the classification loss and the

Wasserstein distance are minimized (λ is a hyperparameter controlling the trade-off between the two losses).

A training iteration is divided into two phases. First, the domain critic is trained n times (with n a hyperparameter). Then, both the classifier and the feature extractor are trained once. This two-phases approach allows to correctly approximate the Wasserstein distance before adversarially training the feature extractor.

Deep joint distribution optimal transport (DeepJDOT) In Damodaran et al. (2018), the authors present deepJDOT, a deep learning version of the JDOT approach (Courty et al., 2017), presented in the previous section. In DeepJDOT, both the feature extractor g and the classifier f are optimized according to the problem:

$$\min_{\gamma\in\Pi(\mu_j,\mu_i),f,g} \frac{1}{n_s}\sum_i \mathcal{L}\big(y_i^s, f(\mathbf{g}(\mathbf{x}_i^s))\big) + \sum_{i,j}\gamma_{i,j}\big[\alpha\|\mathbf{g}(\mathbf{x}_i^s)-\mathbf{g}(\mathbf{x}_j^t)\|^2 + \lambda_t\mathcal{L}\big(y_i^s, f(\mathbf{g}(\mathbf{x}_i^t))\big)\big]$$

The first term of the problem was not present in (Courty et al., 2017). Its purpose is to avoid forgetting the source task, without this term, nothing guarantee that each learned target class matches the right source class. The rest of the problem corresponds to the JDOT problem applied to the feature space, supposed more compact and informative than the original data space. To tackle the DeepJDOT problem with deep learning and to keep a scalable method with the dataset size, the authors propose to approximate their problem over minibatches:

$$\min_{f,g}\ \mathbb{E}\frac{1}{m_s}\sum_{i=1}^{m_s}\mathcal{L}\big(y_i^s, f(\mathbf{g}(\mathbf{x}_i^s))\big) + \min_{\gamma\in\Pi(\hat{\mu}_j,\hat{\mu}_i)}\ \sum_{i,j}^{m_s,m_t}\gamma_{i,j}\big[\alpha\|\mathbf{g}(\mathbf{x}_i^s)-\mathbf{g}(\mathbf{x}_j^t)\|^2 + \lambda_t\mathcal{L}\big(y_i^s, f(\mathbf{g}(\mathbf{x}_i^t))\big)\big]$$

with m_s and m_t respectively the number of source and target examples in a minibatch. As in JDOT, the authors use a two-step training, considering alternatively f and g, and γ fixed. The first step consists in tuning gamma with the problem:

$$\min_{\gamma\in\Pi(\hat{\mu}_j,\hat{\mu}_i)}\ \sum_{i,j}^{m_s,m_t}\gamma_{i,j}\big[\alpha\|\mathbf{g}(\mathbf{x}_i^s)-\mathbf{g}(\mathbf{x}_j^t)\|^2 + \lambda_t\mathcal{L}\big(y_i^s, f(\mathbf{g}(\mathbf{x}_i^t))\big)\big] \text{ with } f \text{ and } g \text{ fixed}$$

The second step consists in training both the feature extractor and the classifier using the objective function:

$$\frac{1}{m_s}\sum_i^{m_s}\mathcal{L}\big(y_i^s, f(\mathbf{g}(\mathbf{x}_i^s))\big) + \sum_{i,j}^{m_s,m_t}\gamma_{i,j}\big[\alpha\|\mathbf{g}(\mathbf{x}_i^s)-\mathbf{g}(\mathbf{x}_j^t)\|^2 + \lambda_t\mathcal{L}\big(y_i^s, f(\mathbf{g}(\mathbf{x}_i^t))\big)\big] \text{ with } \gamma \text{ fixed}$$

1.3.3.2 Sample weighting

Afridi et al. (2018) considers the problem of domain adaptation from multiple sources by selecting only one source. Note that their approach requires some labeled examples on the target

domain (which may be difficult to obtain). On the other hand, the task on the selected source domain can be different from the task on the target one (only the features are transferred) which can give a large choice of source domain. They propose to train a CNN per source domain and a target CNN using the few target labeled data. Then, they use a validation set to rank the source CNN according to the mutual information between the features extracted by each source CNN and the output of the target CNN. The source CNN which gives the most information is used for pre-training the final classifier.

In the currently unpublished work from Schultz et al. (2018), the authors propose to select multiple source domains as training set for a given target domain. The source domains are selected according to a weighted combination of four distances (the χ^2-divergence, the Maximum Mean Discrepancy, the Wasserstein distance and the Kullback-Liebler divergence) and according to the classification performance on each single source domain.

1.4 Learning with imbalanced data

In anomaly detection, we are confronted to the data imbalance since an anomaly rarely occurs: the proportion of *positive* (anomalous) examples is highly inferior to the proportion of *negative* (normal) ones. When a classifier is learned with common methods, the optimized metrics is the accuracy, meaning the proportion of well classified examples. In the case of imbalanced data, as the proportion of positive examples is low, a classifier always predicting negative will have a good accuracy, but, in fact, will be useless in practice.

A positive (resp. negative) example correctly classified is called true positive (TP) (resp. negative (TN)). A positive (resp. negative) example incorrectly classified is called false negative (FN) (resp. positive (FP)). A confusion matrix, as figure 1.13, can be built to summarize the results of a classifier.

class \ pred	*negative*	*positive*
negative	$\#TN$	$\#FP$
positive	$\#FN$	$\#TP$

Figure 1.13 – Confusion matrix. The rows correspond to the true classes, the columns to the predictions, the cells contain the corresponding number of examples.

On imbalanced data, different measures exist to get more information on the performance than the Accuracy:

- The *Recall*, which indicates the proportion of well classified positive examples among all the positives:

$$Re = \frac{TP}{TP + FN}$$

- The *Precision* showing the proportion of well classified positives among all the examples classified as positive:
$$Pr = \frac{TP}{TP + FP}$$
- The F_β*-measure* (van Rijsbergen, 1974) which is the harmonic mean between the *Precision* and the *Recall*:
$$F_\beta = \frac{1}{\frac{\beta^2}{1+\beta^2}\frac{1}{Re} + \frac{1}{1+\beta^2}\frac{1}{Pr}} = \frac{PrRe}{\frac{\beta^2}{1+\beta^2}Pr + \frac{1}{1+\beta^2}Re} = \frac{(1+\beta^2)PrRe}{\beta^2 Pr + Re}$$
where β is a parameter controlling the trade-off between the Precision and the Recall. Using the first formulation we can easily observe that $F_0 = Pr$ and $\lim_{\beta \to \infty} F_\beta = Re$.

The F-measure, which corresponds to the F_β*-measure* with $\beta = 1$, is a widely used measure to assess the performance of a model. Particularly, in imbalanced settings where using the accuracy of the classifier would greatly favor the majority class (Chandola et al., 2009; Lopez et al., 2013). However, the F-measure being non-differentiable, non-separable, and non-convex, we cannot learn a classifier directly optimizing this measure.

Several methods have been studied to solve the F_β-measure optimization problem. They can roughly be separated into two categories:

Decision Theoretic Approaches (DTA) (Dembczyński et al., 2017) This consists in trying to find the classifier that maximizes the expectation of the F-measure. More precisely, these methods usually fit a probabilistic model during training followed by an inference procedure at prediction time (Decubber et al., 2018). The probabilistic model can be learned by optimizing a "simpler" surrogate function (e.g., (Dembczynski et al., 2011; Jansche, 2005; Ye et al., 2012; P.M. Chinta and Murty, 2013)).

Empirical Utility Maximization (EUM) This consists in learning multiple accurate models with different parameters and keep the model which maximizes the F-measure (Busa-Fekete et al., 2015; Joachims, 2005; Musicant et al., 2003; Parambath et al., 2014; Zhao et al., 2013; Narasimhan et al., 2015). The parameters can be the different classification thresholds for probabilistic models (Busa-Fekete et al., 2015; Joachims, 2005; Zhao et al., 2013; Narasimhan et al., 2015) or the costs on the classification errors for cost-sensitive methods (Musicant et al., 2003; Parambath et al., 2014; Koyejo et al., 2014).

EUM methods focus on *estimation* on a possibly infinite training set, while *DTA* approaches are concerned with *generalization* performance (Dembczyński et al., 2017). Ye et al. (2012) shows that both categories of methods give asymptotically the same results and propose heuristics to decide on the category to use depending on the context.

One of the few recent papers addressing the F-measure optimization, from a theoretical point of view, (see also (Busa-Fekete et al., 2015; Zhao et al., 2013; Koyejo et al., 2014; Narasimhan et al., 2015)) is the work from (Parambath et al., 2014). The authors propose a grid-based approach to find the optimal costs for which a cost-sensitive classifier would give

the best F-measure. They theoretically prove that, with a sufficiently precise grid, one can be arbitrarily close to the optimal F-measure. However, this method relies on a relatively loose result which imposes to parse the whole grid leading an unnecessary computational burden. The methods proposed by Koyejo et al. (2014) and by Narasimhan et al. (2015) achieve good performances with a limited time budget using a cost-sensitive approach. They roughly consist of fitting a probabilistic model then using a threshold in order to optimize the F-measure. In the first cases the threshold is tuned on a validation set while an iterative process based on the bisection algorithm (Boyd and Vandenberghe, 2004). However, we will see in Chapter 4, that, despite their simplicity (and the theoretical guarantees provided), it is possible to achieve higher performance by training (a few) number of models. Indeed, tuning a model is not enough, and we need to learn a different hyperplane to take the costs on each class into account.

To optimize the F-measure in deep learning, Pastor-Pellicer et al. (2013) modifies the computation of the F-measure to be differentiable, and thus, allows it to be used as loss function. To do that, the authors changed the discrete counting of the confusion matrix elements into continuous values using the prediction of the network:

$$TP = \sum_{i=1}^{M} \widehat{y}^i y^i \quad FP = \sum_{i=1}^{M} \widehat{y}^i (1 - y^i) \quad FN = \sum_{i=1}^{M} (1 - \widehat{y}^i) y^i$$

In their paper, Sanyal et al. (2018), the authors propose *DAME*, an algorithm to train deep learning techniques to maximize pseudolinear measures, like the F-measure. They first initialize a neural network by pre-training it with a loss optimizing the accuracy. Then they fine-tune only the classifier part with a two stage training. First they sample a minibatch and set a parameter v with the value of the considered measure obtained by the classifier on the minibatch. Then start a training loop over all the dataset, updating the weights of the classifier according to a *valuation function* derived from the performance measure and depending on v. As in, Pastor-Pellicer et al. (2013), the counted values are replaced by *reward function* so that the valuation function can be derived. This process is repeated until all the data has been sampled.

Chapter 2

Datasets and evaluation setting

In this chapter, we present the different datasets used to benchmark our approach. We also present the Bluecime dataset in details. We then present our first contribution: an experimental framework to be associated with the Bluecime dataset. In this framework, we propose some training settings to emulate the different stage of the Bluecime industrial deployment of machine learning approaches. We also compare some performance measures to be used to optimize models on the Bluecime problem.

2.1 Datasets

In this section, we introduce the benchmark datasets we used during this thesis to provide results on publicly available data. Then, we give more technical details on the Bluecime dataset.

2.1.1 Benchmark datasets

We first describe some benchmark datasets dedicated to image processing, then a number of non-image datasets composed of diverse continuous or categorical attributes, taken from UCI (Dua and Graff, 2017).

2.1.1.1 Images

Caltech Two Caltech datasets are available: *Caltech101* (Fei-Fei et al., 2007) and *Caltech256* (Griffin et al., 2007), the digits indicate the number of classes of the corresponding classification problems. The classes are highly diverse, for instance, *airplanes*, *lamps*, or *pandas* in Caltech101. Note that some classes are common between the two datasets, but Caltech101 is not entirely included in Caltech256. The images have various shapes and sizes from around 200 to 700 pixels, and can be color or grayscale images. There are 30 to 800 images per class.

Office Presented in Saenko et al. (2010), *Office* is meant for benchmarking domain adaptation techniques. It is composed of three domains: Amazon, DSLR, and Webcam.

The images are divided into 31 classes, such as *bikes*, *keyboards*, or *monitors*. Amazon is constituted of images taken from Amazon's website, thus, its images present a large diversity of objects. This domain contains 30 to 90 300×300 pixels images per class. DSLR and Webcam correspond to pictures of objects took, respectively with a high resolution camera and a low resolution webcam. DSLR contains 7 to 31 1000×1000 pixels images per class. Webcam is composed of 11 to 43 images per class. Their sizes vary approximately from 400×400 to 800×800.

ImageNet This dataset contains over 14 million web images divided into over 100 000 classes (Deng et al., 2009). The classes are organized into hierarchies from the *WordNet* ontology. In the following, when we refer to the *ImageNet* dataset we actually refer to a subset composed of around 1.2 million images over 1000 classes. This subset was used in the ILSVR competition (Russakovsky et al., 2015). The classes cover a wide range of subjects, such as landscapes, trucks, or various dog breeds. The image resolution varies from less than 100 pixels wide to more than 2000.

2.1.1.2 Attributes

The datasets marked with the "$*$" symbol are taken from the LIBSVM website[1]. The ones marked with the "$\circ$" symbol come from the UCI repository[2]. We call *imbalance ratio* (I.R.) the number of majority class examples per minority class one, so that, the higher the imbalance ratio is the less balanced the dataset is.

Abalone 10/12° The task on *Abalone* dataset is to predict the age (from 1 to 29) of abalones (sea snail) according to different measures. Each individual is characterized by 10 attributes, such as *sex*, *length*, or *height*. The dataset contains 4 174 examples highly unevenly distributed among the 29 classes, with 1 to 638 per class. We converted this multi-class task to two binary tasks by considering a class as positive and the others as negative. With the class 10 as positive we obtain a dataset with an imbalance ratio of 5.64, with the class 12 the dataset presents an imbalance ratio of 15.18.

Adult$^\circ$ Also known as *census dataset*. Here, the task associated is to predict if a person's income is more or less than 50 000\$/year. The examples are represented with 14 attributes, among which, for instance, the *age*, the *education*, or the *occupation* of the person. In practice, we transform the categorical attributes into one hot vectors, from the 14 attributes we then obtain 123 different features. Adult is composed of 48 842 examples, with an imbalance ratio of 3.19.

IJCNN'01* Introduced for the IJCNN 2001 competition (Prokhorov, 2001), each data point corresponds to the state of a 10-cylinder engine at a given time. The task is to determine

[1] https://www.csie.ntu.edu.tw/~cjlin/libsvm/
[2] https://archive.ics.uci.edu/ml/datasets.html

if, at a given time, the engine is normally firing or not. The state of the engine is defined by four attributes: the *cylinder identifier*, the *rotation speed*, the *load*, and the *acceleration of the crankshaft*. Using the same pre-processing as the competition winner (Chang and Lin, 2001) we obtain a representation with 22 features. *IJCNN'01* contains 141 691 examples with an imbalance ratio (I.R.) of 9.39.

Page Blocks 3,4,5° The associated task is to determine the content of a given page block. It can be either a text, a horizontal line, a picture, a vertical line, or a graphic. The dataset contains 5 473 examples, each represented by 10 attributes, such as the *height* and the *length* of the block, or the *percentage of black pixels* the blocks contain. As with *Abalone*, we convert the task to a binary one, taking the 3 last classes as positives (and the two first one as negative), the created dataset has an imbalance ratio of 22.7.

Satimage 4° This dataset is composed of small patches of 3×3 pixels from satellite images. The task is to determine the type of ground appearing in the patch, among seven possible classes, as for instance *red soil* or *cotton crop*. Each pixel has four channels, one for the red color, one for the green color, and two infra-red. An example is thus represented by 36 attributes. *Satimage* is composed of 6 435 images, we used the fourth class (*damp grey soil*) as positive, which creates a dataset with an imbalance ratio of 9.3.

Yeast 4° The task associated to *Yeast* is to predict the localization of proteins in a yeast cell, among 10 possible locations. This dataset contains 1 484 examples, each one is represented by 8 different scores used in biology. We used the fourth class as positive (*ME2*) providing a dataset with an imbalance ratio of 28.1.

Wine 4° Actually named *Red Wine Quality*, the corresponding task is to predict the quality of a wine on a scale from 0 to 10. The examples have 11 attributes, such as the *pH*, the *density*, or the *degree of alcohol*. *Wine* contains 1 599 examples, we used the class 4 as positive, implying an imbalance ratio of 29.17.

Letter° The corresponding task is to predict the letter corresponding to the examples, so, there are 26 classes. The data points have 16 attributes corresponding to different measurements of the letter. For example, its *length*, its *height*, or the *number of pixels* in its bounding box. *Letter* is composed of 20 000 examples, they are approximately evenly distributed, from 734 to 813 examples per class.

News20* This dataset is composed of 19 928 documents, the task is to predict the topic the most related to the examples. There are 20 classes (topics), such as, politics, motorcycle, or medicine. Each example is represented by 62 061 attributes, each providing the *number of occurrences* of a given word in the document. We used a scaled version of the dataset, containing the inverse of the document size instead of the number of occurrences. The classes

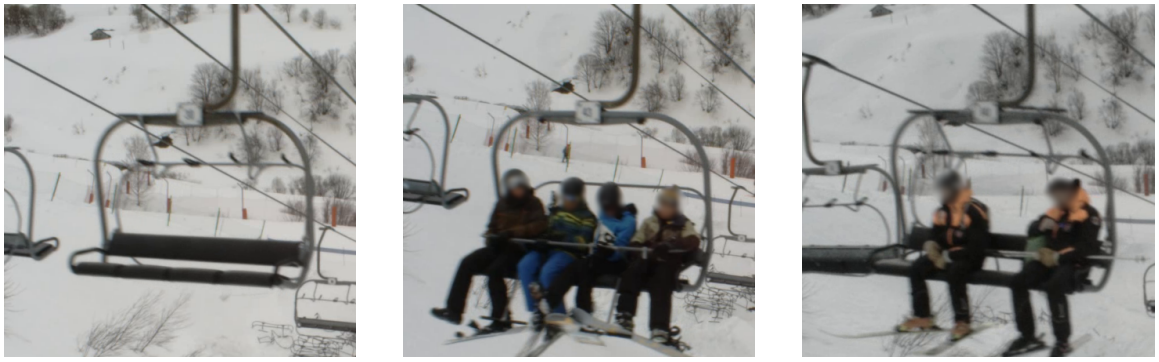

Figure 2.1 – Training images from each class, from left to right: *Empty*, *Safe*, and *Unsafe*.

are well-balanced with a maximum imbalance ratio of 1.12 (ratio between the largest and the smallest classes).

2.1.2 Bluecime dataset

The Bluecime dataset is continuously growing as can be seen in Table 2.1. During the skiing season, several videos are recorded, then, for each video, each passing of a vehicle in front of the camera (called a "track") is manually annotated. From each track, we only keep three frames: the last one, one 5 frames earlier, and one 10 frames earlier. Note that only the last frame is annotated (and the same label is given to the other two), so, the other two may be misclassified (for example if the passengers were in the process of closing the railing bar).

As shown in Figure 2.2, the Bluecime dataset presents a lot of variations. These variations come from natural causes, such as the weather condition (e.g. snow on Chair. O or fog on Chair. I), or the light and the sun position (As we can see the large shadow on Chair. C which will change as the sun moves during the day). There are also variations from the camera, mainly caused by its point of view, as in the extreme case of Chair. N recorded from behind. On chairlifts whose vehicles are close to the camera, the images can also present motion blur, for instance, on Chair. P. Moreover, the chairlifts were designed by different manufacturers at different times: all the chairs in the dataset are different, though some are similar. There are even some unique cases, for instance, on Chair. D the vehicles have a glass bubble as a second protection, or, on Chair. F, the vehicles do not have a complete frame.

The objective of Bluecime is to determine if the passengers of a chairlift vehicle are safe or not. We use three classes: *Empty*, *Safe* and *Unsafe* (Fig. 2.1). In the first case (*Empty*), the vehicle does not carry any passengers. In the second case (*Safe*), the vehicle carries passengers who closed the restraining bar completely. The last case (*Unsafe*) is expected to contain all the possibly unsafe situations, such as passengers falling off the vehicle or children alone on the vehicle. In practice, in the context of this work, this class contains images where the vehicle carries passengers and the restraining bar is slightly or completely open. In the Bluecime context, the *Empty* and *Safe* examples should not trigger an alarm, they are considered as negative classes. *Unsafe*, however, corresponds to situations where the alarm

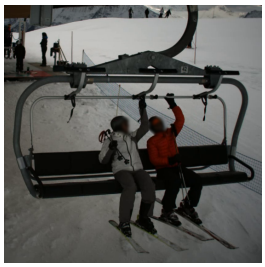
Chair. A (*Unsafe*)


Chair. B (*Safe*)


Chair. C (*Safe*)


Chair. D (*Unsafe*)


Chair. E (*Empty*)


Chair. F (*Safe*)

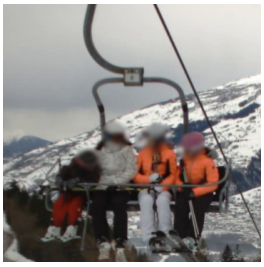
Chair. G (*Safe*)


Chair. H (*Safe*)


Chair. I (*Safe*)

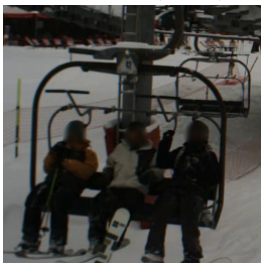
Chair. J (*Unsafe*)


Chair. K (*Unsafe*)


Chair. L (*Empty*)


Chair. M (*Unsafe*)


Chair. N (*Unsafe*)


Chair. O (*Unsafe*)


Chair. P (*Safe*)


Chair. Q (*Unsafe*)


Chair. R (*Empty*)


Chair. S (*Safe*)


Chair. T (*Safe*)


Chair. U (*Unsafe*)

Figure 2.2 – Examples from Bluecime dataset

should be triggered, it is a positive class.

Year	# Chairlifts	# Tracks	# *Empty*	# *Safe*	# *Unsafe*	I.R
2016	5	10 560	6 094 (57.7%)	3 924 (37.2%)	542 (5.1%)	18.5
2017	15	25 112	14 045 (55.9%)	9 129 (36.4%)	1 938 (7.7%)	12.0
2018	21	25 442	13 585 (53.4%)	9 685 (38.1%)	2 172 (8.5%)	10.7
2019	40	77 613	36 225 (46.7%)	33 372 (43.0%)	8 016 (10.3%)	8.7

Table 2.1 – Bluecime dataset size over the years.

Chairlift	# Tracks	# *Empty*	# *Safe*	# *Unsafe*
Chair. A	1420	410 (28.9%)	529 (37.3%)	481 (33.9%)
Chair. B	927	119 (12.8%)	739 (79.7%)	69 (7.4%)
Chair. C	985	817 (82.9%)	105 (10.7%)	63 (6.4%)
Chair. D	757	498 (65.8%)	252 (33.3%)	7 (0.9%)
Chair. E	1621	694 (42.8%)	793 (48.9%)	134 (8.3%)
Chair. F	1188	652 (54.9%)	507 (42.7%)	29 (2.4%)
Chair. G	526	251 (47.7%)	259 (49.2%)	16 (3.0%)
Chair. H	1002	592 (59.1%)	321 (32.0%)	89 (8.9%)
Chair. I	1396	1194 (85.5%)	137 (9.8%)	65 (4.7%)
Chair. J	1624	1011 (62.3%)	498 (30.7%)	115 (7.1%)
Chair. K	1288	623 (48.4%)	521 (40.5%)	144 (11.2%)
Chair. L	2289	1408 (61.5%)	621 (27.1%)	260 (11.4%)
Chair. M	498	136 (27.3%)	306 (61.4%)	56 (11.2%)
Chair. N	344	204 (59.3%)	138 (40.1%)	2 (0.6%)
Chair. O	730	371 (50.8%)	279 (38.2%)	80 (11.0%)
Chair. P	1286	771 (60.0%)	401 (31.2%)	114 (8.9%)
Chair. Q	2291	1201 (52.4%)	1027 (44.8%)	63 (2.7%)
Chair. R	1253	516 (41.2%)	585 (46.7%)	152 (12.1%)
Chair. S	502	361 (71.9%)	86 (17.1%)	55 (11.0%)
Chair. T	930	482 (51.8%)	391 (42.0%)	57 (6.1%)
Chair. U	2585	1274 (49.3%)	1190 (46.0%)	121 (4.7%)

Table 2.2 – Detailed Bluecime 2018 dataset.

As you can see in Table 2.1, in 2016, only 10k examples over 6 chairlifts were available. In 2017, the dataset increased to 25k examples and 15 chairlifts. In 2018, the number of examples stagnated to 25k, but over 21 chairlifts. The stagnation of the dataset size is explained by changes of the camera orientation or position for some of the existing systems, cases in which the images corresponding to the previous positions were removed. In 2019, the number of chairlifts nearly doubled with 40 chairlifts, the number of tracks tripled with

Figure 2.3 – Bluecime image formats, from left to right: *camera*, *pyramid*, and *unity*.

77k examples. Note that the proportion of positive example increases. It is mainly due to a feature implemented in 2017 by Bluecime which allows to automatically save videos of tracks detected positive by the system. In the following, we will refer as Bluecime dataset the 2018 version. You can find detailed statistics on this version on Table 2.2.

2.1.2.1 Choice of Bluecime images format

Three images format can be extracted with SIVAO (see Fig. 2.3):

- *Camera image*: The raw frame capturing all the surrounding environment of the vehicle
- *Pyramid image*: The *camera image* cropped and centered on the tracked vehicle position in the detection pyramid used in SIVAO processes (see Fig. 1)
- *Unitary image*: The *pyramid image* back-warped to a common reference position and to the size of the back of the detections pyramid

The *Camera images* capture all the surrounding environment of the vehicle, thus, they contain a large amount of useless information. Moreover, the SIVAO cameras capture high resolution images, which can be costly if directly used with a deep learning approach. So, to tackle the Bluecime problem with *camera images*, we considered using spatial transformer layers (Jaderberg et al., 2015). This approach consists in learning a network which outputs a transformation matrix, which is, then, applied to the input image. The transformed input is then given to a classification network such as our proposed architecture. As it is trained with the classifier, the spatial transformer network learns to transform the raw input such that it maximizes the classification performance. In the Bluecime context, we could use it to replace the tracking system and directly use the *camera image*.

The *pyramid images* are cropped and centered onto the tracked vehicle position in the detection pyramid, thus, can contain viewing angle and perspective variations. These variations depend on the pyramid definition (one configuration per chairlift), and the progress of the vehicle in the pyramid at the capture instant. Having variations in the dataset can be beneficial to training networks, indeed, it can reduce overfitting and allows learning more robust models. The *unitary images* are a warped version of the *pyramid images*, such that, the vehicle is always centered in the image, thus, the perspective changes through the detection

Setting	Expe.	Accuracy	F-measure
OOC	Pyramid	98.04	87.93
	Unitary	98.28 (+0.24)	89.34 (+1.41)
ALL DA	Pyramid	98.63	91.89
	Unitary	98.72 (+0.09)	92.37 (+0.48)
LOCO DA	Pyramid	97.10	83.82
	Unitary	97.70 (+0.60)	86.58 (+2.76)

Table 2.3 – Comparison between networks trained on *pyramid images* and trained on *unitary images* (using settings presented in section 2.2). In the OOC setting, both the training and the test sets are composed of images from the same chairlift. In the ALL setting both the training and the test sets are composed of images from all the chairlifts. In the LOCO setting the training set is composed of all the chairlifts but one, the test set is composed of the remaining chairlift. We give more details on the evaluation setting in Section 2.2.1.

pyramid are attenuated. The *unitary images* should provide a dataset with fewer variations between the testing and the training sets than the *pyramid images*. Moreover, the *unitary images* can present fewer variations (particularly from viewing angles) between the different chairlifts than the *pyramid images*.

According to Table 2.3, the stability of the *unitary images* is more important than the variety of the *pyramid images*. Indeed, in the three main settings, OOC, ALL DA, and LOCO DA (presented in section 2.2), training with the *unitary images* gives better performances than with *pyramid images* (resp. +0.24%, +0.09%, +0.6% of Accuracy). The system developed by Bluecime to track the vehicle in the detection pyramid (allowing to extract both the *pyramid* and *unitary images*) is currently well performing and easy to configure. We choose to keep this tracking system and use the *unitary* format, instead of the camera model, to reduce our model complexity without loosing efficiency.

2.2 Evaluation

In this section, we present the deep learning architecture and the different settings of our experiments we will use in the following. This work, as well as the Bluecime dataset (the 2016 version), were presented in Bascol et al. (2017), at the sixteenth International Symposium on Intelligent Data Analysis (IDA 2017).

2.2.1 Train and test sets settings

SIVAO is a commercialized product that aims at improving the work of chairlift operators. We use its current performance as an indication of the minimal result requirements for an acceptable quality of service that we aim to surpass with our automatic system.

To study the behavior of our methods, we considered six different experimental settings:

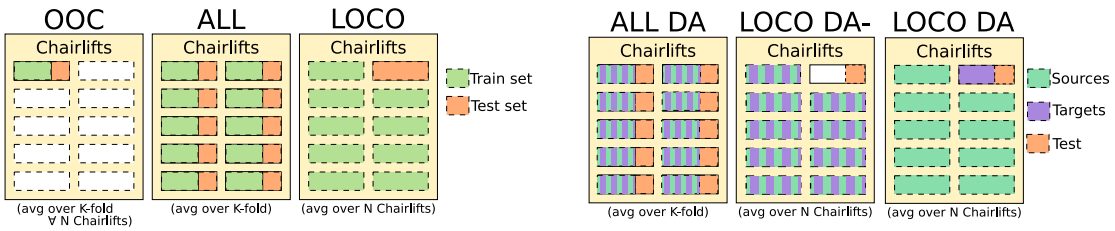

Figure 2.4 – Experimental settings

1. **OOC** ("Only One Chairlift"). Each chairlift is considered independently (as it is done by SIVAO), thus the training and the testing sets are composed of images from a single chairlift. Obviously, with only one chairlift per experiment, the domain adaptation component (described in Section 3.1) is not used on this setting.

2. **ALL** One experiment is performed without using the domain adaptation component. The images are taken from all the chairlifts in the training and the testing set.

3. **ALL DA** Same as ALL setting, adding the domain adaptation component. The target images are the same as the source ones.

4. **LOCO** ("Leave One Chairlift Out") In each experiment, we use only the feature extractor and the classifier, with the images of all the chairlifts but one mixed in the training set and all the images of the remaining chairlift as test set.

5. **LOCO DA-** Same as LOCO but with domain adaptation. The target images are the same as the source ones, so *no example* (labeled or not) from the tested chairlift are used during training, this is thus a *domain generalization* setting.

6. **LOCO DA** Same as LOCO but with classical unsupervised domain adaptation where some *unlabeled* examples of the target chairlift are used by the domain adaptation component.

We show a graphical representation of these settings on Figure 2.4. All the presented results are averaged over five folds. Note that for the LOCO settings, only the test set (and target set for LOCO DA) changes across the different folds.

In Setting 1 (OOC), to reduce the number of experiments, we do not tune the hyperparameters for each domain, but we use one single hyperparameter setting for all the chairlifts. In this setting, we expect the network to quickly overfit our data and also to be penalized by the lack of examples especially for the least represented chairlifts.

In Settings 2 and 3 (ALL and ALL DA), we train our network using all the training data available. We only build one model for all the chairlifts which makes this setting easier to deploy in practice. However, the hyperparameters of the system are also global which may harm the final performance. These settings could be used with the current cameras installed by the company but do not evaluate the real ability of our system to work on *new* chairlifts.

Settings 4 to 6 (LOCO, LOCO DA-, and LOCO DA) really show the benefit of our proposed approach. Ideally, our method should show good enough performance on these settings to allow Bluecime to deploy their system equipped with this model on any new chairlift with no manual labeling. In these settings, we expect a performance drop compared to the OOC or ALL settings because of the variability of the different domains. Note that LOCO DA- is an unusual, challenging and very restricted domain adaptation settings. This setting can be interesting from an operational point of view, as it considers classification on a new chairlift without retraining the entire network.

2.2.2 Performance measures

Accuracy	$A = \frac{TP+TN}{TP+FN+TN+FP}$
Precision	$P = \frac{TP}{TP+FP}$
Recall	$R = \frac{TP}{TP+FN}$
F-measure	$F = \frac{(1+\beta^2)*P*R}{\beta^2*P+R}$

Table 2.4 – Measures formulation

To evaluate their system, the company relies on numerous measures. Among these, 4 statistical measures assess the overall performance of the system: recall, precision, F-measure (van Rijsbergen, 1974), and accuracy (see Table 2.4). We recall that *Unsafe* examples are considered positive (the alarm has to be triggered), and safe examples are considered negative (no alarm needed), thus the classes *Empty* and *Safe* are both considered negative. The *Recall* gives the proportion of examples correctly detected positive among all the examples labeled positive. In our case, it is the ability of the system to trigger an alarm in unsafe situations. The *Precision* gives the proportion of examples correctly detected positive among all the examples detected positive. Thus, it indicates the ability of the system to avoid useless alarms (false positive). The *F-measure* and the accuracy give a more global view on the performance of the system. In the following, we will put the emphasis on the F-measure. Indeed, Bluecime requires a system detecting all the anomalies (high Recall), and no mistakes to ensure the proper functioning of the chairlift (high Precision).

Chapter 3

First approach and training improvement

In this section, we present the deep learning architecture and the different settings of our experiments we will use in the following. This work was presented in Bascol et al. (2017), at the sixteenth International Symposium on Intelligent Data Analysis (IDA 2017).

3.1 Selected architecture

Based on the state-of-the art study presented in Chapter 1, we propose an image classification architecture using domain adaptation and a convolutional residual network pre-trained on ImageNet. This architecture is shown in Figure 3.1 and is divided into three parts:

1. a feature extractor, which learns a new image representation (ResNet50 from He et al. (2016));
2. a classifier, which predicts the class of an image;
3. a domain discriminator, which ensures that the feature extractor is domain invariant, to improve classification accuracy on unseen data (DANN from Ganin et al. (2016)). Note that this part is only added with "DA" settings.

3.1.1 Network architecture

Our network inputs are RGB images of size 224×224 (imposed by constrains on the pre-training) that can be viewed as three-dimensional tensors (two spatial dimensions and one dimension for the RGB channels). After some trial and error (some results are presented in Section 3.1.3), we decided to use the ResNet architecture presented in the previous section with 50 layers and pre-trained on the ImageNet dataset (see the *training tricks* section 1.2.1.3). Networks with more layers gave a slightly better accuracy but were longer to train and the biggest ones (with more than 101 layers) did not allow us to process test images in real time on a CPU. The 50 layers architecture (shown in Fig. 3.1) gave us a good trade-off between

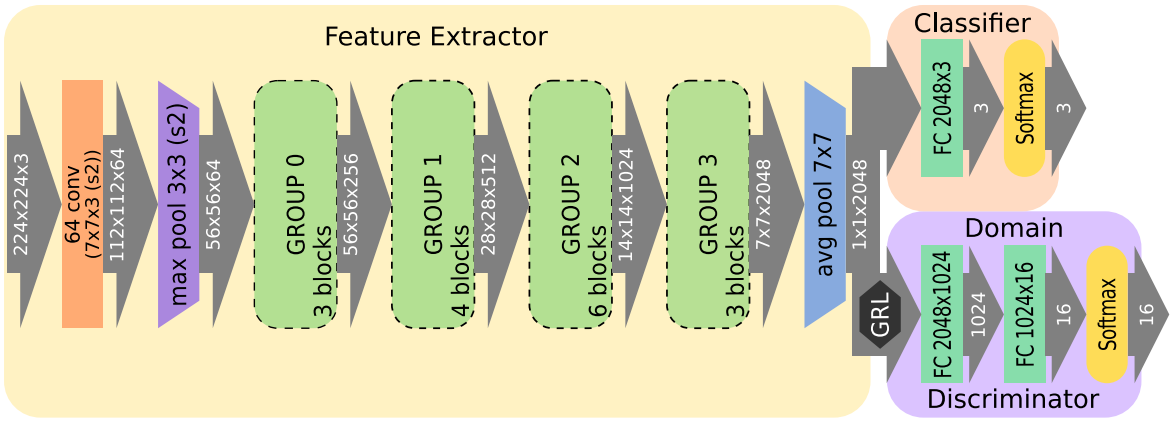

Figure 3.1 – The proposed ResNet architecture with domain adaptation, for a 3-class classification problem with 16 domains (chairlifts).

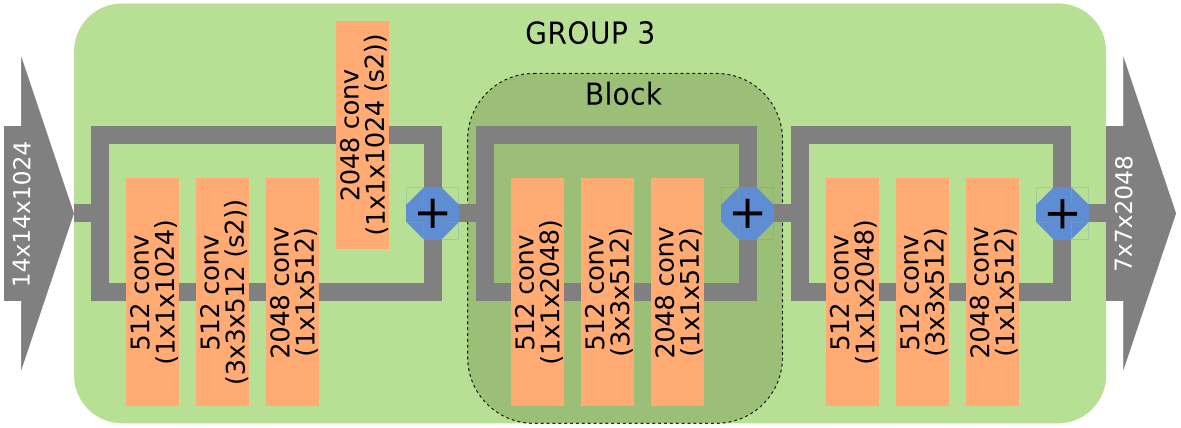

Figure 3.2 – Details of the last group of layers in our architecture (see Fig. 3.1), which is composed of three residual blocks and different convolution filters.

computational efficiency and accuracy. This network is composed of 49 convolutional layers and only one fully connected layer at the output of the network. This last layer is preceded by an average pooling layer which reduces the size of the feature maps to a 1D-vector. The last layer of the original ResNet 50 architecture was changed to fit our 3-classes classification problem (instead of the 1000 classes of the ImageNet classification problem). We used our chairlift dataset to train this last layer and fine-tune the entire network.

In the feature extractor, each group is composed of a set of blocks. Each block is composed of three layers: a 1×1 convolution that acts as a learnable dimensionality reduction step (here over the channel dimension), a 3×3 convolution that extracts some features and a 1×1 convolution that restores the dimensionality. As explained in Section 1.2.1.2, we use the residual connections between each block to ease the training phase.

The first block of each group contains a 3×3 convolution with a stride of 2 which reduces the spatial size by a factor two. To compute the block output with the sum operator, the input needs to have the same dimensions as the output. Therefore, a 1×1 convolutional layer

with a stride of 2 is added to reduce the spatial size and also to match the number of feature maps which changes according to the group. In Figure 3.2, we show in more details the last group of layers in the feature extractor.

3.1.2 Objective function and training

Different losses are classically used in deep learning. The best known for image classification is the cross-entropy (Goodfellow et al., 2016). After experimenting with different losses, we decided to use the more robust multi-class hinge loss (eq. 3.1) commonly used in SVM:

$$\mathcal{L}(\boldsymbol{W}, \boldsymbol{X}, t) = \frac{1}{B} \sum_{i=1}^{B} \frac{1}{|\boldsymbol{C}|} \sum_{c \in \boldsymbol{C} \setminus \{t\}} \max(0, o_c^i - o_t^i + m) \tag{3.1}$$

where W is the set of all the parameters in the network, $\boldsymbol{X}$ is the subset of the input dataset (minibatch) given to the network during a forward pass, B is the minibatch size, $\boldsymbol{C}$ is the set of classes, and t is the ground-truth label corresponding to each example of the minibatch. The margin m can be seen as the minimal "distance" required between the computed probability of the prediction of the target class (o_t^i) and the other classes (o_c^i). Indeed, the loss value is equal to 0 when $o_t^i \geq o_c^i + m$. This loss presents several advantages: (i) it is defined on $p(x) = 0$ which makes it more robust than the cross-entropy; (ii) it does not penalize the weights on well classified examples which could speed up the convergence of the network; (iii) the slope and the margin of the function can be easily changed to give a custom weight to the different type of errors (false positive, false negative). This last advantage will be explored in Chapter 4.

Domains and classes balance Bluecime dataset is imbalanced both in the domain distribution and the class distribution. Having under-represented domains can be harmful, mainly in the ALL setting, as the model would be trained with small data from these domains, thus impairing the results on them. The imbalanced class distribution is also harmful, only a few positive examples would be used during the training of the classifier, thus impairing the results on this class. This would particularly result in a low F-measure, as this measure puts the emphasis on the good classification of the positive examples. To tackle both problems, we propose to artificially balance the training set, by randomly selecting a domain and a class uniformly at each image loading. This implies that each *Unsafe* example is reused more often than the *Empty* examples. We thus have a dataset with less variety, but in return we have virtually more positive examples, which should allow us to obtain better results on this class.

We show on Tables 3.1 and 3.2, results modifying (or not) the balance of both the domains and the classes. We see that balancing the classes is always a better option. This shows that the loss of variety in the training set is more than compensated by the increase of positive examples. However, balancing the domains is beneficial in ALL setting but not in the LOCO one. This confirms our first intuition that having under-represented domains in the training set is harmful only if we test on them. This also suggests that some under-represented chairlifts

Expe.	Accuracy	Recall	Precision	F-measure
ALL DA bcl bdom	98.72	90.54	94.28	92.37
ALL DA ubcl bdom	98.70 (−0.02)	88.90 (−1.64)	95.55 (+1.27)	92.11 (−0.26)
ALL DA bcl ubdom	98.71 (−0.01)	90.19 (−0.35)	94.41 (+0.13)	92.25 (−0.12)
ALL DA ubcl ubdom	98.64 (−0.09)	90.10 (−0.44)	93.68 (−0.60)	91.86 (−0.51)

Table 3.1 – ALL DA results with and without domain and class balancing method. (u)bcl indicates experiments with (un)balanced classes. (u)bdom indicates experiments with (un)balanced domains.

Expe.	Accuracy	Recall	Precision	F-measure
LOCO DA bcl bdom	97.41	89.17	82.94	83.30
LOCO DA ubcl bdom	94.64 (−2.77)	39.92 (−49.26)	93.73 (+10.78)	55.99 (−27.31)
LOCO DA bcl ubdom	97.63 (+0.22)	87.52 (−1.65)	85.17 (+2.23)	86.33 (+3.03)
LOCO DA ubcl ubdom	95.02 (−2.39)	43.32 (−45.85)	96.22 (+13.27)	59.75 (−23.55)

Table 3.2 – LOCO DA results with and without domain and class balancing method. (u)bcl indicates experiments with (un)balanced classes. (u)bdom indicates experiments with (un)balanced domains. Note that, in these experiments, the classes of the target examples are balanced, which implies that it is not a correct unsupervised setting, this matter is discussed in length in the chapter 5.

induce negative transfer as we get better performance if we use fewer examples from them in the LOCO training set. This phenomenon will be studied in more details in Chapter 5.

3.1.3 Feature extractors comparison

We show, in Table 3.3, results, and training and testing times using different feature extractors: ResNet with 50 layers, ResNet with 18 layers, MobileNet-v2, and Inception-v4. We can see that using ResNet50 yields the best results. However, ResNet18 and MobileNet take less time to provide an output. These results confirm our choice to use the ResNet architecture. However, The choice of the number of layers to use is arguable. Indeed, we obviously need to have the best model, but we also need to get the output in real time. So, the choice of ResNet50 or ResNet18 will be dependent on the integration of the model in SIVAO. For instance, if we only use one frame to decide, we should use ResNet50. However, if we want to average the prediction over several frames, ResNet18 would be more appropriate. In addition, currently, the SIVAO system contains only a CPU, reducing the models speed dramatically, which increases the need for speed in our approach.

Expe.	Accuracy	F-measure	train.	test.
ALL DA Rn50	98.72	92.37	900	2.5
ALL DA Rn18	98.66 (−0.06)	91.86 (−0.51)	500	1.3
ALL DA Mv4	98.43 (−0.29)	90.51 (−1.86)	700	1.5
ALL DA Iv4	98.52 (−0.20)	91.21 (−1.16)	1000	2.5

Table 3.3 – Experiments in ALL DA setting comparing our selected feature extractor ResNet50 with ResNet18 (Rn18), inception-v4 (Iv4), and MobileNet-v2 (Mv2). Training time ("train.") corresponds to milliseconds per iteration, Testing time ("test.") to milliseconds per image. All these experiments are conducted using the same GPU model (NVIDIA Geforce GTX 1080Ti).

3.2 Data augmentation strategies

In this section we present the data augmentation techniques we use in our approach. Then, we propose a new data augmentation technique based on covering important portions of the input images.

3.2.1 Classical strategies

We use two classical data augmentation techniques to improve our approach performance: *Cropping*, the original images from Bluecime are of various sizes (depending on the chairlift), we rescale them to 237×237, so that, we can crop 224×224 images from it. The cropping size is limited to avoid cropping too much the vehicle. *Flipping*, as evoked in Section 1.2.1.3, we use horizontal flipping, exploiting the symmetry of the vehicles. In addition, on Bluecime problem, during training, we use different frames of each track as data augmentation. For a given track, the label does not change across the frames. So, the annotation can be incorrect on frames in the beginning of the pyramid where the passengers can be in the process of closing the restraining bar. However, the labeling errors are scarce, and the data augmentation effect is sufficiently efficient, so that, it improves the performance of our network. We considered randomly changing the brightness of the input images. Considering the natural light condition changes, using brightness variations as data augmentation could help training a network more robust to such changes. However, experiments showed that this technique worsens the performance of our approach. We also tried to use rotated data. Applying small rotations to the images could allow us to increase the robustness of the network against the orientation variation of the vehicle. For instance, when only one side of the chair is occupied, the vehicle may lean. Again, the experiment showed no benefit from this data augmentation.

3.2.2 Data augmentation by patching RoI

A simple method to find image features that are important to classify an image consists in hiding zones in the image with black patches and comparing the outputs of the network for the source image and the patched image. If the prediction is badly altered it means that the

patched zone is important for the classification. If the alteration of the prediction is negligible then the patched zone is not interesting for the network.

(a) (b) (c)

Figure 3.3 – Visualization with patch of size 28×28 pixels (without overlapping). 3.3a is the source image, the prediction variation for all the patches is shown on 3.3b (with the source image in the background) and 3.3c (with the variation only). The color of a patch indicates the prediction of the network for the patched image. An orange patch corresponds to a high probability on the *Unsafe* class. A green one indicates a high probability on the *Safe* class.

On the figure 3.3, we observe that if we hide the area around the vehicle the prediction is correct (class *Unsafe* since the security railing is up). However, if we hide the area where the railing should be when it is closed, the probability on the *Safe* class strongly increases so that the images with theses patched areas are predicted *Safe*.

This visualization method shows us that the classification of an image can depend on a small region of interest (RoI). Following this, we tried to include patches inducing high negative prediction variation to the network training. So that, it forced the network to use the whole image, and thus, to increase the robustness of the model. To do that, during each training iteration we do a forward pass with a given number of patched images. We then add to the dataset the images with a patch inducing a decrease of the probability on the true class superior to a given threshold (Fig. 3.4). This approach is similar to the dropout method presented in Zhong et al. (2017) (whose work was done in parallel to ours). However, we propose to guide the discarded areas to produce harder examples, we thus expect a better result than using random patches.

3.2.2.1 Experiments

Randomly sampled batches In Table 3.4 we propose to compare our patching approach to our baseline ALL DA and ALL DA with patches randomly applied on the image loading (similarly to DeVries and Taylor (2017) or Zhong et al. (2017)). We observe that adding patches during the training is beneficial with on average +0.07 pts of Accuracy and +0.30 pts of F-measure. However, our method requires 25 batches of patched images to only match the results using random addition of patches. We could try to increase the number of batches so

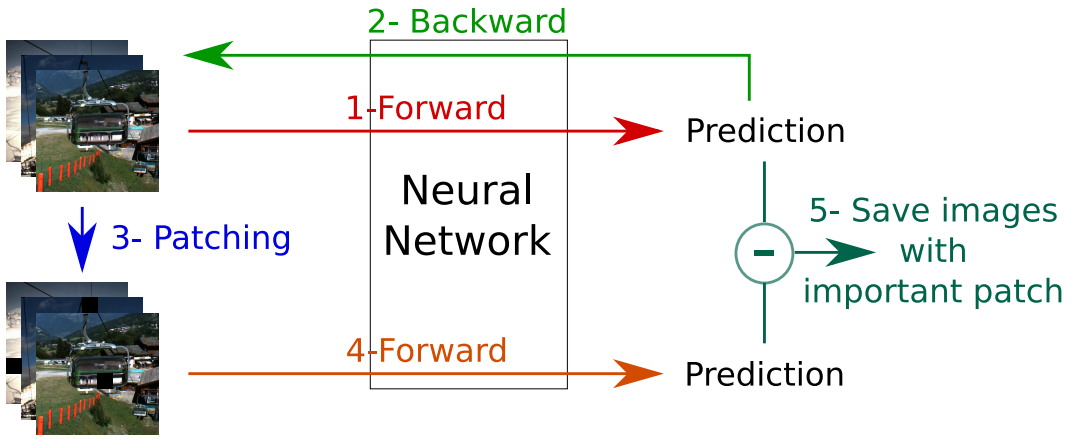

Figure 3.4 – Training iteration with patches in 5 steps: 1- the forward pass of the minibatch. 2- the backward pass updating the weights. 3- sample images in the minibatch and randomly add one patch per image. 4- a forward pass with the patches images. 5- compute the difference between the predictions corresponding to the source images and the one corresponding to their patched version. Finally, save the patches with a high prediction difference.

that more patches are tested and thus more should be kept. Indeed, we can see that from 5 batches to 25 batches we see a small gain of 0.04pts of Accuracy and +0.28 pts of F-measure. However, using 5 batches multiplies approximately the training time by 2, using 25 batches multiplies it by 6. Increasing the training time is not actually a strong constraint as it is done off-line. However, we decided to keep exploring other ways to improve our approach.

Expe.	**Accuracy**	**Recall**	**Precision**	**F-measure**
ALL DA	98.72	90.54	94.28	92.37
ALL DA rp	98.79 (+0.07)	91.62 (+1.08)	94.00 (−0.28)	92.80 (+0.33)
ALL DA 5bp	98.77 (+0.05)	89.09 (−1.45)	96.22 (+1.94)	92.52 (+0.15)
ALL DA 25bp	98.81 (+0.09)	89.87 (−0.67)	95.92 (+1.64)	92.80 (+0.43)

Table 3.4 – Results with patches. “rp” indicates experiment with random patching at the loading of the images. “5bp” and “25bp” respectively correspond to experiments with 5 and 25 batches of randomly patched images tested at each iteration.

Late start The patch selection is done with respect to the output of the network. During the firsts training iterations the relevance of the outputs is uncertain, thus, it may be beneficial to start testing patches only after several simple training iterations. To avoid introducing a shift in the data by delaying the patching, we propose to randomly add patches during the first training iterations. We present in Table 3.5, the results delaying the patching. We can see that delaying the patching of the images is slightly beneficial with +0.02pts of Accuracy and +0.16pts of F-measure compared to patches used directly from the first iteration. However,

adding random patches during the starting delay is slightly harmful with −0.02pts of Accuracy and −0.13pts of F-measure. This may be explained because the network starts learning from images with a large variety of patch positions. Then learns from images with patches at more restrained position with our prediction guided methods. This induces a shift in the patches repartition in the images, thus, a shift in the data distribution. Moreover, as the patched images are iteratively added, few patched images are available in the beginning of the patching. This also induces a shift in the data during the train when switching from a train set with randomly patches to a train set augmented by only a few patched images. To correct this, we could keep adding random patches until we reach a higher iteration, or a given number of saved patched images.

Expe.	**Accuracy**	**Recall**	**Precision**	**F-measure**
ALL DA	98.72	90.54	94.28	92.37
ALL DA 25bp	98.81 (+0.09)	89.87 (−0.67)	95.92 (+1.64)	92.80 (+0.43)
ALL DA 25bp late	98.83 (+0.11)	90.47 (−0.07)	95.57 (+1.29)	92.95 (+0.58)
ALL DA 25bp rlate	98.79 (+0.07)	89.27 (−1.27)	96.32 (+2.04)	92.66 (+0.29)

Table 3.5 – Results with patches. “25bp” corresponds to experiments with 25 batches of randomly patched images tested at each iteration. “late” indicates that the patching starts at the 1000th iteration. “rlate” is “late” setting with random patching during the first 1000 iterations.

Add variations to patches To see the effect of inducing more variability to the patches, we changed the color of the patches and their shape. Adding round patches can also indicate if the prediction variation is induced by hiding the area or by adding a straight border creating a line near the position of a closed security railing. To tackle the border possible issue we also tried to add blurring patch creating a smoother border. In Table 3.6, we show results obtained by modifying the color and the shape of the patches. We present results on the 2017 Bluecime dataset, as we did not perform these experiments on the 2018 dataset for time reasons. We can see that the effect of the patches is nor influenced by its color nor its shape. Mixing the variations seems also to have a negligible impact compared to using only black squares. Blurring instead of coloring the patches areas shows also similar results. These results suggest that our method relies on the loss of information more than the introduction of a straight frontier on the restraining bar position (possible with squares, but not circles).

Using positions of interest of earlier patches Randomly selecting patches requires to test a lot of patched images to have enough interesting patches to add to the dataset so that it increases the classification performance of the network. Doing numerous forward passes is computationally expensive. So, to reduce this cost, we would like to increase the probability of a tested patch to be kept so that we need fewer forward passes to get enough patched images. To do that, we use a probability map (for each class in each domain) which contains, for

Expe.	Accuracy	Recall	Precision	F-measure
ALL DA	97.98	85.83	87.43	86.62
ALL DA blk sq	98.49 (+0.51)	86.71 (+0.89)	94.23 (+6.79)	90.31 (+3.69)
ALL DA wht sq	98.33 (+0.35)	84.78 (+1.04)	94.10 (+6.67)	89.20 (+2.58)
ALL DA mean sq	98.43 (+0.45)	86.71 (+0.89)	93.49 (+6.06)	89.97 (+3.35)
ALL DA blk cir	98.39 (+0.41)	87.44 (+1.61)	92.35 (+4.91)	89.83 (+3.20)
ALL DA vs blk sq	98.33 (+0.35)	83.09 (−2.73)	95.82 (+8.39)	89.00 (+2.38)
ALL DA vs blk cir	98.51 (+0.53)	87.20 (+1.37)	94.01 (+6.58)	90.48 (+3.85)
ALL DA all var	98.54 (+0.56)	87.14 (+1.31)	93.26 (+5.83)	90.09 (+3.47)
ALL DA blur sq	98.55 (+0.57)	87.44 (+1.61)	94.27 (+6.84)	90.73 (+4.10)

Table 3.6 – Results on the same experiment, patches tested over 25 batches per iteration. Note that these experiments were conducted on the 2017 Bluecime dataset. “blk”, “wht”, and “mean” corresponds to the color of the patches, respectively black, white, and average pixel color in the dataset. “sq” and “cir” correspond to square or circle patches. “vs” means that the size of the patches is randomly chosen (between 16 and 64 pixels). “all var” corresponds to patches with randomly chosen color and shape (between the previously enumerated). “blur” indicate patches inducing a blurring effect (without adding color).

each pixel in the images, the probability for a patch to be interesting. The map is initialized uniformly (or with a Gaussian distribution centered in the image), during the training if we encounter an important patch we increase the probability of choosing this position again in the next training iterations (the probabilities are clipped if they exceed 1). Table 3.7 shows results using probability maps in the ALL DA setting. With only 5 patching batches added, the maps has almost no effect. However, with 25 batches we observe a good performance gain with +0.09 of Accuracy and +0.6pts of F-measure when we add uniformly initialized maps. When using Gaussian initialization, we observe no effect. This can be explained by the high probability to add a patch in the center of the image, which implies that we explore much fewer patch locations that initializing uniformly. From this observation, we could explore techniques to avoid having too high probability zones impairing the patch exploration. For instance, we could clip the maps with a value inferior to 1.

In Figure 3.5, we show examples of the probability maps. In red are the zones with a high probability of being patched. We can see that the red zones fit well the chairs of the vehicle, and covers the full size of the passengers. We also note that, on the map of the *Unsafe* class, the red zone is extended higher to the top of the vehicle, where the restraining bar is positioned when it is entirely opened (like on the *Empty* image). This suggests that the red zones may cover all the possible positions of the restraining bar and of its footrests. With this, we improve our patching approach by ignoring nearly all the background and uninformative part of the vehicle such as its frame.

Expe.	Accuracy	Recall	Precision	F-measure
ALL DA	98.72	90.54	94.28	92.37
ALL DA 5bp	98.77 (+0.05)	89.09 (−1.45)	96.22 (+1.94)	92.52 (+0.15)
ALL DA 5bp u+0.1	98.76 (+0.04)	89.92 (−0.62)	95.31 (+1.03)	92.54 (+0.17)
ALL DA 25bp	98.81 (+0.09)	89.87 (−0.67)	95.92 (+1.64)	92.80 (+0.43)
ALL DA 25bp u+0.1	98.91 (+0.19)	90.47 (−0.07)	96.51 (+2.13)	93.39 (+1.02)
ALL DA 25bp g+0.1	98.80 (+0.08)	90.70 (+0.16)	95.03 (+0.75)	92.82 (+0.45)

Table 3.7 – Results with patches. “5bp” and “25bp” respectively correspond to experiments with 5 and 25 batches of randomly patched images tested at each iteration. “u” and “g” respectively indicates that the probabilities maps are initialized with a centered Gaussian distribution and a uniform distribution. “+0.1” indicates that a kept patch increases the probability on his location by 0.1.

(a) *Empty* map. (b) *Safe* map. (c) *Unsafe* map.

Figure 3.5 – Example of resulting probability map on the chairlift Chair. M after “ALL DA 25bp u+0.1” training. The red zones indicate a high probability of applying a patch.

3.2.2.2 Conclusion

Our patching approach shows promising results with at most +0.19 pts of Accuracy and +1.03 pts of F-measure, with the only disadvantage to increase the training time. Moreover, there is still room for improvements, particularly with the approach using the previous patches positions. Indeed, we could increase the probability of a location by using for example the prediction variation. We could also experiment on reducing the probability of a location in the case of a better prediction, this could be tricky as there are few patches of interest among all the tested patches. We could also validate or possibly improve our approach by using other visualization approaches. For instance, with GradCam (Selvaraju et al., 2017) or deep Taylor decomposition (Montavon et al., 2017), we could have regions of interest in an image without testing patch positions, thus reducing the training time and possibly increasing the number of selected patches.

Expe.	Accuracy	Recall	Precision	F-measure
SIVAO	98.54	92.68	90.43	91.54
OOC	98.35 (−0.19)	85.96 (−6.72)	94.20 (+3.77)	89.89 (−1.65)
ALL	98.73 (+0.19)	90.93 (−1.75)	94.00 (+3.58)	92.44 (+0.90)
ALL DA	98.72 (+0.18)	90.54 (−2.14)	94.28 (+3.85)	92.37 (+0.83)
LOCO	95.63 (−2.91)	85.73 (−6.95)	69.87 (−20.56)	76.99 (−14.55)
LOCO DA-	96.72 (−1.82)	81.81 (−10.86)	83.77 (−6.66)	78.23 (−13.31)
LOCO DA	97.70 (−0.84)	87.06 (−5.61)	86.11 (−4.32)	86.58 (−4.95)

Table 3.8 – Baseline results (difference with SIVAO performance between brackets). Note that, in the "DA" experiments, the classes of the target examples are balanced, which implies that the LOCO DA setting is not a correct unsupervised setting, this matter is discussed in length in the chapter 5.

3.3 Baseline results

In Table 3.8, we present the results on all the datasets for all the experimental settings. The first line of the table gives the performance of SIVAO, the current system developed by Bluecime. In the OOC setting, we get poor performances compared to SIVAO (−1.65 pts of F-measure). In this setting as we use only the images of only one chairlift, we have training dataset too small and with too few variations. However, with the ALL setting, we observe an improvement of 0.83 to 0.9 pts of F-measure. Even though the gain is small, the training time of ALL is about 5 hours while the time to configure SIVAO is higher and the configuration is different on each chairlift. So, ALL makes a very attractive solution from an industrial standpoint.

As expected, during the LOCO experiment, performance losses occur for all the measures, with −14.55 pts of F-measure and −2.91 pts of Accuracy. In this setting, performance is too low for industrial deployment. However, adding domain adaptation (LOCO DA) show a high improvement with −4.95 pts of F-measure and only −0.84 pts of Accuracy. This result is worse than SIVAO or ALL, however, in this setting, the chairlift does not have any annotated images. So, we can consider the performance on LOCO DA as promising, considering that in this setting, SIVAO cannot be configured, and we cannot train on ALL setting. Note that, using the LOCO DA-, we obtain results 1pts better than the LOCO setting (in both Accuracy and F-measure), but shows −1 pts of Accuracy and −8.36 pts of F-measure compared to the LOCO DA setting. These results show that we are forced to acquire some data to improve the results on newly installed chairlifts, but, we avoid the labeling process which is more time costly than just acquiring raw data. We show detailed results on F-measure in Table 3.9 (detailed results in Accuracy, Precision, and Recall are available in Appendix B.1). These results show a very challenging aspect of Bluecime dataset which is the high disparity of the response to a new method across the chairlifts. Indeed, if we compare ALL and ALL DA we can see on Chair. O that adding the domain adaptation module decreases the F-measure by

2.55 pts, whereas on Chair. T we gain 3.5 pts of F-measure. Similarly, we observe in LOCO setting that adding domain adaptation is beneficial most of the time but, for instance, on Chair. G or Chair. M. Moreover, we can see that the best results (bold figures) are spread over 5 of the 7 presented settings, emphasizing well the Bluecime dataset challenge.

Chairlift	**SIVAO**	**OOC**	**ALL**	**ALL DA**	**LOCO**	**LOCO DA-**	**LOCO DA**
Chair. A	93.38	94.30	94.22	**94.84**	92.45	92.83	93.52
Chair. B	94.03	89.23	93.43	**95.34**	90.51	91.18	93.62
Chair. C	**93.85**	72.73	83.76	82.56	74.29	76.19	78.95
Chair. D	82.35	25.00	**100.00**	90.00	82.35	93.33	87.50
Chair. E	**96.21**	87.30	89.55	89.47	40.44	40.83	71.56
Chair. F	91.80	**96.43**	94.74	94.55	79.41	89.23	93.33
Chair. G	57.14	85.71	96.97	98.49	**100.00**	93.75	93.75
Chair. H	**96.17**	91.43	92.86	92.54	83.12	81.33	87.80
Chair. I	89.21	83.72	**93.75**	90.04	69.23	76.36	82.81
Chair. J	85.14	82.69	85.47	**86.59**	75.36	72.94	85.34
Chair. K	96.77	97.89	**98.23**	96.82	94.85	96.19	97.18
Chair. L	91.18	92.86	92.25	**92.88**	78.07	78.83	85.41
Chair. M	90.74	81.82	88.50	90.58	**91.59**	89.29	90.43
Chair. N	**50.00**	0.00	0.00	33.33	0.00	0.00	10.26
Chair. O	**99.38**	88.44	94.27	92.62	90.79	90.79	88.31
Chair. P	**95.32**	89.81	92.86	91.36	84.91	87.62	84.36
Chair. Q	77.22	76.36	**87.10**	85.83	75.38	73.68	75.34
Chair. R	85.71	92.62	**94.08**	93.65	91.93	92.99	93.20
Chair. S	**94.64**	85.45	93.58	91.94	88.29	86.49	90.20
Chair. T	93.81	86.54	92.86	**95.40**	75.52	81.82	87.60
Chair. U	90.20	88.89	**91.21**	90.34	52.90	57.14	78.10
Avg.	91.54	89.89	**92.44**	92.37	76.99	78.25	86.58

Table 3.9 – F-measure on each chairlift.

Chapter 4

Cost-sensitive learning for imbalanced data

In this chapter, we will present two approaches developed to improve the performance of our method according to the F-measure. We first show an empirical method, based on the iterative training of the neural network. Then, we present an iterative algorithm based on a theoretical bound on the F-measure. This last work was presented in Bascol et al. (2019b), at the 22nd International Conference on Artificial Intelligence and Statistics (AISTATS 2019).

4.1 F-measure gain-oriented training

In this section we describe our first approach on the F-measure optimization and then present empirical results on the Bluecime dataset.

4.1.1 Introduction

Our first approach on F-measure optimization consists in modifying the training loss at each iteration towards a hypothetical gain of F-measure, measured in the previous iteration.

We recall the Hinge Loss formulation (Sec. 1.2.1.1) used as our training loss:

$$\mathcal{L}_{Hinge}(\hat{\boldsymbol{y}}^i, t) = \frac{1}{C} \sum_{j=1; j \neq t}^{C} \max(0, \mu + \widehat{y}^i_j - \widehat{y}^i_t)$$

Our approach is a cost-sensitive training algorithm, we thus have a weighted loss:

$$\mathcal{L}(\alpha, \widehat{\boldsymbol{Y}}, \boldsymbol{Y}) = \frac{1}{B} \sum_{i=1}^{B} \alpha_{y^i} \mathcal{L}_{Hinge}(\hat{\boldsymbol{y}}^i, \boldsymbol{y}^i)$$

where $\widehat{\boldsymbol{Y}} = (\hat{\boldsymbol{y}}^1, \hat{\boldsymbol{y}}^2, .., \hat{\boldsymbol{y}}^B)$ is the set of classifier outputs on a given batch of size B, and $\boldsymbol{Y} = (\boldsymbol{y}^1, \boldsymbol{y}^2, .., \boldsymbol{y}^B)$ is the set of corresponding labels. α is the vector containing the class weights.

During the first iteration, α is set to a constant vector (e.g. ones, or the class proportions). During training, α is updated a given number of times over *all* the training set. Each class weight corresponds to the gain of F-measure we would have obtained by classifying correctly one more example of the given class:

We recall the Precision, Recall, and F-measure formulations (Table 2.4):

$$Pr = \frac{TP}{TP + FP} \qquad Re = \frac{TP}{TP + FN} \qquad F_\beta = \frac{(1 + \beta^2) Pr Re}{\beta^2 Pr + Re}$$

Gain of Precision and Recall on the negative class, where one FP becomes a TN:

$$Pr^{TN+1} = \frac{TP}{TP + FP - 1} \qquad Re^{TN+1} = \frac{TP}{TP + FN}$$

Gain of Precision and Recall on the positive class, where one FN becomes a TP:

$$Pr^{TP+1} = \frac{TP + 1}{TP + 1 + FP} \qquad Re^{TP+1} = \frac{TP + 1}{TP + 1 + FN - 1}$$

We finally obtain our weights:

$$\alpha = (\underbrace{(F_{\beta^l}^{TN+1} - F_{\beta^l})}_{\text{negatives}}, \underbrace{(F_{\beta^l}^{TP+1} - F_{\beta^l})}_{\text{positives}})$$

So, this method optimizes the F-measure by giving more weights to the classes whose errors are the most harmful to the classifier. We note β^l the F-measure β parameter used when learning a classifier using this F-measure optimization approach.

4.1.2 Experiments

Expe.	**Accuracy**	**Recall**	**Precision**	**F_1-measure**
ALL DA	98.72	90.54	94.28	92.37
ALL DA fmg $\beta^l = 0.0625$	96.29 (−2.43)	57.07 (−33.47)	99.12 (+4.84)	72.43 (−19.94)
ALL DA fmg $\beta^l = 0.125$	98.40 (−0.32)	83.51 (−7.03)	97.32 (+3.04)	89.89 (−2.48)
ALL DA fmg $\beta^l = 1$	98.70 (−0.02)	90.61 (+0.07)	93.98 (−0.30)	92.26 (−0.11)
ALL DA fmg $\beta^l = 4$	98.25 (−0.47)	94.43 (+3.89)	86.35 (−7.93)	90.21 (−2.16)
ALL DA fmg $\beta^l = 16$	91.61 (−7.11)	98.11 (+7.57)	50.45 (−43.83)	66.64 (−25.73)

Table 4.1 – Results on ALL DA setting. "fmg" indicates the use of our F-measure gain oriented training. β^l is the parameter controlling the trade-off between Precision and Recall in the F-measure gain computation.

We present, in Table 4.1, experiments in the ALL DA setting using our F-measure optimization approach and varying the β^l parameter (recall that $F_0 = Pr$ and $\lim_{\beta \to \infty} F_\beta = Re$). Comparing with our baseline approach (ALL DA without optimizing the F-measure), optimizing the F-measure with $\beta^l = 1$ gives worse results than the baseline with -0.11pts of

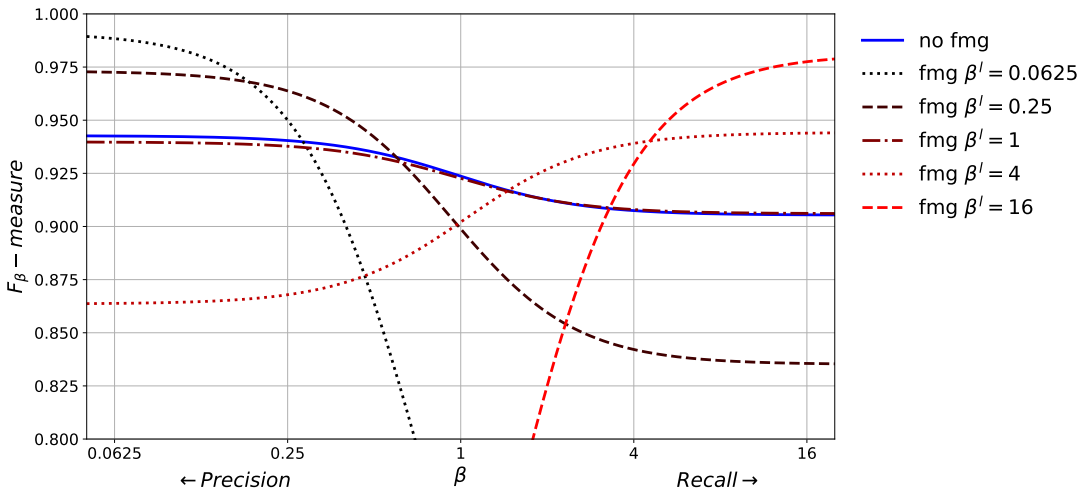

Figure 4.1 – F_β-measure in function of β, "fmg" indicates the use of our F-measure gain oriented training. β^l is the parameter controlling the trade-off between Precision and Recall in the F-measure gain computation.

F-measure. However, if we change the β^l parameter, with our method, we can guide the model to achieve either better precision ($\beta^l < 1$) or better Recall ($\beta^l > 1$). For instance, with $\beta^l = 0.125$ we observe a gain of +3.04pts of Precision and using $\beta^l = 4$ we obtain +3.89pts of Recall. In Figure 4.1, we show the F_β-measure obtained with the models trained with different value of β^l. This figure illustrates well the trade-off between the Precision and the Recall and the effectiveness of our approach to control this trade-off. We observe that the curve corresponding to the training with our approach optimizing the F_1-measure (dark-red dash-dotted one) is slightly flatter than the baseline approach (blue plain one) this suggests that we obtain a better trade-off between Precision and Recall. However, we saw that we obtained a better F_1-measure with the baseline approach. This suggests however that our approach is promising, but this worse performance using $\beta^l = 1$ emphasizes that this approach is approximately optimizing the F-measure. We thus propose in the next section another method to optimize the F-measure, with some theoretical guarantees.

4.2 From cost-sensitive classification to tight F-measure bounds

We present in this section, **CONE**, an algorithm for F-measure optimization derived from a theoretical bound on the F-measure.

4.2.1 Introduction

The work presented in this chapter falls into the *EUM* based methods within a cost-sensitive classification approach (see Section 2.2.2). Indeed, by taking into account some per-class misclassification-costs, cost-sensitive learning aims at dealing with problems induced by class-imbalanced datasets.

Our contributions, in this section, can be summarized as follows:

- we demonstrate tight theoretical guarantees on the F-measure of classifiers obtained from cost-sensitive learning;
- we give a geometric interpretation of the theoretical guarantees: they can be represented as unreachable regions (cones) in a 2D space where the x-axis gives the value of a parameter t that controls the relative costs of the considered classes, and the y-axis gives the F-measure of the corresponding cost-sensitive classifier;
- going beyond traditional asymptotic analysis, we study the actual behavior of our bounds, on real datasets, showing it is much tighter than previous existing results;
- inspired by our bounds and their interpretation, we introduce an algorithm to explore the space of costs: our experiments show the relevance of (i) using our algorithm compared to other baselines (such as Parambath et al. (2014)), and (ii) retraining the model iteratively compared to the previously described methods (Koyejo et al. (2014); Narasimhan et al. (2015)) that only tune an offset or threshold.

In Section 4.2.2, we introduce the notations and present our theoretical bound on the optimal F-measure based on a cost-sensitive approach and the pseudo-linear property of the F-measure. We give a geometric interpretation in Section 4.2.3 and introduce an algorithm that iteratively selects classification costs that lead to a near-optimal F-measure. Section 4.2.4 is devoted to the experiments on real datasets. These experiments show the effectiveness of the proposed bounds from a practical point of view. Furthermore, they show that it is possible to reach higher performance than a single model tuned *a posteriori* or much faster than grid search methods. We finally conclude in Section 4.2.5. In addition, for clarity reasons, we present proofs, developments in multi-classes, and the complete experimental results in Appendix C.

4.2.2 F-measure bound

Notations Let $\mathbf{X} = (\boldsymbol{x}_1, ..., \boldsymbol{x}_m)$, where $\boldsymbol{x}_i \in \mathbb{R}^n$, be the set of m training instances and $\mathbf{Y} = (y_1, ..., y_m)$ their corresponding label, where $y_i \in \{0, 1\}$. Let $\mathcal{H}$ be a family of hypotheses e.g., linear separators. For a given hypothesis $h \in \mathcal{H}$ learned from $(\mathbf{X}, \mathbf{Y})$, the errors that h makes can be summarized in an error profile, noted $\mathbf{E}(h)$, which, in the binary case can be defined as $(FN(h), FP(h))$.

In a binary setting, P is the proportion of positive instances and N the proportion of negative examples. We also denote by $\boldsymbol{e}$ the vector (e_1, e_2) where e_1 and e_2 are respectively the proportion of False Negative (FN) examples and the proportion of False Positive (FP) ones as introduced previously. We then denote as $\mathcal{E}(\mathcal{H})$ the set of all possible error profiles for a given set of hypotheses: an error profile $\boldsymbol{e} = (e_1, e_2)$ is in $\mathcal{E}(\mathcal{H})$ if there exists a hypothesis $h \in \mathcal{H}$ that yields proportions of e_1 false negatives and e_2 false positives.

We first recall the definition of F-measure for any value of β:

$$F_\beta = \frac{(1+\beta^2)(P - FN)}{(1+\beta^2)P - FN + FP}$$

Using the above notations, the F-measure, $F_\beta(\boldsymbol{e})$, defined in terms of the error profile $\boldsymbol{e}$ can be rewritten as:

$$F_\beta(\boldsymbol{e}) = \frac{(1+\beta^2)(P - e_1)}{(1+\beta^2)P - e_1 + e_2}$$

Pseudo linearity property The F-measure is a linear-fractional function, i.e. it can be written as the ratio of two affine functions of the error profile. We briefly recall how to show that the F-measure is a pseudo-linear function, which is one of the main property of linear-fractional functions. This property is the starting point of the demonstration of our main theoretical result.

Definition 4.1. *[from Rapcsák (1991)] A real differentiable function f defined on an open convex set $\mathcal{C} \subset \mathbb{R}^q$ is said to be pseudo-convex if for every $\boldsymbol{e}, \boldsymbol{e}' \in \mathcal{C}$,*

$$\langle \nabla f(\boldsymbol{e}), (\boldsymbol{e}' - \boldsymbol{e}) \rangle \geq 0 \implies f(\boldsymbol{e}') \geq f(\boldsymbol{e})$$

where ∇f denotes the gradient of the function f.

The pseudo-convexity is used to define the pseudo-linearity as we see below.

Definition 4.2. *A function f defined on an open convex $\mathcal{C}$ is said to be pseudo-linear if both f and $-f$ are pseudo-convex.*

It is now easy to show that the F-measure has the property of pseudo-linearity.

Proposition 4.1. *The F-measure is a pseudo-linear function.*

Proof 1. *See Section C.1.1.*

Using this property, we are able, using a result from Cambini and Martein (2009) to give a link between the F-measure and a cost-sensitive function, i.e. a function which assigns weights to each class.

Proposition 4.2. *[Theorem 3.3.9 from Cambini and Martein (2009)] Let f be a non-constant differentiable function on an open convex set $\mathcal{C} \in \mathbb{R}^q, q > 0$. Then f is pseudo-linear on $\mathcal{C}$ if and only if the following properties hold:*
(i) each of the level sets of f is the intersection of $\mathcal{C}$ with a hyperplane;
(ii) $\nabla f(\boldsymbol{e}) \neq 0$ for all $\boldsymbol{e} \in \mathcal{C}$.

Let us consider the set of error profiles $\{\boldsymbol{e} \in \mathbb{R}^2 \mid (1+\beta^2)P - e_1 + e_2 > 0\}$ (which is always the case in practice with the F-measure). Then according to the previous theorem, we rewrite (i) as follows:
There exists $\boldsymbol{a} : \mathbb{R} \to \mathbb{R}^2$ and $b : \mathbb{R} \to \mathbb{R}$ such that

$$F(\boldsymbol{e}) = t \iff \langle \boldsymbol{a}(t), \boldsymbol{e} \rangle + b(t) = 0$$

which can be rewritten :

$$\langle \boldsymbol{a}(F(\boldsymbol{e})), \boldsymbol{e} \rangle + b(F(\boldsymbol{e})) \quad = \quad 0 \tag{4.1}$$

For the F-measure, the functions $\boldsymbol{a}$ and b are defined by $\boldsymbol{a}(t) = (1 + \beta^2 - t, t)$ and $b(t) = (1+\beta^2)P(t-1)$. The term $\langle \boldsymbol{a}(t), \boldsymbol{e} \rangle$ can be seen as a weighted error loss function, and thus $\boldsymbol{a}(t)$ can be seen as the costs to assign to each class.

Bounds on the optimal F-measure We now show the importance of the function $\boldsymbol{a}$ and of the parameter t to characterize the difference of F-measure between any two error profiles.

Step 1: impact of a change in the error profile We first derive the relation between the difference in F-measure (F) and the difference in error profile ($\boldsymbol{e}$). We thus consider $\boldsymbol{e}$ and $\boldsymbol{e}'$ any two error profiles and denote by $F(\boldsymbol{e})$ and $F(\boldsymbol{e}')$ the corresponding F-measures.

From the pseudo-linearity property (Eq. (4.1)), we have:

$$0 \quad = \quad \langle \boldsymbol{a}(F(\boldsymbol{e})), \boldsymbol{e} \rangle + b(F(\boldsymbol{e})) \tag{4.2}$$
$$0 \quad = \quad \langle \boldsymbol{a}(F(\boldsymbol{e}')), \boldsymbol{e}' \rangle + b(F(\boldsymbol{e}')) \tag{4.3}$$

We now develop $\langle \boldsymbol{a}(F(\boldsymbol{e}')), \boldsymbol{e} - \boldsymbol{e}' \rangle$ and make the difference in F-measure appears in its expression.

$$\begin{aligned}
\langle \boldsymbol{a}(F(\boldsymbol{e}')), \boldsymbol{e} - \boldsymbol{e}' \rangle &= \langle \boldsymbol{a}(F(\boldsymbol{e}')), \boldsymbol{e} \rangle + b(F(\boldsymbol{e}')) \\
&= \langle \boldsymbol{a}(F(\boldsymbol{e}')), \boldsymbol{e} \rangle - \langle \boldsymbol{a}(F(\boldsymbol{e})), \boldsymbol{e} \rangle - b(F(\boldsymbol{e})) + b(F(\boldsymbol{e}')) \\
\langle \boldsymbol{a}(F(\boldsymbol{e}')), \boldsymbol{e} - \boldsymbol{e}' \rangle &= \big(F(\boldsymbol{e}') - F(\boldsymbol{e})\big) \cdot \big((1+\beta^2)P_1 - e_1 + e_2\big)
\end{aligned}$$

where the first line uses the linearity of the inner product and Eq. (4.3). The second uses Eq. (4.2) and the last line uses the definition of $\boldsymbol{a}$ and b introduced previously.

Now we can rewrite the difference in F-measure as:

$$F(\boldsymbol{e}') - F(\boldsymbol{e}) \quad = \quad \Phi_{\boldsymbol{e}} \cdot \langle \boldsymbol{a}(F(\boldsymbol{e}')), \boldsymbol{e} - \boldsymbol{e}' \rangle, \tag{4.4}$$

where $\Phi_{\boldsymbol{e}} = \dfrac{1}{(1+\beta^2)P - e_1 + e_2}$.

Step 2: bounds on the F-measure $F(\boldsymbol{e}')$ We suppose that we have a value of t for which a weighted-classifier with weights $\boldsymbol{a}(t)$ has been learned. This classifier has an error profile $\boldsymbol{e}$ and a F-measure $F(\boldsymbol{e})$. Note that the value t used to train the model is not the value of the F-measure, i.e. $F(\boldsymbol{e}) \neq t$. We keep this notation for the sake of simplicity in the following. We now imagine a hypothetical classifier which leads to an error profile $e^\star$ the optimal error profile, i.e. the one that maximized the F-measure and for which we have $F(\boldsymbol{e}^\star) = t^\star$ (see Proposition 4 of Parambath et al. (2014)).

Starting from the result obtained in Eq. (4.4), we have:

$$F(\boldsymbol{e}^\star) - F(\boldsymbol{e}) \quad = \quad \Phi_{\boldsymbol{e}} \left(\langle \boldsymbol{a}(t^\star), \boldsymbol{e} \rangle - \langle \boldsymbol{a}(t^\star), \boldsymbol{e}^\star \rangle \right)$$

$$
\begin{aligned}
&= \Phi_{\boldsymbol{e}}\left(\langle \boldsymbol{a}(t), \boldsymbol{e}\rangle + \langle \boldsymbol{a}(t^\star) - \boldsymbol{a}(t), \boldsymbol{e}\rangle - \langle \boldsymbol{a}(t^\star), \boldsymbol{e}^\star\rangle\right)\\
&= \Phi_{\boldsymbol{e}}\left(\langle \boldsymbol{a}(t), \boldsymbol{e}\rangle + (t^\star - t)(e_2 - e_1) - \langle \boldsymbol{a}(t^\star), \boldsymbol{e}^\star\rangle\right)\\
&\leq \Phi_{\boldsymbol{e}}\left(\langle \boldsymbol{a}(t), \boldsymbol{e}^\star\rangle + \varepsilon_1 - \langle \boldsymbol{a}(t^\star), \boldsymbol{e}^\star\rangle + (t^\star - t)(e_2 - e_1)\right)\\
&\leq \Phi_{\boldsymbol{e}}\left((t - t^\star)(e_2^\star - e_1^\star) + \varepsilon_1 + (t^\star - t)(e_2 - e_1)\right)\\
F(\boldsymbol{e}^\star) - F(\boldsymbol{e}) &\leq \Phi_{\boldsymbol{e}}\varepsilon_1 + \Phi_{\boldsymbol{e}} \cdot (e_2 - e_1 - (e_2^\star - e_1^\star))(t^\star - t)
\end{aligned}
$$

We have successively used the linearity of the inner product, introduced $\boldsymbol{a}(t)$ and its definition in the first three equalities. The first inequality uses $\langle \boldsymbol{a}(t), \boldsymbol{e}\rangle \leq \langle \boldsymbol{a}(t), \boldsymbol{e}_{best}\rangle + \varepsilon_1$, the sub-optimality of the $\boldsymbol{a}(t)$-weighted-error classifier. The value of ε_1 represents the excess of risk of the classifier which aim to minimize the $\boldsymbol{a}(t)$-weighted-error. More precisely, it represents the difference of risk between our classifier and the best classifier h_{best} (in terms on $\boldsymbol{a}(t)$-weight-error) in our set of hypothesis $\mathcal{H}$. We denote by $\boldsymbol{e}_{best}$ the error profile associated to h_{best}.

We are interested in upper bounding the optimal value of the F-measure using equation (4.5). For this purpose, we consider any possible value of t', for which we learn a hypothetical classifier with weights $\boldsymbol{a}(t')$, that gives us an error profile $\boldsymbol{e}'$ and a F-measure $F(\boldsymbol{e}')$. If t' happens to be the optimal value which, by weighting the errors with $\boldsymbol{a}(t')$, maximizes the F-measure then $F(\boldsymbol{e}') = t'$ for $\boldsymbol{e}' = \underset{\hat{\boldsymbol{e}} \in \mathcal{E}(\mathcal{H})}{\arg\min} \langle \boldsymbol{a}(t'), \hat{\boldsymbol{e}}\rangle$. Equation (4.5) can then be applied and gives the following proposition:

Proposition 1. *Let $\boldsymbol{e}$ be the error profile obtained with a classifier trained with the parameter t and $F(\boldsymbol{e})$ its associated F-measure value. Let us also consider $\Phi_{\boldsymbol{e}}$ as defined in Eq. (4.4) and $\varepsilon_1 > 0$ the sub-optimality of our linear classifier. Then for all $t' < t$:*

$$F(\boldsymbol{e}') \leq F(\boldsymbol{e}) + \Phi_{\boldsymbol{e}}\varepsilon_1 + \Phi_{\boldsymbol{e}} \cdot (e_2 - e_1 - M_{max})(t' - t)$$

where $M_{max} = \underset{\substack{\boldsymbol{e}' \in \mathcal{E}(\mathcal{H}) \\ s.t.\ F(\boldsymbol{e}') > F(\boldsymbol{e})}}{\max} (e'_2 - e'_1)$

and, for all $t' > t$:

$$F(\boldsymbol{e}') \leq F(\boldsymbol{e}) + \Phi_{\boldsymbol{e}}\varepsilon_1 + \Phi_{\boldsymbol{e}} \cdot (e_2 - e_1 - M_{min})(t' - t)$$

where $M_{min} = \underset{\substack{\boldsymbol{e}' \in \mathcal{E}(\mathcal{H}) \\ s.t.\ F(\boldsymbol{e}') > F(\boldsymbol{e})}}{\min} (e'_2 - e'_1)$

With this first result, we give an upper bound on the reachable F-measures for any value of t' given an observed value of F-measure with the parameter t. A geometric interpretation and an illustration of this result will be provided in Section 4.2.3.

Corollary 4.1. *Given the same assumptions and considering $t^\star$ the value of t for which the best cost-sensitive learning algorithm leads to a model with an error profile $e^\star$ associated to the optimal F-measure, we have: if $t^\star < t$:*

$$F(\boldsymbol{e}^\star) \leq F(\boldsymbol{e}) + \Phi_{\boldsymbol{e}}\varepsilon_1 + \Phi_{\boldsymbol{e}} \cdot (e_2 - e_1 - M_{\max})(t^\star - t)$$

and, if $t^\star > t$*:*

$$F(\boldsymbol{e}^\star) \leq F(\boldsymbol{e}) + \Phi_{\boldsymbol{e}}\varepsilon_1 + \Phi_{\boldsymbol{e}} \cdot (e_2 - e_1 - M_{\min})(t^\star - t)$$

This means that if we learn a model with a parameter t sufficiently close to $t^\star$ then, we guarantee to reach the optimal F-measure up to a constant equal to $\Phi_{\boldsymbol{e}}\varepsilon_1$.

4.2.3 Geometric interpretation and algorithm

In this section we provide a geometric interpretation of our main result, i.e. Proposition 1 of Section 4.2.2 and compare it to the bound introduced in Parambath et al. (2014). We also show how this theoretical result can be an inspiration to create an algorithm, **CONE**, which optimizes the F-measure by wrapping a cost-sensitive learning algorithm.

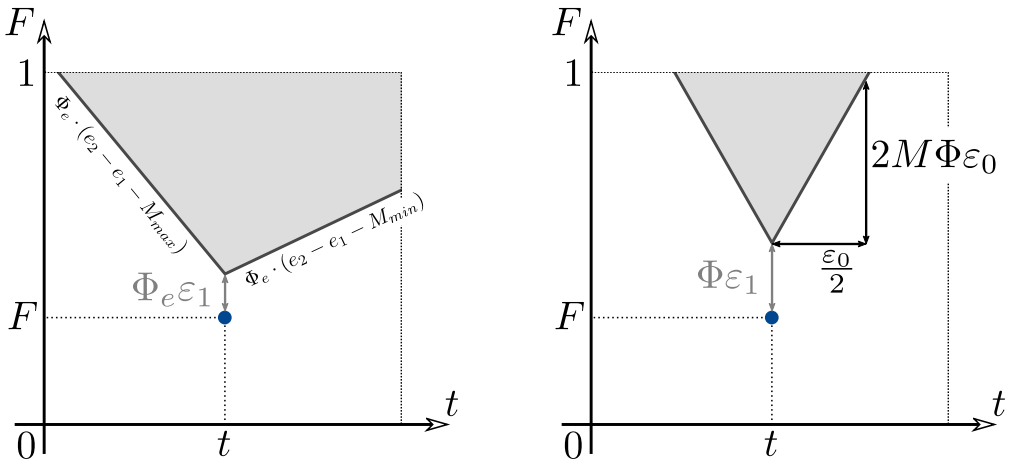

Figure 4.2 – Geometric interpretation of both theoretical results: our bound on the left and the one from Parambath et al. (2014) on the right. Note that our "cone" is not symmetric compared to the other one. On the left, the slanted values represent the slope of our cone on each side : $\Phi_{\boldsymbol{e}} \cdot (e_2 - e_1 - M_{max})$ and $\Phi_{\boldsymbol{e}} \cdot (e_2 - e_1 - M_{min})$.

Unreachable regions In Fig. 4.2 (left), we give a geometric interpretation of the result from Prop. 1 in the 2-D space where t is the x-axis and F is the y-axis. In this (t, F) graph, the previous near-optimality result yields an upper cone of values where $F(\boldsymbol{e}^\star)$ cannot be found. More precisely, when a model is learned for a given value of t (with weights $\boldsymbol{a}(t)$), we measure the value $F(\boldsymbol{e})$ of this model and, given these two numbers, we are able to draw an upper cone which represents the unreachable values of F-measure for any t' on the x-axis. Furthermore, given ε_1, the sub-optimality of the cost-sensitive learning algorithm for the weighted-0/1 loss, $\Phi_{\boldsymbol{e}}\varepsilon_1$ corresponds to the vertical offset of this cone, which means that the peak of the cone is located at $(t, F(\boldsymbol{e}) + \Phi_{\boldsymbol{e}}\varepsilon_1)$.

Note that, even if the authors were focusing on asymptotic results, the bound given in Parambath et al. (2014) can also be interpreted geometrically. Their bound is given as

Input: training set S,
Input: weighted-learning algorithm $wLearn$,
Input: stopping criterion $shouldStop$.

Initialize $L = \{0, 1\}$, $\mathcal{Z}_0 = \varnothing$ and $i = 1$.
repeat
  $t_i = findNextT(\mathcal{Z}_{i-1},\ L)$
  $classifier_i = wLearn(1 + \beta^2 - t_i,\ t_i,\ S)$
  $F_i = F_\beta(classifier_i,\ S)$
  $\mathcal{V}_i = unreachableZone(t_i,\ F_i,\ S,\ classifier_i)$
  $\mathcal{Z}_i = \mathcal{Z}_{i-1} \cup \mathcal{V}_i$
  $L = L \cup \{t_i\}$
  $i = i + 1$
until $shouldStop(i,\ classifier_i,\ \mathcal{Z}_i,\ L)$

(a) Pseudo-code.

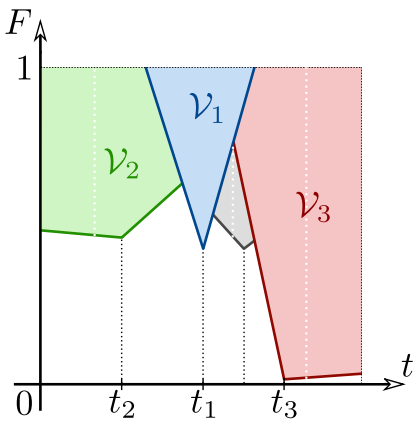

(b) Illustration of the **CONE** algorithm in the middle of its fourth iteration. The colored areas represent the unreachable regions in the (t, F)-space.

Figure 4.3 – **CONE** Algorithm.

follows:

$$F(\boldsymbol{e}^\star) \leq F(\boldsymbol{e}) + \Phi \cdot (2\varepsilon_0 M + \varepsilon_1)$$

where $M = \max_{\boldsymbol{e} \in \mathcal{E}(\mathcal{H})} \|\boldsymbol{e}\|_2$, $\Phi = (\beta^2 P)^{-1}$ and ε_0 is a gap parameter defined as the ℓ_2 norm of the difference between a weighted function $\boldsymbol{a}$ and the optimal one $\boldsymbol{a}^\star$. In Section C.1.3, we detail how this bound can, in fact, be rewritten for all $t, t' \in [0, 1]$ as:

$$F(\boldsymbol{e}') \leq F(\boldsymbol{e}) + \Phi\varepsilon_1 + 4M\Phi|t' - t|$$

This bound also defines a cone which is, this time, symmetric with a slope equal to $4\Phi M$, as illustrated in Fig. 4.2 (right). Using real datasets, Section 4.2.4 compares the cones produced by this bound and ours.

A bound-inspired algorithm We now leverage the geometric interpretation from Section 4.2.3 to design **CONE** (Cone-based Optimal Next Evaluation), an iterative algorithm that wraps a cost-sensitive classification algorithm (e.g., a weighted SVM). At every iteration i, **CONE** proposes a new value t_i to be used by the cost-sensitive algorithm. **CONE** is illustrated in Fig. 4.3b and is explained below.

The choice of t_i is based on the area $\mathcal{Z}_{i-1}$ which we define as the union of all cones obtained from previous iterations. t_i is chosen to reduce the maximum value of F for which (t, F) is not in any previous cone. To achieve this goal, **CONE** keeps track of a list L, initialized with the values 0 and 1, and enriched at each iteration with the values of t that have been considered. The selection of t_i is done as follows: (i) search the value t_{opt} which maximizes $F_{max}(t) = \max\{F, (t, F) \notin \mathcal{Z}_{i-1}\}$, (ii) search for the greatest value t_l in L such that $t_l < t_{opt}$

and the smallest value t_r such that $t_{opt} < t_r$. (iii) take the middle of the interval $[t_l, t_r]$ as the return value, i.e. $t_i = \frac{1}{2}(t_l + t_r)$.

The cost sensitive classification algorithm then provides a new value of F_i obtained from cost t_i, which is used to refine the unreachable area as $\mathcal{Z}_i = \mathcal{Z}_{i-1} \cup \mathcal{V}_i$, where $\mathcal{V}_i$ is the cone corresponding to (t_i, F_i). In the case where there are multiple values of t that maximize $F_{max}(t)$ (e.g., at the beginning, or when some range of t values yield $F = 1$), **CONE** selects as t_{opt} the middle of the widest range at the first stage (i) (see the white dotted lines in Fig. 4.3b).

From a practical perspective, $\mathcal{Z}_i$ can be represented as a combination of linear constraints or as a very dense grid of binary values (a rasterization of $[0, 1] \times [0, 1]$, the (t, F) space). Both approaches can be made efficient (and negligible compared to $wLearn$). The stopping criterion *shouldStop* can take different forms including a fixed number of iterations, a fixed time budget, or some rules on the current best F-measure and the current upper bound $max_t F_{max}(t)$. While the algorithm we describe selects a single next value of t to consider, it can easily be generalized to produce multiple values of t to consider in parallel (to exploit parallel computing of multiple instances of $wLearn$).

By always selecting a t_i that is in the middle of two previously tested t-values, **CONE** performs a progressive refinement of a grid. We can (and do, in practice) restrict the values of t in the (t, F)-space that the algorithm considers. More precisely, we can limit the depth of the progressive refinement to an integer value k. In this case, and **CONE** will do at most $2^k - 1$ iterations, in order to cover all possible values on a grid with stride $\frac{1}{2^k}$. However, as the procedure is informed by the theoretical bounds, we will see in Section 4.2.4 that **CONE** finds good models in its very first iterations.

4.2.4 Experiments

The experiments from this section study the tightness of our bounds and behavior of the **CONE** algorithm.

Datasets and experimental settings Table 4.2 describes the datasets we used for our experiments, with their Imbalance Ratio (I.R.). The higher this ratio, the more one should expect that optimizing the classification accuracy is a bad choice in terms of trade-off between precision and recall. The datasets *IJCNN'01* and *News20* are obtained from LIBSVM[1]. The other ones come from the UCI repository[2].

We reproduce the experimental settings from Parambath et al. (2014) which we describe here. For datasets with no explicit test set, $\frac{1}{4}$ of the data is kept for testing. The training set is split at random, keeping $\frac{1}{3}$ as the validation set, used to select the hyper-parameters using the F_1-measure. The penalty constraint of the classifiers (hyper-parameter C) is considered in $\{2^{-6}, 2^{-5}, ..., 2^6\}$. In the experiments t is taken in $[0, 1]$ as t belongs in the image space of the F-measure. Thus, the class weights $\boldsymbol{a}(t)$ belongs to $[0, 1 + \beta^2]$. The maximal number of

[1] https://www.csie.ntu.edu.tw/~cjlin/libsvm/

[2] https://archive.ics.uci.edu/ml/datasets.html

Table 4.2 – Datasets details. The Imbalance Ratio (I.R.) is the ratio between negative and positive instances (or between sizes of the largest and smallest classes, in a multiclass setting).

Dataset	Instances	Classes	I.R.	Features
Adult	48 842	2	3.19	123
Abalone10	4 174	2	5.64	10
SatImage	6 400	2	9.3	36
IJCNN'01	141 691	2	9.39	22
Abalone12	4 174	2	15.18	10
PageBlocks	5 500	2	22.7	10
Yeast	1 484	2	27.48	8
Wine	1 599	2	28.79	11
Letter	20 000	26	1.32	16
News20	19 928	20	1.12	62 061

training iterations is set to 50 000. Fitting the intercept of the classifiers is achieved by adding a constant feature with value 1. We report test-time F_1-measure averaged over 5 experiments.

We consider two different base cost-sensitive classification algorithms (both implementations use LIBLINEAR): linear SVM and Logistic Regression (LR) for a fair comparison with Koyejo et al. (2014). We report the performance of 5 different approaches: using a single standard classification algorithm with hyperparameters tuned on the F-measure, the **Grid** wrapper proposed in Parambath et al. (2014) that regularly splits the interval $[0, 1]$ of t values, the algorithm derived from our theoretical study, algorithm 2 from Narasimhan et al. (2015) based on the bisection method, and finally, an additional baseline (with the $_{I.R.}$ subscript), which consists in using a cost that re-balances the classes (the cost c of a False Negative is the proportion of positive examples in the dataset and the cost of False Positive is $1 - c$).

About ε_1 The value of ε_1 (in all presented bounds) represents the $\boldsymbol{a}(t)$-weighted sub-optimality of the classifier, compared to the best one from the hypothesis class. This sub-optimality cannot be computed efficiently as it would require a learning algorithm that produces optimal classifiers in terms of $\boldsymbol{a}(t)$-weighted error. We thus start by studying the impact of ε_1 in Section 4.2.4 on our bounds. As the focus of this work is not on estimating ε_1, we then set $\varepsilon_1 = 0$ which is computationally free, and shown by the experiment to be a reasonable choice both in terms of bound analysis (the bound is most of the time respected) and in terms of overall results from the **CONE** algorithm.

Evaluation of the tightness of the bound In this section, we aim at illustrating and showing the tightness of our bounds. To do so, we consider the (t, F) values obtained by 19 weighted-SVM learned on a regular grid of t values. For these same 19 models, we consider the cones obtained from our bounds and previous work (see Section 4.2.3 for details). For clarity,

Table 4.3 – Classification F-measures for $\beta = 1$ with SVM and Logistic Regression algorithms. SVM_G and LR^T_G are reproduced experiments of Parambath et al. (2014) and the subscript $_{I.R.}$ is used for the classifiers trained with a cost depending on the Imbalance Ratio. The subscript $_B$ corresponds to the bisection algorithm presented by Narasimhan et al. (2015). LR^T and $\text{LR}^T_{I.R.}$ are reproduced experiments of Koyejo et al. (2014). Finally the $_C$ stands for our wrapper **CONE** and SVM^T_C designed as a combination using the **CONE** + threshold. Reported F-measure values are averaged over 5 experiments (standard deviation between brackets).

Dataset	SVM	$\text{SVM}_{I.R.}$	SVM_G	SVM_C	SVM^T_C	LR^T	$\text{LR}^T_{I.R.}$	LR^T_G	LR_B
Adult	62.5 (0.2)	64.9 (0.3)	66.4 (0.1)	66.5 (0.1)	66.4 (0.1)	66.5 (0.1)	66.5 (0.1)	66.5 (0.1)	66.6 (0.1)
Abalone10	0.0 (0.0)	30.9 (1.2)	32.4 (1.3)	32.2 (0.8)	31.8 (1.9)	30.8 (2.2)	30.7 (1.9)	30.7 (1.9)	31.6 (0.6)
Satimage	0.0 (0.0)	23.4 (4.3)	20.4 (5.3)	20.6 (5.6)	30.9 (2.0)	21.2 (11.1)	28.6 (1.9)	28.6 (1.9)	21.4 (4.6)
IJCNN	44.5 (0.4)	53.3 (0.4)	61.6 (0.6)	61.6 (0.6)	62.6 (0.4)	59.4 (0.5)	56.5 (0.3)	56.5 (0.3)	59.2 (0.3)
Abalone12	0.0 (0.0)	16.8 (2.7)	16.8 (4.2)	18.3 (3.3)	16.3 (3.0)	15.5 (3.1)	17.0 (3.3)	17.0 (3.3)	17.7 (3.7)
Pageblocks	48.1 (5.8)	39.6 (4.7)	66.4 (3.2)	62.8 (3.9)	67.6 (4.0)	59.2 (8.1)	55.9 (6.4)	55.9 (6.4)	55.7 (5.7)
Yeast	0.0 (0.0)	29.4 (2.9)	38.6 (7.1)	39.0 (7.5)	35.4 (15.6)	37.4 (10.1)	39.9 (6.5)	27.6 (6.8)	27.6 (6.8)
Wine	0.0 (0.0)	15.6 (5.2)	20.0 (6.4)	22.7 (6.0)	19.3 (7.9)	21.5 (3.7)	25.2 (4.5)	25.2 (4.5)	18.3 (7.2)
Letter	75.4 (0.7)	74.9 (0.8)	80.8 (0.5)	81.0 (0.3)	81.0 (0.4)	82.9 (0.3)	82.9 (0.3)	82.9 (0.3)	74.9 (0.5)
News20	90.9 (0.1)	91.0 (0.2)	91.1 (0.1)	91.0 (0.1)	91.0 (0.1)	90.6 (0.1)	90.6 (0.1)	90.6 (0.1)	89.4 (0.2)
Average	32.1 (0.7)	44.0 (2.3)	49.5 (2.9)	49.6 (2.8)	50.4 (3.0)	48.8 (1.0)	48.2 (2.3)	49.1 (3.6)	47.0 (3.9)

we show only two illustrations, with two different datasets, but the Appendix C contains similar illustrations for all datasets.

Impact of ε_1 Both our bounds and the one from previous work are impacted by ε_1 which shows up as an offset, multiplied by $\Phi_{\boldsymbol{e}}$ for our bounds, and by Φ in previous work. As $\Phi_{\boldsymbol{e}} \leq \Phi$, our bounds are less impacted by an increased ε_1. With the 19-SVM setting, Fig. 4.4 shows the evolution of the maximum still-achievable F-measure depending on the value of ε_1, with a hard maximum at 1. The values of ε_1 are expressed in number of points for an easier interpretation.

The bound from Parambath et al. (2014) gives loose guarantees and the aggregate bound is most of the time above 1. The values, before being clipped to 1 can for example start at $F = 7$ and end up at $F = 40$ (on Yeast, if plotted on the same range of ε_1 values). This representation shows once again that our bounds are very tight. On Abalone10 and Letter, where the other bound starts below 1, the graph also confirms the fact that our bounds are less sensitive to the value of ε_1 ($\Phi_{\boldsymbol{e}} \leq \Phi$).

Visualizing unreachable zones The grayed-out areas in Fig. 4.5 are the unreachable zones. This figure shows that the guarantees obtained with our bounds are much more relevant than the ones from Parambath et al. (2014). Indeed, it is only on two datasets (Abalone10 and Letter) that the previously existing bound actually gives a maximum possible F-measure that is below 1. Our bounds give unreachable zones that go very close to the empirical points.

Looking at the cones with our tight bounds, we see that sometimes a point is in the cone

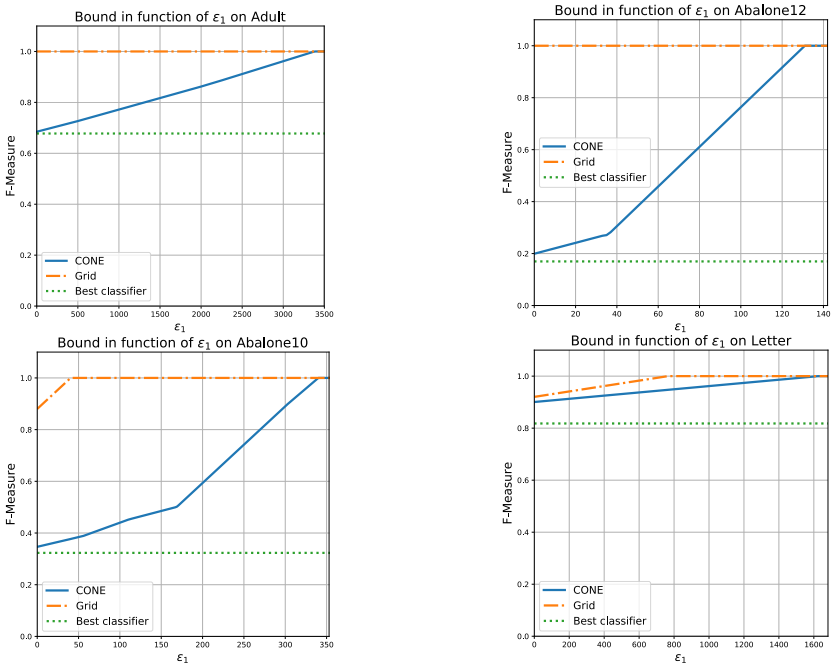

Figure 4.4 – Bounds on the F-measure as a function of ε_1, the unknown sub-optimality of the SVM learning algorithm. Both bounds are computed with (t, F) values obtained by 19 weighted-SVM learned on a regular grid of t values. Results are shown on four datasets: Adult (top left), Abalone12 (top right), Abalone10 (bottom left), and Letter (bottom right).

generated by another point. This looks like a violation of our bounds but it rather shows that ε_1 cannot be considered to be 0 in the current setting. Naturally, $\varepsilon_1 \neq 0$ comes from the fact that the weighted-SVM is not robust and not optimal in terms of weighted-0/1 loss. Our intuition is that the SVM is less and less optimal as the weights become more extreme, such as when t gets closer to 0.

Bounds' evolution across iterations We now study, with **CONE**, how the training performance and the overall bound evolve as a function of the training budget. The training budget of a method is the number of times it can learn a model (SVM or LR). In **CONE** incrementing the budget means doing one more iteration, while with the grid approach Parambath et al. (2014) it requires to re-learn all models (as all grid locations change). Fig. 4.6 (and Sec. C.3.3) illustrates that **CONE** tends to produce better models at a lower cost. These figures also outline the fact that our upper bound is tight and goes down quickly as we add models.

Performance in F-measure at test time Finally, we compare the performance of **CONE** (SVM_C), based on SVM algorithm against its competitors: LR_B for the method of Narasimhan et al. (2015), $\text{LR}_{I.R.}$ and LR^T for Koyejo et al. (2014) and SVM_G/LR_G for the method of Parambath et al. (2014). We present the results of all methods in Tab. 4.3, giving a budget of 19 models for relevant algorithms. Overall, **CONE** performs at least as well as its competitors

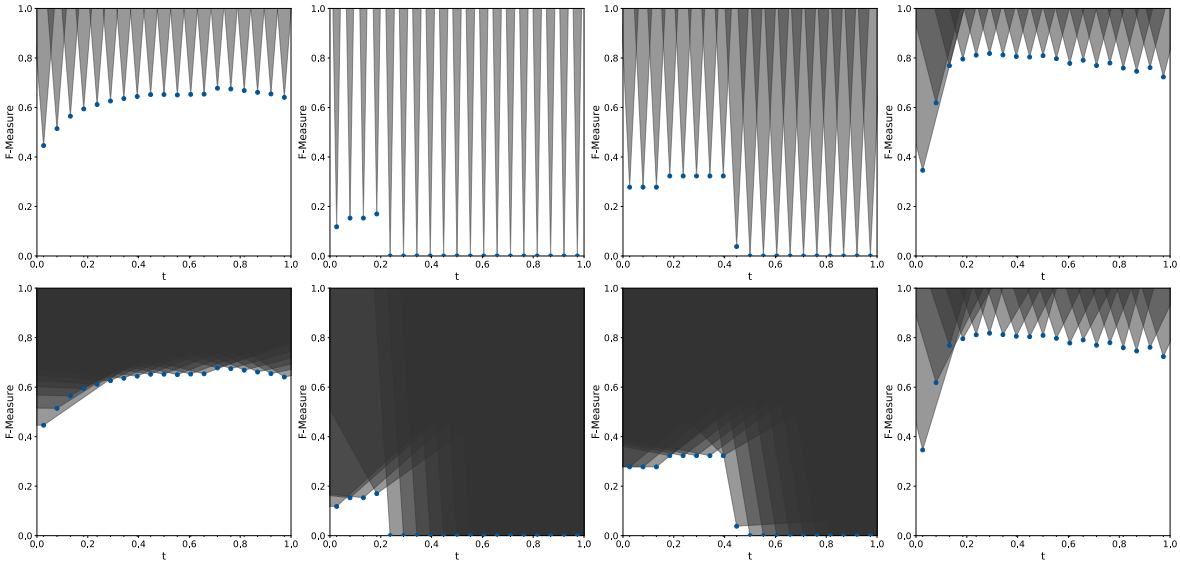

Figure 4.5 – Unreachable region obtained from the same 19 (t, F) points corresponding to learning weighted-SVMs on a grid of t values. Cones are shown for the datasets from left to right: Adult, Abalone12, Abalone10, and Letter. With the bound from Parambath et al. (2014) (top) and with our tighter bounds presented in Section 4.2.2 (bottom).

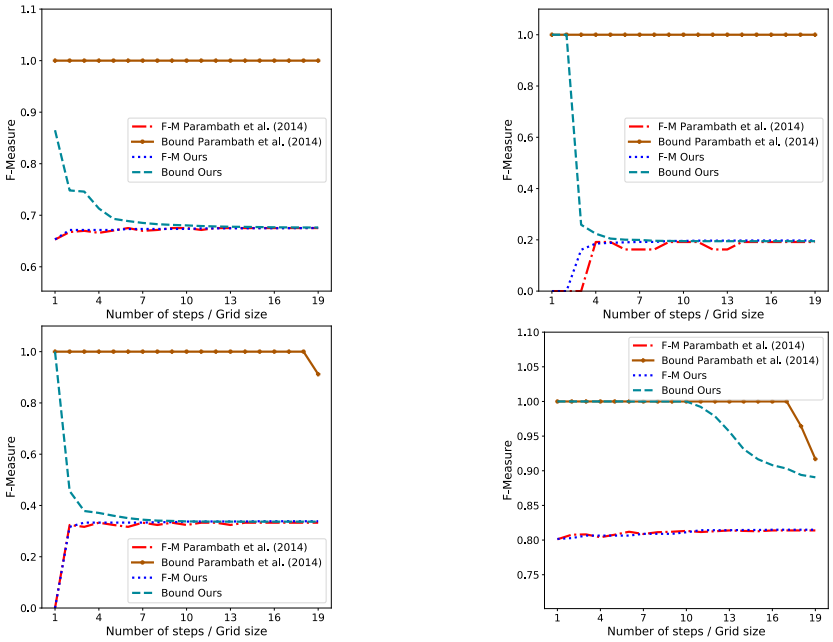

Figure 4.6 – Training performance of **CONE** versus the grid approach from Parambath et al. (2014), together with their respective bounds (on Adult (top left), Abalone12 (top right), Abalone10 (bottom left), and Letter (bottom right)). We suppose $\varepsilon_1 = 0$, which explains that we observe empirical values that are higher than our upper bound (on Abalone12).

in average, and the very best results are obtained by combining **CONE** with thresholding.

The baseline of using a simple SVM completely fails on half of the datasets. The improved SVM which consists in rebalancing the classes ($\text{SVM}_{I.R.}$) still performs worse than other approaches in average, and on most datasets. Even with thresholding, the approaches that learn a single model (LR^T and $\text{LR}^T_{I.R.}$) are still outperformed by the ones that learn multiple models with different class-weights like ours (all subscripts $_C$) and the grid one (subscripts $_G$). This last result shows that it is insufficient to solely rely on tuning the threshold of a single model.

In average, both our approach and the grid approach outperform all other considered approaches, including the bisection algorithm LR_B. We see that the results of **CONE** are very similar to the grid approach SVM_G. However, looking at Fig. 4.7 (but also in Sec. C.3.4), we see that the proposed method is able to reach higher values with a limited number of iterations, i.e. after training fewer models.

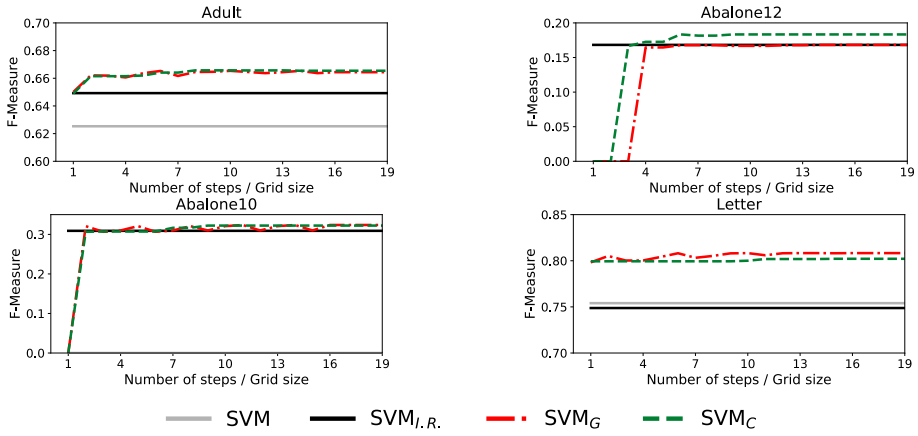

Figure 4.7 – F-measure obtained on the test set for four considered approaches on Adult (top left), Abalone12 (top right), Abalone10 (bottom left), and Letter (bottom right) datasets, plotted as a function of the computing budget (number of weighted SVM to learn).

4.2.5 Conclusion

In this work, we have presented new bounds on the F-measure based on a cost-sensitive classification approach. These bounds have been shown to be tighter than existing ones and less sensitive to the sub-optimality of the learned classifier (ε_1). Furthermore, we have shown that our bounds are useful from a practical point of view by deriving **CONE**, an algorithm which iteratively selects class weights to reduce the overall upper bound on the optimal F-measure. Finally, **CONE** has been shown to perform at least as well as its competitors on various datasets.

If this work focuses on the F-measure, it can be generalized to any other linear-fractional performance measure.

Our perspectives include estimating ε_1 (for example using (Bousquet et al., 2004)), refining our framework to improve the search space exploration, and deriving generalization guarantees.

We will also explore solutions to adapt it to SGD-based learning algorithms, so that we could apply it with our architecture on the Bluecime dataset.

Chapter 5

Questioning the usual domain adaptation results

Domain adaptation is often presented as a technique to learn a model on labeled examples from one data distribution (Source) and apply it on unlabeled example from another data distribution (Target). In this Chapter, we explore domain adaptation in the multi-Source setting where two question arise: Should we use all our sources? What if there is a discrepancy between the sources and the target class distribution? To answer these questions, we will first propose an approach on selecting the best sources domains for a target. We then question our domain adaptation results in our context with varying class distribution.

5.1 Source domains selection for domain adaptation

We present in this section our approach on selection the best sources domains used in the training set for learning the best classifier for a given target domain. This work was presented in Bascol et al. (2019a), at The 26th International Conference on Image Processing (ICIP 2019).

5.1.1 Introduction

The currently unpublished work from Schultz et al. (2018) is the closest to ours. The authors propose to select multiple domains according to four possible distances (the χ^2-divergence, the Maximum Mean Discrepancy, the Wasserstein distance and the Kullback-Liebler divergence) and according to the classification performance on each single source domain. Both the distance and the performance features are weighted by a parameter β computed as:

$$\boldsymbol{\beta} = \arg\min_{\boldsymbol{\beta} \geq 0} \sum_{i=1}^{D} \sum_{k=1;k\neq i}^{D} |\xi(\boldsymbol{Z}_i, \boldsymbol{Z}_k) - \boldsymbol{\beta} f(\boldsymbol{Z}_i, \boldsymbol{Z}_k)|$$

with $\boldsymbol{Z}_{1...D}$ the examples from the different domains, f the set of comparison operators considered by the authors and $\xi(\boldsymbol{Z}_i, \boldsymbol{Z}_k)$ the performance of the classifier trained on Z_i and

tested on Z_k. The authors show that on a homogeneous dataset, their method is better than randomly selecting the domains but not better than when using all of them. However, on a heterogeneous dataset, selecting the sources with their proposed distance is better than both selecting all the domains and selecting them randomly. Note that to optimize $\boldsymbol{\beta}$, D classifiers should be trained which can be costly in practice (especially for deep neural networks). Besides, the authors do not provide any criterion to set the number of selected sources.

Domain Selection and Weighting Considering a target domain j and D source domains, we propose an approach that automatically computes a weight vector $p^j \in \Delta^{D-1} \subset \mathbb{R}^D$ (probability simplex) and uses p^j to reweight the domains (when sampling minibatches) during "domain-adversarial training" (Ganin et al., 2016). This training phase is usually done to fine-tune a pre-trained network. The proposed approach is modular as we decompose the computation of the domains weight vector p^j in three configurable steps :

1. the distance vector $\boldsymbol{d}^j = \left\{d_i^j\right\}_{i=1}^D$ is computed (distance of each source domain, i, to the target one, j),
2. it is mapped to a score vector $\boldsymbol{s}^j = score(\boldsymbol{d}^j)$,
3. it is normalized to a probability vector $\boldsymbol{p}^j = \boldsymbol{s}^j / \sum_i s_i^j$.

5.1.2 Distance between domains

We define, in this section, the different distances we explored in our work. To reduce the computational charge, and also to obtain more relevant distances, we compute the distances on features extracted from the convolutional part of a ResNet50 pre-trained on ImageNet.

Euclidean distance The first distance is simply computed by taking the average minimal Euclidean distance between the examples of every domains, so that:

$$d_i^j = \frac{1}{|\boldsymbol{X}_i|} \sum_{x_1 \in \boldsymbol{X}_i} \min_{x_2 \in \boldsymbol{X}_j} \|x_1 - x_2\|$$

with $\boldsymbol{X}_i$ and $\boldsymbol{X}_j$ the examples of the ith and jth domains, and $|\boldsymbol{X}_i|$ the number of examples in domains i.

Silhouette score If we consider the different domains sets as different clusters we can use metrics measuring if clusters are well-defined. In our case, we can compute the Silhouette score on examples from two domains. If the score is high, the clusters are well-defined, thus the domains are far from each other. If the score is small, the clusters are difficult to distinguish, thus the domains are close. So, we can use this score directly as a distance between the domains (the smaller the closer).

The Silhouette score is computed on a set of point $\boldsymbol{X}$ by:

$$S_s(\boldsymbol{X}) = \frac{1}{|\boldsymbol{X}|}\sum_{x\in\boldsymbol{X}}\frac{f(x,\boldsymbol{C}_n)-f(x,\boldsymbol{C}_x)}{\max(f(x,\boldsymbol{C}_x),f(x,\boldsymbol{C}_n))}$$

where $f(x, C_x)$ is the mean distance between x and all the examples of the cluster containing x. $\boldsymbol{C}_n$ corresponds to the nearest cluster (other that $\boldsymbol{C}_x$) to x. In our context, to obtain our distance we can formulate this score as:

$$d_i^j = \frac{1}{|\boldsymbol{X}_j|}\sum_{x\in\boldsymbol{X}_j}\frac{f(x,\boldsymbol{X}_i)-f(x,\boldsymbol{X}_j)}{\max(f(x,\boldsymbol{X}_j),f(x,\boldsymbol{X}_i))}$$

Calinski-Harabaz score In the same way as the Silhouette score, we can use the Calinski-Harabaz score which also measures if clusters are well-defined.

The Calinski-Harabaz score is computed on a set of point $\boldsymbol{X}$ by:

$$S_{ch}(\boldsymbol{X}) = \frac{Tr(B(\boldsymbol{X}))}{Tr(W(\boldsymbol{X}))}\times\frac{|\boldsymbol{X}|-k}{k-1}$$

$$B(\boldsymbol{X}) = \sum_{c=1}^{k}|\boldsymbol{X}_c|(cen(\boldsymbol{X}_c)-cen(\boldsymbol{X}))(cen(\boldsymbol{X}_c)-cen(\boldsymbol{X}))^T$$

$$W(\boldsymbol{X}) = \sum_{c=1}^{k}\sum_{x\in\boldsymbol{X}_c}(x-cen(\boldsymbol{X}_c))(x-cen(\boldsymbol{X}_c))^T$$

with k the number of clusters, $\boldsymbol{X_c}$ the cluster of index c, and $cen(X)$ the centroid of the set of points $\boldsymbol{X}$. We can then define our distance:

$$d_i^j = S_{ch}(\boldsymbol{X}_i\cup\boldsymbol{X}_j) \quad \text{such that } \boldsymbol{X}_i \text{ and } \boldsymbol{X}_j \text{ are considered as two clusters}$$

Auto-encoders We consider that if a source example is well reconstructed by an auto-encoder trained on a target domain, the example should belong to a domain close to the target one. We thus can use the reconstruction error directly as a distance (the smaller the closer). So, to compute the distances we train an auto-encoder per domain. Then, we do forward passes with the examples from the other domains and average the reconstruction errors obtained, so that: $d_i^j = average_{x\in\boldsymbol{X}_i}\|x-AE_j(x)\|^2$.

Wasserstein distance In the optimal transport problem (see Section 1.3.2), the minimal displacement cost is called the *Wasserstein distance* and constitutes a distance between distribution. In our discrete case (samples of points), the distance can be expressed as:

$$d_i^j = \sum_{x\in\boldsymbol{X}_j}\sum_{y\in\boldsymbol{X}_i}\boldsymbol{\gamma}^\star_{x,y}\boldsymbol{C}_{x,y}$$

where C is a distance matrix between all pair of elements of the two domains, and $\boldsymbol{\gamma}^\star$ is the optimal transport plan. Note that, two sets of points, even if drawn from the same distribution, will exhibit a variable non-zero Wasserstein distance.

We will present, in Section 5.1.4, different experiments we conducted during the development of our approach to compare the different distances cited above. We will see that these results led us to choose the *Wasserstein distance*.

5.1.3 Domains selection method

One way to select the source domains in the training set could be to completely remove the domains too far from the target one. The threshold value should then represent a trade-off between the benefit of adding data from a domain and the possible negative transfer it would induce. Such thresholding method raises a question on what to do with domains with distances surrounding the threshold value. Indeed, is it right to equally consider a domain associated with a distance just above the threshold and the nearest domain? Conversely, is a domain with a distance slightly below the threshold completely harmful to the training? These questions led us to use to consider another method to select the source domains. We present in this section a smoother method to select the domains based on the derivation of selection probabilities from the distances, then used to change the domain proportions in the training set.

Transforming distances into scores Possible score functions include the inverse distances ($\frac{1}{d}$) or the inverse squared distances ($\frac{1}{d^2}$). Here, we focus on the negative exponential scoring function:

$$s_i^j = e^{-\lambda d_i^j}$$

The parameter λ allows a smooth interpolation between putting all the weight on the closest domain and having a uniform distribution of all domains. Thanks to this parameter, we will be able to control the variety of the subset of domains we are considering (see below).

Ensuring training set variety In case of many source domains and when some of them have a very small number of training examples, it becomes important to avoid selecting too few domains in the process (e.g., a single one). For generalization (i.e. avoiding overfitting) and transfer purpose, the training set should exhibit enough *variety*. For domain sizes $n \in \mathbb{N}^D$, a probability vector p^j and a draw of N training samples (with replacement), we define the training set variety as the expected number of distinct samples we will use during each epoch. The variety can be approximated as:

$$variety(p^j, n, N) \approx \sum_i n_i \cdot \left[1 - \left(1 - \frac{p_i^j}{n_i}\right)^N\right]$$

Our probability vector p^j depends on the λ parameter. As such, by varying λ from ∞ to 0, we can move from a minimal variety (sampling from the closest domain i, getting a diversity of approximately n_i, the number of examples in this closest domain) to a maximal one (using a uniform p^j, getting a variety of $N - N\left(\frac{N-1}{N}\right)^N \approx 0.63N$ in case of a balanced n). In the experiments, we consider one *epoch* (with replacement) of $N = \sum_i n_i$ samples. We use p^j and n to find the highest value of λ for which the variety is below a target variety.

5.1.4 Experiments

In this section, we first present the datasets settings used in our domain adaptation experiments. We then presents results, first on the choice of a distance, then on the complete approach.

5.1.4.1 Datasets

Office-Caltech (O-C) This dataset, published by Gong et al. (2012), is a classical domain adaptation benchmark with four domains: Amazon (A), DSLR (D), Webcam (W) and Caltech (C). It is composed of the 10 classes (Backpack, Bike, Calculator, Headphones, Keyboard, Laptop, Monitor, Mouse, Mug, and Video-projector) common between the datasets Office-31 (Saenko et al., 2010) and Caltech256 (Griffin et al., 2007), both presented in Section 2.1.1.

ImageNet-Caltech (I-C) To control the discrepancy between each domain and validate our chosen domain similarity measure, we have designed a dataset using images from Caltech101 (Fei-Fei et al., 2007) (C1), Caltech256 (Griffin et al., 2007) (C2) and from ImageNet (Deng et al., 2009) (IN), all presented in Section 2.1.1. This dataset is composed of three different types of domain: the "Good" (G_) domains are created with images with their true original classes, the "Bad" (B_) domains are created with images associated to different but similar original classes, and the "Random" (R_) domains are created with images labeled with randomly chosen classes in the corresponding datasets. We use five classes: "bird", "car", "chair", "dog", and "person" (following, among others, Khosla et al. (2012); Fang et al. (2013)). We give the corresponding true classes for each domain in Table 5.1. With this design, the "Good" domains are expected to be closer to each other since their corresponding images are showing the same objects. The "Bad" domains should be farther away from the "Good" ones and the "Random" domains should be the farthest (and are expected to be far from each others too).

Bluecime. Here, we use the 2018 release of the Bluecime dataset (see Section 2.1.2).

5.1.4.2 Distance choice

We present in Table 5.2, results obtained at different development stages of our approach leading us to choose the Wasserstein distance as our preferred distance between the domains. The first four experiments are conducted on the 2017 Bluecime dataset, "7S" indicates that we use the seven nearest sources in the training sets according to the silhouette score ("silh"), to the Calinski-Harabaz score ("chs"), and to autoencoders reconstruction errors ("ae"). Using a distance based on the autoencoders reconstruction error provides better results than blindly using all the domains (chairlifts), which validates our approach. Moreover, this setting also yields better results than using the seven nearest domains according to both silhouette and Calinski-Harabaz clustering scores.

Domains	Class	Dataset Classes	# Ex
G_C1	bird	"pigeon", "flamingo", "ibis", "rooster", "emu"	294
	car	"car_side"	123
	chair	"chair"; "windsor_chair"	118
	dog	"dalmatian"	67
	person	"Faces"; "Faces_easy"	870
G_IN	bird	"birds" (56)	1456
	car	"motorcar" (8)	1496
	chair	"chair" (3)	1500
	dog	"domestic dog" (117)	1404
	person	"individual" (2)	1500
B_C1	bird	"butterfly"; "dragonfly"	159
	car	"Motorbikes"	798
	chair	"grand_piano"	99
	dog	"cougar_body"	47
	person	"buddha"	85
B_C2	bird	"024.butterfly"	112
	car	"072.fire-truck", "178.school-bus"	216
	chair	"011.billiards"	278
	dog	"105.horse"	270
	person	"038.chimp"; "090.gorilla"	322
B_IN	bird	"butterfly" (6)	1500
	car	"motortruck" (9)	1494
	chair	"dining table, board"	1500
	dog	"domestic cat" (5)	1500
	person	"apes" (5)	1500
R_C1	bird	"brain"	98
	car	"chandelier"	107
	chair	"watch"	239
	dog	"ketch"	114
	person	"bonsai"	128
R_IN	bird	"saltshaker"	1473
	car	"fiddler crab"	1182
	chair	"brown bear"	1500
	dog	"banana"	1409
	person	"dough"	1249

Table 5.1 – Classes used in each dataset to create the different domains (G = "good"; B = "bad"; R = "random", C1: from Caltech101; C2: from Caltech256; IN: from ImageNet). In parentheses: number of classes composing the superclass that has been used (e.g. 56 classes of birds).

In the next four experiments, we present results on three well represented chairlifts from the 2018 Bluecime dataset (Chair. E, Chair. I, and Chair. Q). Again, using the autoencoder-based distance performs better than all the other experiments. Using the Euclidean distance proves to be harmful on this dataset. Using the Wasserstein distance slightly improves the results on this dataset.

The last four experiments are conducted on the ImageNet-Caltech dataset. On this dataset, our approach improves all the other baseline results. Contrarily to the previous four experiments, using autoencoders yields worst results than both experiments using Euclidean and Wasserstein distances. This difference can result from the need to tune the autoencoders

differently for each new dataset. Considering this drawback and the average gain we obtained with our approach on Bluecime and ImageNet-Caltech datasets we choose to only use the Wasserstein distance in the remaining experiments.

Expe.	Accuracy	Recall	Precision	F-measure
LOCO DA	92.95	77.38	54.17	63.73
LOCO DA 7S silh	94.33 (+1.38)	70.83 (−6.55)	62.96 (+8.80)	66.67 (+2.94)
LOCO DA 7S chs	90.47 (−2.48)	73.81 (−3.57)	44.29 (−9.88)	55.36 (−8.37)
LOCO DA 7S ae	94.80 (+1.86)	75.00 (−2.38)	65.28 (+11.12)	69.81 (+6.08)
LOCO DA	97.16	85.88	66.37	74.88
OURS eucl	96.70 (−0.45)	86.26 (+0.38)	61.92 (−4.45)	72.09 (−2.79)
OURS ae	97.49 (+0.34)	85.50 (−0.38)	70.22 (+3.85)	77.11 (+2.23)
OURS wass	97.23 (+0.08)	84.73 (−1.15)	67.48 (+1.11)	75.13 (+0.25)
LODO DA (I-C)	92.07	91.00	91.06	91.02
OURS eucl (I-C)	92.46 (+0.39)	91.69 (+0.64)	91.34 (+0.33)	91.50 (+0.49)
OURS ae (I-C)	92.14 (+0.08)	91.43 (+0.43)	90.91 (−0.15)	91.15 (+0.14)
OURS wass (I-C)	92.81 (+0.74)	91.77 (+0.76)	91.92 (+0.86)	91.84 (+0.82)

Table 5.2 – Experiments on the different distances. The first four lines provides experiments on the 2017 Bluecime dataset. The next four lines provide experiments on chairs Chair. E, Chair. I, and Chair. Q from the 2018 Bluecime dataset (chairlifts with a large enough amount of data to be relevant). The last four lines show experiments on the ImageNet-Caltech dataset "(I-C)". "7S" corresponds to thresholding the number of source domains to 7. We indicate the chosen distance: "silh" corresponds to the Silhouette score, "chs" to the Calinski-Harabaz score, "ae" to the autoencoders-based distance, "eucl" to the Euclidean distance, and "wass" to the Wasserstein distance.

5.1.4.3 Complete approach

We report the average test-accuracy on the target domain using a 5-fold cross validation procedure. We use the following names to report the model performance:
– **Target (only):** models trained on the *labeled* target dataset. Note that this is an ideal but unrealistic situation since, in our actual applications, there is no target label. This setting requires the target domain to be split into training/test sets.
– **Only near.:** models trained using only the nearest domain (according to our distance measure) to the target one;
– **Only far.:** models trained using only the farthest domain (according to our distance measure) to the target one;
– **LODO:** models trained using all domains but the target one, using domain adaptation on the remaining target domain, without using our domain selection method;
– **w/o near.:** models trained using all domains but two: the target and the closest domain to the target one (according to our distance measure) are not used.

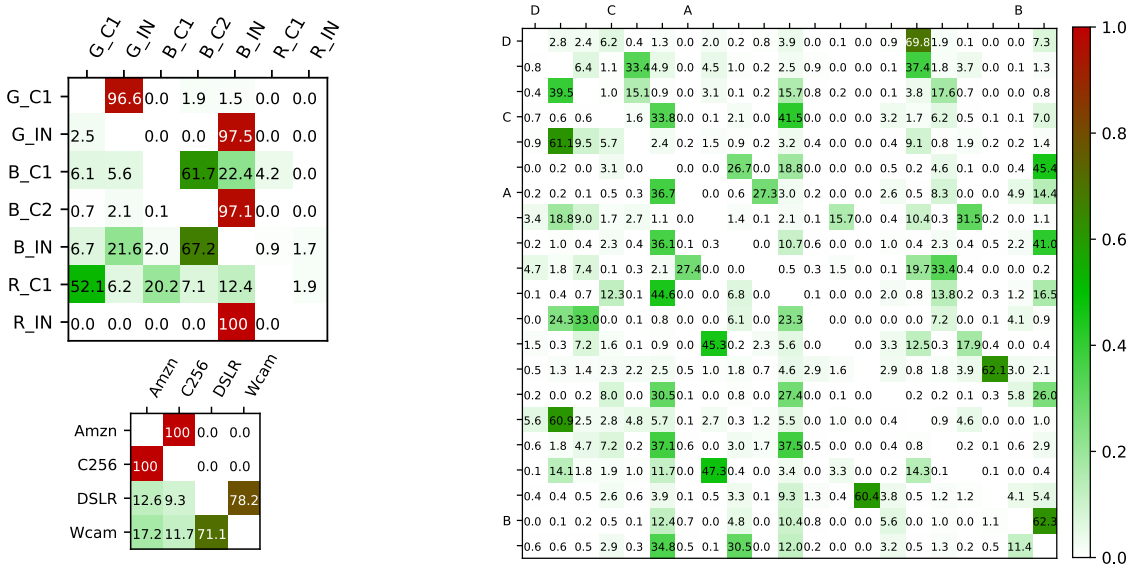

Figure 5.1 – Probabilities used to reweight the different domains: ImageNet-Caltech (top-left), Office-Caltech (bottom-left), Bluecime (right).

– **w/o far.:** models trained using all domains but two: the target and the farthest domain to the target one (according to our distance measure) are not used.
– **OURS:** models trained by weighting the source domains with our method, using the variety criterion (with a target variety of half its maximum value).

Setting	**A**	**C**	**D**	**W**	*AVG*
target	95.10	94.44	92.11	92.46	*93.53*
Only near.	95.30	91.32	100.0	96.43	*95.76*
Only far.	83.80	84.19	95.07	98.01	*90.27*
LODO	94.41	92.76	99.26	98.44	*96.22*
w/o near.	91.06	83.20	93.92	96.22	*91.10*
w/o far.	95.38	91.52	100.0	98.57	*96.37*
OURS	94.98	92.70	100.0	98.57	*96.56*

Table 5.3 – Accuracy averaged over 5 experiments on the Office-Caltech datasets. We use a ResNet50 pretrained on ImageNet, and train it for 50 epochs (batch-size 64, learning rate 10^{-5}). The last column is grayed-out as it gives the average including the "Random" domains.

In Figure 5.1, we show the probabilities we obtain using the selection process described in Section 5.1.1 on the 3 datasets. For most datasets, only up to three domains have a selection probably greater than 0.1 and more than half the source domains are totally unused. For instance, during training with "Bad" ImageNet as the target domain, 67.2% of the training images come from "Bad" Caltech256, 21.6% from "Good" ImageNet, 6.7% from "Good" Caltech101, and only 4.6% from the three other source domains.

In Table 5.4, we show the results on the Office-Caltech (O-C, first five columns) and ImageNet-Caltech (I-C, last nine columns) datasets. On both datasets, using only the nearest

Setting	G_C1	G_IN	B_C1	B_C2	B_IN	*AVG*	R_C1	R_IN	*AVG*
target	99.81	96.17	99.56	98.32	98.23	*98.42*	100.0	98.21	*98.61*
Only near.	98.09	68.84	34.85	83.79	81.61	*86.03*	0.00	2.66	*61.83*
Only far.	0.88	14.39	38.97	28.42	24.95	*21.52*	3.17	12.53	*17.62*
LODO	94.40	87.24	93.86	91.80	91.88	*91.67*	11.76	9.01	*68.56*
w/o near.	77.77	75.56	95.72	81.88	86.43	*83.47*	11.99	5.68	*62.15*
w/o far.	97.20	86.66	96.90	90.16	91.99	*92.58*	18.27	12.40	*70.51*
OURS	97.54	84.93	97.38	94.73	91.13	*93.14*	8.89	16.81	*70.20*

Table 5.4 – Accuracy averaged over 5 experiments on the datasets created from ImageNet and Caltech. We use a ResNet50 pretrained on ImageNet, and train it for 50 epochs (batch-size 64, learning rate 10^{-5}). The last column is grayed-out as it gives the average including the "Random" domains.

Setting	Chair. A	Chair. B	Chair. C	Chair. D	All 21
LODO	95.70	98.26	98.28	98.69	95.94
OURS	95.63	98.38	98.07	98.94	97.06

Table 5.5 – Accuracy on the Bluecime dataset, averaged on 5 experiments, on a selection of 4 domains and on all available domains.

source domains is beneficial compared to using the farthest one (+5.49 accuracy points on O-C and +44.21 pts on I-C) which suggests that our distance is meaningful. On Office-Caltech, using the target domain as source (*Target* line) gives worse performance than using the nearest source (-2.23 pts), which can be explained by the lack of training data which induces an overfitting phenomena. Since ImageNet-Caltech contains more data, the *Target* setting is much more suited, as expected, than the *Only nearest* one (+36.78 pts).

Using the *LODO* setting (all source domains are used during training), we observe better performance than with the *Only nearest* and *Only farthest* ones thanks to a more diverse training set (respectively, on O-C, +0.46 pts and +5.95 pts, on I-C, +6.73 pts and +50.94 pts). This means that there is a real trade-off between the domain selection and the number of remaining training data. However, if we remove the nearest source domain, the performance becomes worse than for the *LODO* setting (-5.12 pts on O-C and -6.41 pts on I-C), on Office-Caltech we even get worse performance than using the *Only nearest* setting (-4.66 pts). If we remove the farthest source domain, we do obtain better performance than with the *LODO* setting (+0.15 pts on O-C and +1.95 pts on I-C). We can conclude that using many data (*LODO* setting) is important and always better than choosing a single domain (even the most similar one) but selecting a good number of sources can be beneficial.

Our distance-based weighting approach provides better performance than removing the farthest source domain on Office-Caltech (+0.19 pts). On ImageNet-Caltech, we get worse results than when removing the farthest domain (-0.31 pts), but, still notably better than with the *LODO* setting (+1.64 pts). However, if we ignore the results on the "Random" domains (which are close to random by design), on average, the *LODO* setting gives 91.67% of accuracy,

w/o farthest 92.58%, and our approach allows us to get the best accuracy performance of 93.14% which confirms the relevance of our approach.

In Table 5.5, we show the results on the Bluecime dataset. We detail the results on 4 relevant domains and give the averaged results over the 21 domains. As with the other datasets, we obtain better results by selecting the source domains (+1.12 pts). This shows that the proposed method works well even when there are much more source domains to select from.

5.2 Multi-source domain adaptation with varying class distribution

In this section, we discuss the standard domain adaptation setting in presence of varying class distributions across the domains. We also present the effects of varying the imbalance ratio on our different domain adaptation results. Then, we study different methods to apply domain adaptation in such context.

5.2.1 Discussion on our previous results

In this section, we discuss our baseline domain adaption results and the ones presented in Section 5.1.

5.2.1.1 Bluecime baseline results

The results on LOCO DA setting presented in the previous sections turned out to be over-optimistic. Indeed, we realized, quite late during this PhD, that due to a mistake in our code, the unlabeled target examples used during the training phase to train the adversarial network were automatically balanced over the classes. However, in reality, no labels could have been used to balance the target classes. This mistake led us also to question the robustness of the state-of-the-art domain adaptation techniques. We present in Table 5.6 the LOCO performance according to (i) the use of domain adaptation or not (ii) the relative classes balancing in the source and target sets. "bs" means that the source examples are balanced, "ibs" means that the sources examples are imbalanced. Conversely, "bt" and "ibt" mean that the target set is respectively balanced and imbalanced. We observe that domain adaptation increases the performance of our network only when both the source and the target sets are balanced. Without domain adaptation, balancing the source is not effective (-0.20 pts of Accuracy compared to imbalanced sources), however, with domain adaptation the opposite occurs. Indeed, keeping balancing the source set but not the target set (LOCO DA bs ibt) is the worst case (-19.53 pts of Accuracy compared to the balanced setting, LOCO bs). In the hypothetical setting where the source set is imbalanced whereas the target is (LOCO DA ibs bt), the Accuracy drop is relatively small (-1.45 pts compared to the setting LOCO ibs) but we observe a dramatic drop of F-measure (-20.62 pts). If both sets are imbalanced (LOCO DA ibs ibt) we also observe a drop of performance (-0.83 pts of Accuracy and -5.62 pts of

F-measure compared to the LOCO ibs setting), which indicates that domain adaptation does not help in this setting.

From these results, we hypothesize that domain adaptation techniques relying on adversarial feature training, such as in Ganin et al. (2016), requires both the source and target class distributions to be similar to improve the performance.

Expe.	Accuracy	Recall	Precision	F-measure
LOCO bs	96.52	81.90	81.58	76.73
LOCO DA bs bt	97.41 (+0.89)	89.17 (+7.27)	82.94 (+1.36)	83.30 (+6.56)
LOCO DA bs ibt	76.99 (−19.53)	89.69 (+7.79)	27.83 (−53.76)	38.64 (−38.10)
LOCO ibs	96.72 (+0.20)	81.01 (−0.90)	82.33 (+0.75)	77.12 (+0.39)
LOCO DA ibs bt	94.87 (−1.65)	42.17 (−39.73)	88.75 (+7.17)	56.11 (−20.62)
LOCO DA ibs ibt	95.89 (−0.63)	80.40 (−1.50)	73.36 (−8.22)	71.51 (−5.23)

Table 5.6 – LOCO results with and without balancing the target and the sources sets. (i)b indicates experiments with (im)balanced set, s indicates source set and t indicates target set.

To get a better insight into the imbalanced class distributions problem over the sources and the target domains, we present results with the One Versus One (OVO) setting, i.e. using one domain as source and one other domain as target. We present, in Table 5.7, the results with this setting between chairlifts (domains) with similar and dissimilar class distributions (we show some additional results in Section B.2). These results confirm that having similar class distributions is a requirement for domain adaptation to be effective. Moreover, we note that, in the mono-source setting, adding domain adaptation with imbalanced sets is beneficial, while we observe the opposite in the multi-source setting. This observation may indicate that in the multi-source domain adaptation setting, with a sufficiently large number of source domains, the training set contains enough variety to generalize well. This could mean that using domain adaptation in the multi-source setting could be ineffective. In Table 5.8, we show results with domain adaptation and balanced sets such that either both source and target sets have a uniform class distribution (LOCO DA bs bt), or both have the natural target class distribution (LOCO DA tcdbs ibt). We observe that in both cases the domain adaptation is effective. This shows that using multi-source adaptation is possibly effective, but requires that the sources class distributions match the target one. In addition, we also observe that using uniform class distribution gives better results in F-measure than the other three settings. Using natural target class distribution however gives the best results in Accuracy. This is coherent with our class balancing approach presented in Section 3.1.1.

5.2.1.2 Source selection results

In Tables 5.9 and 5.10, we show the same kind of results as the ones from Section 5.1 on Office-Caltech without balancing the target set and respectively using balanced and imbalanced sources sets. In mono-source domain adaptation ("only near.", and "only far." rows), adding domain adaptation is effective in both "only near." and one "only far." settings. These

Expe.	≈ class dist.	≠ class dist.
OVO bs	86.84	86.84
OVO DA bs bt	91.77 (+4.93)	90.77 (+3.94)
OVO ibs	79.20 (−7.64)	71.14 (−15.69)
OVO DA ibs ibt	93.20 (+6.36)	85.07 (−1.76)

Table 5.7 – One versus one (ovo) Accuracy averaged over domains with similar class distributions and over domains with highly dissimilar class distributions (see more results in Tables B.4, B.5, and B.6). (i)bt and (i)bs indicate experiments with (im)balanced target and source sets.

Expe.	Accuracy	Recall	Precision	F-measure
LOCO bs	96.52	81.90	81.58	76.73
LOCO DA bs bt	97.41 (+0.89)	89.17 (+7.27)	82.94 (+1.36)	83.30 (+6.56)
LOCO ibs	96.72 (+0.20)	81.01 (−0.90)	82.33 (+0.75)	77.12 (+0.39)
LOCO DA tcdbs ibt	98.24 (+1.72)	80.38 (−1.52)	85.71 (+4.13)	82.70 (+5.97)

Table 5.8 – LOCO results with the same imbalance ratio between the target and sources sets. (i)b indicates experiments with (im)balanced set, s indicates the source set and t indicates the target set. tcdbs indicates that the source is balanced so that it has the same class distribution as the imbalanced target set (using the target labels, given only as reference).

results confirm the effectiveness of the domain adaptation approach in the mono-source setting. Moreover, it also confirms the benefit of our approach on selecting the source domain. However, in multi-source domain adaptation ("LOCO", "w/o near.", "w/o far.", and "OURS" rows), in both balanced settings only the "w/o far." setting presents successful domain adaptation results. This suggests that our domain selection approach is effective when thresholding the number of sources. However, changing the selection probability of the source examples according to the domain requires to have similar class distribution in both the target and the source sets.

5.2.2 Improving our approach

In this section we study two possible methods to deal with the discrepancy between the sources class distribution and the target class distribution.

5.2.2.1 Finding the target class distribution

In Hoffman et al. (2016), the authors propose to apply domain adaptation on semantic segmentation problems, a field of machine learning where each pixel of an image is classified. Their approach is an adversarial method, such as Ganin et al. (2016), but adapted to semantic segmentation. Indeed, the prediction of the domain discriminator is considered over all the

Setting	A	A+DA	C	C+DA	D	D+DA	W	W+DA	*AVG*	*AVG+DA*
target	95.52	95.59	95.88	95.61	98.11	98.11	97.50	98.65	*96.75*	*96.99*
only near.	94.66	94.64	87.20	89.71	98.85	100.00	99.64	97.14	*95.09*	*95.37*
only far.	85.88	86.38	79.46	83.14	94.74	90.48	91.04	95.17	*87.78*	*88.79*
LOCO	94.26	91.55	91.16	91.53	100.00	96.63	98.93	98.29	*96.09*	*94.50*
w/o near.	88.87	89.57	83.96	79.94	90.07	89.25	90.68	93.82	*88.40*	*88.15*
w/o far.	94.89	94.97	90.81	91.99	100.00	100.00	98.93	98.93	*96.16*	*96.47*
OURS	94.35	93.81	87.40	91.35	99.26	99.59	99.29	97.22	*95.49*	*95.08*

Table 5.9 – Results (in Accuracy) comparable to the ones in Table 5.4 but with **imbalanced target** set, and **balanced source** set. The columns with "+DA" indicates the results using the domain adaptation component.

Setting	A	A+DA	C	C+DA	D	D+DA	W	W+DA	*AVG*	*AVG+DA*
target	95.91	95.84	95.61	95.70	96.63	95.81	97.29	97.58	*96.36*	*96.23*
only near.	94.76	94.16	86.35	90.58	100.00	100.00	97.86	96.43	*94.74*	*95.29*
only far.	81.29	72.13	77.30	67.16	93.11	92.70	89.40	94.18	*85.27*	*81.54*
LOCO	94.89	93.75	90.40	92.49	100.00	97.70	98.65	95.94	*95.98*	*94.97*
w/o near.	86.82	82.16	81.84	75.64	89.66	88.59	87.41	95.38	*86.43*	*85.44*
w/o far.	95.09	94.63	90.38	91.99	100.00	99.26	98.29	99.29	*95.94*	*96.29*
OURS	94.16	92.97	86.51	90.70	99.26	95.89	99.29	96.07	*94.80*	*93.91*

Table 5.10 – Results (in Accuracy) comparable to the ones in Table 5.4 but with **imbalanced target** set, and **imbalanced source** set. The columns with "+DA" indicates the results using the domain adaptation component.

pixels of the last feature map extracted by the feature extractor. Moreover, they propose to constrain their model so that the proportion of pixels predicted in a class must be similar to the average proportion of this class in the source domain. This allows to train the target model with more information, in particular some information on a coherent proportion of each class which should be predicted in the target images. In addition, they propose to down-weight the gradient generated by the constraints on the proportion of the most represented classes (classes representing at least 10% of the pixels in the source images) by a factor of 0.1. By doing so, the authors suggest that it allows them to get closer to having a balanced dataset and thus to reduce the over-fitting induced by the constraints on the well-represented classes.

Since we established in our experiments that domain adaptation works best when both source and target examples have the same class distribution and since this information is not available for the target, we propose to estimate it. We propose to find weak labels for our target examples and use them to find a "weakly-balanced" setting improving domain adaptation. This setting is similar to the gradient down-weighting in Hoffman et al. (2016). However, we propose, here, to change the proportion of each class during the training, so that they are exactly uniformly distributed across the domains, according to the pseudo-labels. We also propose another "weakly-balanced" setting where the sources class distributions are re-balanced to match the target one instead of the uniform. In the uniform settings, note that

our first results using target labels to find the right balance between the classes (cf Table 5.8) is now our superior bound on the balanced approaches. To find pseudo-labels for the target domain, we propose to use a model trained with LOCO setting, and simply use its outputs.

We show, in Table 5.11, our results using such pseudo-labels. If we balance both the source and target class distributions ("LOCO DA bs tplbt" row), we still obtain worse Accuracy results than without domain adaptation (−0.71 pts). However, this setting shows an increase in F-measure (+1.50 pts) compared to the setting with no domain adaptation which is consistent with our class balancing approach for F-measure optimization improvement. We still have room for improvements since we still have worse performance than using the target labels (−1.6 pts of Accuracy, −5.07 pts of F-measure). However, we show much better results than without balancing the target examples (+18.82 pts of Accuracy, +39.59 pts of F-measure).

The setting where we use the target pseudo-labels to balance the source set in order to match the target class distribution ("LOCO DA tplbs ibt" row), gives worse performance than the setting without domain adaptation (and without balancing the source set), with −0.16 pts of Accuracy and −0.30 pts of F-measure. However, we obtain better results than using domain adaptation with both source and target sets imbalanced, with +0.67 pts of Accuracy, and +5.32 pts of F-measure. As with the previous method, this suggests that using pseudo-labels can improve the adaptation. Again, there is still room for improvement since we have −1.68 pts of Accuracy and −5.88 pts of F-measure compared to the same setting using the target labels.

Expe.	**Accuracy**	**Recall**	**Precision**	**F-measure**
LOCO bs	96.52	81.90	81.58	76.73
LOCO DA bs ibt	76.99 (−19.53)	89.69 (+7.79)	27.83 (−53.76)	38.64 (−38.10)
LOCO DA bs bt	97.41 (+0.89)	89.17 (+7.27)	82.94 (+1.36)	83.30 (+6.56)
LOCO DA bs tplbt	95.81 (−0.71)	87.69 (+5.78)	78.29 (−3.30)	78.23 (+1.50)
LOCO ibs	96.72 (+0.20)	81.01 (−0.90)	82.33 (+0.75)	77.12 (+0.39)
LOCO DA ibs ibt	95.89 (−0.63)	80.40 (−1.50)	73.36 (−8.22)	71.51 (−5.23)
LOCO DA tcdbs ibt	98.24 (+1.72)	80.38 (−1.52)	85.71 (+4.13)	82.70 (+5.97)
LOCO DA tplbs ibt	96.56 (+0.04)	78.03 (−3.87)	85.87 (+4.29)	76.82 (+0.09)

Table 5.11 – LOCO results comparable to Table 5.8, without groundtruth knowledge on the target labels. (i)b indicates experiments with (im)balanced set, s indicates the source set and t indicates the target set. tbbs indicates that the source is balanced so that it has the same class distribution as the imbalanced target set (using the target labels). tplbt indicates that the target set is uniformly balanced using the pseudo-labels information. tplbs indicates that the source set class distribution is rebalanced to match the pseudo-labeled target set one.

Using pseudo-labels for rebalancing either the source or the target set improves domain adaptation. However, we obtain performance arguably better than in settings without domain adaptation. Considering the good results using the target labels, and the improvement of the domain adaptation with pseudo-labels, this approach could potentially give better results. For

instance, for each target example we used the highest output probability to obtain the class of the examples. However, we could use all the outputs and average over all the examples to get a possible class distribution. We could also use another algorithm to get the class distribution, such as JCPOT (Redko et al., 2018).

Setting	**A**	**A+DA**	**C**	**C+DA**	**D**	**D+DA**	**W**	**W+DA**	*AVG*	*AVG+DA*
target	95.52	96.46	95.88	95.26	98.11	97.78	97.50	98.57	*96.75*	*97.02*
only near.	94.66	95.06	87.20	91.52	98.85	98.52	99.64	97.14	*95.09*	*95.56*
only far.	85.88	85.06	79.46	80.94	94.74	96.55	91.04	95.87	*87.78*	*89.60*
LOCO	94.26	93.02	91.16	91.25	100.00	98.44	98.93	98.57	*96.09*	*95.32*
w/o near.	88.87	85.86	83.96	83.29	90.07	94.00	90.68	94.15	*88.40*	*89.33*
w/o far.	94.89	95.61	90.81	91.94	100.00	98.85	98.93	98.57	*96.16*	*96.24*
OURS	94.35	94.90	87.40	92.13	99.26	99.18	99.29	98.57	*95.49*	*96.20*

Table 5.12 – Results (Accuracy) comparable to Table 5.4 but with **pseudo-balanced target** set (with uniform class distribution using pseudo-labels from LOCO setting), and **balanced source** set. The columns with "+DA" indicates the results using domain adaptation.

Setting	**A**	**A+DA**	**C**	**C+DA**	**D**	**D+DA**	**W**	**W+DA**	*AVG*	*AVG+DA*
target	95.66	95.64	94.86	95.17	96.62	96.55	98.40	98.21	*96.39*	*96.39*
only near.	93.25	94.88	86.56	90.91	99.07	98.11	99.11	99.64	*94.50*	*95.88*
only far.	87.04	87.83	77.95	73.79	90.46	95.81	93.89	97.93	*87.34*	*88.84*
LOCO	94.38	94.33	90.00	91.19	100.00	99.18	99.65	98.57	*96.01*	*95.82*
w/o near.	88.19	86.30	82.53	76.34	87.59	96.40	90.23	96.50	*87.13*	*88.88*
w/o far.	94.15	94.98	90.22	91.35	100.00	98.85	97.86	97.86	*95.56*	*95.76*
OURS	94.28	94.76	87.70	91.18	99.07	97.37	99.55	98.21	*95.15*	*95.38*

Table 5.13 – Results (Accuracy) comparable to Table 5.4 but with **imbalanced target** set, and **pseudo-imbalanced source** set (with class distribution matching the target pseudo-labels one). The columns with "+DA" indicates the results using domain adaptation.

Tables 5.12 and 5.13, gives similar results as the ones of Section 5.1 using pseudo-labels to change the balance of, respectively, the target set (to a uniform class distribution), and the source set (to the same class distribution as the target one). We compare Table 5.12 with Table 5.9 since the corresponding settings use uniformly balanced source class distributions. Conversely, we compare Table 5.13 with Table 5.10, both created without changing the target class balance. We observe that all mono-source settings ("only near.", and "only far." rows) benefit from both the rebalanced settings, leading to an effective domain adaptation in every mono-source settings. In multi-source domain adaptation ("LOCO", "w/o near.", "w/o far.", and "OURS" rows), using the LOCO setting with domain adaptation benefits from the rebalancing, however the results are still worse than the ones obtained without domain adaptation. However, in the three other settings applying domain adaptation becomes effective with both rebalancing settings. This confirms our hypothesis that our source selection approach changing the sampling probability requires to have similar class distribution. However, removing

the farthest source domain gives better performance than our approach which thus needs to be improved. We could explore solutions to include the class distribution in the distance, for instance, using the regularized optimal transport presented in Courty et al. (2014).

5.2.2.2 Domain adaptation with optimal transport

We propose, in this section, to experiment domain adaptation using DeepJDOT (Damodaran et al., 2018). This domain adaptation approach is designed to be effective with imbalanced data. Indeed, DeepJDOT considers the transport between the source and the target sets both in terms of data distribution and class distribution. In Table 5.14, we compare our previous domain adaptation approach based on Ganin et al. (2016) (GDA) and DeepJDOT (Damodaran et al., 2018) (JDA) on a mono-source domain adaptation setting on Bluecime dataset. In the balanced setting, using DeepJDOT gives better results than using Ganin methods, in both similar and dissimilar class distribution settings (respectively +0.94 and +0.51 of Accuracy). This suggests that DeepJDOT allows learning better features than the method from Ganin et al. that we use in this thesis (DANN). This improvement could be a benefit of considering the class distribution in DeepJDOT making features less sensitive to the discrepancy between the training and testing sets class distributions. Moreover, unlike DANN, when the source and target sets are imbalanced, we obtain with DeepJDOT good performance with both similar and dissimilar class distributions between source and target sets. These results show the effectiveness of their approach in mono-source domain adaptation with varying imbalance.

Expe.	**$\approx$ class dist.**	**$\neq$ class dist.**
OVO bs	86.84	86.84
OVO GDA bs bt	91.77 (+4.93)	90.77 (+3.93)
OVO JDA bs bt	92.71 (+5.87)	91.28 (+4.44)
OVO ibs	79.20 (−7.64)	71.14 (−15.69)
OVO GDA ibs ibt	93.20 (+6.36)	85.07 (−1.76)
OVO JDA ibs ibt	94.18 (+7.34)	91.37 (+4.53)

Table 5.14 – One versus one (OVO) Accuracy averaged over domains with similar class distributions and over domains with highly dissimilar class distributions (more results in Tables B.4, B.5, and B.6). (i)bt and (i)bs indicate experiments with (im)balanced target and source sets. GDA indicates experiments with DANN, JDA the experiments using DeepJDOT (Damodaran et al., 2018), with the hyperparameters $\alpha = 0.001$ and $\lambda_t = 0.0001$ as proposed in the paper.

In Table 5.15, we show results using DeepJDOT and DANN approaches in the multi-source domain adaptation problem. In this setting, DeepJDOT gives much worse results −1.73 pts of Accuracy and −13.28 pts of F-measure comparing to DANN. DeepJDOT requires to split the minibatches equally between source and target. Considering that, in the multi-source setting, all the sources are mixed, we tried to increase the size of each minibatch to 80 (the

highest number reachable with one GPU) to sample more examples from each source. In this configuration, we have a slight improvement but still have bad results. To produce these results we simply used all the sources as one, the results in Table 5.15 may suggest that to use DeepJDOT in a multi-source setting, we need to modify our approach.

In the table 5.16, we explore the use of another set of parameters taken from the authors code[1] ("hpc" row). The new set of parameters gives more weight to the term controlling the transport over the class distribution than to the term over the data distribution. In this setting, we get even worse results as the setting using the paper parameter ("hpp" row). This result shows how much the parameters value is important for this method, and so, should be carefully tuned. For time reasons, we only explore another setting and the effects of balancing the training sets. In the initial DeepJDOT problem, only one source is used, so, using several sources may be harmful with the transport component, especially with the reduced size of source examples (recall that in DeepJDOT, an optimal transport problem is optimized on each minibatch). To cope with this problem, we propose another setting where we sample the source examples from only one source per minibatch ("oos" row). Again, we observe a drop of performance. Considering our conclusions of Section 5.1.2, this performance in "oos" setting may be the consequence of the introduction of minibatches entirely composed of examples coming from highly distant domains impairing the training phase.

We present in Table 5.17 the results with DeepJDOT and when changing the class distribution of the training set. We can see that using a balanced set of source examples impairs the performance with a loss of 20 pts of Accuracy compared to the setting using an imbalanced source set. This bad performance could be caused by a bad choice of hyperparameters as we give a high weight on the class distribution term while both the source and the target sets are balanced.

Expe.	**Accuracy**	**Recall**	**Precision**	**F-measure**
LOCO ibs	96.72	81.01	82.33	77.12
LOCO GDA ibs ibt	95.89 (−0.83)	80.40 (−0.60)	73.36 (−8.97)	71.51 (−5.62)
LOCO JDA ibs ibt	94.16 (−2.56)	60.57 (−20.44)	72.07 (−10.27)	58.32 (−18.80)
LOCO JDA ibs ibt b80	94.29 (−2.43)	63.39 (−17.61)	72.52 (−9.81)	59.60 (−17.52)

Table 5.15 – LOCO results with DANN and DeepJDOT domain adaptation. (i)bt and (i)bs indicate experiments with (im)balanced target and source sets. GDA indicates experiments with DANN, JDA the experiments using DeepJDOT (Damodaran et al., 2018), with the hyperparameters $\alpha = 0.001$ and $\lambda_t = 0.0001$ as proposed in the paper. "b80" indicates that the batch size has been increased from 64 to 80 examples.

[1] https://github.com/bbdamodaran/deepJDOT

Expe.	Accuracy	Recall	Precision	F-measure
LOCO	96.72	81.01	82.33	77.12
LOCO DA	95.89 (−0.83)	80.40 (−0.60)	73.36 (−8.97)	71.51 (−5.62)
LOCO DA hpc	91.29 (−5.43)	42.54 (−38.47)	48.87 (−33.46)	41.78 (−35.34)
LOCO DA oos hpc	88.54 (−8.18)	31.42 (−49.58)	40.38 (−41.95)	29.46 (−47.66)
LOCO DA hpp	94.16 (−2.56)	60.57 (−20.44)	72.07 (−10.27)	58.32 (−18.80)

Table 5.16 – LOCO results with DeepJDOT domain adaptation. Both target and source sets are imbalanced. "hpp" indicates the use of the DeepJDOT hyperparameters proposed in (Damodaran et al., 2018) ($\alpha = 0.001$ and $\lambda_t = 0.0001$). "hpc" corresponds to another set of parameters used by default in the authors' code ($\alpha = 0.01$ and $\lambda_t = 1$). "oos" means that the sources examples in each minibatch are sampled from only one randomly chosen source.

Expe.	Accuracy	Recall	Precision	F-measure
LOCO bs	96.52	81.90	81.58	76.73
LOCO DA bs bt	68.08 (−28.44)	56.45 (−25.46)	15.59 (−65.99)	21.90 (−54.83)
LOCO DA bs ibt	67.04 (−29.47)	48.98 (−32.92)	11.39 (−70.19)	16.99 (−59.74)
LOCO ibs	96.72 (+0.20)	81.01 (−0.90)	82.33 (+0.75)	77.12 (+0.39)
LOCO DA ibs ibt	88.54 (−7.98)	31.42 (−50.48)	40.38 (−41.21)	29.46 (−47.27)

Table 5.17 – LOCO results with DeepJDOT domain adaptation, with hyperparameters from the authors' code ($\alpha = 0.01$ and $\lambda_t = 1$), and only one source represented in each minibatch. (i)bt and (i)bs indicate experiments with (im)balanced target and source sets.

5.3 Conclusion

We have shown that unsupervised domain adaptation can be improved by selecting and weighting a relevant subset of the sources that are the most similar to the target domain. Our approach weights the sources according to the Wasserstein distance between unlabeled domain distributions and according to the variety of the data in the selected sources. Extensive experiments show the relevance of our proposed weighting scheme.

Then, we showed that domain adaptation techniques are impaired and can become harmful when the class distribution is different between the sources and the target domains. This result is often overlooked in the literature since the classical domain adaptation experiments are mainly tackling the mono-source setting with balanced datasets. However, real life applications, such as the Bluecime problem, are not so convenient.

We proposed a method to improve domain adaptation by approximating the target balance with pseudo-labels. We also explore a domain adaptation method (DeepJDOT) which takes into account the class distribution during the adaptation. Both methods still have room for improvement. Indeed, we could refine the pseudo-labels either by adding retraining phases or using another estimation method. Adapting DeepJDOT technique in the multi-source setting is still an open problem. In addition to these improvements, we could explore other techniques

to better tackle domain adaptation with varying class balance. For instance, we could use the SAN approach (Cao et al., 2018) where each class has a dedicated domain discriminator. This approach considering each class independently may improve our performance even with different imbalance ratio.

Conclusion and perspectives

In this thesis, we studied techniques to tackle Bluecime's chairlift safety problem and the different challenges it implies:

1. large variety of chairlifts and weather conditions;
2. lack of labeled data (particularly on newly installed chairlifts);
3. imbalance in the data;
4. real-time decisions.

These challenges are not independent. For instance, we showed in this document that domain adaptation techniques, used to solve the first two challenges, are impaired by the third one. However, we managed to develop effective techniques (mainly based on deep learning) to tackle Bluecime's problem. Deep learning techniques are currently being implemented in SIVAO for passengers counting or bubble detection (the glass bubble on Chair. D in Fig. 2.2) and provide great performance.

Contributions

The first contribution presented in this thesis is a complete knowledge discovery pipeline (task definition, data preprocessing, model, and evaluation framework) for Bluecime dataset. We proposed to explore fully supervised settings (OOC and ALL), but also a setting simulating a newly installed chairlift with no label available (LOCO). Our baseline model is based on a state-of-the-art deep learning architecture (ResNet) allowing to tackle the first challenge in reasonable time, thus also tackling the fourth challenge. We also propose to add a domain adaptation component to address the second challenge.

The subsequent contributions tackle the different challenges more specifically. Our second contribution consists in improving the robustness of our approach (first two challenges) using a patching method. This method consists in creating new images by hiding small areas in the original input image which are critically important for the network classification process. Thus, we aim at forcing the network to use the whole image and maximize the amount of information used by the network. This approach can be considered either as data augmentation or a way to regularize the learning process (as with "dropout").

Our third and fourth contributions are both considering cost-sensitive learning to optimize the F-measure. This measure helps us focusing on the errors made by our classifier on the minority class (here, the unsafe cases). Optimizing it instead of the usual accuracy addresses

our class imbalance challenge. Both methods showed good results that can be generalized to other applications. These methods allowed us to trade-off the precision and recall of our system which is interesting for Bluecime since the number of false positives and false negatives cases depends, among other factors, on the chairlift and the distance between the boarding station and the SIVAO camera.

The fifth contribution of this thesis is a method to improve the multi-source domain adaptation problem by selecting the most relevant sources in the training set. With this contribution, we analyze how domain adaptation behaves in this multi-source setting but also when the class distributions vary between the source and target examples. Here we question the general knowledge about domain adaptation and propose a few successful solutions for this particular setting that are also useful to Bluecime.

Perspectives

Many opportunities to improve our different contributions are still to be explored. Our baseline approach could be improved with a more systematic comparison of the different architectures in the literature. Indeed, many existing architectures were not considered, mainly for time reasons, but also because new deep learning models are constantly developed (and improved), making it difficult to keep up with the state-of-the-art.

On our patching approach, we could further explore the use of the previous positions of the selected patches. In particular, we could increase differently the probability of a patch location to come back, and decrease it on locations inducing uninteresting patches.

On **CONE**, our algorithm for F-measure optimization, we could find a way to better adapt it to deep learning. For instance, we could use the first model weights as pre-training for the next trained model reducing the training time required to obtain enough classifiers to explore the (t, F) space.

On the selection of the source domains, we could use other distances or improve the ones we proposed. For instance, the autoencoder-based distance obviously depends on the autoencoders training, thus, modifying its architecture or tuning differently the hyperparameter (e.g. the learning rate) may highly improve this method. We could also modify our variety term, for instance by integrating a constraint on a minimum number of selected sources. Indeed, if a domain is very well represented and "close" to the target domain, it may be the only one selected, thus, inducing a training set with low variety.

We could also explore, theoretically, the negative results of domain adaptation with imbalance class distributions between the target and source examples. On the practical side, we could improve our pseudo-labels method or find a better way to use DeepJDOT in a multi-source setting.

Moreover, all these methods have been designed independently to tackle the original problem proposed by Bluecime. We have not studied if these methods are complementary, redundant or maybe adversary to tackle our end goal. We could use them all and hope for the best or try to find the best combination. For instance, we could guide the patching methode considering the F-measure and not only the prediction loss. We could also try to improve our

domain selection strategy using, for instance, the constrained optimal transport from Courty et al. (2014), when computing the Wasserstein distance to better take into consideration the class distributions.

Last but not least, in Bluecime's context, we could conduct work on improving the network efficiency. This could be done, for instance, by *pruning* the useless weights in the network, or *quantizing* the weights (Han et al., 2015). We could also explore ways to improve the performance of smaller architectures, for instance, with *knowledge distillation* (Hinton et al., 2015). Having a more effective network has two advantages: the most obvious one is to increase the inference speed, allowing us to have a real-time approach. The second advantage is to decrease the computation and memory load required by our deep learning approach. This would allow Bluecime to provide other services, such as real-time statistics on the chairlift occupation, without requiring to upgrade the system hardware.

List of publications

Publications in international conferences

Kevin Bascol, Rémi Emonet, Elisa Fromont, and Raluca Debusschere. Improving chairlift security with deep learning. In *International Symposium on Intelligent Data Analysis (IDA 2017)*, 2017

Kevin Bascol, Rémi Emonet, Elisa Fromont, Amaury Habrard, Guillaume Metzler, and Marc Sebban. From cost-sensitive classification to tight f-measure bounds. In *Proceedings of the Twenty-Second International Conference on Artificial Intelligence and Statistics (AISTATS-19)*, volume 89 of *Proceedings of Machine Learning Research*. PMLR, 2019b

Kevin Bascol, Rémi Emonet, and Elisa Fromont. Improving domain adaptation by source selection. In *2019 IEEE International Conference on Image Processing (ICIP)*, 2019a

The following paper was published during the PhD, but was the result of a second year Master internship. Thus it is unrelated to the main topic of the thesis.

Kevin Bascol, Rémi Emonet, Elisa Fromont, and Jean-Marc Odobez. Unsupervised interpretable pattern discovery in time series using autoencoders. In *The joint IAPR International Workshops on Structural and Syntactic Pattern Recognition (SSPR 2016)*, 2016

Communications in national conferences

Kevin Bascol, Rémi Emonet, Elisa Fromont, Amaury Habrard, Guillaume Metzler, and Marc Sebban. Un algorithme d'optimisation de la f-mesure par pondération des erreurs de classification. In *Conférence francophone sur l'Apprentissage Automatique (CAp-18)*, 2018

Appendix A

Pattern discovery in time series using autoencoders

A.1 Introduction

Unsupervised discovery of patterns in temporal data is an important data mining topic due to numerous application domains like finance, biology or video analysis. In some applications, the patterns are solely used as features for classification and thus the classification accuracy is the only criterion. This chapter considers different applications where the patterns can also be used for data analysis, data understanding, and novelty or anomaly detection Emonet et al. (2011, 2014); Du et al. (2009); Sallaberry et al. (2011).

Not all time series are of the same nature. In this work, we consider the difficult case of multivariate time series whose observations are the result of a combination of different recurring phenomena that can overlap. Examples include traffic videos where the activity of multiple cars causes the observed sequence of images Emonet et al. (2014), or aggregate power consumption where the observed consumption is due to a mixture of appliances Kolter and Jaakkola (2012). Unlike many techniques from the data mining community, our aim is not to list *all* recurrent patterns in the data with their frequency but to reconstruct the entire temporal documents by means of a *limited and unknown* number of recurring patterns together with their occurrence times in the data. In this view, we want to un-mix multivariate time series to recover how they can be decomposed in terms of recurrent temporally-structured patterns. Following the conventions used in Emonet et al. (2014), we will call a temporal pattern a *motif*, and an input multivariate time series a *temporal document*.

Artificial neural networks (or deep learning architectures) have (re)become tremendously popular in the last decade due to their impressive, and so far not beaten, results in image classification, speech recognition and natural language processing. In particular, autoencoders are artificial neural networks used to learn a compressed, distributed representation (encoding) for a set of data, typically for the purpose of dimensionality reduction. It is thus an unsupervised learning method whose (hidden) layers contain representations of the input data sufficiently powerful for compressing (and decompressing) the data while loosing as little information as

possible. Given the temporal nature of our data, our pattern discovery task is fundamentally convolutional (the same network is applied at any instant and is thus time-shift invariant) since it needs to identify motifs whatever their time(s) of occurrence. To tackle this task, we will thus focus on a particular type of autoencoders, the convolutional ones. However, while well adapted for discriminative tasks like classification Baccouche et al. (2012), the patterns captured by (convolutional) autoencoders are not fully interpretable and often correlated.

In this appendix, we address the discovery of interpretable motifs using convolutional auto-encoders and make the following contributions:

- we show that the interpretability of standard convolutional autoencoders is limited;
- we introduce an adaptive rectified linear unit (AdaReLU) which allows hidden layers to capture clear occurrences of motifs,
- we propose a regularization inspired by group-lasso to automatically select the number of filters in a convolutional neural net,
- we show, through experiments on synthetic and real data, how these elements (and others) allow recovering interpretable motifs[1].

It is important to note that some previous *generative models* Varadarajan et al. (2013); Emonet et al. (2014) have obtained very good results on this task. However, their extensions to semi-supervised settings (i.e. with partially labeled data) or hierarchical schemes are cumbersome to achieve. In contrast, in this chapter, to solve the same modeling problem we present a radically different method which will lend itself to more flexible and systematic end-to-end training frameworks and extensions.

The chapter is organized as follows. In Section A.2, we clarify the link between our data mining technique and previous work. Section A.3 gives the details of our method while Section A.4 shows experiments both on synthetic and real data. We conclude and draw future directions in Section A.5.

A.2 Related work

Our work shows how to use a popular method (autoencoders) to tackle a task (pattern discovery in time series) that has seldom been considered for this type of methods. We thus briefly review other methods used in this context and then, other works that use neural networks for unsupervised time series modeling.

A.2.1 Unsupervised pattern discovery in time series.

Traditional unsupervised approaches that deal with time series do not aim at modeling series but rather at extracting interesting pieces of the series that can be used as high level descriptions for direct analysis or as input features for other algorithms. In this category fall all the event-based (e.g. Y.-C. Chen and Lee (2015); W.-S. Chu and la Torre (2012); H. Shao and Ramakrishnan (2013)), sequence Mooney and Roddick (2013) and trajectory mining methods

[1]The complete source code will be made available online

Zheng (2015). On the contrary of the previously cited methods, we do not know in advance the occurrence time, type, length or number of (possibly) overlapping patterns that can be used to describe the entire multivariate time series. These methods cannot be directly used in our application context.

The *generative methods* for modeling time series assume an a priori model and estimate its parameters. In the precursor work of Oates (2002), the unsupervised problem of finding patterns was decomposed into two steps, a supervised step involving an oracle which identifies patterns and series containing such patterns and an EM-step where a model of the series is generated according to those patterns. In Mehta and Gray (2009), the authors propose a functional independent component analysis method for finding linearly varying patterns of activation in the data. They assume the availability of pre-segmented data where the occurrence time of each possible pattern is known in advance. Authors of Kolter and Jaakkola (2012) address the discovery of overlapping patterns to disaggregate the energy level of electric consumption. They propose to use additive factorial hidden Markov models, assuming that the electrical signal is univariate and that the known devices (each one represented by one HMM) have a finite known number of states. This also imposes that the motif occurrences of one particular device can not overlap. The work of Emonet et al. (2014) proposes to extract an a priori unknown number of patterns and their possibly overlapping occurrences in documents using Dirichlet processes. The model automatically finds the number of patterns, their length and occurrence times by fitting infinite mixtures of categorical distributions to the data. This approach achieved very good results, but its extensions to semi-supervised settings Tavenard et al. (2013) or hierarchical schemes Chockalingam et al. (2013) were either not so effective Tavenard et al. (2013) or more cumbersome Chockalingam et al. (2013). In contrast, the neural network approach in this work will lend itself to more flexible and systematic end-to-end training frameworks and extensions.

A.2.2 Networks for time series mining.

A recent survey M. Längkvist and Loutfi (2014) reviews the network-based unsupervised feature learning methods for time series modeling. As explained in Sec. A.1, autoencoders Ranzato et al. (2006) and also Restricted Boltzmann Machines (RBM) Hinton and Salakhutdinov (2006) are neural networks designed to be trained from unsupervised data. The two types of networks can achieve similar goals but differ in the objective function and related optimization algorithms. Both methods were extended to handle time series Memisevic and Hinton (2007); Baccouche et al. (2012), but the goal was to minimize a reconstruction error without taking care of the interpretability or of finding the relevant number of patterns. In this chapter, we show that convolutional autoencoders can indeed capture the spatio-temporal structure in temporal documents. We build on the above works and propose a model to discover the right number of meaningful patterns in the convolution filters, and to generate sparse activations.

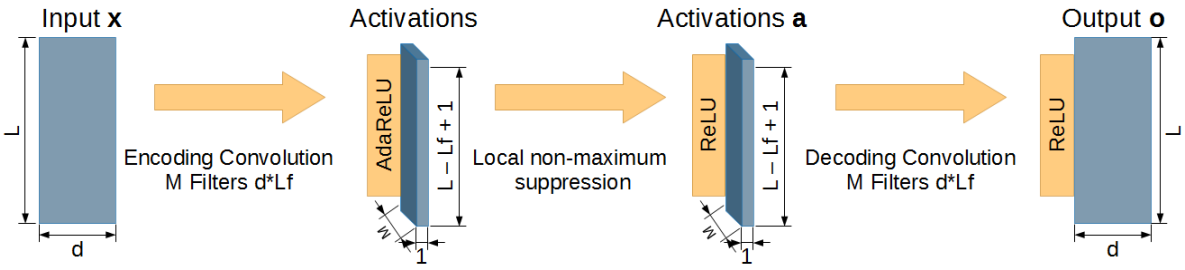

Figure A.1 – Autoencoder architecture. Temporal documents of L time steps of d dimensional observations are encoded (here using M convolutional filters of size $d \times L_f$ forming the ${}^{\mathbf{e}}\mathbf{W}$ weights) to produce an activation layer. A decoding process (symmetric to encoding; parameterized by the weights ${}^{\mathbf{d}}\mathbf{W}$ of M decoding convolutional filters of size $d \times L_f$) regenerates the data.

A.3 Motif mining with convolutional autoencoders (AE)

Convolutional AEs Masci et al. (2011) are particular AEs whose connection weights are constrained to be convolution kernels. In practice, this means that most of the learned parameters are shared within the network and that the weight matrices which store the convolution filters can be directly interpreted and visualized. Below, we first present the traditional AE model and then introduce our contributions to enforce at the same time a good interpretability of the convolutional filters and a clean and sparse activation of these filters.

A.3.1 Classical convolutional autoencoders

A main difference between an AE and a standard neural network is the loss function used to train the network. In an AE, the loss does not depend on labels, it is the reconstruction error between the input data and the network output. Fig. A.1 illustrates the main network modeling components of our model. In our case, a training example is a multivariate time series $\mathbf{x}$ whose L time steps are described by a vector $\mathbf{x}_{(:,t)} \in \mathbb{R}^d$, and the network is parameterized by the set of weights $\mathbf{W} = ({}^{\mathbf{e}}\mathbf{W}, {}^{\mathbf{d}}\mathbf{W})$ involved in the coding and decoding processes. If we denote by $\mathbf{X} = (\mathbf{x}^b \in \mathbb{R}^{L \times d},\ b = 1 \dots N)$ the set of all training elements, the estimation of these weights is classically conducted by optimizing the cost function $C(\mathbf{W}, \mathbf{X}) = MSE(\mathbf{W}, \mathbf{X}) + R_{reg}(\mathbf{W}, \mathbf{X})$ where the Mean Squared Error (MSE) reconstruction loss can be written as:

$$MSE(\mathbf{W}, \mathbf{X}) = \frac{1}{N} \sum_{b=1}^{N} \sum_{i=1}^{d} \sum_{t=1}^{L} \left(\mathbf{x}^b_{(i,t)} - \mathbf{o}^b_{(i,t)} \right)^2 \tag{A.1}$$

where $\mathbf{o}^b$ (which depends on parameters $\mathbf{W}$) is the AE output of the b^{th} input document. To avoid learning trivial and unstable mappings, a regularization term R_{reg} is often added to the MSE and usually comprises two terms. The first one, known as weight decay as it avoids unnecessary high weight values, is a ℓ_2 norm on the matrix weights. The second one (used with binary activations) consists of a Kullback-Leibler divergence $\sum_{j=1}^{M} KL(\rho || \hat{\rho}_j)$ encouraging *all* hidden activation units to have their probability of activation $\hat{\rho}_j$ estimated across samples to be close to a chosen parameter ρ, thus enforcing some activation sparsity when ρ is small.

The parameters are typically learned using a stochastic gradient descent algorithm (SGD) with momentum using an appropriate rate scheduling Darken and Moody (1990).

A.3.2 Interpretable pattern discovery with autoencoders

In our application, the learned convolution filters should not only minimize the reconstruction error but also be directly interpretable. Ideally, we would like to only extract filters which capture and represent interesting data patterns, as illustrated in Fig. A.2-c-d. To achieve this, we add a number of elements in the network architecture and in our optimization cost function to constrain our network appropriately.

A.3.2.1 Enforcing non-negative decoding filters.

As the AE output is somehow defined as a linear combination of the *decoding* filters, then these filters can represent the patterns we are looking for, and we can interpret the hidden layers activations $\mathbf{a}$ (see Fig. A.1) as the occurrences of these patterns. Thus, as our input is non-negative (a temporal document), we constraint the decoding filters weights to be non-negative by thresholding them at every SGD iteration. The assumption that the input is non-negative holds in our case and it will also hold in deeper AEs provided that we use ReLU-like activation functions. Note that for encoding, we do not constrain filters, so they can have negative values to compensate for the pattern auto-correlation (see below).

A.3.2.2 Sparsifying the filters.

The traditional ℓ_2 regularization allows many small but non-zero values. To force these values to zero and thus get sparser filters, we replaced the ℓ_2 norm by the sparsity-promoting norm ℓ_1 known as lasso:

$$R_{las}(\mathbf{W}) = \sum_{f=1}^{M}\sum_{i=1}^{d}\sum_{k=1}^{L_f}\left|{}^{\mathbf{e}}\mathbf{W}^{f}_{(i,k)}\right| + \sum_{f=1}^{M}\sum_{i=1}^{d}\sum_{k=1}^{L_f}\left|{}^{\mathbf{d}}\mathbf{W}^{f}_{(i,k)}\right| \tag{A.2}$$

A.3.2.3 Encouraging sparse activations.

The traditional KL divergence aims at making *all* hidden units equally useful *on average*, whereas our goal is to have the activation layer to be as sparse as possible for each given input document. We achieve this by encouraging peaky activations, i.e. of low entropy when seen as a document-level probability distribution, as was proposed in Varadarajan et al. (2010) when dealing on topic models for motif discovery. This results in an entropy-based regularization expressed on the set $\mathbf{A} = \{\mathbf{a}^b\}$ of document-level activations:

$$R_{ent}(\mathbf{A}) = -\frac{1}{N}\sum_{b=1}^{N}\left(\sum_{f=1}^{M}\sum_{t=1}^{L-L_f+1}\hat{\mathbf{a}}^b_{f,t}\log\left(\hat{\mathbf{a}}^b_{f,t}\right)\right) \text{ with } \hat{\mathbf{a}}^b_{f,t} = \mathbf{a}^b_{f,t}\Big/\sum_{f=1}^{M}\sum_{t=1}^{L-L_f+1}\mathbf{a}^b_{f,t} \tag{A.3}$$

A.3.2.4 Local non-maximum activation removal.

The previous entropy regularizer encourages peaked activations. However, as the encoding layer remains a convolutional layer, if a filter is correlated in time with itself or another filter, then the activations cannot be sparse. This phenomenon is due to the feed forward nature of the network, where activations depend on the input, not on each others: hence, no activation can inhibit its neighboring activations. To handle this issue we add a local non-maximum suppression layer which, from a network perspective, is obtained by convolving activations with a temporal Gaussian filter, subtracting from the result the activation intensities, and applying a ReLU, focusing in this way spread activations into central peaks.

A.3.2.5 Handling distant filter correlations with AdaReLU.

The Gaussian layer cannot handle non-local (in time) correlations. To handle this, we propose to replace the traditional ReLU activation function by a novel one called adaptive ReLU. AdaReLU works on groups of units and sets to 0 all the values that are below a percentage (e.g., 60%) of the maximal value in the group. In our architecture, AdaReLU is applied separately on each filter activation sequence.

A.3.2.6 Finding the true number of patterns.

One main advantage and contribution of our AE-based method compared to methods presented in Section A.2 is the possibility to discover the "true" number of patterns in the data. One solution to achieve this is to introduce in the network a large set of filters and "hope" that the learning leads to only a few non null filters capturing the interesting patterns. However, in practice, standard regularization terms and optimizations tend to produce networks "using" all or many more filters than the number of true patterns which results in partial and less interpretable patterns. To overcome this problem, we propose to use a group lasso regularization term called $\ell_{2,1}$ norm Yuan and Lin (2006) that constrains the network to "use" as few filters as possible. It can be formulated for our weight matrix as:

$$R_{grp}(\mathbf{W}) = \sum_{f=1}^{M} \sqrt{\sum_{i=1}^{d} \sum_{k=1}^{L_f} \left({}^{\mathbf{e}}\mathbf{W}^{f}_{(i,k)} \right)^2} + \sum_{f=1}^{M} \sqrt{\sum_{i=1}^{d} \sum_{k=1}^{L_f} \left({}^{\mathbf{d}}\mathbf{W}^{f}_{(i,k)} \right)^2} \tag{A.4}$$

A.3.2.7 Overall objective function.

Combining equations (A.1), (A.2), (A.4) and (A.3), we obtain the objective function that is optimized by our network:

$$C(\mathbf{W}, \mathbf{X}) = MSE(\mathbf{W}, \mathbf{X}) + \lambda_{las} R_{las}(\mathbf{W}) + \lambda_{grp} R_{grp}(\mathbf{W}) + \lambda_{ent} R_{ent}(\mathbf{A}(\mathbf{W}, \mathbf{X})) \tag{A.5}$$

A.4 Experiments

A.4.1 Experimental setting

A.4.1.1 Datasets.

To study the behavior of our approach, we experimented with both synthetic and real video datasets. The synthetic data were obtained using a known generation process: temporal documents were produced by sampling random observations of random linear combinations of motifs along with salt-and-pepper noise whose amount was defined as a percentage of the total document intensities (noise levels: 0%, 33%, 66%). Six motifs (defined as letter sequences for ease of visualization) were used. A document example is shown in Fig. A.2-a, where the feature dimension ($d = 25$) is represented vertically, and time horizontally ($L = 300$). For each experiment, 100 documents were generated using this process and used to train the autoencoders. This controlled environment allowed us to evaluate the importance of modeling elements. In particular, we are interested in i) the number of patterns discovered (defined as the non-empty decoding filters[2]; ii) the "sharpness" of the activations; and iii) the robustness of our method according to parameters like $\lambda_{lasso}, \lambda_{grp}, \lambda_{ent}$, the number of filters M, and the noise level.

We also applied our approach on videos recorded from fixed cameras. We used videos from the QMUL Hospedales et al. (2009) and the far-field datasets Varadarajan et al. (2013). The data pre-processing steps from the companion code of Emonet et al. (2014) were applied. Optical flow features were obtained by estimating, quantifying, and locally collecting optical flow over 1 second periods. Then, temporal documents were obtained by reducing the dimensionality of these to $d = 100$, and by cutting videos into temporal documents of size $L = 300$ time steps.

A.4.1.2 Architecture details and parameter setting.

The proposed architecture is given in Fig. A.1. As stated earlier, the goal of this chapter is to make the most of a convolutional AE with a *single* layer (corresponding to the activation layer)[3]. Weights are initialized according to a uniform distribution between 0 and $\frac{1}{d*L_f}$.

In general, the filter length L_f should be large enough to capture the longest expected recurring pattern of interest in the data. The filter length has been set to $L_f = 45$ in synthetic experiments, which is beyond the longer motif of the ground-truth. In the video examples, we used $L_f = 11$, corresponding to 10 seconds, and which allows to capture the different traffic activities and phases of our data Varadarajan et al. (2013).

A.4.2 Results on the synthetic dataset

Since we know the "true" number of patterns and their expected visualization, we first validate our approach by showing (see Fig. A.2-c) that we can find a set of parameters such that our filters exactly capture our given motifs and the number of non-empty filters is exactly the

[2]We consider a filter *empty* if the sum of its weights is lower or equal to $\frac{1}{2}$ (the average sum value after initialization).

[3]Note however that the method can be generalized to hierarchical motifs using more layers, but then the interpretation of results would slightly differ.

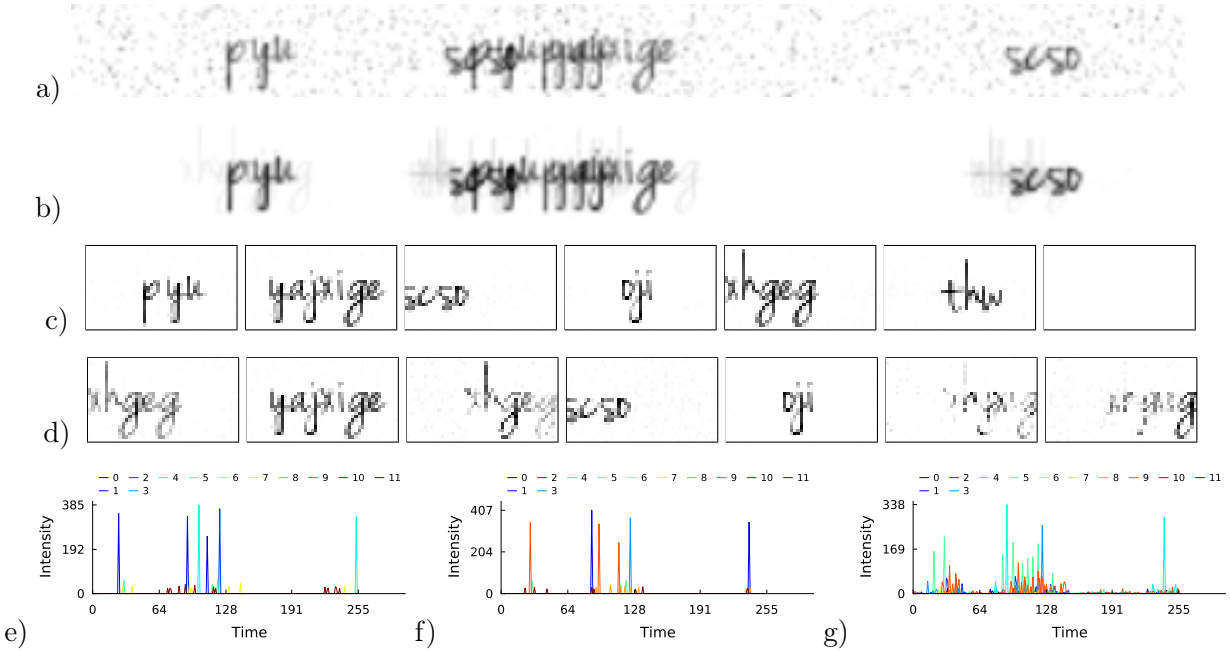

Figure A.2 – Results on the synthetic data built from 6 patterns, with 66% of noise, $M = 12$ filters, and unless stated otherwise $\lambda_{las} = 0.004$, $\lambda_{grp} = 2$, $\lambda_{ent} = 0.2$. a) Sample document; b) Obtained output reconstructed document; c) Weights of seven out of the 12 obtained filters (the 5 remaining filters are empty); d) Weights of seven filters when not using group lasso, i.e. with $\lambda_{grp} = 0$ (note that the 5 remaining filters are non empty); (e,f,g) Examples of activation intensities (colors correspond to a given filter) with default parameters (e); without the entropy sparsifying term ($\lambda_{ent} = 0$) (f); with ReLU instead of AdaReLU (g).

"true" number of motifs in the dataset even when this dataset is noisy (this is also true for a clean dataset). In this case (see Fig.A.2-e) the activations for the complete document are, as expected, sparse and "peaky". The output document (see Fig.A.2-b) is a good un-noisy reconstruction of the input document shown in Fig.A.2-a.

In Fig. A.3, we evaluate the influence of the given number of filters M and the noise level on both the number of recovered motifs and the MSE while fixing the parameters as in Fig. A.2. We can see that with this set of parameters, the AE is able to recover the true number of filters for the large majority of noise levels and values of M. For all noise levels, we see from the low MSE that the AEs is able to well reconstruct the original document as long as the number of given filters is at least equal to the number of "true" patterns in the document.

A.4.2.1 Model selection: influence of λ_{grp}.

Fig.A.4 shows the number of non-zero filters in function of λ_{grp} and of the noise level for the synthetic dataset with 6 known motifs when using 12 filters (left) and 16 filters (right). The light blue area is the area in which the AEs was able to discover the true number of patterns. With no group lasso regularization ($\lambda_{grp} = 0$), the AE systematically uses all the available

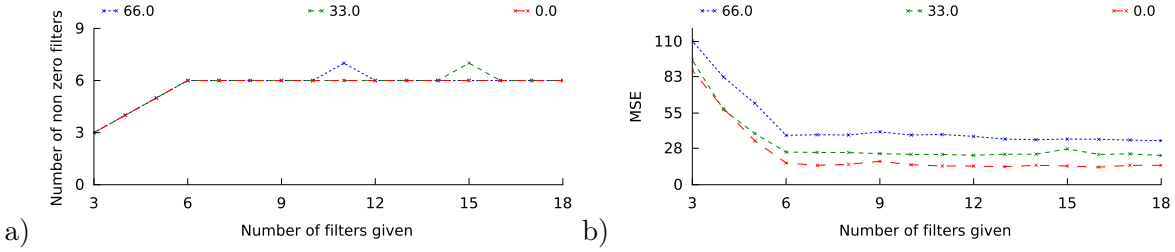

Figure A.3 – Influence of the given number of filters M and the noise level (0%, 33% and 66%) on: a) the number of recovered motifs and b) the Mean Squared Error. Experiments on the synthetic dataset with $\lambda_{las} = 0.004$, $\lambda_{grp} = 2$, $\lambda_{ent} = 0.2$.

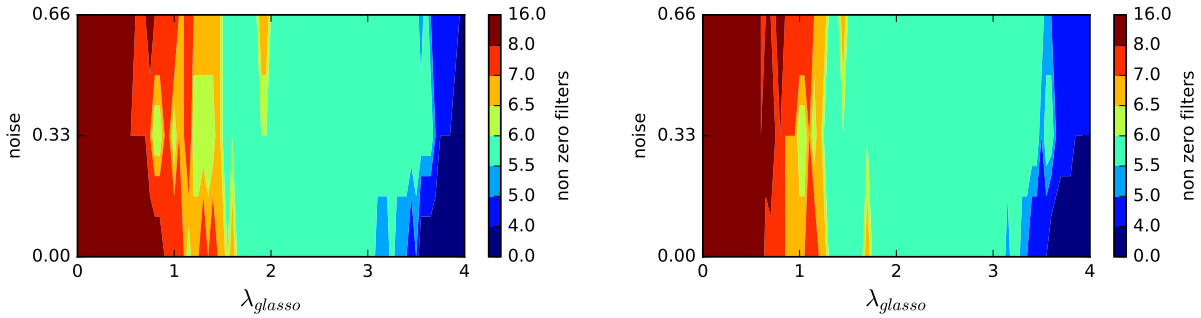

Figure A.4 – Evolution of the number of non-zero filters (sparsity) with respect to the noise level when we vary the parameter λ_{grp} (λ_{glasso} in the figure) that controls the group lasso regularization for the synthetic dataset with 6 known motifs when using 12 filters (right) and 16 filters (left).

filters capturing the original patterns (see $2^{nd}, 4^{th}$ or 5^{th} filters in Fig. A.2-d), redundant variants of the same pattern (filters 1^{st} and 3^{rd} in Fig. A.2-d) or a more difficult to interpret mix of the patterns (filters 6^{th} and 7^{th} in Fig. A.2-d). On the contrary, with too high values of λ_{grp}, the AE does not find any patterns (resulting in a high MSE). A good heuristic to set the value of λ_{grp} could thus be to increase it as much as possible until the resulting MSE starts increasing. In the rest of the experiments, λ_{grp} is set equal to 2.

A.4.2.2 Influence of λ_{ent}, λ_{lasso}, AdaReLU, and non-local maxima suppression.

We have conducted the same experiments as in Fig. A.2 on clean and noisy datasets (up to 66% of noise) with M =3, M =6 M =12 to assess the behavior of our system when canceling the parameters: 1) λ_{ent} that controls the entropy of the activation layer, 2) λ_{las}, the lasso regularizer 3) the AdaReLU function (we used a simple ReLU in the encoding layer instead) and 4) the Non-Local Maxima activation suppression layer. In all cases, all parameters but one were fixed according to the best set of values given in Fig.A.2.

The λ_{ent} is particularly important in the presence of noise. Without noise and when this parameter is set to 0, the patterns are less sharp and smooth and the activations are more spread along time with much smaller intensities. However, the MSE is as low as for the

default parameters. In the presence of noise (see Fig.A.2-f), the AE is more likely to miss the recovery of some patterns even when the optimal number of filters is given (e.g. in some experiments only 5 out of the 6 filters were not empty) and the MSE increases a lot compared to experiments on clean data. This shows again that the MSE can be a good heuristic to tune the parameters on real data. The λ_{las} has similar effects with and without noise: it helps to remove all the small activation values resulting in much sharper (and thus interpretable) patterns.

The non-local maximum suppression layer (comprising the *Gaussian* filter) is compulsory in our proposed architecture. Indeed, without it, the system was not able to recover any patterns when M =3 (and only one blurry "false" pattern in the presence of noise). When M =6, it only captured 4 patterns (out of 6) in the clean dataset and did not find any in the noisy ones. When M =12, it was able to recover the 6 original true patterns in the clean dataset but only one blurry "false" pattern in the noisy ones.

The AdaReLU function also plays an important role to recover interpretable patterns. Without it (using ReLU instead) the patterns recognized are not the "true" patterns, they have a very low intensity and are highly auto-correlated (as illustrated by the activations in Fig.A.2-g).

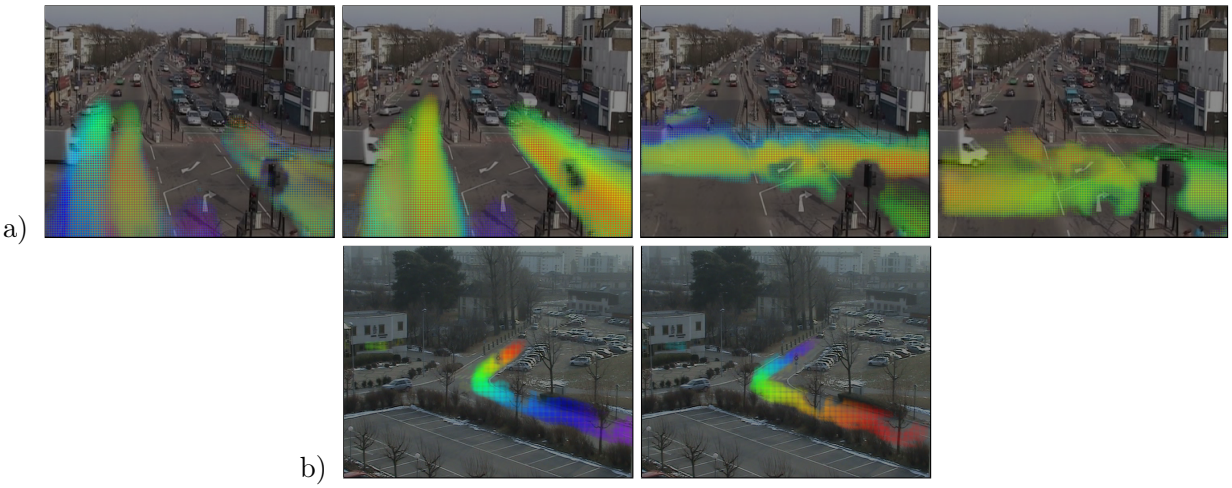

Figure A.5 – Traffic patterns. M =10 filters. a) The four motifs recovered on the Junction 1 dataset, (6 empty ones are not shown). b) Two filters (out of the five recovered) on the far-field dataset.

A.4.3 Results on the real video dataset

We show in Fig. A.5 some of the obtained results. The parameters were selected using grid search by minimizing the MSE on the targeted dataset. For instance, on the Junction 1 dataset, the final parameters used are $\lambda_{las} = 0.2$, $\lambda_{grp} = 50$, $\lambda_{ent} = 5$. Note that this is larger than in the synthetic case but the observation size is also much larger (100 vs 25) and the filters are thus sparser in general. In the Junction 1 dataset, the autoencoder recovers 4

non-empty and meaningful filters capturing the car activities related to the different traffic signal cycles, whereas in the far-field case, the main trajectories of cars were recovered as also reported in Varadarajan et al. (2013).

A.5 Conclusion

We have shown that convolutional AEs are good candidate unsupervised data mining tools to discover interpretable patterns in time series. We have introduced a number of layers and regularization terms to the standard convolutional AEs to enforce the interpretability of both the convolutional filters and the activations in the hidden layers of the network. The filters are directly interpretable as spatio-temporal patterns while the activations give the occurrence times of each pattern in the temporal document. This allows us to un-mix multivariate time series. A direct perspective of this work is the use of multi-layer AEs to capture combination of motifs. If this was not the aim of this work, it may help to reduce the number of parameters needed to obtain truly interpretable patterns and capture more complex patterns in data.

Appendix B

Additional results

B.1 Baseline results

In this section we show detailed baseline result (from Section 3.3) over each chairlift on Accuracy, Precision, and Recall.

Chairlift	SIVAO	OOC	ALL	ALL DA	LOCO	LOCO DA-	LOCO DA
Chair. A	95.70	96.20	96.20	**96.52**	94.93	95.14	95.77
Chair. B	99.14	98.49	99.03	**99.29**	98.60	98.71	99.03
Chair. C	**99.19**	96.95	98.07	98.07	97.26	97.46	97.56
Chair. D	99.60	99.21	**100.00**	99.80	99.60	99.87	99.74
Chair. E	**99.38**	98.03	98.27	98.25	76.74	77.11	94.26
Chair. F	99.58	**99.83**	99.75	99.75	98.82	99.41	99.66
Chair. G	95.44	99.24	99.81	99.91	**100.00**	99.62	99.62
Chair. H	**99.30**	98.50	98.80	98.75	97.41	97.21	98.00
Chair. I	98.93	98.50	**99.43**	99.10	97.71	98.14	98.42
Chair. J	97.72	97.78	97.91	**98.12**	95.81	95.75	97.91
Chair. K	99.30	99.53	**99.61**	99.30	98.84	99.15	99.38
Chair. L	97.90	98.43	98.25	**98.43**	95.63	95.89	96.99
Chair. M	97.99	95.98	97.39	97.89	**98.19**	97.59	97.79
Chair. N	99.42	99.42	99.42	**99.56**	99.42	99.42	89.83
Chair. O	**99.86**	97.67	98.77	98.42	98.08	98.08	97.53
Chair. P	**99.14**	98.29	98.76	98.52	97.51	97.98	97.43
Chair. Q	98.43	98.87	**99.30**	99.23	98.60	98.47	98.43
Chair. R	96.88	98.24	**98.56**	98.48	97.92	98.24	98.32
Chair. S	**98.80**	96.81	98.61	98.31	97.41	97.01	98.01
Chair. T	99.25	98.49	99.14	**99.46**	96.24	97.42	98.39
Chair. U	99.03	99.03	**99.19**	99.09	92.15	93.50	97.68
Avg.	98.54	98.35	**98.73**	98.72	95.63	95.94	97.70

Table B.1 – Accuracy on each chairlift.

Chairlift	SIVAO	OOC	ALL	ALL DA	LOCO	LOCO DA-	LOCO DA
Chair. A	89.40	92.93	91.48	**94.49**	91.68	92.93	90.02
Chair. B	91.30	84.06	92.75	**96.38**	89.86	89.86	95.65
Chair. C	**96.83**	63.49	77.78	71.43	61.90	63.49	71.43
Chair. D	**100.00**	14.29	100.00	92.85	100.00	100.00	100.00
Chair. E	94.78	82.09	89.55	90.30	**95.52**	95.52	87.31
Chair. F	96.55	93.10	93.10	89.66	93.10	**100.00**	96.55
Chair. G	**100.00**	75.00	100.00	100.00	100.00	93.75	93.75
Chair. H	**98.88**	89.89	87.64	87.08	71.91	68.54	80.90
Chair. I	**95.38**	83.08	92.31	86.92	55.38	64.62	81.54
Chair. J	**92.17**	74.78	86.96	85.66	90.43	80.87	86.09
Chair. K	93.75	**96.53**	96.53	95.14	95.83	96.53	95.83
Chair. L	**95.38**	90.00	91.54	90.39	68.46	67.31	77.69
Chair. M	87.50	80.36	89.29	90.18	87.50	89.29	**92.86**
Chair. N	50.00	0.00	0.00	25.00	0.00	0.00	**100.00**
Chair. O	**100.00**	81.25	92.50	90.00	86.25	86.25	85.00
Chair. P	**98.25**	85.09	91.23	88.16	78.95	80.70	78.07
Chair. Q	**96.83**	66.67	85.71	84.12	77.78	77.78	87.30
Chair. R	77.48	90.79	94.08	92.11	**97.37**	96.05	94.74
Chair. S	**96.36**	85.45	92.73	88.18	89.09	87.27	83.64
Chair. T	92.98	78.95	91.23	91.22	**94.74**	94.74	92.98
Chair. U	**95.04**	82.64	90.08	90.50	94.21	92.56	88.43
Avg.	**92.68**	85.96	90.93	90.54	85.73	85.54	87.06

Table B.2 – Recall on each chairlift.

Chairlift	SIVAO	OOC	ALL	ALL DA	LOCO	LOCO DA-	LOCO DA
Chair. A	**97.73**	95.72	97.13	95.19	93.23	92.74	97.30
Chair. B	**96.92**	95.08	94.12	94.33	91.18	92.54	91.67
Chair. C	91.04	85.11	90.74	**97.83**	92.86	95.24	88.24
Chair. D	70.00	**100.00**	100.00	87.50	70.00	87.50	77.78
Chair. E	**97.69**	93.22	89.55	88.65	25.65	25.96	60.62
Chair. F	87.50	**100.00**	96.43	100.00	69.23	80.56	90.32
Chair. G	40.00	**100.00**	94.12	97.06	100.00	93.75	93.75
Chair. H	93.62	93.02	98.73	98.72	98.46	**100.00**	96.00
Chair. I	83.78	84.38	**95.24**	93.38	92.31	93.33	84.13
Chair. J	79.10	**92.47**	84.03	87.56	64.60	66.43	84.62
Chair. K	**100.00**	99.29	100.00	98.56	93.88	95.86	98.57
Chair. L	87.32	**95.90**	92.97	95.53	90.82	95.11	94.84
Chair. M	94.23	83.33	87.72	90.99	**96.08**	89.29	88.14
Chair. N	50.00	**100.00**	100.00	100.00	100.00	100.00	5.41
Chair. O	**98.77**	97.01	96.10	95.41	95.83	95.83	91.89
Chair. P	92.56	95.10	94.55	94.81	91.84	**95.83**	91.75
Chair. Q	64.21	**89.36**	88.52	87.69	73.13	70.00	66.27
Chair. R	**95.90**	94.52	94.08	95.24	87.06	90.12	91.72
Chair. S	92.98	85.45	94.44	96.04	87.50	85.71	**97.87**
Chair. T	94.64	95.74	94.55	**100.00**	62.79	72.00	82.81
Chair. U	85.82	**96.15**	92.37	90.23	36.77	41.33	69.93
Avg.	90.43	94.20	94.00	**94.28**	69.87	72.10	86.11

Table B.3 – Precision on each chairlift.

B.2 Domain adaptation with imbalanced data

We show in this section the details of the results presented in Sections 5.2.1 and 5.2.2.2.

Target	**Chair. C**		**Chair. I**		**Chair. R**	
Src / **Setting**	**C. I**	**C. R**	**C. C**	**C. R**	**C. C**	**C. I**
OVO bs	89.74	94.43	95.20	91.31	86.59	76.50
OVO GDA bs bt	+3.05	+1.30	−17.82	−33.13	+8.78	+7.36
OVO JDA bs bt	+3.97	+2.53	+0.86	−12.01	+5.51	+14.79
OVO ubs	−19.31	−22.18	−0.86	−34.35	+1.60	−15.12
OVO GDA ubs ubt	+4.28	−3.47	−1.36	+2.81	−13.45	−2.82
OVO JDA ubs ubt	+4.28	−4.56	+0.14	+3.96	+1.28	+11.45

Table B.4 – One Versus One (OVO) results. (u)bt and (u)bs indicate experiments with (un)balanced Target and Source sets. GDA indicates experiments with the domain adaptation module presented in section 3.1, JDA the experiments using DeepJDOT (Damodaran et al., 2018), with the hyperparameters $\alpha = 0.001$ and $\lambda_t = 0.0001$ as proposed in the paper. Chair. C and Chair. I have similar classes distribution (resp. 82.9% and 85.5% *Empty*, 10.7% and 9.8% *Safe*, and 6.4% and 4.7% *Unsafe*). Chair. R presents a different classes distribution than the two other (41.2% *Empty*, 46.7% *Safe*, and 12.1% *Unsafe*)

Target	**Chair. K**		**Chair. O**		**Chair. B**	
Src / **Setting**	**C. O**	**C. B**	**C. K**	**C. B**	**C. K**	**C. O**
OVO bs	89.21	95.12	62.36	92.87	63.12	91.55
OVO GDA bs bt	+6.90	+1.38	+34.91	+3.86	+24.87	+3.68
OVO JDA bs bt	+0.75	+0.69	+31.49	+0.83	+26.77	−1.63
OVO ubs	−6.18	−1.63	−13.36	−2.57	−25.26	−28.17
OVO GDA ubs ubt	−1.91	−10.29	+33.52	−16.81	+7.44	−13.33
OVO JDA ubs ubt	+5.75	−5.59	+32.03	−3.70	+28.63	+2.40

Table B.5 – One Versus One (OVO) results. (u)bt and (u)bs indicate experiments with (un)balanced Target and Source sets. GDA indicates experiments with the domain adaptation module presented in section 3.1, JDA the experiments using DeepJDOT (Damodaran et al., 2018), with the hyperparameters $\alpha = 0.001$ and $\lambda_t = 0.0001$ as proposed in the paper. Chair. K and Chair. O have similar classes distribution (resp. 48.4% and 50.8% *Empty*, 40.5% and 38.2% *Safe*, and 11.2% and 11.0% *Unsafe*). Chair. B present a different classes distribution than the two other (12.8% *Empty*, 79.7% *Safe*, and 7.4% *Unsafe*)

Target	Chair. H			Chair. J			Chair. P		
Setting \ Src	C. J	C. P	C. B	C. H	C. P	C. B	C. H	C. J	C. B
OVO bs	92.14	93.52	92.72	84.87	80.45	78.85	94.96	86.01	85.83
OVO GDA bs bt	+2.17	+4.08	+4.88	+2.01	+3.14	+9.32	+0.92	+9.89	+10.91
OVO JDA bs bt	+0.76	+3.39	+1.98	+2.38	+7.06	+10.56	+0.77	+7.25	+8.50
OVO ubs noda	−4.50	+0.40	−18.30	−26.55	−8.17	−52.34	−1.33	+3.43	−17.87
OVO GDA ubs ubt	+4.27	+3.79	+3.01	+3.25	+7.84	+11.67	−0.63	+10.50	+9.74
OVO JDA ubs ubt	+1.49	+1.30	−1.19	+8.79	+13.09	+14.25	−2.42	+8.86	+5.31

Table B.6 – One Versus One (OVO) results. (u)bt and (u)bs indicate experiments with (un)balanced Target and Source sets. GDA indicates experiments with the domain adaptation module presented in section 3.1, JDA the experiments using DeepJDOT (Damodaran et al., 2018), with the hyperparameters $\alpha = 0.001$ and $\lambda_t = 0.0001$ as proposed in the paper. Chair. H, Chair. J, and Chair. P have similar classes distribution (resp. 59.1%, 62.3%, and 60.0% *Empty*, 32.0%, 30.7%, and 31.2% *Safe*, and 8.9%, 7.1%, and 8.9% *Unsafe*). Chair. B present a different classes distribution than the two other (12.8% *Empty*, 79.7% *Safe*, and 7.4% *Unsafe*)

Appendix C

Appendix of Chapter 4.2

For the sake of clarity, we will remind each statement before giving its proof. We also recall the notations and the definitions that are used for our purpose.

In chapter 4.2, the error profile of a hypothesis h as been defined as $\mathbf{E}(h) = (e_1(h), e_2(h)) = (FN(h), FP(h))$. In the binary setting and using the previous notations, the F-Measure is defined by:

$$F(\boldsymbol{e}) = \frac{(1+\beta^2)(P - e_1)}{(1+\beta^2)P - e_1 + e_2}. \tag{C.1}$$

C.1 Main results of the chapter

In this section, we provide all the proofs of Chapter 4.2, but only in the binary setting.

C.1.1 Pseudo-linearity of F-Measure

We aim to prove the following proposition, which plays a key role to provide the bound on the F-measure.

Proposition C.1. *The F-measure, F, is a pseudo-linear function.*

Proof. We need to show that both F and $-F$ are pseudo-convex, i.e. that we have:

$$\langle \nabla F(\boldsymbol{e}), (\boldsymbol{e}' - \boldsymbol{e}) \rangle \geq 0 \implies F(\boldsymbol{e}') \geq F(\boldsymbol{e}). \tag{C.2}$$

The gradient of the F-measure is defined by:

$$\nabla F(\boldsymbol{e}) = -\frac{1+\beta^2}{((1+\beta^2)P - e_1 + e_2)^2} \begin{pmatrix} \beta^2 P + e_2 \\ P - e_1 \end{pmatrix}.$$

We now develop the left-hand side of the implication (C.2):

$$\begin{aligned} \langle \nabla F(\boldsymbol{e}), (\boldsymbol{e}' - \boldsymbol{e}) \rangle &\geq 0, \\ -\frac{1+\beta^2}{((1+\beta^2)P - e_1 + e_2)^2} \left[(\beta^2 P + e_2)(e_1' - e_1) + (P - e_1)(e_2' - e_2) \right] &\geq 0, \end{aligned}$$

so,

$$\begin{aligned}
-(\beta^2 P + e_2)(e_1' - e_1) - (P - e_1)(e_2' - e_2) &\geq 0,\\
-\beta^2 P(e_1' - e_1) - e_1' e_2 + e_1 e_2 + P(e_2 - e_2') + e_1 e_2' - e_1 e_2 &\geq 0,\\
-\beta^2 P(e_1' - e_1) + P(e_2 - e_2') + e_1 e_2' - e_1' e_2 &\geq 0,\\
-\beta^2 P e_1' + \beta^2 P e_1 + P e_2 - P e_2' + e_1 e_2' - e_1' e_2 &\geq 0.
\end{aligned}$$

so

$$-\beta^2 P e_1' + P e_2 - e_1' e_2 \geq -\beta^2 P e_1 + P e_2' - e_1 e_2'.$$

Now we add $-P(e_1 + e_1')$ on both side of the inequality, so we have:

$$\begin{aligned}
-\beta^2 P e_1' + P e_2 - e_1' e_2 - P(e_1 + e_1') &\geq -\beta^2 P e_1 + P e_2' - e_1 e_2' - -P(e_1 + e_1'),\\
-(1+\beta^2) P e_1' + P e_2 - e_1' e_2 - P e_1 &\geq -(1+\beta^2) P e_1 + P e_2' - e_1 e_2' - P e_1'.
\end{aligned}$$

Then, we add $e_1 e_1'$ on both sides:

$$\begin{aligned}
-(1+\beta^2) P e_1' + P e_2 - e_1' e_2 - P e_1 + e_1 e_1' &\geq -(1+\beta^2) P e_1 + P e_2' - e_1 e_2' - P e_1' + e_1 e_1',\\
-(1+\beta^2) P e_1' - (P - e_1') e_1 + (P - e_1') e_2 &\geq -(1+\beta^2) P e_1 - (P - e_1) e_1' + (P - e_1) e_2'.
\end{aligned}$$

Finally, by adding $(1+\beta^2)P^2$ on both sides of the inequality and factorizing with the terms $-(1+\beta^2)Pe_1'$ on the left (respectively $-(1+\beta^2)Pe_1$ on the right), we get:

$$\begin{aligned}
(1+\beta^2) P(P - e_1') - (P - e_1') e_1 + (P - e_1') e_2 &\geq (1+\beta^2) P(P - e_1) - (P - e_1) e_1' + (P - e_1) e_2',\\
(1+\beta^2) P(P - e_1') - (P - e_1') e_1 + (P - e_1') e_2 &\geq (1+\beta^2) P(P - e_1) - (P - e_1) e_1' + (P - e_1) e_2',\\
(P - e_1')((1+\beta^2) P - e_1 + e_2) &\geq (P - e_1)((1+\beta^2) P e_1' + e_2'),\\
(1+\beta^2)(P - e_1')((1+\beta^2) P - e_1 + e_2) &\geq (1+\beta^2)(P - e_1)((1+\beta^2) P e_1' + e_2'),\\
\frac{(P - e_1')}{(1+\beta^2) P - e_1' + e_2'} &\geq \frac{(P - e_1)}{(1+\beta^2) P - e_1 + e_2},\\
\frac{(1+\beta^2)(P - e_1')}{(1+\beta^2) P - e_1' + e_2'} &\geq \frac{(1+\beta^2)(P - e_1)}{(1+\beta^2) P - e_1 + e_2},\\
F(\boldsymbol{e}') &\geq F(\boldsymbol{e}).
\end{aligned}$$

The proof is similar for $-F$.
We have shown that both F and $-F$ are pseudo-convex so F is pseudo-linear. □

We can now use this property to derive our bound. However, we have seen that the bound still depends on to other parameters M_{min} and M_{max} that we should compute.

C.1.2 Computation of the values of M_{min} and M_{max}.

We aim to show how we can solve the optimization problems that define M_{min} and M_{max} and show how it can be reduced to a simple convex optimization problem where the set of constraints is a convex polygon.

Computation of M_{max}

Now, we would like to give an explicit value for M_{max}. This value can be obtained by solving the following optimization problem:

$$\max_{\boldsymbol{e'}\in\mathcal{E}(\mathcal{H})} e'_2 - e'_1 \quad s.t. \quad F_\beta(\boldsymbol{e'}) > F_\beta(\boldsymbol{e}).$$

In the binary case, setting $\boldsymbol{e} = (e_1, e_2)$ and $\boldsymbol{e'} = (e'_1, e'_2)$. We can write $F_\beta(\boldsymbol{e'}) > F_\beta(\boldsymbol{e})$ as:

$$\frac{(1+\beta^2)(P-e'_1)}{(1+\beta^2)P - e'_1 + e'_2} > \frac{(1+\beta^2)(P-e_1)}{(1+\beta^2)P - e_1 + e_2},$$

Now we develop and reduce these expressions.

$$\begin{aligned}
(P-e'_1)[(1+\beta^2)P - e_1 + e_2] &> (P-e_1)[(1+\beta^2)P - e'_1 + e'_2]),\\
(1+\beta^2)P^2 - (1+\beta^2)Pe'_1 + (P-e'_1)(e_2-e_1) &> (1+\beta^2)P^2 - (1+\beta^2)Pe_1 + (P-e_1)(e'_2-e'_1),\\
(1+\beta^2)P(e_1-e'_1) + P(e_2-e_1+e'_1-e'_2) &> e_2e'_1 - e_1e'_2 + e'_1e_1 - e_1e'_1.
\end{aligned}$$

Now, we set: $e'_1 = e_1 + \alpha_1$ and $e'_2 = e_2 + \alpha_2$. In other words, we study how much we have to change $\boldsymbol{e'}$ from $\boldsymbol{e}$ to solve our problem. We can then write:

$$\begin{aligned}
-(1+\beta^2)P\alpha_1 + P(\alpha_1 - \alpha_2) &> e_2(e_1+\alpha_1) - e_1(e_2+\alpha_2),\\
\alpha_1(-(1+\beta^2)P + P - e_2) + \alpha_2(-P+e_1) &> 0,\\
\alpha_1(\beta^2P + e_2) &< -\alpha_2(P-e_1).
\end{aligned}$$

Thus, the optimization problem can be rewritten as:

$$\begin{aligned}
\max_{\boldsymbol{\alpha}} \quad & \alpha_2 - \alpha_1,\\
s.t. \quad & \alpha_1 < \frac{-\alpha_2(P-e_1)}{\beta^2P + e_2},\\
& \alpha_1 \in [-e_1, P-e_1],\\
& \alpha_2 \in [-e_2, N-e_2].
\end{aligned}$$

The optimization problem consists of maximizing a difference under a polygon set of constraints. In the binary setting, the set of constraints can be represented as shown in Fig. C.1 where the line $\mathcal{D}$ is defined by the following equation:

$$\alpha_1 = \frac{-\alpha_2(P-e_1)}{\beta^2P + e_2}. \tag{C.3}$$

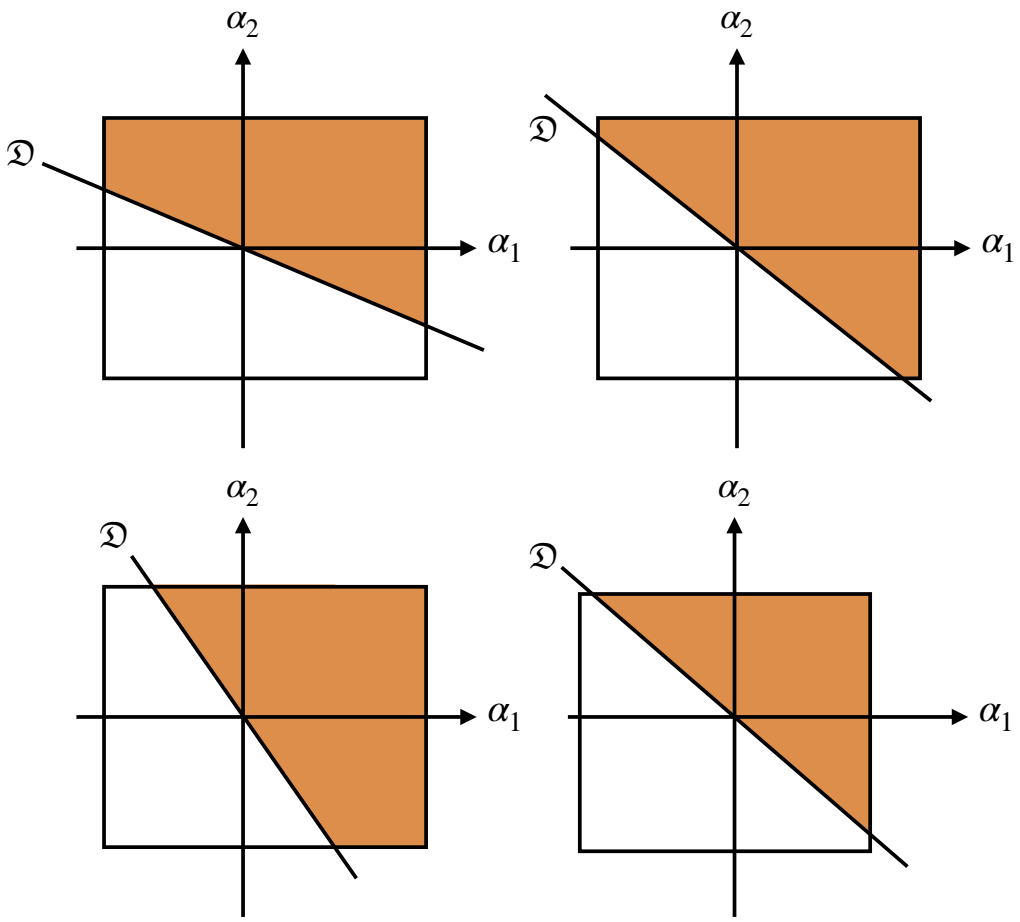

Figure C.1 – Geometric representation of the optimization problem. The rectangle represents the constraint $(\alpha_2, \alpha_1) \in [-e_2, N - e_2] \times [e_1, P - e_1]$. The white area represents the set of value (α_2, α_1) for which the inequality constraint holds. The four figures represent the four possibilities for the position of the line $\mathcal{D}$ on the rectangle. See the computation of M_{min} to see that cases represented by the two figures at the bottom never happen.

To maximize the difference, we should maximize the value of α_2 and minimize the value of α_1, i.e. the solution is located in the bottom right region of each figure. A quick study of these figures shows that the lowest value of α_1 we can reach is $-e_1$.

We shall now study where the line $\mathcal{D}$ intersects the rectangle to have the solution with respect to α_2. If $\mathcal{D}$ does not intersect the line of equation $\alpha_1 = -e_1$ in the rectangle (i.e. it intersects with the right side of the rectangle) then $\alpha_2 = N - e_2$. Else, it intersects with the bottom face of the rectangle, then we determine the value of α_2 using Eq. (C.3) and $\alpha_2 = \dfrac{(\beta^2 P + e_2)e_1}{P - e_1}$.

Finally, the solution of the optimization problem is:

$$(\alpha_1, \alpha_2) = \left(-e_1, \min\left(N - e_2, \frac{(\beta^2 P + e_2)e_1}{P - e_1}\right)\right),$$

and the optimal value M_{max} is defined by:

$$M_{max} = e_2 + \min\left(N - e_2, \frac{(\beta^2 P + e_2)e_1}{P - e_1}\right).$$

Computation of M_{min}

We now aim to solve the following optimization problem:

$$\min_{\boldsymbol{e'} \in \mathcal{E}(\mathcal{H})} e'_2 - e'_1 \quad s.t. \quad F_\beta(\boldsymbol{e'}) > F_\beta(\boldsymbol{e}).$$

As it has been done and using the same notations as in the previous section, we can rewrite the optimization problem as follows:

$$\begin{aligned} \min_{\boldsymbol{\alpha}} \quad & \alpha_2 - \alpha_1, \\ s.t. \quad & \alpha_1 < \frac{-\alpha_2(P - e_1)}{\beta^2 P + e_2}, \\ & \alpha_1 \in [-e_1, P - e_1], \\ & \alpha_2 \in [-e_2, N - e_2]. \end{aligned}$$

The constraints remain unchanged. However, to minimize this difference, we have to maximize the value of α_1 and minimize the value of α_2, i.e. we are interested in the upper left region of each rectangle. In each case represented in Fig C.1, we see that the minimum of α_2 is equal to $-e_2$.

If we have a look at the two figures at the bottom of Fig. C.1, we see that the optimal value of α_1 is equal to $P - e_1$. However, this value is not in the image of the function of α_2 defined by Eq (C.3). In fact, according to Eq. (C.3), the image of $\alpha_2 = -e_2$ is equal to $\frac{e_2(P - e_1)}{\beta^2 P + e_2}$ which is lower than $P - e_1$. So the two figures at the bottom represent cases that never happen and the intersection of $\mathcal{D}$ with the rectangle of constraint is on left part of the rectangle.

Finally, the solution of the optimization problem is:

$$(\alpha_1, \alpha_2) = \left(\frac{e_2(P - e_1)}{\beta^2 P + e_2}, -e_2\right),$$

and the optimal value M_{min} is defined by:

$$M_{min} = -e_1 - \frac{e_2(P - e_1)}{\beta^2 P + e_2}.$$

Now that we have provided all the details to compute and plot our bound, it remains to explain how to compute the bound from Parambath et al. (2014) with respect to any cost parameters t, t' for a fair comparison.

C.1.3 Rewriting the bound of Parambath et al. (2014)

For the sake of clarity we restate the Proposition 5 of Parambath et al. (2014) for our purpose:

Proposition C.2. *Let $t, t \in [0,1]$ and $\varepsilon_1 \geq 0$. Suppose that there exists $\Phi > 0$ such that for all $\boldsymbol{e}, \boldsymbol{e}' \in \mathcal{E}(\mathcal{H})$ satisfying $F(\boldsymbol{e}') > F(\boldsymbol{e})$, we have:*

$$F(\boldsymbol{e}') - F(e) \geq \Phi \langle \boldsymbol{a}(t'), \boldsymbol{e} - \boldsymbol{e}' \rangle. \tag{C.4}$$

Furthermore, suppose that we have the two following conditions

$$(i)\ \ \|\boldsymbol{a}(t) - \boldsymbol{a}(t')\|_2 \leq 2|t - t'| \qquad (ii)\ \ \langle \boldsymbol{a}(t), \boldsymbol{e} \rangle \leq \min_{\boldsymbol{e}'' \in \mathcal{E}(\mathcal{H})} \langle \boldsymbol{a}(t), \boldsymbol{e}'' \rangle + \varepsilon_1$$

Let us also set $M = \max_{\boldsymbol{e}'' \in \mathcal{E}(\mathcal{H})} \|\boldsymbol{e}''\|_2$, then we have:

$$F(\boldsymbol{e}') \leq F(\boldsymbol{e}) + \Phi\varepsilon_1 + 4M\Phi|t' - t|.$$

According to the authors, the point (i) is a consequence of a of being Lipschitz continuous with Lipschitz constant equal to 2. The point (ii) is just the expression of the sub-optimality of the learned classifier.

Proof. For all $\boldsymbol{e}, \tilde{\boldsymbol{e}} \in \mathcal{E}(\mathcal{H})$ and $t, t' \in [0,1]$, we have:

$$\begin{aligned} \langle \boldsymbol{a}(t), \tilde{\boldsymbol{e}} \rangle &= \langle \boldsymbol{a}(t) - \boldsymbol{a}(t'), \tilde{\boldsymbol{e}} \rangle + \langle a(t'), \tilde{\boldsymbol{e}} \rangle, \\ &\leq \langle \boldsymbol{a}(t'), \tilde{\boldsymbol{e}} \rangle + 2M|t' - t|. \end{aligned}$$

Where we have successively applied the Cauchy-Schwarz inequality and (i). Then:

$$\min_{\boldsymbol{e}'' \in \mathcal{E}(\mathcal{H})} \langle \boldsymbol{a}(t), \boldsymbol{e}'' \rangle \leq \min_{\boldsymbol{e}'' \in \mathcal{E}(\mathcal{H})} \langle \boldsymbol{a}(t'), \boldsymbol{e}'' \rangle + 2M|t' - t| = \langle \boldsymbol{a}(t'), \boldsymbol{e}' \rangle + 2M|t' - t|, \tag{C.5}$$

where $\boldsymbol{e}'$ denote the error profile learned by the optimal classifier trained with the cost function $\boldsymbol{a}(t')$ and is such that $F(\boldsymbol{e}') > F(\boldsymbol{e})$. Then, writing $\langle \boldsymbol{a}(t'), \boldsymbol{e} \rangle = \langle \boldsymbol{a}(t') - \boldsymbol{a}(t), \boldsymbol{e} \rangle + \langle \boldsymbol{a}(t), \boldsymbol{e} \rangle$ and applying the Cauchy-Schwarz inequality, we have:

$$\begin{aligned} \langle \boldsymbol{a}(t'), \boldsymbol{e} \rangle &\leq \langle \boldsymbol{a}(t), \boldsymbol{e} \rangle + 2M|t' - t|, \\ &\leq \min_{\boldsymbol{e}'' \in \mathcal{E}(\mathcal{H})} \langle \boldsymbol{a}(t), \boldsymbol{e}'' \rangle + \varepsilon_1 + 2M|t' - t|, \\ &\leq \langle \boldsymbol{a}(t'), \boldsymbol{e}' \rangle + \varepsilon_1 + 4M|t' - t|, \end{aligned}$$

where the second inequality comes from (ii) and the last inequality comes from Eq. (C.5). By plugging this last inequality in inequality (C.4), we get the result.
Furthermore, the existence of the constant Φ has been proved by the authors and is equal to $(\beta^2 P)^{-1}$ □

Remark. This bound can be used in both binary and multi-class setting.

C.2 The multi-class setting

For a given hypothesis $h \in \mathcal{H}$ learned from $\mathbf{X}$, the errors that h makes can be summarized in an error profile defined as $\mathbf{E}(h) \in \mathbb{R}^{2L}$:

$$\mathbf{E}(h) = (FN_1(h), FP_1(h), ..., FN_L(h), FP_L(h)),$$

where $FN_i(h)$ (resp. $FP_i(h)$) is the proportion of False Negative (resp. False Positive) that h yields for class i.

In a multi-class setting with L classes P_k, $k = 1, ..., L$ denotes the proportion of examples in class k and $\boldsymbol{e} = (e_1, e_2, ..., e_{2L-1}, e_{2L})$ denotes the proportions of misclassified examples composing the error profile.

The multi-class-micro F-measure, $mcF(\boldsymbol{e})$ with L classes is defined by:

$$mcF(\boldsymbol{e}) = \frac{(1+\beta^2)(1 - P_1 - \sum_{k=2}^{L} e_{2k-1})}{(1+\beta^2)(1-P_1) - \sum_{k=2}^{L} e_{2k-1} + e_1}.$$

In this section, we aim to derive all the results presented in the binary case in a multi-class setting.

C.2.1 Pseudo-linearity

Proposition C.3. *The multi-class-micro F-measure, mcF, is a pseudo-linear function with respect to* $\boldsymbol{e}$.

Proof. As in the binary cases, we have to prove that both mcF and $-mcF$ are pseudo-convex.

The gradient of the multi-class-micro F-measure, mcF_β, is defined by:

$$\nabla mcF(\boldsymbol{e}) = \frac{-(1+\beta^2)}{(1+\beta^2)(1-P_1) - \sum_{k=2}^{L} e_{2k-1} + e_1} \begin{cases} 1 - P_1 - \sum_{k=2}^{L} e_{2k-1} & \text{w.r.t. } e_1, \\ \beta^2(1-P_1) + e_1 & \text{w.r.t. } e_k \ \forall k = 2, ..., L. \end{cases}$$

The proof is similar to the proof of Proposition C.1. The scheme is the same, we simply have to do the following changes of notation in the proof:

$$\begin{aligned} e_1 &\leftarrow \sum_{k=2}^{L} e_{2k-1}, \\ e_2 &\leftarrow e_1, \\ P &\leftarrow 1 - P_1. \end{aligned}$$

□

C.2.2 Derivation of the bound

As it was done in the binary case, we will use the property of pseudo-linearity of $mcF(\boldsymbol{e})$ to bound the difference of micro F-measure in terms of the parameters of our weighted function. First, we introduce the definition of our weighted function $\boldsymbol{a} : \mathbb{R} \to \mathbb{R}^{2L}$ and express the difference of micro F-measure of two error profiles in function of the two error profiles.
In this section, for the sake of clarity, we will set $\hat{e} = \sum_{k=2}^{L} e_{2k-1}$.

First step: impact of a change in the error profile

Using the property of pseudo-linearity, we can show that there are two functions $\boldsymbol{a} : \mathbb{R} \to \mathbb{R}^{2L}$ and $b : \mathbb{R} \to \mathbb{R}$ defined by:

$$0 = \langle \boldsymbol{a}(mcF(\boldsymbol{e})), \boldsymbol{e} \rangle + b(mcF(\boldsymbol{e})),$$

where:

$$\boldsymbol{a}(t) = \begin{cases} 1 + \beta^2 - t & \text{for } e_{2k-1},\ k = 2, ..., L \\ t & \text{for } e_1, \\ 0 & \text{otherwise,} \end{cases} \qquad \text{and} \quad b(t) = (t-1)(1+\beta^2)(1-P_1).$$

From these definitions we can write:

$$\begin{aligned} \langle \boldsymbol{a}(mcF(\boldsymbol{e}')), \boldsymbol{e} - \boldsymbol{e}' \rangle &= \langle \boldsymbol{a}(mcF(\boldsymbol{e}')), \boldsymbol{e} \rangle + b(mcF(\boldsymbol{e}')), \\ &= \langle \boldsymbol{a}(mcF(\boldsymbol{e}')) - \boldsymbol{a}(mcF(\boldsymbol{e})), \boldsymbol{e} \rangle - b(mcF(\boldsymbol{e})) + b(mcF(\boldsymbol{e}')), \\ &= (mcF(\boldsymbol{e}') - mcF(\boldsymbol{e}))(1+\beta^2)(1-P_1) \\ &\quad + (mcF(\boldsymbol{e}') - mcF(\boldsymbol{e}))e_1 + (mcF(\boldsymbol{e}) - mcF(\boldsymbol{e}'))\hat{e}, \\ &= (mcF(\boldsymbol{e}') - mcF(\boldsymbol{e}))\left((1+\beta^2)(1-P_1) - \hat{e} + e_1\right). \end{aligned}$$

We can now write the difference of micro-F-measure as:

$$mcF(\boldsymbol{e}') - mcF(\boldsymbol{e}) = \Phi_{\boldsymbol{e}} \cdot \langle \boldsymbol{a}(t), \boldsymbol{e} - \boldsymbol{e}' \rangle,$$

where:

$$\Phi_{\boldsymbol{e}} = \frac{1}{(1+\beta^2)(1-P_1) - \hat{e} + e_1},$$

Second step: a bound on the micro F-measure $mcF(\boldsymbol{e})$

We suppose that we have a value of t for which a weighted-classifier with weights $a(t)$ has been learned. This classifier has an error profile $\boldsymbol{e}$ and a F-measure $mcF(\boldsymbol{e})$. We now imagine a hypothetical classifier that is learned with weights $a(t')$, and we denote by $\boldsymbol{e}'$ the error profile of this classifier. For any value of t', we derive an upper bound on the F-measure $mcF(\boldsymbol{e}')$ that this hypothetical classifier can achieve.

$$mcF(\boldsymbol{e}') - mcF(\boldsymbol{e}) = \Phi_{\boldsymbol{e}} \cdot \langle \boldsymbol{a}(t'), \boldsymbol{e} - \boldsymbol{e}' \rangle,$$

$$
\begin{aligned}
&= \Phi_{\boldsymbol{e}} \cdot \left(\langle \boldsymbol{a}(t'), \boldsymbol{e} \rangle - \langle \boldsymbol{a}(t'), \boldsymbol{e} \rangle \right), \\
&= \Phi_{\boldsymbol{e}} \cdot \left(\langle \boldsymbol{a}(t') - \boldsymbol{a}(t), \boldsymbol{e} \rangle + \langle \boldsymbol{a}(t), \boldsymbol{e} \rangle - \langle \boldsymbol{a}(t'), \boldsymbol{e}' \rangle \right), \\
&= \Phi_{\boldsymbol{e}} \cdot \left(\langle (t'-t, t-t'), \boldsymbol{e} \rangle + \langle \boldsymbol{a}(t), \boldsymbol{e} \rangle - \langle \boldsymbol{a}(t'), \boldsymbol{e}' \rangle \right), \\
&= \Phi_{\boldsymbol{e}} \cdot \left((t'-t)(e_1 - \hat{e}) + \langle \boldsymbol{a}(t), \boldsymbol{e} \rangle - \langle \boldsymbol{a}(t'), \boldsymbol{e}' \rangle \right), \\
&\leq \Phi_{\boldsymbol{e}} \cdot \left(\langle \boldsymbol{a}(t), \boldsymbol{e}' \rangle + \varepsilon_1 - \langle \boldsymbol{a}(t'), \boldsymbol{e}' \rangle + (t'-t)(e_1 - \hat{e}) \right), \\
&\leq \Phi_{\boldsymbol{e}} \cdot \left((t'-t)(e_1 - \hat{e}) + \varepsilon_1 - (t'-t)(e'_1 - \hat{e}') \right), \\
&\leq \Phi_{\boldsymbol{e}} \varepsilon_1 + \Phi_{\boldsymbol{e}} \cdot (e_1 - \hat{e} - (e'_1 - \hat{e}'))(t'-t).
\end{aligned}
$$

In the previous development, we have used the linearity of the inner product and the definition of $\boldsymbol{a}$. The first inequality uses the sub-optimality of the learned classifier. We then use the definition of the function $\boldsymbol{a}$.
As in the binary cases, the quantity $(e'_1 - \hat{e}')$ remains unknown. However, we are looking for a vector $\boldsymbol{e}'$ such that $mcF(\boldsymbol{e}') > mcF(\boldsymbol{e})$. So the last inequality becomes, if $t' < t$:

$$mcF(\boldsymbol{e}') - mcF(\boldsymbol{e}) \leq \Phi_{\boldsymbol{e}} \varepsilon_1 + \Phi_{\boldsymbol{e}} (e_2 - e_1 - M_{max})(t'-t),$$

and, if $t' > t$:

$$mcF(\boldsymbol{e}') - mcF(\boldsymbol{e}) \leq \Phi_{\boldsymbol{e}}\ \varepsilon_1 + \Phi_{\boldsymbol{e}} (e_2 - e_1 - M_{min})(t'-t).$$

C.2.3 Computation of M_{max} and M_{min} in a multiclass setting

To compute the value of both M_{max} and M_{min}, we use the same development as done in the binary setting. We have to search how to modify the vector $\boldsymbol{e}$ in order to improve the F-Measure and to maximize (or minimize) the difference: $e'_1 - \sum_{k=2}^{L} e'_{2k-1}$, where $\boldsymbol{e}' = \boldsymbol{e} + \boldsymbol{\alpha}$. As in the previous section, $\boldsymbol{\alpha}$ is the solution of the following optimization problem:

$$
\begin{aligned}
\max_{\boldsymbol{\alpha}} \quad & \alpha_1 - \sum_{k=2}^{L} \alpha_{2k-1}, \\
s.t. \quad & \alpha_1 < - \sum_{k=2}^{L} \alpha_{2k-1} \frac{\beta^2 (1 - P_1) + e_1}{1 - P_1 - \sum_{k=2}^{L} e_{2k-1}} \\
& \alpha_1 \in [-e_1, P_1 - e_1], \\
& \alpha_{2k-1} \in [-e_{2k-1}, P_{2k-1} - e_{2k-1}],\ \forall k = 2, ..., L.
\end{aligned}
$$

Then we add the quantity $e_1 - \sum_{k=2}^{L} e_{2k-1}$ to this result to have the value M_{max}.
Similarly, we solve the following optimization problem:

$$
\begin{aligned}
\min_{\boldsymbol{\alpha}} \quad & \alpha_1 - \sum_{k=2}^{L} \alpha_{2k-1}, \\
s.t. \quad & \alpha_1 < - \sum_{k=2}^{L} \alpha_{2k-1} \frac{\beta^2 (1 - P_1) + e_1}{1 - P_1 - \sum_{k=2}^{L} e_{2k-1}}
\end{aligned}
$$

$$\alpha_1 \in [-e_1, P_1 - e_1],$$
$$\alpha_{2k-1} \in [-e_{2k-1}, P_{2k-1} - e_{2k-1}],\ \forall k = 2, ..., L.$$

Then we add the quantity $e_1 - \sum_{k=2}^{L} e_{2k-1}$ to this result to have the value M_{min}.

C.3 Extended Experiments

This section is dedicated to the experiments. We provide the complete set of graphs and tables for all datasets.

C.3.1 Illustrations of unreachable regions

In this section we provide the unreachable regions (see Fig. C.2) of both presented bounds, our vs. the one obtained from Parambath et al. (2014). As it was noticed previously, our result gives a tighter bound on the optimal reachable F-measure. Moreover, we see that the more the data is imbalanced, the tightest is our bound.
The fact that some points lie in the unreachable regions is explained by our setting. Indeed, we recall that we made the assumption that $\varepsilon_1 = 0$, i.e. we suppose that learned classifier is the optimal one, in terms of $0 - 1$ loss, but it is not the case in practice.

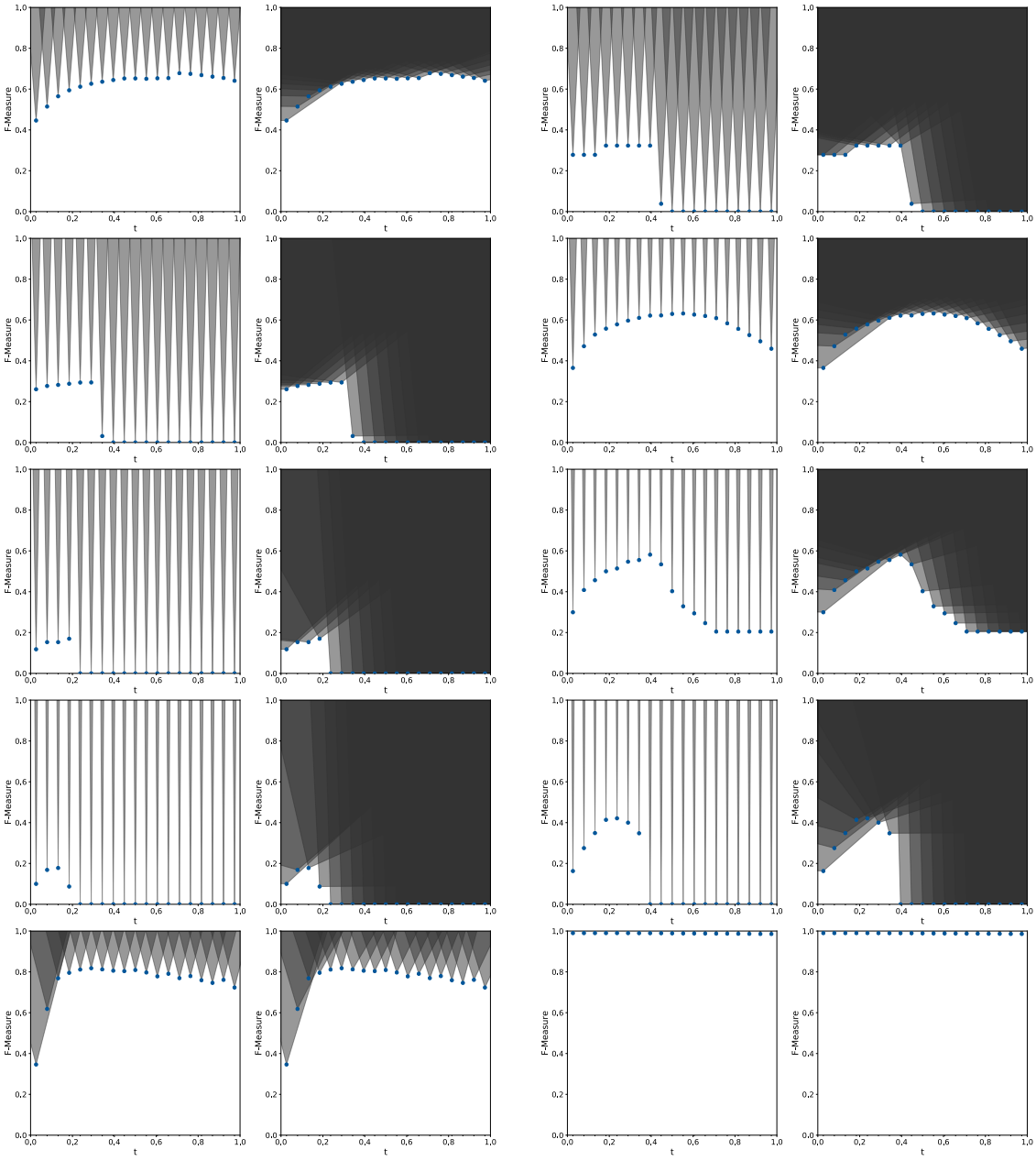

Figure C.2 – Unreachable regions obtained from the same 19 (t_1, F_i) points corresponding to learning weighted SVM on a grid of t values. Cones are shown for all datasets. The bound from Parambath et al. (2014) is represented on the left and our bound on the right.

C.3.2 Theoretical bound versus ε_1

In this section we compare our bound with the one from Parambath et al. (2014) with respect to ε_1. The graphics presented in Fig. C.3 show that the bound from Parambath et al. (2014) is uninformative since the value of the best reachable F-measure is always equal to 1 except on Abalone10 dataset. We see that our bound increases mostly linearly with ε_1. The evolution

is not exactly linear because the value of Φ_e depends on the error profile, so it depends on the value of the parameter t in our cost function $\boldsymbol{a}$. Note that the best classifier reaches the best F-measure in some cases (on Letter dataset for instance) which emphasizes the need to look for an estimation of ε_1.

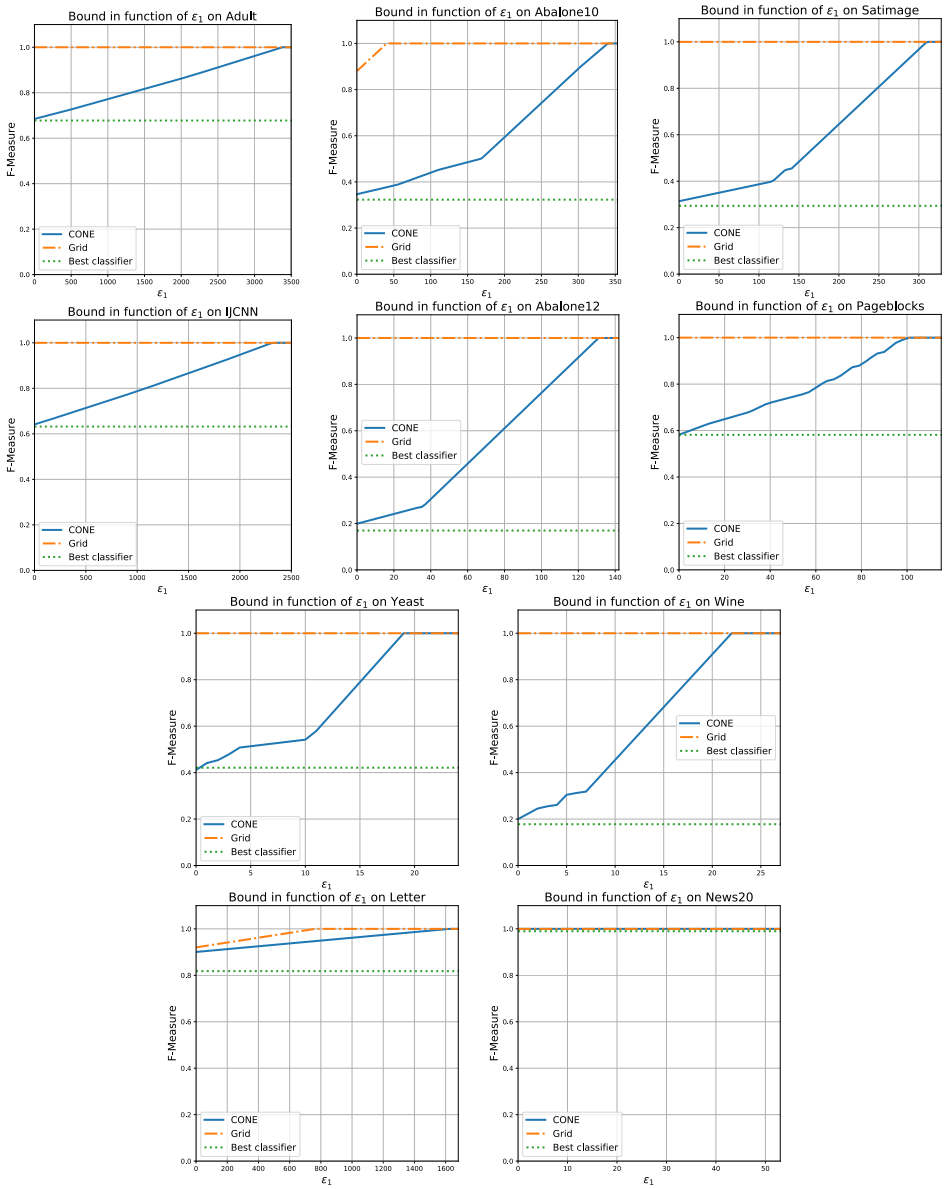

Figure C.3 – Bounds on the F-measure as a function of ε_1, the unknown sub-optimality of the SVM learning algorithm. Results are given on all datasets.

C.3.3 Evolution of Bounds vs. iterations/grid size

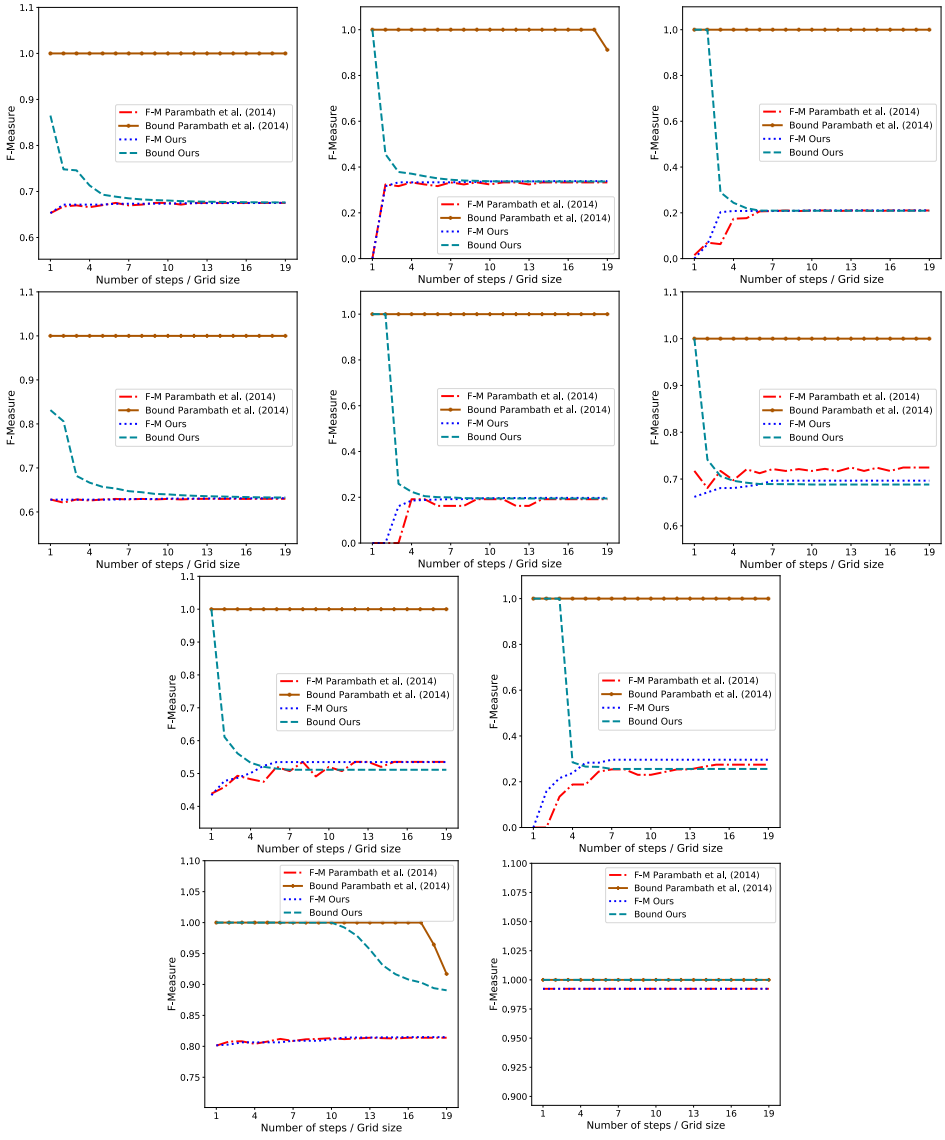

Figure C.4 – Comparison of our bound and the one from Parambath et al. (2014) with respect to the number of iteration/ the size of the grid. We also represent the evolution of both associated algorithms.

C.3.4 Test-time results and result tables of results

For the sake of clarity, only a few algorithms have been chosen to be represented graphically in Fig. C.5.

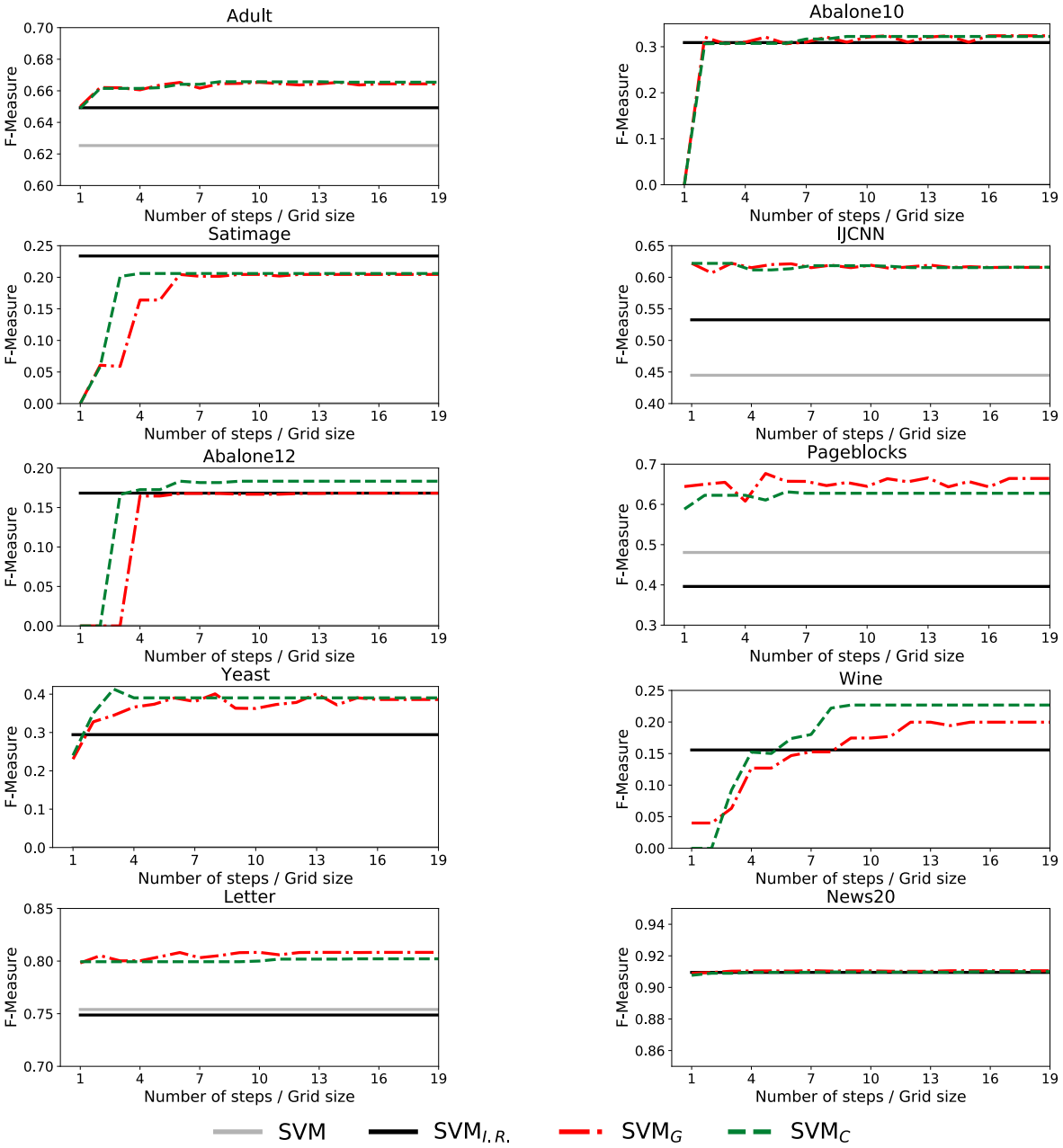

Figure C.5 – F-measure value with respect to the number of iterations or the size of the grid of four different algorithms, all of them are based on SVM.

To complete the results given previously, we provide two tables below. Table C.1 gives the value of the F-measure for all experiments with SVM or Logisitic Regression based algorithms. Because we compare our method to some which use a threshold to predict the class of an

example (Narasimhan et al., 2015; Koyejo et al., 2014), we also provide a thresholded version of all algorithms in Table C.2.

Table C.1 – Classification F-Measure for $\beta = 1$ with SVM algorithm. SVM_G are reproduced from (Parambath et al., 2014) and the subscript $_{I.R.}$ is used for the classifiers trained with a cost depending on the Imbalance Ratio. The subscript $_B$ corresponds to the bisection algorithm presented in (Narasimhan et al., 2015). Finally the $_C$ stands for our wrapper CONE. The presented values are obtained by taking the mean F-Measure over 5 experiments (standard deviation between brackets).

Dataset	SVM	$\text{SVM}_{I.R.}$	SVM_G	SVM_C	LR	$\text{LR}_{I.R.}$	LR_B	LR_G	LR_C
Adult	62.5 (0.2)	64.9 (0.3)	66.4 (0.1)	66.5 (0.1)	63.1 (0.1)	66.0 (0.1)	66.6 (0.1)	66.5 (0.1)	66.5 (0.1)
Abalone10	0.0 (0.0)	30.9 (1.2)	32.4 (1.3)	32.2 (0.8)	0.0 (0.0)	31.9 (1.4)	31.6 (0.6)	31.7 (0.7)	30.9 (1.9)
Satimage	0.0 (0.0)	23.4 (4.3)	20.4 (5.3)	20.6 (5.6)	0.5 (0.9)	24.2 (5.3)	21.4 (4.6)	20.7 (4.8)	20.5 (5.0)
IJCNN	44.5 (0.4)	53.3 (0.4)	61.6 (0.6)	61.6 (0.6)	46.2 (0.3)	51.6 (0.3)	59.2 (0.3)	58.2 (0.2)	58.2 (0.3)
Abalone12	0.0 (0.0)	16.8 (2.7)	16.8 (4.2)	18.3 (3.3)	0.0 (0.0)	18.0 (3.5)	17.7 (3.7)	17.2 (3.1)	18.4 (2.3)
Pageblocks	48.1 (5.8)	39.6 (4.7)	66.4 (3.2)	62.8 (3.9)	48.6 (3.3)	42.4 (5.2)	55.7 (5.7)	62.8 (8.2)	59.4 (7.5)
Yeast	0.0 (0.0)	29.4 (2.9)	38.6 (7.1)	39.0 (7.5)	2.5 (5.0)	29.0 (3.5)	35.4 (15.6)	39.1 (10.1)	39.5 (9.3)
Wine	0.0 (0.0)	15.6 (5.2)	20.0 (6.4)	22.7 (6.0)	0.0 (0.0)	14.6 (3.2)	18.3 (7.2)	18.7 (4.5)	21.1 (5.2)
Letter	75.4 (0.7)	74.9 (0.8)	80.8 (0.5)	81.0 (0.4)	82.9 (0.3)	82.9 (0.3)	74.9 (0.5)	82.9 (0.2)	82.9 (0.3)
News20	90.9 (0.1)	91.0 (0.2)	91.1 (0.1)	91.0 (0.1)	90.6 (0.1)	90.6 (0.1)	89.4 (0.2)	90.6 (0.2)	90.6 (0.2)
Average	32.1 (0.7)	44.0 (2.3)	49.5 (2.9)	49.6 (2.8)	33.4 (1.0)	45.1 (2.3)	47.0 (3.9)	48.8 (3.2)	48.8 (3.2)

Table C.2 – Classification F-Measure for $\beta = 1$ with **thresholded** SVM algorithm. SVM_G are reproduced from (Parambath et al., 2014) and the subscript $_{I.R.}$ is used for the classifiers trained with a cost depending on the Imbalance Ratio. The subscript $_B$ corresponds to the bisection algorithm presented in (Narasimhan et al., 2015). Finally the $_C$ stands for our wrapper CONE. The presented values are obtained by taking the mean F-Measure over 5 experiments (standard deviation between brackets).

Dataset	SVM	$\text{SVM}_{I.R.}$	SVM_G	SVM_C	LR	$\text{LR}_{I.R.}$	LR_G	LR_C
Adult	65.6 (0.3)	66.1 (0.2)	66.4 (0.2)	66.4 (0.1)	66.5 (0.1)	66.5 (0.1)	66.5 (0.1)	66.5 (0.1)
Abalone10	27.8 (1.2)	30.7 (2.0)	31.9 (0.6)	31.8 (1.9)	30.8 (2.2)	30.7 (1.9)	30.7 (1.9)	30.8 (2.1)
Satimage	26.7 (4.9)	29.2 (2.6)	31.6 (1.7)	30.9 (2.0)	21.2 (11.1)	28.6 (1.9)	25.3 (12.7)	25.6 (12.8)
IJCNN	63.2 (0.6)	57.4 (0.3)	62.4 (0.5)	62.6 (0.4)	59.4 (0.5)	56.5 (0.3)	59.3 (0.4)	59.3 (0.2)
Abalone12	10.2 (3.6)	16.6 (2.7)	14.5 (3.2)	16.3 (3.0)	15.5 (3.1)	17.0 (3.3)	15.5 (3.2)	16.2 (3.5)
Pageblocks	66.6 (4.3)	57.5 (6.6)	66.7 (5.2)	67.6 (4.0)	59.2 (8.1)	55.9 (6.4)	62.6 (7.6)	59.0 (7.8)
Yeast	36.2 (12.9)	27.2 (8.5)	38.6 (12.1)	37.4 (10.1)	39.9 (6.5)	27.6 (6.8)	39.3 (4.3)	37.9 (4.8)
Wine	11.0 (6.1)	24.7 (2.0)	14.2 (9.3)	19.3 (7.9)	21.5 (3.7)	25.2 (4.5)	18.6 (5.8)	22.4 (6.4)
Letter	75.4 (0.7)	74.9 (0.8)	80.8 (0.5)	81.0 (0.4)	82.9 (0.3)	82.9 (0.3)	82.9 (0.2)	82.9 (0.2)
News20	90.9 (0.1)	91.0 (0.2)	91.1 (0.1)	91.0 (0.1)	90.6 (0.1)	90.6 (0.1)	90.6 (0.2)	90.6 (0.2)
Average	47.4 (3.5)	47.5 (2.6)	49.8 (3.7)	50.4 (3.0)	48.8 (3.6)	48.2 (2.6)	49.1 (3.6)	49.1 (3.8)

Finally, we give here exhaustive tabular results, giving test-time F-measure results obtained by different methods when varying the budget (when meaningful) from 1 to 18 call to the weight classifier learning algorithm to complete the previous graphs.

Table C.3 – Mean F-Measure over 5 experiments and **limiting the number of iterations/grid steps to 1** (standard deviation between brackets).

Dataset	SVM	$SVM_{I.R.}$	SVM_G	SVM_C	LR	$LR_{I.R.}$	LR_B	LR_G	LR_C
Adult	62.5 (0.2)	64.9 (0.3)	65.0 (0.4)	65.0 (0.4)	63.1 (0.1)	66.0 (0.1)	66.6 (0.1)	66.1 (0.1)	66.1 (0.1)
Abalone10	0.0 (0.0)	30.9 (1.2)	0.0 (0.0)	0.0 (0.0)	0.0 (0.0)	31.9 (1.4)	31.6 (0.6)	24.4 (1.2)	24.4 (1.3)
Satimage	0.0 (0.0)	23.4 (4.3)	0.9 (1.9)	0.0 (0.0)	0.5 (0.9)	24.2 (5.3)	21.4 (4.6)	3.5 (6.9)	3.5 (6.9)
IJCNN	44.5 (0.4)	53.3 (0.4)	61.6 (0.5)	61.6 (0.5)	46.2 (0.3)	51.6 (0.3)	59.2 (0.3)	58.3 (0.3)	58.3 (0.3)
Abalone12	0.0 (0.0)	16.8 (2.7)	0.0 (0.0)	0.0 (0.0)	0.0 (0.0)	18.0 (3.5)	17.7 (3.7)	0.0 (0.0)	0.0 (0.0)
Pageblocks	48.1 (5.8)	39.6 (4.7)	64.4 (2.9)	59.1 (3.8)	48.6 (3.3)	42.4 (5.2)	55.7 (5.7)	55.3 (4.7)	54.5 (4.4)
Yeast	0.0 (0.0)	29.4 (2.9)	12.1 (10.6)	22.9 (15.7)	2.5 (5.0)	29.0 (3.5)	35.4 (15.6)	24.9 (16.0)	24.4 (16.1)
Wine	0.0 (0.0)	15.6 (5.2)	0.0 (0.0)	0.0 (0.0)	0.0 (0.0)	14.6 (3.2)	18.3 (7.2)	5.5 (10.9)	11.6 (10.8)
Letter	75.4 (0.7)	74.9 (0.8)	80.2 (0.3)	80.3 (0.3)	82.9 (0.3)	82.9 (0.3)	74.9 (0.5)	82.6 (0.3)	82.6 (0.3)
News20	90.9 (0.1)	91.0 (0.2)	90.9 (0.2)	90.9 (0.2)	90.6 (0.1)	90.6 (0.1)	89.4 (0.2)	90.6 (0.2)	90.6 (0.2)
Average	32.1 (0.7)	44.0 (2.3)	37.5 (1.7)	38.0 (2.1)	33.4 (1.0)	45.1 (2.3)	47.0 (3.9)	41.1 (4.1)	41.6 (4.0)

Table C.4 – Mean F-Measure over 5 experiments and **limiting the number of iterations/grid steps to 2** (standard deviation between brackets).

Dataset	SVM	$SVM_{I.R.}$	SVM_G	SVM_C	LR	$LR_{I.R.}$	LR_B	LR_G	LR_C
Adult	62.5 (0.2)	64.9 (0.3)	66.4 (0.2)	66.2 (0.3)	63.1 (0.1)	66.0 (0.1)	66.6 (0.1)	66.6 (0.1)	66.2 (0.1)
Abalone10	0.0 (0.0)	30.9 (1.2)	32.6 (1.4)	30.7 (1.1)	0.0 (0.0)	31.9 (1.4)	31.6 (0.6)	31.9 (1.7)	32.4 (1.9)
Satimage	0.0 (0.0)	23.4 (4.3)	6.1 (12.2)	5.9 (11.8)	0.5 (0.9)	24.2 (5.3)	21.4 (4.6)	6.2 (12.3)	6.1 (12.2)
IJCNN	44.5 (0.4)	53.3 (0.4)	60.7 (0.4)	61.6 (0.5)	46.2 (0.3)	51.6 (0.3)	59.2 (0.3)	56.8 (0.3)	58.3 (0.3)
Abalone12	0.0 (0.0)	16.8 (2.7)	0.0 (0.0)	0.0 (0.0)	0.0 (0.0)	18.0 (3.5)	17.7 (3.7)	2.8 (3.4)	13.3 (3.5)
Pageblocks	48.1 (5.8)	39.6 (4.7)	65.0 (7.6)	63.3 (4.1)	48.6 (3.3)	42.4 (5.2)	55.7 (5.7)	62.7 (7.1)	58.3 (6.8)
Yeast	0.0 (0.0)	29.4 (2.9)	30.9 (17.2)	25.4 (17.5)	2.5 (5.0)	29.0 (3.5)	35.4 (15.6)	27.8 (20.0)	33.0 (18.3)
Wine	0.0 (0.0)	15.6 (5.2)	0.0 (0.0)	11.7 (11.1)	0.0 (0.0)	14.6 (3.2)	18.3 (7.2)	8.7 (11.2)	15.6 (6.7)
Letter	75.4 (0.7)	74.9 (0.8)	80.7 (0.5)	80.4 (0.5)	82.9 (0.3)	82.9 (0.3)	74.9 (0.5)	82.9 (0.2)	82.8 (0.2)
News20	90.9 (0.1)	91.0 (0.2)	90.9 (0.2)	91.0 (0.2)	90.6 (0.1)	90.6 (0.1)	89.4 (0.2)	90.6 (0.2)	90.6 (0.1)
Average	32.1 (0.7)	44.0 (2.3)	43.3 (4.0)	43.6 (4.7)	33.4 (1.0)	45.1 (2.3)	47.0 (3.9)	43.7 (5.6)	45.7 (5.0)

Table C.5 – Mean F-Measure over 5 experiments and **limiting the number of iterations/grid steps to 3** (standard deviation between brackets).

Dataset	SVM	$SVM_{I.R.}$	SVM_G	SVM_C	LR	$LR_{I.R.}$	LR_B	LR_G	LR_C
Adult	62.5 (0.2)	64.9 (0.3)	66.1 (0.2)	66.2 (0.3)	63.1 (0.1)	66.0 (0.1)	66.6 (0.1)	66.2 (0.1)	66.2 (0.1)
Abalone10	0.0 (0.0)	30.9 (1.2)	30.7 (1.1)	31.0 (1.4)	0.0 (0.0)	31.9 (1.4)	31.6 (0.6)	32.5 (1.5)	31.3 (2.2)
Satimage	0.0 (0.0)	23.4 (4.3)	5.9 (11.8)	20.2 (4.7)	0.5 (0.9)	24.2 (5.3)	21.4 (4.6)	6.1 (12.1)	20.3 (5.1)
IJCNN	44.5 (0.4)	53.3 (0.4)	61.6 (0.5)	61.6 (0.5)	46.2 (0.3)	51.6 (0.3)	59.2 (0.3)	58.3 (0.3)	58.3 (0.3)
Abalone12	0.0 (0.0)	16.8 (2.7)	0.0 (0.0)	16.7 (2.7)	0.0 (0.0)	18.0 (3.5)	17.7 (3.7)	14.2 (3.0)	16.6 (3.4)
Pageblocks	48.1 (5.8)	39.6 (4.7)	65.5 (2.0)	63.3 (4.1)	48.6 (3.3)	42.4 (5.2)	55.7 (5.7)	60.4 (6.4)	58.3 (6.8)
Yeast	0.0 (0.0)	29.4 (2.9)	32.6 (18.3)	37.8 (7.8)	2.5 (5.0)	29.0 (3.5)	35.4 (15.6)	32.1 (11.9)	32.6 (12.0)
Wine	0.0 (0.0)	15.6 (5.2)	11.8 (11.1)	19.5 (5.1)	0.0 (0.0)	14.6 (3.2)	18.3 (7.2)	17.5 (5.8)	20.0 (3.8)
Letter	75.4 (0.7)	74.9 (0.8)	80.5 (0.2)	80.4 (0.5)	82.9 (0.3)	82.9 (0.3)	74.9 (0.5)	82.9 (0.2)	82.9 (0.2)
News20	90.9 (0.1)	91.0 (0.2)	91.0 (0.2)	91.0 (0.2)	90.6 (0.1)	90.6 (0.1)	89.4 (0.2)	90.6 (0.2)	90.6 (0.1)
Average	32.1 (0.7)	44.0 (2.3)	44.6 (4.5)	48.8 (2.7)	33.4 (1.0)	45.1 (2.3)	47.0 (3.9)	46.1 (4.2)	47.7 (3.4)

Table C.6 – Mean F-Measure over 5 experiments and **limiting the number of iterations/grid steps to 4** (standard deviation between brackets).

Dataset	SVM	SVM$_{I.R.}$	SVM$_{G}$	SVM$_{C}$	LR	LR$_{I.R.}$	LR$_{B}$	LR$_{G}$	LR$_{C}$
Adult	62.5 (0.2)	64.9 (0.3)	66.0 (0.2)	66.2 (0.3)	63.1 (0.1)	66.0 (0.1)	66.6 (0.1)	66.4 (0.1)	66.2 (0.1)
Abalone10	0.0 (0.0)	30.9 (1.2)	31.0 (1.0)	31.0 (1.4)	0.0 (0.0)	31.9 (1.4)	31.6 (0.6)	30.9 (1.7)	31.3 (2.2)
Satimage	0.0 (0.0)	23.4 (4.3)	16.4 (9.5)	20.6 (5.6)	0.5 (0.9)	24.2 (5.3)	21.4 (4.6)	17.0 (9.8)	20.5 (5.0)
IJCNN	44.5 (0.4)	53.3 (0.4)	61.5 (0.4)	61.1 (0.5)	46.2 (0.3)	51.6 (0.3)	59.2 (0.3)	57.8 (0.4)	58.3 (0.3)
Abalone12	0.0 (0.0)	16.8 (2.7)	16.5 (4.0)	16.9 (4.3)	0.0 (0.0)	18.0 (3.5)	17.7 (3.7)	17.6 (3.0)	17.6 (3.1)
Pageblocks	48.1 (5.8)	39.6 (4.7)	61.0 (6.0)	63.3 (4.1)	48.6 (3.3)	42.4 (5.2)	55.7 (5.7)	62.1 (7.8)	58.4 (6.7)
Yeast	0.0 (0.0)	29.4 (2.9)	35.4 (8.7)	39.0 (7.5)	2.5 (5.0)	29.0 (3.5)	35.4 (15.6)	31.1 (18.0)	32.5 (12.0)
Wine	0.0 (0.0)	15.6 (5.2)	11.5 (7.8)	19.5 (5.1)	0.0 (0.0)	14.6 (3.2)	18.3 (7.2)	17.9 (2.8)	20.0 (3.8)
Letter	75.4 (0.7)	74.9 (0.8)	80.5 (0.3)	80.4 (0.5)	82.9 (0.3)	82.9 (0.3)	74.9 (0.5)	82.9 (0.2)	82.9 (0.3)
News20	90.9 (0.1)	91.0 (0.2)	91.0 (0.1)	91.0 (0.2)	90.6 (0.1)	90.6 (0.1)	89.4 (0.2)	90.6 (0.2)	90.7 (0.1)
Average	32.1 (0.7)	44.0 (2.3)	47.1 (3.8)	48.9 (2.9)	33.4 (1.0)	45.1 (2.3)	47.0 (3.9)	47.4 (4.4)	47.8 (3.4)

Table C.7 – Mean F-Measure over 5 experiments and **limiting the number of iterations/grid steps to 5** (standard deviation between brackets).

Dataset	SVM	SVM$_{I.R.}$	SVM$_{G}$	SVM$_{C}$	LR	LR$_{I.R.}$	LR$_{B}$	LR$_{G}$	LR$_{C}$
Adult	62.5 (0.2)	64.9 (0.3)	66.4 (0.3)	66.2 (0.2)	63.1 (0.1)	66.0 (0.1)	66.6 (0.1)	66.6 (0.1)	66.5 (0.1)
Abalone10	0.0 (0.0)	30.9 (1.2)	32.6 (1.4)	31.7 (1.0)	0.0 (0.0)	31.9 (1.4)	31.6 (0.6)	31.3 (0.7)	31.2 (2.3)
Satimage	0.0 (0.0)	23.4 (4.3)	16.4 (9.5)	20.6 (5.6)	0.5 (0.9)	24.2 (5.3)	21.4 (4.6)	17.0 (9.8)	20.5 (5.0)
IJCNN	44.5 (0.4)	53.3 (0.4)	61.4 (0.6)	61.1 (0.5)	46.2 (0.3)	51.6 (0.3)	59.2 (0.3)	58.3 (0.3)	58.3 (0.3)
Abalone12	0.0 (0.0)	16.8 (2.7)	16.5 (4.0)	16.5 (4.0)	0.0 (0.0)	18.0 (3.5)	17.7 (3.7)	17.6 (3.0)	18.1 (2.6)
Pageblocks	48.1 (5.8)	39.6 (4.7)	67.7 (4.0)	62.1 (5.0)	48.6 (3.3)	42.4 (5.2)	55.7 (5.7)	61.8 (7.3)	59.6 (7.3)
Yeast	0.0 (0.0)	29.4 (2.9)	31.8 (10.5)	39.0 (7.5)	2.5 (5.0)	29.0 (3.5)	35.4 (15.6)	30.1 (17.2)	38.8 (8.5)
Wine	0.0 (0.0)	15.6 (5.2)	11.5 (7.8)	20.4 (5.6)	0.0 (0.0)	14.6 (3.2)	18.3 (7.2)	17.9 (2.8)	21.2 (5.1)
Letter	75.4 (0.7)	74.9 (0.8)	80.5 (0.4)	80.4 (0.5)	82.9 (0.3)	82.9 (0.3)	74.9 (0.5)	82.9 (0.2)	82.9 (0.3)
News20	90.9 (0.1)	91.0 (0.2)	91.0 (0.1)	91.0 (0.2)	90.6 (0.1)	90.6 (0.1)	89.4 (0.2)	90.6 (0.2)	90.7 (0.1)
Average	32.1 (0.7)	44.0 (2.3)	47.6 (3.9)	48.9 (3.0)	33.4 (1.0)	45.1 (2.3)	47.0 (3.9)	47.4 (4.2)	48.8 (3.2)

Table C.8 – Mean F-Measure over 5 experiments and **limiting the number of iterations/grid steps to 6** (standard deviation between brackets).

Dataset	SVM	SVM$_{I.R.}$	SVM$_{G}$	SVM$_{C}$	LR	LR$_{I.R.}$	LR$_{B}$	LR$_{G}$	LR$_{C}$
Adult	62.5 (0.2)	64.9 (0.3)	66.5 (0.1)	66.4 (0.1)	63.1 (0.1)	66.0 (0.1)	66.6 (0.1)	66.4 (0.2)	66.5 (0.1)
Abalone10	0.0 (0.0)	30.9 (1.2)	30.7 (1.1)	31.7 (1.0)	0.0 (0.0)	31.9 (1.4)	31.6 (0.6)	31.6 (1.0)	31.4 (2.2)
Satimage	0.0 (0.0)	23.4 (4.3)	20.4 (5.3)	20.6 (5.6)	0.5 (0.9)	24.2 (5.3)	21.4 (4.6)	20.1 (4.6)	20.5 (5.0)
IJCNN	44.5 (0.4)	53.3 (0.4)	62.1 (0.5)	61.3 (0.6)	46.2 (0.3)	51.6 (0.3)	59.2 (0.3)	58.0 (0.4)	58.1 (0.3)
Abalone12	0.0 (0.0)	16.8 (2.7)	16.9 (2.9)	18.2 (3.3)	0.0 (0.0)	18.0 (3.5)	17.7 (3.7)	15.5 (6.2)	17.7 (3.4)
Pageblocks	48.1 (5.8)	39.6 (4.7)	64.8 (3.1)	64.2 (4.6)	48.6 (3.3)	42.4 (5.2)	55.7 (5.7)	60.6 (9.1)	59.5 (7.4)
Yeast	0.0 (0.0)	29.4 (2.9)	32.0 (10.4)	39.0 (7.5)	2.5 (5.0)	29.0 (3.5)	35.4 (15.6)	33.0 (18.8)	38.8 (8.5)
Wine	0.0 (0.0)	15.6 (5.2)	19.4 (5.3)	19.0 (7.0)	0.0 (0.0)	14.6 (3.2)	18.3 (7.2)	19.6 (5.1)	21.1 (5.2)
Letter	75.4 (0.7)	74.9 (0.8)	80.8 (0.5)	80.5 (0.4)	82.9 (0.3)	82.9 (0.3)	74.9 (0.5)	82.9 (0.2)	82.9 (0.3)
News20	90.9 (0.1)	91.0 (0.2)	91.0 (0.2)	91.0 (0.2)	90.6 (0.1)	90.6 (0.1)	89.4 (0.2)	90.6 (0.1)	90.7 (0.1)
Average	32.1 (0.7)	44.0 (2.3)	48.5 (2.9)	49.2 (3.0)	33.4 (1.0)	45.1 (2.3)	47.0 (3.9)	47.8 (4.6)	48.7 (3.2)

Table C.9 – Mean F-Measure over 5 experiments and **limiting the number of iterations/grid steps to 7** (standard deviation between brackets).

Dataset	SVM	$SVM_{I.R.}$	SVM_G	SVM_C	LR	$LR_{I.R.}$	LR_B	LR_G	LR_C
Adult	62.5 (0.2)	64.9 (0.3)	66.2 (0.1)	66.4 (0.1)	63.1 (0.1)	66.0 (0.1)	66.6 (0.1)	66.4 (0.1)	66.5 (0.1)
Abalone10	0.0 (0.0)	30.9 (1.2)	31.0 (1.0)	32.5 (1.0)	0.0 (0.0)	31.9 (1.4)	31.6 (0.6)	32.2 (0.6)	31.4 (2.2)
Satimage	0.0 (0.0)	23.4 (4.3)	20.2 (4.7)	20.6 (5.6)	0.5 (0.9)	24.2 (5.3)	21.4 (4.6)	20.3 (5.0)	20.5 (5.0)
IJCNN	44.5 (0.4)	53.3 (0.4)	61.5 (0.4)	61.5 (0.5)	46.2 (0.3)	51.6 (0.3)	59.2 (0.3)	58.3 (0.3)	58.1 (0.3)
Abalone12	0.0 (0.0)	16.8 (2.7)	16.9 (2.9)	18.3 (3.3)	0.0 (0.0)	18.0 (3.5)	17.7 (3.7)	17.5 (3.4)	17.7 (3.4)
Pageblocks	48.1 (5.8)	39.6 (4.7)	65.7 (2.6)	62.8 (3.9)	48.6 (3.3)	42.4 (5.2)	55.7 (5.7)	61.3 (9.9)	59.9 (7.0)
Yeast	0.0 (0.0)	29.4 (2.9)	38.8 (7.0)	39.0 (7.5)	2.5 (5.0)	29.0 (3.5)	35.4 (15.6)	32.7 (11.8)	38.9 (8.6)
Wine	0.0 (0.0)	15.6 (5.2)	19.5 (6.2)	19.0 (7.0)	0.0 (0.0)	14.6 (3.2)	18.3 (7.2)	18.7 (4.5)	21.1 (5.2)
Letter	75.4 (0.7)	74.9 (0.8)	80.6 (0.1)	80.5 (0.4)	82.9 (0.3)	82.9 (0.3)	74.9 (0.5)	82.9 (0.2)	82.9 (0.3)
News20	90.9 (0.1)	91.0 (0.2)	91.1 (0.1)	91.0 (0.2)	90.6 (0.1)	90.6 (0.1)	89.4 (0.2)	90.6 (0.1)	90.7 (0.1)
Average	32.1 (0.7)	44.0 (2.3)	49.2 (2.5)	49.2 (3.0)	33.4 (1.0)	45.1 (2.3)	47.0 (3.9)	48.1 (3.6)	48.8 (3.2)

Table C.10 – Mean F-Measure over 5 experiments and **limiting the number of iterations/grid steps to 8** (standard deviation between brackets).

Dataset	SVM	$SVM_{I.R.}$	SVM_G	SVM_C	LR	$LR_{I.R.}$	LR_B	LR_G	LR_C
Adult	62.5 (0.2)	64.9 (0.3)	66.4 (0.1)	66.5 (0.1)	63.1 (0.1)	66.0 (0.1)	66.6 (0.1)	66.5 (0.1)	66.5 (0.1)
Abalone10	0.0 (0.0)	30.9 (1.2)	32.6 (1.4)	32.6 (1.0)	0.0 (0.0)	31.9 (1.4)	31.6 (0.6)	32.1 (0.8)	31.4 (2.2)
Satimage	0.0 (0.0)	23.4 (4.3)	20.2 (4.7)	20.6 (5.6)	0.5 (0.9)	24.2 (5.3)	21.4 (4.6)	20.3 (5.0)	20.5 (5.0)
IJCNN	44.5 (0.4)	53.3 (0.4)	61.9 (0.7)	61.5 (0.5)	46.2 (0.3)	51.6 (0.3)	59.2 (0.3)	58.0 (0.4)	58.1 (0.3)
Abalone12	0.0 (0.0)	16.8 (2.7)	16.9 (2.9)	18.3 (3.3)	0.0 (0.0)	18.0 (3.5)	17.7 (3.7)	17.5 (3.4)	18.1 (3.7)
Pageblocks	48.1 (5.8)	39.6 (4.7)	65.8 (4.3)	62.8 (3.9)	48.6 (3.3)	42.4 (5.2)	55.7 (5.7)	60.0 (8.8)	59.4 (7.5)
Yeast	0.0 (0.0)	29.4 (2.9)	33.3 (12.2)	39.0 (7.5)	2.5 (5.0)	29.0 (3.5)	35.4 (15.6)	39.4 (8.5)	38.9 (8.6)
Wine	0.0 (0.0)	15.6 (5.2)	19.5 (6.2)	22.4 (6.1)	0.0 (0.0)	14.6 (3.2)	18.3 (7.2)	18.7 (4.5)	21.1 (5.2)
Letter	75.4 (0.7)	74.9 (0.8)	80.6 (0.4)	80.5 (0.4)	82.9 (0.3)	82.9 (0.3)	74.9 (0.5)	82.9 (0.2)	82.9 (0.3)
News20	90.9 (0.1)	91.0 (0.2)	91.0 (0.1)	91.0 (0.2)	90.6 (0.1)	90.6 (0.1)	89.4 (0.2)	90.6 (0.1)	90.6 (0.1)
Average	32.1 (0.7)	44.0 (2.3)	48.8 (3.3)	49.5 (2.9)	33.4 (1.0)	45.1 (2.3)	47.0 (3.9)	48.6 (3.2)	48.8 (3.3)

Table C.11 – Mean F-Measure over 5 experiments and **limiting the number of iterations/grid steps to 9** (standard deviation between brackets).

Dataset	SVM	$SVM_{I.R.}$	SVM_G	SVM_C	LR	$LR_{I.R.}$	LR_B	LR_G	LR_C
Adult	62.5 (0.2)	64.9 (0.3)	66.4 (0.1)	66.5 (0.1)	63.1 (0.1)	66.0 (0.1)	66.6 (0.1)	66.4 (0.1)	66.5 (0.1)
Abalone10	0.0 (0.0)	30.9 (1.2)	31.0 (1.0)	32.2 (0.8)	0.0 (0.0)	31.9 (1.4)	31.6 (0.6)	31.5 (0.4)	31.4 (2.2)
Satimage	0.0 (0.0)	23.4 (4.3)	20.4 (5.3)	20.6 (5.6)	0.5 (0.9)	24.2 (5.3)	21.4 (4.6)	20.8 (4.9)	20.5 (5.0)
IJCNN	44.5 (0.4)	53.3 (0.4)	61.5 (0.4)	61.5 (0.5)	46.2 (0.3)	51.6 (0.3)	59.2 (0.3)	58.3 (0.3)	58.1 (0.3)
Abalone12	0.0 (0.0)	16.8 (2.7)	16.7 (4.1)	18.3 (3.3)	0.0 (0.0)	18.0 (3.5)	17.7 (3.7)	15.1 (5.9)	18.0 (3.6)
Pageblocks	48.1 (5.8)	39.6 (4.7)	65.4 (2.3)	62.8 (3.9)	48.6 (3.3)	42.4 (5.2)	55.7 (5.7)	62.7 (8.3)	59.4 (7.5)
Yeast	0.0 (0.0)	29.4 (2.9)	38.3 (3.8)	39.0 (7.5)	2.5 (5.0)	29.0 (3.5)	35.4 (15.6)	38.9 (10.9)	38.9 (8.6)
Wine	0.0 (0.0)	15.6 (5.2)	15.5 (6.0)	22.7 (6.0)	0.0 (0.0)	14.6 (3.2)	18.3 (7.2)	20.7 (6.0)	21.1 (5.2)
Letter	75.4 (0.7)	74.9 (0.8)	80.8 (0.5)	80.5 (0.5)	82.9 (0.3)	82.9 (0.3)	74.9 (0.5)	82.9 (0.2)	82.9 (0.3)
News20	90.9 (0.1)	91.0 (0.2)	91.1 (0.1)	91.0 (0.2)	90.6 (0.1)	90.6 (0.1)	89.4 (0.2)	90.6 (0.2)	90.6 (0.1)
Average	32.1 (0.7)	44.0 (2.3)	48.7 (2.4)	49.5 (2.8)	33.4 (1.0)	45.1 (2.3)	47.0 (3.9)	48.8 (3.7)	48.7 (3.3)

Table C.12 – Mean F-Measure over 5 experiments and **limiting the number of iterations/grid steps to 10** (standard deviation between brackets).

Dataset	SVM	SVM$_{I.R.}$	SVM$_{G}$	SVM$_{C}$	LR	LR$_{I.R.}$	LR$_{B}$	LR$_{G}$	LR$_{C}$
Adult	62.5 (0.2)	64.9 (0.3)	66.5 (0.1)	66.4 (0.1)	63.1 (0.1)	66.0 (0.1)	66.6 (0.1)	66.5 (0.1)	66.5 (0.1)
Abalone10	0.0 (0.0)	30.9 (1.2)	32.6 (1.4)	32.2 (0.8)	0.0 (0.0)	31.9 (1.4)	31.6 (0.6)	31.8 (1.0)	31.1 (2.0)
Satimage	0.0 (0.0)	23.4 (4.3)	20.4 (5.3)	20.6 (5.6)	0.5 (0.9)	24.2 (5.3)	21.4 (4.6)	20.8 (4.9)	20.5 (5.0)
IJCNN	44.5 (0.4)	53.3 (0.4)	61.9 (0.7)	61.5 (0.5)	46.2 (0.3)	51.6 (0.3)	59.2 (0.3)	58.0 (0.4)	58.1 (0.3)
Abalone12	0.0 (0.0)	16.8 (2.7)	16.7 (4.1)	18.3 (3.3)	0.0 (0.0)	18.0 (3.5)	17.7 (3.7)	15.1 (5.9)	17.8 (3.4)
Pageblocks	48.1 (5.8)	39.6 (4.7)	65.6 (4.1)	62.8 (3.9)	48.6 (3.3)	42.4 (5.2)	55.7 (5.7)	61.3 (7.3)	59.4 (7.5)
Yeast	0.0 (0.0)	29.4 (2.9)	32.5 (10.4)	39.0 (7.5)	2.5 (5.0)	29.0 (3.5)	35.4 (15.6)	38.9 (10.9)	39.5 (9.3)
Wine	0.0 (0.0)	15.6 (5.2)	15.5 (6.0)	22.7 (6.0)	0.0 (0.0)	14.6 (3.2)	18.3 (7.2)	20.7 (6.0)	21.1 (5.2)
Letter	75.4 (0.7)	74.9 (0.8)	80.8 (0.5)	80.7 (0.4)	82.9 (0.3)	82.9 (0.3)	74.9 (0.5)	82.9 (0.2)	82.9 (0.3)
News20	90.9 (0.1)	91.0 (0.2)	91.0 (0.1)	91.0 (0.2)	90.6 (0.1)	90.6 (0.1)	89.4 (0.2)	90.6 (0.2)	90.6 (0.1)
Average	32.1 (0.7)	44.0 (2.3)	48.4 (3.3)	49.5 (2.8)	33.4 (1.0)	45.1 (2.3)	47.0 (3.9)	48.7 (3.7)	48.8 (3.3)

Table C.13 – Mean F-Measure over 5 experiments and **limiting the number of iterations/grid steps to 11** (standard deviation between brackets).

Dataset	SVM	SVM$_{I.R.}$	SVM$_{G}$	SVM$_{C}$	LR	LR$_{I.R.}$	LR$_{B}$	LR$_{G}$	LR$_{C}$
Adult	62.5 (0.2)	64.9 (0.3)	66.4 (0.1)	66.5 (0.1)	63.1 (0.1)	66.0 (0.1)	66.6 (0.1)	66.5 (0.1)	66.5 (0.1)
Abalone10	0.0 (0.0)	30.9 (1.2)	32.4 (1.3)	32.2 (0.8)	0.0 (0.0)	31.9 (1.4)	31.6 (0.6)	31.9 (0.7)	30.9 (1.9)
Satimage	0.0 (0.0)	23.4 (4.3)	20.2 (4.7)	20.6 (5.6)	0.5 (0.9)	24.2 (5.3)	21.4 (4.6)	20.7 (4.8)	20.5 (5.0)
IJCNN	44.5 (0.4)	53.3 (0.4)	61.4 (0.5)	61.8 (0.5)	46.2 (0.3)	51.6 (0.3)	59.2 (0.3)	58.3 (0.3)	58.1 (0.4)
Abalone12	0.0 (0.0)	16.8 (2.7)	16.7 (4.1)	18.3 (3.3)	0.0 (0.0)	18.0 (3.5)	17.7 (3.7)	17.2 (3.1)	17.8 (3.4)
Pageblocks	48.1 (5.8)	39.6 (4.7)	66.4 (3.5)	62.8 (3.9)	48.6 (3.3)	42.4 (5.2)	55.7 (5.7)	62.6 (8.0)	59.4 (7.5)
Yeast	0.0 (0.0)	29.4 (2.9)	38.4 (7.1)	39.0 (7.5)	2.5 (5.0)	29.0 (3.5)	35.4 (15.6)	38.7 (8.1)	39.5 (9.3)
Wine	0.0 (0.0)	15.6 (5.2)	16.4 (5.9)	22.7 (6.0)	0.0 (0.0)	14.6 (3.2)	18.3 (7.2)	20.5 (6.0)	21.1 (5.2)
Letter	75.4 (0.7)	74.9 (0.8)	80.7 (0.3)	80.9 (0.4)	82.9 (0.3)	82.9 (0.3)	74.9 (0.5)	82.9 (0.2)	82.9 (0.3)
News20	90.9 (0.1)	91.0 (0.2)	91.0 (0.2)	91.0 (0.2)	90.6 (0.1)	90.6 (0.1)	89.4 (0.2)	90.6 (0.2)	90.6 (0.1)
Average	32.1 (0.7)	44.0 (2.3)	49.0 (2.8)	49.6 (2.8)	33.4 (1.0)	45.1 (2.3)	47.0 (3.9)	49.0 (3.1)	48.7 (3.3)

Table C.14 – Mean F-Measure over 5 experiments and **limiting the number of iterations/grid steps to 12** (standard deviation between brackets).

Dataset	SVM	SVM$_{I.R.}$	SVM$_{G}$	SVM$_{C}$	LR	LR$_{I.R.}$	LR$_{B}$	LR$_{G}$	LR$_{C}$
Adult	62.5 (0.2)	64.9 (0.3)	66.4 (0.1)	66.5 (0.1)	63.1 (0.1)	66.0 (0.1)	66.6 (0.1)	66.4 (0.1)	66.5 (0.1)
Abalone10	0.0 (0.0)	30.9 (1.2)	31.0 (1.0)	32.2 (0.8)	0.0 (0.0)	31.9 (1.4)	31.6 (0.6)	32.0 (0.7)	30.9 (1.9)
Satimage	0.0 (0.0)	23.4 (4.3)	20.4 (5.3)	20.6 (5.6)	0.5 (0.9)	24.2 (5.3)	21.4 (4.6)	20.3 (5.0)	20.5 (5.0)
IJCNN	44.5 (0.4)	53.3 (0.4)	61.8 (0.4)	61.6 (0.6)	46.2 (0.3)	51.6 (0.3)	59.2 (0.3)	58.0 (0.4)	58.2 (0.3)
Abalone12	0.0 (0.0)	16.8 (2.7)	16.9 (2.9)	18.3 (3.3)	0.0 (0.0)	18.0 (3.5)	17.7 (3.7)	17.5 (3.4)	17.8 (3.4)
Pageblocks	48.1 (5.8)	39.6 (4.7)	64.7 (3.2)	62.8 (3.9)	48.6 (3.3)	42.4 (5.2)	55.7 (5.7)	61.5 (10.0)	59.4 (7.5)
Yeast	0.0 (0.0)	29.4 (2.9)	38.1 (7.6)	39.0 (7.5)	2.5 (5.0)	29.0 (3.5)	35.4 (15.6)	39.1 (10.1)	39.5 (9.3)
Wine	0.0 (0.0)	15.6 (5.2)	20.0 (6.4)	22.7 (6.0)	0.0 (0.0)	14.6 (3.2)	18.3 (7.2)	18.7 (4.5)	21.1 (5.2)
Letter	75.4 (0.7)	74.9 (0.8)	80.8 (0.5)	80.9 (0.4)	82.9 (0.3)	82.9 (0.3)	74.9 (0.5)	82.9 (0.3)	82.9 (0.3)
News20	90.9 (0.1)	91.0 (0.2)	91.0 (0.1)	91.0 (0.2)	90.6 (0.1)	90.6 (0.1)	89.4 (0.2)	90.6 (0.1)	90.6 (0.2)
Average	32.1 (0.7)	44.0 (2.3)	49.1 (2.7)	49.6 (2.8)	33.4 (1.0)	45.1 (2.3)	47.0 (3.9)	48.7 (3.5)	48.7 (3.3)

Table C.15 – Mean F-Measure over 5 experiments and **limiting the number of iterations/grid steps to 13** (standard deviation between brackets).

Dataset	SVM	$SVM_{I.R.}$	SVM_G	SVM_C	LR	$LR_{I.R.}$	LR_B	LR_G	LR_C
Adult	62.5 (0.2)	64.9 (0.3)	66.4 (0.1)	66.5 (0.1)	63.1 (0.1)	66.0 (0.1)	66.6 (0.1)	66.5 (0.1)	66.5 (0.1)
Abalone10	0.0 (0.0)	30.9 (1.2)	32.6 (1.4)	32.2 (0.8)	0.0 (0.0)	31.9 (1.4)	31.6 (0.6)	32.3 (1.1)	30.9 (1.9)
Satimage	0.0 (0.0)	23.4 (4.3)	20.4 (5.3)	20.6 (5.6)	0.5 (0.9)	24.2 (5.3)	21.4 (4.6)	20.3 (5.0)	20.5 (5.0)
IJCNN	44.5 (0.4)	53.3 (0.4)	61.9 (0.7)	61.6 (0.6)	46.2 (0.3)	51.6 (0.3)	59.2 (0.3)	58.2 (0.2)	58.2 (0.3)
Abalone12	0.0 (0.0)	16.8 (2.7)	16.9 (2.9)	18.3 (3.3)	0.0 (0.0)	18.0 (3.5)	17.7 (3.7)	17.5 (3.4)	17.8 (3.4)
Pageblocks	48.1 (5.8)	39.6 (4.7)	66.6 (3.1)	62.8 (3.9)	48.6 (3.3)	42.4 (5.2)	55.7 (5.7)	60.2 (9.0)	59.4 (7.5)
Yeast	0.0 (0.0)	29.4 (2.9)	33.3 (12.2)	39.0 (7.5)	2.5 (5.0)	29.0 (3.5)	35.4 (15.6)	39.1 (10.1)	39.5 (9.3)
Wine	0.0 (0.0)	15.6 (5.2)	20.0 (6.4)	22.7 (6.0)	0.0 (0.0)	14.6 (3.2)	18.3 (7.2)	18.7 (4.5)	21.1 (5.2)
Letter	75.4 (0.7)	74.9 (0.8)	80.8 (0.5)	80.9 (0.4)	82.9 (0.3)	82.9 (0.3)	74.9 (0.5)	82.9 (0.3)	82.9 (0.3)
News20	90.9 (0.1)	91.0 (0.2)	91.0 (0.1)	91.0 (0.2)	90.6 (0.1)	90.6 (0.1)	89.4 (0.2)	90.6 (0.1)	90.6 (0.2)
Average	32.1 (0.7)	44.0 (2.3)	49.0 (3.3)	49.6 (2.8)	33.4 (1.0)	45.1 (2.3)	47.0 (3.9)	48.6 (3.4)	48.7 (3.3)

Table C.16 – Mean F-Measure over 5 experiments and **limiting the number of iterations/grid steps to 14** (standard deviation between brackets).

Dataset	SVM	$SVM_{I.R.}$	SVM_G	SVM_C	LR	$LR_{I.R.}$	LR_B	LR_G	LR_C
Adult	62.5 (0.2)	64.9 (0.3)	66.5 (0.1)	66.5 (0.1)	63.1 (0.1)	66.0 (0.1)	66.6 (0.1)	66.5 (0.1)	66.5 (0.1)
Abalone10	0.0 (0.0)	30.9 (1.2)	32.4 (1.3)	32.2 (0.8)	0.0 (0.0)	31.9 (1.4)	31.6 (0.6)	31.4 (0.5)	30.9 (1.9)
Satimage	0.0 (0.0)	23.4 (4.3)	20.4 (5.3)	20.6 (5.6)	0.5 (0.9)	24.2 (5.3)	21.4 (4.6)	20.8 (4.9)	20.5 (5.0)
IJCNN	44.5 (0.4)	53.3 (0.4)	61.6 (0.6)	61.6 (0.6)	46.2 (0.3)	51.6 (0.3)	59.2 (0.3)	58.0 (0.4)	58.2 (0.3)
Abalone12	0.0 (0.0)	16.8 (2.7)	16.8 (4.2)	18.3 (3.3)	0.0 (0.0)	18.0 (3.5)	17.7 (3.7)	15.1 (5.9)	17.8 (3.4)
Pageblocks	48.1 (5.8)	39.6 (4.7)	65.5 (4.2)	62.8 (3.9)	48.6 (3.3)	42.4 (5.2)	55.7 (5.7)	62.8 (8.2)	59.4 (7.5)
Yeast	0.0 (0.0)	29.4 (2.9)	38.0 (4.4)	39.0 (7.5)	2.5 (5.0)	29.0 (3.5)	35.4 (15.6)	38.2 (11.2)	39.5 (9.3)
Wine	0.0 (0.0)	15.6 (5.2)	19.1 (6.9)	22.7 (6.0)	0.0 (0.0)	14.6 (3.2)	18.3 (7.2)	18.9 (4.6)	21.1 (5.2)
Letter	75.4 (0.7)	74.9 (0.8)	80.8 (0.5)	80.9 (0.4)	82.9 (0.3)	82.9 (0.3)	74.9 (0.5)	82.9 (0.2)	82.9 (0.3)
News20	90.9 (0.1)	91.0 (0.2)	91.1 (0.1)	91.0 (0.2)	90.6 (0.1)	90.6 (0.1)	89.4 (0.2)	90.6 (0.2)	90.6 (0.2)
Average	32.1 (0.7)	44.0 (2.3)	49.2 (2.8)	49.6 (2.8)	33.4 (1.0)	45.1 (2.3)	47.0 (3.9)	48.5 (3.6)	48.7 (3.3)

Table C.17 – Mean F-Measure over 5 experiments and **limiting the number of iterations/grid steps to 15** (standard deviation between brackets).

Dataset	SVM	$SVM_{I.R.}$	SVM_G	SVM_C	LR	$LR_{I.R.}$	LR_B	LR_G	LR_C
Adult	62.5 (0.2)	64.9 (0.3)	66.4 (0.1)	66.5 (0.1)	63.1 (0.1)	66.0 (0.1)	66.6 (0.1)	66.4 (0.1)	66.5 (0.1)
Abalone10	0.0 (0.0)	30.9 (1.2)	31.0 (1.0)	32.2 (0.8)	0.0 (0.0)	31.9 (1.4)	31.6 (0.6)	31.9 (0.5)	30.9 (1.9)
Satimage	0.0 (0.0)	23.4 (4.3)	20.4 (5.3)	20.6 (5.6)	0.5 (0.9)	24.2 (5.3)	21.4 (4.6)	20.7 (4.8)	20.5 (5.0)
IJCNN	44.5 (0.4)	53.3 (0.4)	61.8 (0.4)	61.6 (0.6)	46.2 (0.3)	51.6 (0.3)	59.2 (0.3)	58.2 (0.2)	58.2 (0.3)
Abalone12	0.0 (0.0)	16.8 (2.7)	16.8 (4.2)	18.3 (3.3)	0.0 (0.0)	18.0 (3.5)	17.7 (3.7)	17.2 (3.1)	18.4 (2.3)
Pageblocks	48.1 (5.8)	39.6 (4.7)	65.7 (2.1)	62.8 (3.9)	48.6 (3.3)	42.4 (5.2)	55.7 (5.7)	62.7 (8.3)	59.4 (7.5)
Yeast	0.0 (0.0)	29.4 (2.9)	39.0 (6.8)	39.0 (7.5)	2.5 (5.0)	29.0 (3.5)	35.4 (15.6)	39.1 (10.1)	39.5 (9.3)
Wine	0.0 (0.0)	15.6 (5.2)	20.0 (6.4)	22.7 (6.0)	0.0 (0.0)	14.6 (3.2)	18.3 (7.2)	18.7 (4.5)	21.1 (5.2)
Letter	75.4 (0.7)	74.9 (0.8)	80.8 (0.5)	80.9 (0.4)	82.9 (0.3)	82.9 (0.3)	74.9 (0.5)	82.9 (0.2)	82.9 (0.3)
News20	90.9 (0.1)	91.0 (0.2)	91.1 (0.1)	91.0 (0.1)	90.6 (0.1)	90.6 (0.1)	89.4 (0.2)	90.6 (0.2)	90.6 (0.2)
Average	32.1 (0.7)	44.0 (2.3)	49.3 (2.7)	49.6 (2.8)	33.4 (1.0)	45.1 (2.3)	47.0 (3.9)	48.8 (3.2)	48.8 (3.2)

Table C.18 – Mean F-Measure over 5 experiments and **limiting the number of iterations/grid steps to 16** (standard deviation between brackets).

Dataset	SVM	SVM$_{I.R.}$	SVM$_{G}$	SVM$_{C}$	LR	LR$_{I.R.}$	LR$_{B}$	LR$_{G}$	LR$_{C}$
Adult	62.5 (0.2)	64.9 (0.3)	66.4 (0.1)	66.5 (0.1)	63.1 (0.1)	66.0 (0.1)	66.6 (0.1)	66.5 (0.1)	66.5 (0.1)
Abalone10	0.0 (0.0)	30.9 (1.2)	32.4 (1.3)	32.2 (0.8)	0.0 (0.0)	31.9 (1.4)	31.6 (0.6)	31.7 (0.7)	30.9 (1.9)
Satimage	0.0 (0.0)	23.4 (4.3)	20.4 (5.3)	20.6 (5.6)	0.5 (0.9)	24.2 (5.3)	21.4 (4.6)	20.7 (4.8)	20.5 (5.0)
IJCNN	44.5 (0.4)	53.3 (0.4)	61.6 (0.6)	61.6 (0.6)	46.2 (0.3)	51.6 (0.3)	59.2 (0.3)	58.0 (0.4)	58.2 (0.3)
Abalone12	0.0 (0.0)	16.8 (2.7)	16.8 (4.2)	18.3 (3.3)	0.0 (0.0)	18.0 (3.5)	17.7 (3.7)	17.2 (3.1)	18.4 (2.3)
Pageblocks	48.1 (5.8)	39.6 (4.7)	65.5 (4.2)	62.8 (3.9)	48.6 (3.3)	42.4 (5.2)	55.7 (5.7)	62.8 (8.2)	59.4 (7.5)
Yeast	0.0 (0.0)	29.4 (2.9)	38.6 (7.1)	39.0 (7.5)	2.5 (5.0)	29.0 (3.5)	35.4 (15.6)	39.1 (10.1)	39.5 (9.3)
Wine	0.0 (0.0)	15.6 (5.2)	20.0 (6.4)	22.7 (6.0)	0.0 (0.0)	14.6 (3.2)	18.3 (7.2)	18.7 (4.5)	21.1 (5.2)
Letter	75.4 (0.7)	74.9 (0.8)	80.8 (0.5)	81.0 (0.4)	82.9 (0.3)	82.9 (0.3)	74.9 (0.5)	82.9 (0.2)	82.9 (0.3)
News20	90.9 (0.1)	91.0 (0.2)	91.1 (0.1)	91.0 (0.1)	90.6 (0.1)	90.6 (0.1)	89.4 (0.2)	90.6 (0.2)	90.6 (0.2)
Average	32.1 (0.7)	44.0 (2.3)	49.4 (3.0)	49.6 (2.8)	33.4 (1.0)	45.1 (2.3)	47.0 (3.9)	48.8 (3.2)	48.8 (3.2)

Table C.19 – Mean F-Measure over 5 experiments and **limiting the number of iterations/grid steps to 17** (standard deviation between brackets).

Dataset	SVM	SVM$_{I.R.}$	SVM$_{G}$	SVM$_{C}$	LR	LR$_{I.R.}$	LR$_{B}$	LR$_{G}$	LR$_{C}$
Adult	62.5 (0.2)	64.9 (0.3)	66.4 (0.1)	66.5 (0.1)	63.1 (0.1)	66.0 (0.1)	66.6 (0.1)	66.5 (0.1)	66.5 (0.1)
Abalone10	0.0 (0.0)	30.9 (1.2)	32.4 (1.3)	32.2 (0.8)	0.0 (0.0)	31.9 (1.4)	31.6 (0.6)	31.7 (0.7)	30.9 (1.9)
Satimage	0.0 (0.0)	23.4 (4.3)	20.4 (5.3)	20.6 (5.6)	0.5 (0.9)	24.2 (5.3)	21.4 (4.6)	20.7 (4.8)	20.5 (5.0)
IJCNN	44.5 (0.4)	53.3 (0.4)	61.6 (0.6)	61.6 (0.6)	46.2 (0.3)	51.6 (0.3)	59.2 (0.3)	58.2 (0.2)	58.2 (0.3)
Abalone12	0.0 (0.0)	16.8 (2.7)	16.8 (4.2)	18.3 (3.3)	0.0 (0.0)	18.0 (3.5)	17.7 (3.7)	17.2 (3.1)	18.4 (2.3)
Pageblocks	48.1 (5.8)	39.6 (4.7)	66.4 (3.2)	62.8 (3.9)	48.6 (3.3)	42.4 (5.2)	55.7 (5.7)	62.8 (8.2)	59.4 (7.5)
Yeast	0.0 (0.0)	29.4 (2.9)	38.6 (7.1)	39.0 (7.5)	2.5 (5.0)	29.0 (3.5)	35.4 (15.6)	39.1 (10.1)	39.5 (9.3)
Wine	0.0 (0.0)	15.6 (5.2)	20.0 (6.4)	22.7 (6.0)	0.0 (0.0)	14.6 (3.2)	18.3 (7.2)	18.7 (4.5)	21.1 (5.2)
Letter	75.4 (0.7)	74.9 (0.8)	80.8 (0.5)	81.0 (0.4)	82.9 (0.3)	82.9 (0.3)	74.9 (0.5)	82.9 (0.2)	82.9 (0.3)
News20	90.9 (0.1)	91.0 (0.2)	91.1 (0.1)	91.0 (0.1)	90.6 (0.1)	90.6 (0.1)	89.4 (0.2)	90.6 (0.2)	90.6 (0.2)
Average	32.1 (0.7)	44.0 (2.3)	49.5 (2.9)	49.6 (2.8)	33.4 (1.0)	45.1 (2.3)	47.0 (3.9)	48.8 (3.2)	48.8 (3.2)

Table C.20 – Mean F-Measure over 5 experiments and **limiting the number of iterations/grid steps to 18** (standard deviation between brackets).

Dataset	SVM	SVM$_{I.R.}$	SVM$_{G}$	SVM$_{C}$	LR	LR$_{I.R.}$	LR$_{B}$	LR$_{G}$	LR$_{C}$
Adult	62.5 (0.2)	64.9 (0.3)	66.4 (0.1)	66.5 (0.1)	63.1 (0.1)	66.0 (0.1)	66.6 (0.1)	66.5 (0.1)	66.5 (0.1)
Abalone10	0.0 (0.0)	30.9 (1.2)	32.4 (1.3)	32.2 (0.8)	0.0 (0.0)	31.9 (1.4)	31.6 (0.6)	31.7 (0.7)	30.9 (1.9)
Satimage	0.0 (0.0)	23.4 (4.3)	20.4 (5.3)	20.6 (5.6)	0.5 (0.9)	24.2 (5.3)	21.4 (4.6)	20.7 (4.8)	20.5 (5.0)
IJCNN	44.5 (0.4)	53.3 (0.4)	61.6 (0.6)	61.6 (0.6)	46.2 (0.3)	51.6 (0.3)	59.2 (0.3)	58.2 (0.2)	58.2 (0.3)
Abalone12	0.0 (0.0)	16.8 (2.7)	16.8 (4.2)	18.3 (3.3)	0.0 (0.0)	18.0 (3.5)	17.7 (3.7)	17.2 (3.1)	18.4 (2.3)
Pageblocks	48.1 (5.8)	39.6 (4.7)	66.4 (3.2)	62.8 (3.9)	48.6 (3.3)	42.4 (5.2)	55.7 (5.7)	62.8 (8.2)	59.4 (7.5)
Yeast	0.0 (0.0)	29.4 (2.9)	38.6 (7.1)	39.0 (7.5)	2.5 (5.0)	29.0 (3.5)	35.4 (15.6)	39.1 (10.1)	39.5 (9.3)
Wine	0.0 (0.0)	15.6 (5.2)	20.0 (6.4)	22.7 (6.0)	0.0 (0.0)	14.6 (3.2)	18.3 (7.2)	18.7 (4.5)	21.1 (5.2)
Letter	75.4 (0.7)	74.9 (0.8)	80.8 (0.5)	81.0 (0.4)	82.9 (0.3)	82.9 (0.3)	74.9 (0.5)	82.9 (0.2)	82.9 (0.3)
News20	90.9 (0.1)	91.0 (0.2)	91.1 (0.1)	91.0 (0.1)	90.6 (0.1)	90.6 (0.1)	89.4 (0.2)	90.6 (0.2)	90.6 (0.2)
Average	32.1 (0.7)	44.0 (2.3)	49.5 (2.9)	49.6 (2.8)	33.4 (1.0)	45.1 (2.3)	47.0 (3.9)	48.8 (3.2)	48.8 (3.2)

Appendix D

French translations

Table des matières

D.1 Introduction

Chaque hiver, des millions de personnes à travers le monde font du ski, du snowboard ou de la luge dans les stations de ski. En été également, les stations peuvent être ouvertes à la randonnée ou au vélo. Quelle que soit la saison, les télésièges sont un moyen de transport très répandu pour traverser une station. En haute saison, un télésiège peut transporter des milliers de personnes par jour. Leur sécurité est une grande préoccupation pour les gestionnaires des centres de villégiature.

En France, une étude a analysé les 108 accidents *graves* qui se sont produits sur les télésièges entre 2006 et 2014[1]. Le résultat de l'étude a montré que 70 % des accidents sont survenus soit à l'embarquement, soit au débarquement des télésièges. De plus, ils ont montré que 90 % des accidents étaient causés par le comportement des passagers. Ainsi, s'assurer que les passagers soient correctement assis dans le véhicule et qu'ils aient correctement fermé la barre de retenue peut permettre aux stations d'éviter de nombreux accidents.

En 2015, Bluecime a été créée pour concevoir un système de surveillance permettant de détecter les situations à risque à la station d'embarquement d'un télésiège. Le système proposé s'appelle "Système Intelligent de Vision Artificielle par Ordinateur" (SIVAO) (Fig.1), et est composé d'une caméra, d'un ordinateur, d'une alarme, et depuis l'hiver 2018 d'un panneau de signalisation. Si une situation à risque est détectée, l'alarme est déclenchée pour avertir l'opérateur du télésiège, et le panneau est allumé pour enjoindre aux passagers de fermer la barre de retenue. Pour des raisons de confidentialité, nous ne donnons pas les noms des télésièges dans ce manuscrit et les désignons par "Chair. A-U".

Pour chaque télésiège, une "pyramide de détection" est configurée (zone bleue sur la Fig. 1b), marquant la zone où le véhicule est suivi. Nous appelons *l'arrière* de la pyramide le point d'entrée du véhicule dans la zone de détection. Nous appelons *l'avant* de la pyramide, le point de sortie du véhicule de la zone de détection, donc, le point où la décision, de déclencher ou non l'alarme, est prise. A chaque image à l'intérieur de la pyramide de détection, différentes détections, utilisant des techniques de traitement d'images non basées sur l'apprentissage, sont effectuées :

- Présence de passagers
- Garde-corps en position *up* (complètement ouverte)
- Garde-corps en position *down* (totalement fermée)

À la dernière image de la pyramide de détection, selon les détections effectuées lors du suivi du véhicule, le système doit évaluer le danger d'une situation. Par exemple, si aucun passager n'est détecté ou si des passagers sont détectés et que le garde-corps est détectée en position *down*, alors la situation est sûre (l'alarme ne doit pas être déclenchée). Alors que, si des passagers sont détectés et que le garde-corps est détectée en position *up* (ou ni *up* ni *down*), la situation est risquée (l'alarme doit être déclenchée).

[1] http://www.domaines-skiables.fr/fr/smedia/filer_private/41/b9/41b95513-e9d4-4159-a261-5925e6d9f030/magazine-39.pdf#page=28

Chaque année, de plus en plus de télésièges sont équipés de SIVAO, permettant à Bluecime d'obtenir de plus en plus de données. Parallèlement, les processus de SIVAO évoluent pour améliorer les détections et faciliter la configuration du système. De plus, des projets de recherche sont actuellement en cours pour étendre l'éventail des détections. Par exemple, le système pourrait localiser, évaluer la hauteur et compter le nombre de passagers d'un véhicule : cela permettrait à Bluecime de donner à la station un aperçu de la présence et de la répartition des passagers dans le télésiège, ou d'avertir l'opérateur du télésiège si un enfant est seul dans un véhicule.

Même après une série d'améliorations du processus de configuration, la mise en place d'un système prend du temps pour les ingénieurs de Bluecime. De plus, pendant la saison de ski, de nouvelles conditions peuvent apparaître. Par exemple, la position du soleil change légèrement d'un mois à l'autre, de sorte que différentes ombres peuvent apparaître sur la vidéo, ce qui peut obliger Bluecime à reconfigurer manuellement le système. L'utilisation de techniques d'apprentissage automatique dans cette situation permettrait à Bluecime de configurer automatiquement le système. De plus, les performances des techniques d'apprentissage automatiques reposent sur une bonne généralisation des modèles appris. Cela rend les modèles plus robustes aux variations dans les données, telles que les nouvelles ombres mentionnées précédemment.

Depuis 2012, l'apprentissage profond donne des résultats remarquables, notamment dans le traitement de l'image, et attire ainsi de plus en plus l'attention de l'industrie. Dans ce contexte, Bluecime envisage d'utiliser des techniques d'apprentissage profond pour s'attaquer à leur problème de détection. De plus, SIVAO contient un ordinateur qui pourrait fournir la puissance de calcul requise par les techniques d'apprentissage profond. Cela rend ces techniques très prometteuses dans le contexte de Bluecime.

Cette thèse CIFRE est réalisée en collaboration avec Bluecime et le laboratoire Hubert Curien. Les objectifs sont de proposer des techniques d'apprentissage automatique (en particulier d'apprentissage profond) pour améliorer les performances de SIVAO et, plus généralement, améliorer les processus Bluecime.

Dans ce contexte, différentes contributions ont été apportées au cours de cette thèse :

Un cadre expérimental Nous proposons un cadre expérimental complet pour évaluer les cas d'utilisation possibles des approches d'apprentissage automatique dans le contexte de Bluecime. Ceci a été décrit dans l'article *Improving Chairlift Security with Deep Learning* à IDA 2017 (Bascol et al., 2017).

Une architecture de base Nous proposons une architecture d'apprentissage profond comme base de référence pour résoudre le problème de l'évaluation des risques de Bluecime. L'architecture utilise différentes techniques de pointe : une architecture de classification d'objets (ici : ResNet), une composante d'adaptation de domaine, et plusieurs augmentations de données et astuces d'apprentissage (certaines proposées comme contributions). Ces contributions ont été en partie présentées dans l'article intitulé *Improving Chairlift Security with Deep Learning* à IDA 2017 (Bascol et al., 2017).

Deux techniques d'optimisation de la F-mesure La F-mesure est une mesure de performance bien connue qui fournit un compromis entre le Rappel et la Précision d'un classifieur donné. En tant que telle, elle est bien adaptée lorsque l'on s'intéresse particulièrement à la performance du classifieur sur une classe donnée : celle en minorité (ici, celle en minorité est la classe risquée). Nous avons donc proposé deux méthodes pour mieux optimiser la performance de notre modèle en termes de F-mesure. Les deux méthodes consistent à pondérer chaque erreur commise lors de l'entraînement en fonction de l'étiquette de l'exemple correspondant. Tout d'abord, nous proposons une méthode adaptée à l'apprentissage itératif habituel d'un réseau neuronal. A chaque itération, l'entraînement est orienté par le gain en F-mesure que nous aurions pu obtenir à l'itération précédente sans faire l'erreur à pondérer. La deuxième méthode est une méthode itérative basée sur une borne théorique sur la F-mesure obtenue en entraînement. Les poids des classes dépendent d'un paramètre t. Avec un classifieur formé selon un t donné, la borne indique les valeurs F-mesure inaccessibles pour tout autre classifieur formé avec les valeurs t avoisinantes. Nous proposons un algorithme d'exploration qui élimine itérativement les valeurs F-mesure inaccessibles, permettant de tester un ensemble réduit de valeurs t. Cette deuxième méthode a été présentée dans *From Cost-Sensitive Classification to Tight F-measure Bounds* à AISTATS 2019 (Bascol et al., 2019b).

Une technique d'optimisation d'ensemble d'entraînement Les phases d'annotation des données et de configuration du système prennent beaucoup de temps mais sont nécessaires pour obtenir des résultats satisfaisants pour Bluecime et ses clients. Dans ce contexte, nous proposons d'entraîner un modèle spécialisé pour chaque télésiège nouvellement installé. Cependant, l'utilisation d'images de télésièges trop différentes de la nouvelle remontée peut nuire à la performance, ce phénomène est appelé *transfert négatif*. Pour résoudre ce problème, nous proposons de construire les ensembles d'entraînement de manière à ce qu'ils soient composés uniquement des télésièges déjà labellisés les plus proches visuellement de la nouvelle. Cette approche est présentée dans *Improving Domain Adaptation By Source Selection* à ICIP 2019 (Bascol et al., 2019a).

Une étude de l'adaptation de domaine avec un déséquilibre de classe variable Nous montrons que l'utilisation de l'adaptation de domaine dans un environnement multisource peut en fait nuire à la performance. Nous montrons que nous pouvons lier ce phénomène à la variation du rapport de déséquilibre entre les domaines sources et cibles. Compte tenu de ce constat, nous proposons deux façons d'améliorer notre approche dans un contexte multisource. Tout d'abord, l'utilisation de pseudo-étiquettes acquises à partir d'un modèle appris sans le domaine cible. La deuxième méthode consiste à changer notre technique d'adaptation de domaine de base pour une technique qui prend en compte la distribution des classes pendant l'adaptation de domaine.

Plan

Chapitre 1 Ce premier chapitre est consacré à la présentation de généralités sur l'apprentissage automatique dans le contexte de notre problème de sécurité des télésièges. Nous définissons d'abord les deux paradigmes d'apprentissage automatique que nous rencontrons dans cette thèse. Ensuite, nous explorons les algorithmes d'apprentissage automatique, en nous concentrant sur les algorithmes et architectures d'apprentissage profond, mais aussi en présentant d'autres algorithmes utilisés dans cette thèse. Ensuite, nous présentons le problème de l'adaptation de domaine et montrons les différentes techniques utilisées dans l'apprentissage automatique et en particulier les techniques basées sur l'apprentissage profond. Enfin, nous présentons le défi d'apprendre avec des ensembles de données déséquilibrés et des techniques pour optimiser la F-mesure.

Chapitre 2 Dans la première partie de ce second chapitre, nous présentons les ensembles de données utilisés lors de cette thèse: les ensembles de données de référence, puis, plus en détail, l'ensemble de données de Bluecime. Dans la deuxième partie, nous présentons nos cadres expérimentaux. Tout d'abord, la configuration des ensembles d'entraînement et de test, puis, les différentes mesures de performance que nous utilisons.

Chapitre 3 Nous proposons dans ce troisième chapitre deux contributions. Tout d'abord, une approche de base reposant sur de l'apprentissage profond et de l'adaptation du domaine. Nous montrons que cette approche présente un grand potentiel, même dans les situations les plus difficiles. Nous présentons ensuite notre deuxième contribution, qui est une nouvelle technique d'augmentation des données. Cette technique est basée sur l'occlusion de régions d'intérêt dans les images, ce qui permet de former un modèle plus robuste.

Chapitre 4 Ce quatrième chapitre nous permet de présenter nos contributions en optimisation de la F-mesure. Nous présentons, tout d'abord, notre méthode d'entraînement orienté par le gain en F-mesure. Nous montrons que cette méthode basée sur l'apprentissage avec pondération des erreurs nous permet de choisir le compromis entre la Précision et le Rappel. Nous présentons ensuite un autre algorithme pour optimiser la F-mesure. Cet algorithme est basé sur une limite théorique sur la F-mesure en fonction d'un poids appliqué à chaque classe.

Chapitre 5 Nous concluons cette thèse par un chapitre questionnant les résultats habituels de l'adaptation de domaine. Nous proposons, dans un premier temps, une méthode pour améliorer l'adaptation d'un domaine multisource en sélectionnant les sources appropriées pour un domaine cible. Cette méthode vise à réduire l'effet du *transfert négatif*. Ce phénomène altère les performances des méthodes d'adaptation de domaine lors de l'utilisation de domaines sources trop différents du domaine cible. Nous discutons ensuite des résultats de l'adaptation de domaine dans le cas d'une adaptation à partir de domaines sources multiples avec un rapport de déséquilibre variable. Nous montrons comment la variation du rapport de déséquilibre

dans l'ensemble d'entraînement peut impliquer que les techniques d'adaptation du domaine empirent les résultats. Nous proposons également des méthodes pour résoudre ce problème.

D.2 Résumés des chapitres

D.2.1 Chapitre 1

Dans ce premier chapitre nous proposons des connaissances de bases utiles à la compréhension de cette thèse. Nous commençons par des généralités sur l'apprentissage automatique, nous décrirons notamment l'apprentissage supervisé ou non et justifierons notre choix d'utiliser des approches supervisées. Nous continuerons avec la présentation de différents algorithmes d'apprentissage automatique. Tout d'abord nous présentons des algorithmes d'apprentissage profond, sur lesquels cette thèse se concentre. Nous partirons des premières et plus simples architectures profondes, pour ensuite montrer des architectures de pointe spécialisées dans les tâches de classification d'images, telles que le problème de Bluecime. Pour terminer sur l'apprentissage profond nous présentons différentes techniques et astuces utilisées pour optimiser l'entraînement d'architectures profondes. Nous présentons ensuite deux algorithmes d'apprentissage automatique que nous utilisons dans le chapitre 4: la régression logistique et les machines à vecteurs de support linéaires.

Par la suite nous introduisons le concept d'adaptation de domaine. Il s'agit d'apprendre un modèle à partir d'exemple étiquetés provenant d'une ou plusieurs distribution *source* pour l'appliquer sur des exemples non labellisés provenant d'une distribution *cible*. Nous présentons différentes techniques d'adaptation de domaine en général, puis nos donnerons plus de détails sur des méthodes spécifiques à apprentissage profond.

Nous finissons ce chapitre par la présentation des challenges induits par l'apprentissage de modèle sur des données déséquilibrées (c'est à dire ayant une ou plusieurs classes peu représentées dans les données). Nous introduisons alors la F-mesure, une mesure de performance conçue pour les cas déséquilibré, et présentons différents papiers tentant d'apprendre des modèles optimisant cette mesure.

D.2.2 Chapitre 2

Dans ce chapitre, nous commençons par introduire les différentes bases de données utilisées dans cette thèse. D'abord des bases de données ouvertes que nous utilisons pour fournir des résultats comparables à la littérature, mais aussi qui puissent être reproduites. Puis, nous présentons les données de Bluecime en détails.

Ensuite, nous présentons les différentes configurations de nos expériences. Nous proposons notamment trois principales configurations: OOC, où une expérience consiste à utiliser des données d'une même remontée en entraînement et en test. Cette configuration devrait donner les meilleurs résultats mais requière une importante quantité de données pour chaque télésiège. ALL, cette configuration consiste à mélanger, et dans l'ensemble d'entraînement et dans celui de test, les exemples provenant de toutes les remontées. Dans cette configurations, l'ensemble

d'entraînement est le plus fourni possible et présente une forte variété, utile à l'apprentissage de réseaux neuronaux, notamment pour améliorer la généralisation. Nous devrions donc, ici, obtenir de meilleurs résultats qu'avec la configuration OOC, notamment sur les remontées les moins représentées. La dernière configurations est LOCO, il s'agit d'utiliser les exemples d'une remontée en test et d'entraîner le modèles avec les exemples des autres remontées. Cette configuration simule les résultats de nos modèles dans le cas de télésièges nouvellement installés, et donc sans donnée étiqueté. Comme il s'agit d'utiliser des données d'autres remontées sur une remontées non étiqueté on s'attend ici à avoir de moins bonnes performances que OOC ou ALL. Cependant elle permet d'évaluer nos méthodes lors d'un démarrage à froid du système, voire d'étudier la possibilité de se passer d'étiquettes qui prennent du temps à obtenir.

Nous concluons ce chapitre par la présentation des mesures de performance utilisées pour évaluer les performances de nos méthodes dans les différentes configurations.

D.2.3 Chapitre 3

Ce chapitre est dédié à la présentation du choix de notre architecture de base, des stratégies d'augmentation de donnée que nous utilisons et que nous avons développées, et on conclue ce chapitre par la présentation des résultats de référence obtenus dans les différentes configurations introduites dans le chapitre précédent. Nous commençons donc par présenter en détails l'architecture ResNet que nous avons choisie d'utiliser dans cette thèse. Nous fournissons ensuite des détails sur l'entraînement (fonction de coût utilisée et constitution des minibatches). Nous montrons également une comparaison entre différentes architectures en termes de performances mais aussi de temps de calcul, ce qui nous mène à privilégier l'architecture ResNet.

Par la suite, nous présentons les augmentations de données que nous utilisons, puis la stratégie d'augmentation de données que nous proposons comme contribution. Cette stratégie consiste à masquer des zones dans les images au cours de l'entraînement. Si cacher une zone implique que l'image devient difficile à classer pour le réseau (voire implique une erreur de classification), on ajoute cette image à la base de données. Par ce processus nous augmentons la taille de la base de données, et en plus, nous ajoutons des images difficiles à classer. Cette stratégie nous permet donc d'éviter que le réseau ne se concentre que sur des zones réduites des images, ce qui le rend plus robuste.

Finalement nous montrons les performances de notre méthode de base sur les différentes configurations, nous montrons également l'apport de l'adaptation de domaine.

D.2.4 Chapitre 4

Ce chapitre nous permet d'introduire nos deux contributions pour l'optimisation de la F-mesure. Tout d'abord nous présentons une méthode basée sur l'apprentissage par pondération des erreurs guidant l'entraînement vers un gain en F-mesure. Régulièrement, pendant l'entraînement, les poids utilisés sont mis à jour comme suit : tout l'ensemble d'entraînement est passé dans le réseau pour obtenir les prédictions correspondantes, et à partir des ces

prédictions on obtient une valeur de F-mesure. Chaque erreur est alors pondérée selon la différence entre cette valeur de F-mesure et celle qu'on aurait obtenue si l'erreur n'avait pas été commise (donc si un faux négatif avait été un vrai positif, ou si un faux positive avait été un vrai négatif). On obtient donc un poids différent selon la classe de l'exemple correspondant, on va donc mettre plus de poids sur les classes impliquant le plus grand gain en F-mesure possible.

Notre seconde méthode d'optimisation de la F-mesure est également basée sur de l'apprentissage par pondération des erreurs. Nous avons aussi un poids différent pour chaque classe, qui, ici, dépend d'un paramètre t. Une borne théorique sur la F-mesure nous donne, à partir de la F-mesure obtenue par un classifieur entraîné avec un t donné, la F-mesure maximale que l'on peut obtenir avec un classifieur entraîné avec un paramètre t' dans le voisinage de t. Nous proposons donc un algorithme basé sur cette borne où on entraîne des classifieurs itérativement de sorte qu'on explore l'espace (Fm, t) jusqu'à converger vers la plus haute F-mesure atteignable selon notre borne.

D.2.5 Chapitre 5

Dans ce dernier chapitre, nous commençons par proposer une méthode pour améliorer l'adaptation de domaine, tout particulièrement dans le cas multisource. Cette méthode consiste à sélectionner les domaines sources les plus proches du domaine cible, afin d'éliminer les sources non pertinentes pouvant introduire le phénomène de "transfert négatif" nuisant aux performances du modèle. Cette méthode se déroule en 4 étapes : d'abord on calcul les distance entre le domaine cible et chaque domaine source (via la distance de Wasserstein). Ensuite on transforme ces distances via une fonction de score que l'on normalisera pour obtenir un vecteur de probabilités de sélection de domaine source. Durant cette étape, on ajoute un paramètre optimisé de sorte que les sources sélectionnées constituent un ensemble d'entraînement avec suffisamment de variété pour entraîner correctement le modèle. Finalement pendant l'entraînement, le vecteur de probabilités est utilisé pour modifier la distribution des domaines de sorte que les domaines les plus pertinents soient plus représentés que les domaines moins pertinents (qui peuvent être totalement éliminés).

Dans un second temps, nous nous proposons d'étudier les résultats d'adaptation de domaine dans le cas multisource avec une distribution de classe variable entre les domaines. En effet, on observe qu'utiliser une technique d'adaptation de domaine classique dans cette configuration peut impliquer une perte en performance par rapport à un modèle entraîné sans adaptation de domaine. À partir de cette observation nous évaluons deux solution possibles. D'abord l'utilisation de pseudo-étiquettes sur l'ensemble cible, obtenues à partir des prédictions d'un modèle entraîné uniquement sur les domaines sources. Ces pseudo-étiquettes nous permettent alors de changer artificiellement l'équilibrage des classes cibles et sources. Une deuxième solution consiste à utiliser une technique d'adaptation de domaine qui prend en compte la distribution des classes lors de l'adaptation. Nous proposons d'utiliser la méthode DeepJDOT.

D.3 Conclusion et perspectives

Dans cette thèse, nous avons étudié des techniques permettant d'aborder le problème de sécurité des télésièges de Bluecime et les différents défis qu'il implique :

1. la grande variété de télésièges et de conditions météorologiques ;
2. l'absence de données étiquetées (surtout pour les télésièges nouvellement installés) ;
3. le déséquilibre dans les données ;
4. la contrainte temps réel.

De plus, ces défis ne sont pas indépendants. Par exemple, nous avons vu que les techniques d'adaptation de domaine, utilisées pour résoudre les deux premiers défis, sont pénalisées par le troisième. Cependant, nous avons réussi à développer des techniques efficaces (basées principalement sur l'apprentissage profond) pour améliorer le système de Bluecime. Actuellement, des techniques d'apprentissage profond sont implémentées dans SIVAO, pour le comptage de passagers et la détection de bulles (la bulle de verre sur Chair. D dans la Fig. 2.2). Toutes deux offrent d'excellentes performances et confirment le potentiel des techniques basées sur l'apprentissage profond pour résoudre le problème de Bluecime.

Contributions

La première contribution présentée dans cette thèse consistait à fournir un pipeline complet de découverte des connaissances (définition des tâches, prétraitement des données, modèle et cadre d'évaluation) pour le jeu de données Bluecime. Nous avons proposé d'explorer des configurations entièrement supervisées (OOC et ALL), mais aussi une configuration simulant un télésiège nouvellement installé sans étiquette disponible (LOCO). Notre modèle de base repose sur une architecture d'apprentissage profond de pointe (ResNet) permettant de relever le premier défi dans un délai raisonnable, relevant ainsi le quatrième défi. Nous proposons également d'ajouter une composante d'adaptation de domaine pour relever le deuxième défi.

Les contributions qui suivent abordent plus spécifiquement les différents défis. Notre deuxième contribution consiste à améliorer la robustesse de notre approche (deux premiers défis) à l'aide d'une méthode de patch. Cette méthode consiste à créer de nouvelles images en masquant de petites zones qui étaient d'une importance critique pour le processus de classification du réseau. Ainsi, nous visons à forcer le réseau à utiliser l'image entière, c'est-à-dire à maximiser la quantité d'information utilisée par le réseau. Cette approche peut être considérée soit comme une augmentation des données, soit comme un moyen de régulariser le processus d'apprentissage (comme dans le cas du "dropout").

Nos troisième et quatrième contributions examinent toutes deux l'apprentissage avec pondération des erreurs afin d'optimiser la F-mesure. Cette mesure nous aide à nous concentrer sur les erreurs commises par notre classifieur sur la classe minoritaire (ici, les cas dangereux). L'optimiser au lieu de la précision habituelle permet de résoudre notre problème de déséquilibre de classe. Les deux méthodes ont donné de bons résultats qui peuvent être généralisés à d'autres applications. Ces méthodes nous ont permis de choisir le compromis

entre la Précision et le Rappel de notre système, ce qui est intéressant pour Bluecime puisque le nombre de faux positifs et de faux négatifs dépend, entre autres facteurs, du télésiège et de la distance entre le poste d'embarquement et la caméra SIVAO.

La cinquième contribution de cette thèse est une méthode pour résoudre le problème de l'adaptation dans un domaine multisource en sélectionnant les sources les plus pertinentes dans l'ensemble d'entraînement. Avec cette contribution, nous analysons le comportement de l'adaptation de domaine dans le contexte multisource mais aussi lorsque les distributions de classes varient entre les exemples source et cible. Nous nous interrogeons donc sur les connaissances générales de cette méthode et proposons quelques solutions pour ce contexte particulier qui sont également utiles à Bluecime.

Perspectives

De nombreuses possibilités d'améliorer nos différentes contributions restent à explorer. Notre approche de base pourrait être améliorée par une comparaison plus systématique des différentes architectures de la littérature. En effet, de nombreuses architectures existantes n'ont pas été prises en compte, principalement pour des raisons de temps, mais aussi parce que les modèles d'apprentissage profond sont constamment développés (et améliorés), ce qui rend difficile la mise à jour des connaissances actuelles. Sur notre approche de patch, nous pouvons encore explorer plus avant l'utilisation des positions précédentes des patchs sélectionnés. En particulier, nous pourrions augmenter différemment la probabilité qu'un emplacement de patch revienne, et la diminuer sur des emplacements induisant des patchs inintéressants. **CONE**, notre algorithme d'optimisation de la F-mesure, nous pourrions trouver un moyen de mieux l'adapter à l'apprentissage profond. Par exemple, nous pourrions utiliser les poids du premier modèle comme pré-entraînement pour le modèle suivant, ce qui réduirait le temps d'entraînement nécessaire pour obtenir suffisamment de classifieurs pour explorer l'espace (t, F). Sur la sélection des domaines sources, nous pourrions utiliser d'autres distances ou améliorer la distance actuelle. Par exemple, la distance basée sur l'autoencodeur dépend évidemment de l'entraînement des autoencodeurs, donc, modifier son architecture ou régler différemment les hyperparamètres (par exemple le taux d'apprentissage) peut grandement améliorer cette méthode. Nous pourrions également modifier notre terme de variété, par exemple en intégrant une contrainte sur un nombre minimum de sources sélectionnées. En effet, si un domaine est très bien représenté et "proche" du domaine cible, il peut être le seul sélectionné, induisant ainsi un ensemble d'entraînement peu varié. Nous devons encore explorer plus avant, théoriquement, les résultats négatifs de l'adaptation de domaine avec des distributions de classes différentes entre les exemples cible et source. Sur le plan pratique, nous pourrions améliorer nos méthodes de pseudo-étiquettes ou trouver une meilleure façon d'utiliser DeepJDOT dans un environnement multisource.

De plus, toutes ces méthodes ont été conçues indépendamment pour résoudre le problème initial proposé par Bluecime. Nous n'avons pas étudié si ces méthodes sont complémentaires, redondantes ou peut-être adverses pour atteindre notre objectif final. Nous pourrions toutes les utiliser et espérer le meilleur ou essayer de trouver la meilleure combinaison. Par exemple,

nous pourrions guider le patch en considérant le F-mesure et pas seulement la variation de la prédiction. Nous pourrions aussi essayer d'améliorer notre stratégie de sélection de domaine en utilisant, par exemple, le transport optimal contraint de Courty et al. (2014), lors du calcul de la distance de Wasserstein pour mieux prendre en compte les distributions des classes.

Enfin et surtout, dans le contexte de Bluecime, nous pourrions travailler à l'amélioration de l'efficacité du réseau. Ceci pourrait être fait, par exemple, en *élaguant* les poids inutiles dans le réseau, ou en *quantifiant* les poids (Han et al., 2015). Nous pourrions également explorer des moyens d'améliorer les performances des architectures plus petites, par exemple, avec *la distillation des connaissances* (Hinton et al., 2015). Disposer d'un réseau plus efficace présente deux avantages : l'avantage le plus évident est l'augmentation de la vitesse du modèle, ce qui nous permet d'avoir une approche en temps réel. Le deuxième avantage est la diminution de la charge de calcul et de mémoire requise par notre approche d'apprentissage profond. Cela permettrait à Bluecime de fournir d'autres services, tels que des statistiques en temps réel sur l'occupation du télésiège, sans avoir à améliorer le matériel du système.

Bibliography

Muhammad Jamal Afridi, Arun Ross, and Erik M Shapiro. On automated source selection for transfer learning in convolutional neural networks. *Pattern Recognition*, 73:65–75, 2018. 33

M. Baccouche, F. Mamalet, C. Wolf, C. Garcia, and A. Baskurt. Spatio-Temporal Convolutional Sparse Auto-Encoder for Sequence Classification. In *British Machine Vision Conference (BMVC)*, 2012. 102, 103

Kevin Bascol, Rémi Emonet, Elisa Fromont, and Jean-Marc Odobez. Unsupervised interpretable pattern discovery in time series using autoencoders. In *The joint IAPR International Workshops on Structural and Syntactic Pattern Recognition (SSPR 2016)*, 2016. 9

Kevin Bascol, Rémi Emonet, Elisa Fromont, and Raluca Debusschere. Improving chairlift security with deep learning. In *International Symposium on Intelligent Data Analysis (IDA 2017)*, 2017. 7, 44, 47, 142

Kevin Bascol, Rémi Emonet, Elisa Fromont, Amaury Habrard, Guillaume Metzler, and Marc Sebban. Un algorithme d'optimisation de la f-mesure par pondération des erreurs de classification. In *Conférence francophone sur l'Apprentissage Automatique (CAp-18)*, 2018.

Kevin Bascol, Rémi Emonet, and Elisa Fromont. Improving domain adaptation by source selection. In *2019 IEEE International Conference on Image Processing (ICIP)*, 2019a. 7, 75, 143

Kevin Bascol, Rémi Emonet, Elisa Fromont, Amaury Habrard, Guillaume Metzler, and Marc Sebban. From cost-sensitive classification to tight f-measure bounds. In *Proceedings of the Twenty-Second International Conference on Artificial Intelligence and Statistics (AISTATS-19)*, volume 89 of *Proceedings of Machine Learning Research*. PMLR, 2019b. 7, 59, 143

Shai Ben-David, John Blitzer, Koby Crammer, Alex Kulesza, Fernando Pereira, and Jennifer Wortman Vaughan. A theory of learning from different domains. *Machine Learning*, 79(1):151–175, May 2010. 21, 24

Jean-David Benamou, Guillaume Carlier, Marco Cuturi, Luca Nenna, and Gabriel Peyré. Iterative bregman projections for regularized transportation problems. *SIAM Journal on Scientific Computing*, 37(2):A1111–A1138, 2015. 26, 27

Yoshua Bengio, Pascal Lamblin, Dan Popovici, and Hugo Larochelle. Greedy layer-wise training of deep networks. In *Advances in neural information processing systems*, pages 153–160, 2007. 14

Himanshu S Bhatt, Arun Rajkumar, and Shourya Roy. Multi-source iterative adaptation for cross-domain classification. In *IJCAI*, pages 3691–3697, 2016. 24

Christopher M Bishop. *Pattern recognition and machine learning*. springer, 2006. 9, 21

John Blitzer, Ryan McDonald, and Fernando Pereira. Domain adaptation with structural correspondence learning. In *Proceedings of the 2006 conference on empirical methods in natural language processing*, pages 120–128. Association for Computational Linguistics, 2006. 23, 24

Olivier Bousquet, Stéphane Boucheron, and Gábor Lugosi. *Introduction to Statistical Learning Theory*, pages 169–207. Springer Berlin Heidelberg, 2004. 73

Stephen Boyd and Lieven Vandenberghe. *Convex Optimization*. Cambridge University Press, New York, NY, USA, 2004. ISBN 0521833787. 36

Kristian Bredies, Dirk A Lorenz, and Peter Maass. A generalized conditional gradient method and its connection to an iterative shrinkage method. *Computational Optimization and Applications*, 42(2):173–193, 2009. 26

Róbert Busa-Fekete, Balázs Szörényi, Krzysztof Dembczynski, and Eyke Hüllermeier. Online f-measure optimization. In *NIPS*, 2015. 35

Alberto Cambini and Laura Martein. *Generalized Convexity and Optimization: Theory and Applications*. Lecture Notes in Economics and Mathematical Systems 616. Springer-Verlag Berlin Heidelberg, 1 edition, 2009. ISBN 978-3-540-70875-9,978-3-540-70876-6. 63

Zhangjie Cao, Mingsheng Long, Jianmin Wang, and Michael I Jordan. Partial transfer learning with selective adversarial networks. In *Proceedings of the IEEE Conference on Computer Vision and Pattern Recognition*, pages 2724–2732, 2018. 29, 93

Fabio Maria Cariucci, Lorenzo Porzi, Barbara Caputo, Elisa Ricci, and Samuel Rota Bulò. Autodial: Automatic domain alignment layers. In *2017 IEEE International Conference on Computer Vision (ICCV)*, pages 5077–5085. IEEE, 2017. 30

Varun Chandola, Arindam Banerjee, and Vipin Kumar. Anomaly detection: A survey. *ACM Comput. Surv.*, 2009. 35

Chih-chung Chang and Chih-Jen Lin. Ijcnn 2001 challenge: Generalization ability and text decoding. In *IJCNN'01. International Joint Conference on Neural Networks. Proceedings (Cat. No. 01CH37222)*, volume 2, pages 1031–1036. IEEE, 2001. 39

Ken Chatfield, Karen Simonyan, Andrea Vedaldi, and Andrew Zisserman. Return of the devil in the details: Delving deep into convolutional nets. In *BMVC*, 2014. 18

Rita Chattopadhyay, Qian Sun, Wei Fan, Ian Davidson, Sethuraman Panchanathan, and Jieping Ye. Multisource domain adaptation and its application to early detection of fatigue. *ACM Transactions on Knowledge Discovery from Data (TKDD)*, 6(4):18, 2012. 23

T. Chockalingam, R. Emonet, and J-M. Odobez. Localized anomaly detection via hierarchical integrated activity discovery. In *AVSS*, 2013. 103

Nicolas Courty, Rémi Flamary, and Devis Tuia. Domain adaptation with regularized optimal transport. In *Joint European Conference on Machine Learning and Knowledge Discovery in Databases*, pages 274–289. Springer, 2014. 25, 26, 28, 90, 97, 150

Nicolas Courty, Rémi Flamary, Devis Tuia, and Alain Rakotomamonjy. Optimal transport for domain adaptation. *IEEE transactions on pattern analysis and machine intelligence*, 39 (9):1853–1865, 2016. 25

Nicolas Courty, Rémi Flamary, Amaury Habrard, and Alain Rakotomamonjy. Joint distribution optimal transportation for domain adaptation. In *Advances in Neural Information Processing Systems*, pages 3730–3739, 2017. 26, 33

Marco Cuturi. Sinkhorn distances: Lightspeed computation of optimal transport. In *Advances in neural information processing systems*, pages 2292–2300, 2013. 25, 26

Bharath Bhushan Damodaran, Benjamin Kellenberger, Rémi Flamary, Devis Tuia, and Nicolas Courty. Deepjdot: Deep joint distribution optimal transport for unsupervised domain adaptation. In *European Conference on Computer Vision*, pages 467–483. Springer, 2018. 33, 90, 91, 92, 115, 116

C. Darken and J. E. Moody. Note on learning rate schedules for stochastic optimization. In *NIPS*, pages 832–838, 1990. 105

Stijn Decubber, Thomas Mortier, Krzysztof Dembczynski, and Willem Waegeman. Deep f-measure maximization in multi-label classification: A comparative study. page 16, 2018. 35

Krzysztof Dembczyński, Wojciech Kotłowski, Oluwasanmi Koyejo, and Nagarajan Natarajan. Consistency analysis for binary classification revisited. In Doina Precup and Yee Whye Teh, editors, *Proceedings of the 34th International Conference on Machine Learning*, volume 70 of *Proceedings of Machine Learning Research*, pages 961–969, International Convention Centre, Sydney, Australia, 06–11 Aug 2017. PMLR. 35

Krzysztof J Dembczynski, Willem Waegeman, Weiwei Cheng, and Eyke Hüllermeier. An exact algorithm for f-measure maximization. In *NIPS*, 2011. 35

Jia Deng, Wei Dong, Richard Socher, Li-Jia Li, Kai Li, and Li Fei-Fei. Imagenet: A large-scale hierarchical image database. In *Computer Vision and Pattern Recognition, 2009. CVPR 2009. IEEE Conference on*, pages 248–255. Ieee, 2009. 18, 38, 79

Terrance DeVries and Graham W Taylor. Improved regularization of convolutional neural networks with cutout. *arXiv preprint arXiv:1708.04552*, 2017. 20, 52

X. Du, R. Jin, l. Ding, V.E. Lee, and J.H. Thornton. Migration motif: a spatial - temporal pattern mining approach for financial markets. In *KDD*, pages 1135–1144. ACM, 2009. 101

Dheeru Dua and Casey Graff. UCI machine learning repository, 2017. URL `http://archive.ics.uci.edu/ml`. 37

Lixin Duan, Dong Xu, and Shih-Fu Chang. Exploiting web images for event recognition in consumer videos: A multiple source domain adaptation approach. In *Computer Vision and Pattern Recognition (CVPR), 2012 IEEE Conference on*, pages 1338–1345. IEEE, 2012. 23

R. Emonet, J. Varadarajan, and J.-M. Odobez. Multi-camera open space human activity discovery for anomaly detection. In *IEEE Int. Conf. on Advanced Video and Signal-Based Surveillance (AVSS), Klagenfurt, Austria*, aug 2011. 101

R. Emonet, J. Varadarajan, and J-M. Odobez. Temporal analysis of motif mixtures using dirichlet processes. *IEEE PAMI*, 2014. 101, 102, 103, 107

Chen Fang, Ye Xu, and Daniel N Rockmore. Unbiased metric learning: On the utilization of multiple datasets and web images for softening bias. In *Proceedings of the IEEE International Conference on Computer Vision*, pages 1657–1664, 2013. 79

Li Fei-Fei, Rob Fergus, and Pietro Perona. Learning generative visual models from few training examples: An incremental bayesian approach tested on 101 object categories. *Computer vision and Image understanding*, 106(1):59–70, 2007. 37, 79

Damien Fourure, Rémi Emonet, Elisa Fromont, Damien Muselet, Alain Tremeau, and Christian Wolf. Residual conv-deconv grid network for semantic segmentation. In *BMVC 2017*, 2017. 19

Yaroslav Ganin, Evgeniya Ustinova, Hana Ajakan, Pascal Germain, Hugo Larochelle, François Laviolette, Mario Marchand, and Victor Lempitsky. Domain-adversarial training of neural networks. *The Journal of Machine Learning Research*, 17(1):2096–2030, 2016. 28, 29, 30, 31, 47, 76, 85, 86, 90

Léo Gautheron, Ievgen Redko, and Carole Lartizien. Feature selection for unsupervised domain adaptation using optimal transport. In *Joint European Conference on Machine Learning and Knowledge Discovery in Databases*, pages 759–776. Springer, 2018. 25

Liang Ge, Jing Gao, Hung Ngo, Kang Li, and Aidong Zhang. On handling negative transfer and imbalanced distributions in multiple source transfer learning. *Statistical Analysis and Data Mining: The ASA Data Science Journal*, 7(4):254–271, 2014. 23

Golnaz Ghiasi, Tsung-Yi Lin, and Quoc V Le. Dropblock: A regularization method for convolutional networks. In *Advances in Neural Information Processing Systems*, pages 10727–10737, 2018. 20

Boqing Gong, Yuan Shi, Fei Sha, and Kristen Grauman. Geodesic flow kernel for unsupervised domain adaptation. In *2012 IEEE Conference on Computer Vision and Pattern Recognition*, pages 2066–2073. IEEE, 2012. 79

Ian Goodfellow, Yoshua Bengio, and Aaron Courville. *Deep Learning*. MIT Press, 2016. `http://www.deeplearningbook.org`. 10, 15, 49

Yves Grandvalet and Yoshua Bengio. Semi-supervised learning by entropy minimization. In *Advances in neural information processing systems*, pages 529–536, 2005. 31

Gregory Griffin, Alex Holub, and Pietro Perona. Caltech-256 object category dataset. 2007. 37, 79

M. Marwah H. Shao and N. Ramakrishnan. A temporal motif mining approach to unsupervised energy disaggregation: Applications to residential and commercial buildings. In *Proceedings of the 27th AAAI conference*, 2013. 102

Song Han, Huizi Mao, and William J Dally. Deep compression: Compressing deep neural networks with pruning, trained quantization and huffman coding. *arXiv preprint arXiv:1510.00149*, 2015. 97, 150

Kaiming He, Xiangyu Zhang, Shaoqing Ren, and Jian Sun. Deep residual learning for image recognition. In *Computer Vision and Pattern Recognition (CVPR)*, 2016. 16, 47

G E Hinton and R R Salakhutdinov. *Science*, 313(5786):504–507, July 2006. 103

Geoffrey Hinton, Oriol Vinyals, and Jeff Dean. Distilling the knowledge in a neural network. *arXiv preprint arXiv:1503.02531*, 2015. 97, 150

Judy Hoffman, Dequan Wang, Fisher Yu, and Trevor Darrell. Fcns in the wild: Pixel-level adversarial and constraint-based adaptation. *arXiv preprint arXiv:1612.02649*, 2016. 86, 87

T. Hospedales, S. Gong, and T. Xiang. A markov clustering topic model for mining behavior in video. In *ICCV*, 2009. 107

Andrew G Howard, Menglong Zhu, Bo Chen, Dmitry Kalenichenko, Weijun Wang, Tobias Weyand, Marco Andreetto, and Hartwig Adam. Mobilenets: Efficient convolutional neural networks for mobile vision applications. *arXiv preprint arXiv:1704.04861*, 2017. 18

Sergey Ioffe and Christian Szegedy. Batch normalization: Accelerating deep network training by reducing internal covariate shift. In *ICML*, pages 448–456, 2015. 16, 19

Max Jaderberg, Karen Simonyan, Andrew Zisserman, et al. Spatial transformer networks. In *Advances in neural information processing systems*, pages 2017–2025, 2015. 43

M. Jansche. Maximum expected f-measure training of logistic regression models. In *EMNLP*, 2005. 35

T. Joachims. A support vector method for multivariate performance measures. In *ICML*, 2005. 35

Aditya Khosla, Tinghui Zhou, Tomasz Malisiewicz, Alexei A Efros, and Antonio Torralba. Undoing the damage of dataset bias. In *European Conference on Computer Vision*, pages 158–171. Springer, 2012. 79

Philip A Knight. The sinkhorn–knopp algorithm: convergence and applications. *SIAM Journal on Matrix Analysis and Applications*, 30(1):261–275, 2008. 25

J. Z. Kolter and T. Jaakkola. Approximate inference in additive factorial hmms with application to energy disaggregation. In *Proc. of AISTATS Conf.*, 2012. 101, 103

Oluwasanmi O Koyejo, Nagarajan Natarajan, Pradeep K Ravikumar, and Inderjit S Dhillon. Consistent binary classification with generalized performance metrics. In Z. Ghahramani, M. Welling, C. Cortes, N. D. Lawrence, and K. Q. Weinberger, editors, *Advances in Neural Information Processing Systems 27*, pages 2744–2752. Curran Associates, Inc., 2014. URL `http://papers.nips.cc/paper/5454-consistent-binary-classification-with-generalized-performance-metrics.pdf`. 35, 36, 62, 69, 70, 71, 131

Alex Krizhevsky, Ilya Sutskever, and Geoffrey E. Hinton. Imagenet classification with deep convolutional neural networks. In *NIPS*, 2012. 15

Yanghao Li, Naiyan Wang, Jianping Shi, Jiaying Liu, and Xiaodi Hou. Revisiting batch normalization for practical domain adaptation. *arXiv preprint arXiv:1603.04779*, 2016. 30

Victoria Lopez, Alberto Fernandez, Salvador Garcia, Vasile Palade, and Francisco Herrera. An insight into classification with imbalanced data: Empirical results and current trends on using data intrinsic characteristics. *Information Sciences*, 250:113 – 141, 2013. 35

L. Karlsson M. Längkvist and A. Loutfi. A review of unsupervised feature learning and deep learning for time-series modeling. *Pattern Recognition Letters*, 2014. 103

J. Masci, U. Meier, D. Cireşan, and J. Schmidhuber. Stacked convolutional auto-encoders for hierarchical feature extraction. In *Proc. of ICANN*, 2011. 104

N. A. Mehta and A. G. Gray. Funcica for time series pattern discovery. In *Proceedings of the SIAM International Conference on Data Mining*, pages 73–84, 2009. 103

R. Memisevic and G. E. Hinton. Unsupervised learning of image transformations. In *Computer Vision and PatternRecognition (CVPR)*, 2007. 103

Takeru Miyato, Shin-ichi Maeda, Masanori Koyama, and Shin Ishii. Virtual adversarial training: a regularization method for supervised and semi-supervised learning. *IEEE transactions on pattern analysis and machine intelligence*, 41(8):1979–1993, 2018. 32

Grégoire Montavon, Sebastian Lapuschkin, Alexander Binder, Wojciech Samek, and Klaus-Robert Müller. Explaining nonlinear classification decisions with deep taylor decomposition. *Pattern Recognition*, 65:211–222, 2017. 56

C. H. Mooney and J. F. Roddick. Sequential pattern mining – approaches and algorithms. *ACM Comput. Surv.*, 45(2):19:1–19:39, March 2013. 102

David R Musicant, Vipin Kumar, Aysel Ozgur, et al. Optimizing f-measure with support vector machines. In *FLAIRS*, 2003. 35

Harikrishna Narasimhan, Harish Ramaswamy, Aadirupa Saha, and Shivani Agarwal. Consistent multiclass algorithms for complex performance measures. In Francis Bach and David Blei, editors, *Proceedings of the 32nd International Conference on Machine Learning*, volume 37 of *Proceedings of Machine Learning Research*, pages 2398–2407, Lille, France, 07–09 Jul 2015. PMLR. 35, 36, 62, 69, 70, 71, 131

Tim Oates. Peruse: An unsupervised algorithm for finding recurring patterns in time series. In *ICDM*, 2002. 103

Shameem Puthiya Parambath, Nicolas Usunier, and Yves Grandvalet. Optimizing f-measures by cost-sensitive classification. In *NIPS*, pages 2123–2131, 2014. 35, 62, 66, 68, 69, 70, 71, 72, 122, 126, 127, 129, 131, 161, 162

Joan Pastor-Pellicer, Francisco Zamora-Martínez, Salvador España-Boquera, and María José Castro-Bleda. F-measure as the error function to train neural networks. In *International Work-Conference on Artificial Neural Networks*, pages 376–384. Springer, 2013. 36

S.K. Shevade P.M. Chinta, P. Balamurugan and M.N. Murty. Optimizing f-measure with non-convex loss and sparse linear classifiers. In *IJCNN*, 2013. 35

Danil Prokhorov. Ijcnn 2001 neural network competition. *Slide presentation in IJCNN*, 1:97, 2001. 38

M. Ranzato, C. Poultney, S. Chopra, and Y. LeCun. Efficient learning of sparse representations with an energy-based model. In *NIPS*. MIT Press, 2006. 103

T. Rapcsák. On pseudolinear functions. *European Journal of Operational Research*, 50(3): 353–360, feb 1991. doi: 10.1016/0377-2217(91)90267-y. URL `https://doi.org/10.1016/0377-2217(91)90267-y`. 63

Ievgen Redko, Nicolas Courty, Rémi Flamary, and Devis Tuia. Optimal transport for multi-source domain adaptation under target shift. *arXiv preprint arXiv:1803.04899*, 2018. 26, 89

Frank Rosenblatt. The perceptron: a probabilistic model for information storage and organization in the brain. *Psychological review*, 65(6):386, 1958. 10

Michael T Rosenstein, Zvika Marx, Leslie Pack Kaelbling, and Thomas G Dietterich. To transfer or not to transfer. In *NIPS 2005 workshop on transfer learning*, volume 898, pages 1–4, 2005. 22

Olga Russakovsky, Jia Deng, Hao Su, Jonathan Krause, Sanjeev Satheesh, Sean Ma, Zhiheng Huang, Andrej Karpathy, Aditya Khosla, Michael Bernstein, Alexander C. Berg, and Li Fei-Fei. ImageNet Large Scale Visual Recognition Challenge. *International Journal of Computer Vision (IJCV)*, 115(3):211–252, 2015. doi: 10.1007/s11263-015-0816-y. 38

Kate Saenko, Brian Kulis, Mario Fritz, and Trevor Darrell. Adapting visual category models to new domains. In *European conference on computer vision*, pages 213–226. Springer, 2010. 37, 79

A. Sallaberry, N. Pecheur, S. Bringay, M. Roche, and M. Teisseire. Sequential patterns mining and gene sequence visualization to discover novelty from microarray data. *Journal of Biomedical Informatics*, 44(5):760 – 774, 2011. 101

Mark Sandler, Andrew Howard, Menglong Zhu, Andrey Zhmoginov, and Liang-Chieh Chen. Mobilenetv2: Inverted residuals and linear bottlenecks. In *Proceedings of the IEEE Conference on Computer Vision and Pattern Recognition*, pages 4510–4520, 2018. 18

Amartya Sanyal, Pawan Kumar, Purushottam Kar, Sanjay Chawla, and Fabrizio Sebastiani. Optimizing non-decomposable measures with deep networks. *Machine Learning*, 107(8-10): 1597–1620, 2018. 36

Lex Razoux Schultz, Marco Loog, and Peyman Mohajerin Esfahani. Distance based source domain selection for sentiment classification. *arXiv preprint arXiv:1808.09271*, 2018. 34, 75

Ramprasaath R Selvaraju, Michael Cogswell, Abhishek Das, Ramakrishna Vedantam, Devi Parikh, and Dhruv Batra. Grad-cam: Visual explanations from deep networks via gradient-based localization. In *Proceedings of the IEEE International Conference on Computer Vision*, pages 618–626, 2017. 56

Jian Shen, Yanru Qu, Weinan Zhang, and Yong Yu. Wasserstein distance guided representation learning for domain adaptation. In *Thirty-Second AAAI Conference on Artificial Intelligence*, 2018. 32

Rui Shu, Hung H Bui, Hirokazu Narui, and Stefano Ermon. A dirt-t approach to unsupervised domain adaptation. In *Proc. 6th International Conference on Learning Representations*, 2018. 31

Karen Simonyan and Andrew Zisserman. Very deep convolutional networks for large-scale image recognition. *arXiv preprint arXiv:1409.1556*, 2014. 16

Nitish Srivastava, Geoffrey Hinton, Alex Krizhevsky, Ilya Sutskever, and Ruslan Salakhutdinov. Dropout: a simple way to prevent neural networks from overfitting. *The Journal of Machine Learning Research*, 15(1):1929–1958, 2014. 19, 20

Baochen Sun and Kate Saenko. Deep coral: Correlation alignment for deep domain adaptation. In *European Conference on Computer Vision*, pages 443–450. Springer, 2016. 30

Baochen Sun, Jiashi Feng, and Kate Saenko. Return of frustratingly easy domain adaptation. In *Thirtieth AAAI Conference on Artificial Intelligence*, 2016. 29

Christian Szegedy, Wei Liu, Yangqing Jia, Pierre Sermanet, Scott Reed, Dragomir Anguelov, Dumitru Erhan, Vincent Vanhoucke, and Andrew Rabinovich. Going deeper with convolutions. In *IEEE Conference on Computer Vision and Pattern Recognition*, pages 1–9, 2015. 16

Christian Szegedy, Sergey Ioffe, Vincent Vanhoucke, and Alexander A Alemi. Inception-v4, inception-resnet and the impact of residual connections on learning. In *Thirty-First AAAI Conference on Artificial Intelligence*, 2017. 16

R. Tavenard, R. Emonet, and J-M. Odobez. Time-sensitive topic models for action recognition in videos. In *Int. Conf. on Image Processing (ICIP)*, Mebourne, 2013. 103

Eric Tzeng, Judy Hoffman, Kate Saenko, and Trevor Darrell. Adversarial discriminative domain adaptation. In *2017 IEEE Conference on Computer Vision and Pattern Recognition, CVPR*, pages 2962–2971, 2017. 28, 30, 31

C. J. van Rijsbergen. Further experiments with hierarchic clustering in document retrieval. *Information Storage and Retrieval*, 10(1):1–14, 1974. 35, 46

J. Varadarajan, R. Emonet, and J.-M. Odobez. A sparsity constraint for topic models - application to temporal activity mining. In *NIPS Workshop on Practical Applications of Sparse Modeling: Open Issues and New Directions*, 2010. 105

J. Varadarajan, R. Emonet, and J-M. Odobez. A sequential topic model for mining recurrent activities from long term video logs. *Int. jl of computer vision*, 2013. 102, 107, 111

Cédric Villani. *Optimal transport: old and new*, volume 338. Springer Science & Business Media, 2008. 24

Pascal Vincent, Hugo Larochelle, Yoshua Bengio, and Pierre-Antoine Manzagol. Extracting and composing robust features with denoising autoencoders. In *Proceedings of the 25th international conference on Machine learning*, pages 1096–1103. ACM, 2008. 15

F. Zhou W.-S. Chu and F. De la Torre. Unsupervised temporal commonality discovery. In *Computer Vision – ECCV 2012*, 2012. 102

W.-C. Peng Y.-C. Chen and S.-Y. Lee. Mining temporal patterns in time interval-based data. *IEEE Transactions on Knowledge and Data Engineering*, 2015. 102

Nan Ye, Kian Ming Adam Chai, Wee Sun Lee, and Hai Leong Chieu. Optimizing f-measure: A tale of two approaches. In *Proceedings of the 29th International Conference on Machine Learning, ICML 2012*, 2012. 35

M. Yuan and Y. Lin. Model selection and estimation in regression with grouped variables. *Journal of the Royal Statistical Society (B)*, 68(1):49–67, 2006. 106

Matthew D. Zeiler and Rob Fergus. Visualizing and understanding convolutional networks. In *European Conference on Computer Vision*, pages 818–833. Springer, 2014. 14

Ming-Jie Zhao, Narayanan Edakunni, Adam Pocock, and Gavin Brown. Beyond fano's inequality: Bounds on the optimal f-score, ber, and cost-sensitive risk and their implications. *JMLR*, 2013. 35

Y. Zheng. Trajectory data mining: An overview. *ACM Trans. Intell. Syst. Technol.*, 6(3): 29:1–29:41, May 2015. ISSN 2157-6904. 103

Zhun Zhong, Liang Zheng, Guoliang Kang, Shaozi Li, and Yi Yang. Random erasing data augmentation. *arXiv preprint arXiv:1708.04896*, 2017. 20, 52

List of Figures

List of Tables

Abstract: Bluecime has designed a camera-based system to monitor the boarding station of chairlifts in ski resorts, which aims at increasing the safety of all passengers. This already successful system does not use any machine learning component and requires an expensive configuration step. Machine learning is a subfield of artificial intelligence which deals with studying and designing algorithms that can learn and acquire knowledge from examples for a given task. Such a task could be classifying safe or unsafe situations on chairlifts from examples of images already labeled with these two categories, called the training examples. The machine learning algorithm learns a model able to predict one of these two categories on unseen cases. Since 2012, it has been shown that deep learning models are the best suited machine learning models to deal with image classification problems when many training data are available. In this context, this PhD thesis, funded by Bluecime, aims at improving both the cost and the effectiveness of Bluecime's current system using deep learning. We first propose to formalize the Bluecime problem as a classification task with different training settings emulating use cases. We also propose a deep learning baseline providing competitive results in most of the settings, for a low configuration cost. We then propose different approaches to improve our baseline method. First, a data augmentation strategy to improve the robustness of our model. Then, two methods to better optimize the F-measure, a performance measure used in anomaly detection and better suited to evaluate our imbalanced problem than the usual accuracy measure. Finally, we propose selection strategies for the training data to improve results on newly installed chairlift for which no labeled training data is available. With this work we also show negative but interesting results on domain adaption in case of different imbalanced class distributions between the source and target domains.

Résumé: Bluecime a mis au point un système de vidéosurveillance à l'embarquement de télésièges qui a pour but d'améliorer la sécurité des passagers. Ce système est déjà performant, mais il n'utilise pas de techniques d'apprentissage automatique et nécessite une phase de configuration chronophage. L'apprentissage automatique est un sous-domaine de l'intelligence artificielle qui traite de l'étude et de la conception d'algorithmes pouvant apprendre et acquérir des connaissances à partir d'exemples pour une tâche donnée. Une telle tâche pourrait consister à classer les situations sûres ou dangereuses dans les télésièges à partir d'exemples d'images déjà étiquetées dans ces deux catégories, appelés exemples d'entraînement. L'algorithme d'apprentissage automatique apprend un modèle capable de prédire la catégories de nouveaux cas. Depuis 2012, il a été démontré que les modèles d'apprentissage profond sont les modèles d'apprentissage machine les mieux adaptés pour traiter les problèmes de classification d'images lorsque de nombreuses données d'entraînement sont disponibles. Dans ce contexte, cette thèse, financée par Bluecime, vise à améliorer à la fois le coût et l'efficacité du système actuel de Bluecime grâce à l'apprentissage profond. Nous proposons d'abord de formaliser le problème de Bluecime en tant que tâche de classification avec différents paramètres d'entraînement simulant des cas d'utilisation. Nous proposons également une approche par apprentissage profond fournissant des résultats compétitifs dans la plupart des paramètres d'entraînement, pour un faible coût de configuration. Nous proposons ensuite différentes approches pour améliorer notre méthode de référence. Tout d'abord, une stratégie d'augmentation des données pour améliorer la robustesse de notre modèle. Ensuite, deux méthodes pour mieux optimiser la F-measure, une mesure de performance utilisée dans la détection d'anomalies et mieux adaptée pour évaluer notre problème de déséquilibre que la mesure de précision habituelle. Enfin, nous proposons des stratégies de sélection des données d'entraînement afin d'améliorer les résultats sur les télésièges nouvellement installés pour lesquels aucune donnée d'entraînement étiquetée n'est disponible. Avec ces travaux, nous montrons également des résultats négatifs mais intéressants sur l'adaptation des domaines dans le cas de distributions de classes déséquilibrées différemment entre le domaine source et le domaine cible.